UNIVERSITÀ DEGLI STUDI
DI GENOVA

Corso di Dottorato in Geofisica
Scuola di Dottorato di Scienze e Tecnologie per l'Ingegneria (ciclo XXIV)

Tesi di Dottorato

INFORMATION FROM SEISMIC AMBIENT NOISE:
TECHNIQUES TO INVESTIGATE GEOLOGICAL PROPERTIES

Chiara Ladina

Tutor interno:
Prof. Daniele Spallarossa (Università di Genova, Dip.Te.Ris.)

Tutor esterno:
Dr. Simone Marzorati (INGV-Centro Nazionale Terremoti)

INDEX

1. Introduzione

Questa ricerca si propone come spunto per approfondire la conoscenza delle caratteristiche del *noise* sismico ambientale attraverso osservazioni di dati sperimentali.

L'utilizzo di registrazioni di **noise** sismico ambientale è funzionale alla conoscenza del segnale che si sta trattando e alla strumentazione impiegata. Le prime informazioni per quanto riguarda l'analisi del noise riguardano la sua origine e la sua natura. Inoltre il segnale sismico ambientale riguarda un'ampia banda di frequenze, la quale potrebbe non essere intercettata completamente da un sensore sismico oppure con ampiezze così ridotte da non essere riprodotte dal sistema di registrazione (per limiti di fabbricazione dello strumento). Quindi prima di effettuare una qualsiasi indagine di *noise* sismico ambientale è necessario saper scegliere la giusta strumentazione. Lo strumento deve poter rappresentare le frequenze volute e restituire il segnale.

Ad oggi gli strumenti hanno un elevato livello tecnologico tale da poter registrare il segnale generato da un sensore sollecitato dal moto del terreno. Alle registrazioni dei terremoti si sovrappongono registrazioni di altri segnali che hanno differenti origine e che degradano la qualità della traccia sismica. Questo tipo di segnale che interferisce con la registrazione di un terremoto è definito rumore: '*noise*'. Recentemente, per alcune applicazioni sismologiche si è preferito utilizzare rumore sismico ambientale rispetto a registrazioni di terremoti. Il *noise* è generato da sorgenti che immettono energia nel terreno che tende a propagarsi sotto forma di onde. Il noise generalmente produce vibrazioni continue del terreno dette microtremori (Okada, 2003). In zone urbanizzate le sorgenti del *noise* possono essere un qualsiasi strumento meccanico che interagisce col terreno. Questo noise è definito antropico, cioè causato dall'attività dell'uomo, ed ha contenuto in frequenza a partire da circa 1 Hz. Il *noise* ambientale, invece, non viene percepito dall'uomo ed è prodotto da sorgenti naturali a frequenze più basse (0.1-1 Hz).

I microtremori sono utilizzati comunemente in sismologia in quanto lo studio dell'origine e sulla natura del rumore sismico sono stati approfonditi. Quindi il noise sismico viene ricercato ed utilizzato per molti studi; esso è composto da diversi tipi di onde elastiche: onde di Rayleigh e Love, che forniscono informazioni anche di tipo geologico sul sottosuolo. La situazione più semplice che permette lo studio delle onde è 1D, in questo caso la velocità delle onde di taglio è un parametro fondamentale (Vs). questo parametro può essere individuato attraverso metodi come SASW (Spectral Analysis of Superficial Waves), processi di inversione permettono di ricavare profili di velocità.

Utilizzando le tecniche dei rapporti spettrali, è possibile determinare l'amplificazione delle ordinate spettrali del moto orizzontale di un sito rispetto ad uno di riferimento (SSR, Standard Spectral

Ratio: Borcherdt, 1970), oppure è possibile calcolare la funzione di trasferimento attraverso il rapporto tra lo spettro della componente orizzontale del moto rispetto a quella verticale (HVSR, Horizontal to Vertical Spectral Ratio: Lermo and Chavez-Garcia, 1993). Tali tecniche necessitano di un buon rapporto segnale/disturbo in modo da rappresentare le proprietà medie del mezzo di propagazione.

Lo studio delle strutture geologiche locali e superficiali è legato al fatto che esse siano la causa determinante degli 'effetti di sito' generati dalla propagazione delle onde di un terremoto in prossimità della superficie terrestre.

Studi di forti terremoti hanno evidenziato nel tempo come le caratteristiche geologiche superficiali possono determinare amplificazioni e prolungamento della sollecitazione del moto sismico del terreno. L'entità dei danni subiti in alcune aree poste all'interno di bacini sedimentari ha dato un forte impulso agli studi di microzonazione con lo scopo di ridurre e mitigare il rischio sismico.

Gli effetti di sito sono legati alla topografia superficiale del substrato affiorante o sommerso, presenza di sedimenti soffici e presenza di forti discontinuità laterali. Le maggiori amplificazioni sono state osservate su stratificazioni sedimentarie tipo bacini lacustri o valli riempite di sedimenti alluvionali (Bindi et al., 2001, Shapiro et al. 2001; Boore, 2004). L'applicazione di tecniche per ottenere informazioni sulle caratteristiche geologiche e geotecniche, utili per gli effetti di sito, incontra problemi pratici quando gli esperimenti vengono effettuati in zone altamente urbanizzate. Queste difficoltà pratiche sono state superate utilizzando metodi basati sullo studio dei microtremori, i quali sempre presenti in ogni momento, hanno un ampio contenuto in frequenza e sono composti principalmente da onde superficiali. Con i microtremori è possibile ottenere informazioni sui periodi dei picchi di amplificazione (tecnica dei rapporti spettrali di Nakamaura: Nakamura, 1989), mentre attraverso tecniche in array vengono ricavate le curve di dispersione per ottenere profili di velocità degli strati geologici superficiali.

La raccolta dei dati utilizzati in questa ricerca è stata svolta in questi tre anni di lavoro.

I dati sono stati reperiti attraverso campagne sismiche di misura con lo scopo di apprendere le modalità di acquisizione del dato direttamente sul campo. Le campagne di misure sono state eseguite a seguito del terremoto de L'Aquila del 6 Aprile 2009. Questo tipo di attività è stato eseguito con l'ausilio di stazioni sismiche velocimetriche ed accelerometriche disponibili della Sezione di Milano dell'Istituto Nazionale di Geofisica e Vulcanologia (INGV-MI) nell'ambito dell'attività di microzonazione svolta con il Dipartimento di Protezione Civile (DPC). In particolare sempre a causa del terremoto del 6 Aprile uno studio particolare è stato richiesto per il paese di Castelvecchio Subequo. Questo centro abitato sorge a 40 km di distanza della zona epicentrale ma

ha riscontrato un elevato livello di danno ritenuto elevato per la distanza del centro dall'epicentro del terremoto. Il paese come molti altri vicini ha subito un differente livello di danno tra la zona centrale, nonché parte più storica del paese e la zona relativamente più moderna. Una caratteristica specifica di questo centro è inoltre la conformazione geologica e morfologica del rilievo sul quale è costruito. Infatti, la litologia è caratterizzata da un diverso grado di fratturazione lungo la sua dorsale. A questo scopo due diverse campagne di misura per registrare il noise sismico sono state eseguite. La prima ha interessato la parte abitata del paese con maggior attenzione per la parte storica e la seconda uno studio più approfondito delle caratteristiche geologiche della formazione rocciosa e la relativa risposta sismica. La prima parte ha portato ad eseguire misure nella parte centrale e sul lato orientale ed occidentale del paese. Questo ha permesso di verificare la diversa amplificazione nelle varie parti del paese. Inoltre alcune misure sono state svolte anche in rilievi di interessi pubblico, come ad esempio la scuola elementare e vicino alla Chiesa.

La seconda parte ha permesso di caratterizzare i pinnacoli che si trovano alla fine del paese e che coincidono con la parte finale del centro storico. Su queste strutture sono state eseguite misure di noise sismico alla base e in sommità. Queste misure hanno mostrato che queste strutture non hanno nessun tipo di amplificazione e che quindi i danni all'interno del paese sono dati da una concomitanza di caratteristiche geologiche e morfologiche insieme.

Visto la particolare posizione del paese si è anche installata una rete di monitoraggio composta da tre stazioni: una sulle pendici del Monte Urano, una alla base e una installata su roccia nella parte finale del centro storico. Il M. Urano si trova vicino all'abitato di Castelvecchio Subequo. Questa attività di monitoraggio ha permesso di verificare il diverso grado di amplificazione. È risultata maggiormente amplificata la componente orizzontale registrata nel centro storico.

Un'attività parallela, ma sempre riguardante campagne di misure sismica, si è svolta nella conca Subequana. Lo scopo di questa attività è stato quello di ricostruire attraverso osservazioni geologiche, del gruppo geologico che stava studiando l'area, e analisi di registrazioni sismiche l'ipotetico andamento in profondità del substrato roccioso. Le osservazioni geologiche hanno evidenziato diverse litologie per l'area e un graduale passaggio da una formazione rocciosa a sedimenti proprio nella zona della conca. Il passaggio dalla formazione rocciosa ai sedimenti sarebbe poi marcato da un segmento della faglia della conca Subequana. Le indagini geofisiche e geologiche si sono ritrovate concordi sui relativi risultati e hanno permesso di ipotizzare l'approfondimento della valle.

In questa attività di campagna i dati sono stati reperiti direttamente sul terreno ed in seguito sono stati analizzati con la tecnica Horizontal to Vertical Spectra Ratio (HVSR), utilizzata sia per quanto riguarda il noise che per le registrazioni dei terremoti della rete temporanea di monitoraggio.

L’analisi del dato, il suo processamento ha interessato maggiormente la seconda fase del lavoro. In questa fase il reperimento di dati è stato eseguito direttamente presso la sede di Ancona del Centro Nazionale Terremoti (CNT). I dati in questo caso sono stati analizzati a partire dal loro formato originale, in questo caso MSEED, fino alla trasformazione nel formato richiesto per eseguire le analisi. In particolare ci si è interessati dell’area dell’Alto Val Tiberina una zona a confine tra Umbria-Marche. Quest’area, ritenuta sede ci continua attività sismica, è monitorata da una rete di monitoraggio che permette di raccogliere i dati in continuo. Questi dati possono essere reperiti presso la Sede di Ancona, dove vengono archiviati e una parte di questi viene inviata al centro acquisizione di Roma del CNT. Questi dati sono stati processati attraverso il calcolo delle cross-correlazioni utilizzando la tecnica Multi Window Cross-Spectrum (MWCS) per la prima volta eseguita da Poupinet et al. (1984). L’utilizzo di questa tecnica ha permesso di ottenere variazioni di velocità dell’area interessata confrontando i dati con l’attività sismica della zone e la possibile influenza di microsismi nelle variazioni riscontrate.

Quindi una parte importante e considerevole di questo lavoro è stata l’esperienza acquisita durante l’attività di campo per l’installazione delle stazioni sismiche, la loro manutenzione e la consistente attività di processamento con l’applicazione di procedure di conversione dai dati originali in dati utili per le analisi.

Chapter 2.

Site effects investigated by seismic ambient noise temporary measurements

In seismology the study of the site effects due to local geological properties is important to understand the causes to evaluate the seismic risk. The site effects are geologic, geotechnical and physical.

The seismic effects are influenced by lithological features of the superficial structures. These structures may induce resonance phenomena caused by the topography of the surface layers.

The influence of local site conditions on the amplitude of ground motion is supported by damage evidences after earthquakes such as on November 23, 1980, Mw 6.9, Irpinia earthquake (Faccioli, 1986), on March 3,1985, Mw 7.8, Chile earthquake (Celebi, 1987), on August 17, 1999, Mw 7.6, Izmit earthquake (Sadik Bakir et al., 2002), on April 6, 2009, Mw 6.3, L'Aquila earthquake (Cultrera- Luzi et al., 2009), and many experimental studies performed in different settings (alluvial basin or topographies) (Celebi, 1987; Paolucci, 1999; Zawlaski and Shapira, 2000; Fletcher et al., 2003; Spudich et al., 2006; Ferretti et al., 2007; Bindi at al., 2009; Buech et al., 2010).

The site effects are the causes for local seismic amplifications for the geological properties of the soils; topographic effects; induced effects such as rock collapses, landslides, subsidence.

Besides, the seismic amplification phenomena due to stratigraphic effects, it can be considered amplification phenomena such as a deep alluvial basin (for example Gubbio basin, Bindi et al., 2009) whose studies are fundamental for microzonation of big urban areas developed in correspondence of alluvial valley. The seismic response of a valley depend on its geometry. In this case the surface waves are trapped in the basin and are subjected to reflections with basin edge. Also the surface waves interfere each others and with the body waves. A consequence is a different local response. In particular, for the stations installed at edges of the basin and those ones installed in the centre there is a difference in the amplitude and in the duration of the seismic motion. An example is the Gubbio earthquake, Ml 3.6 (Bindi et al., 2009).

Structural damage near topographic irregularities such as ridge means that this type of morphology might be affected by the propagation of seismic motion leading amplified ground-shaking.

Several studies pointed out the occurrence of seismic amplifications along topographic 'irregularities' (Bard 1982; Çelebi 1987; Kawase and Aki 1990; Ponti and Wells 1991; Pedersen 1994; Chávez-García et al. 1996; Spudich et al. 1996; Athanasopoulos et al. 1999; Faccioli et al. 2002; Massa et al. 2010; Pischiutta et al. 2010). In particular, the morphological conditions are used to simulate the amplification on hills and crests (Boore 1972; Griffiths and Bollinger 1979; Sanchez-Sesma et al. 1982; Bard and Tucker 1985; Sánchez-Seisma 1985; Géli and Bard 1988; Sánchez-Seisma 1990; Sánchez-Sesma and Campillo 1991; Chávez-García et al. 1996; Bouchon and Barker 1996; Komatitsch and Vilotte 1998; Le Brun et al. 1999; Paolucci 2002). In many cases the simulations underestimate the amplifications, then in other case studies seismic amplification

are explained with surface weathering (Le Brun et al. 1999; Graizer 2009), presenxce of faults (Rovelli et al. 2002), and the jointing conditions of the rock masses (Martino et al. 2006; Hailemikael et al. 2010).

Seismic amplification caused by topographic irregularities were observed during the past earthquakes. In the past, same examples from June 11, 1909, Mw 6.0, Lambesc earthquake (Levret, 1986), March 27,1964, Mw 9.2, Alaska earthquake (Idriss and Seed, 1967), February 9, 1971, Mw 6.6, San Ferdinando earthquake (Davis and West, 1973), March 3, 1985, Mw 7.8, Chile earthquake (Celebi, 1987) up to September 26, 1997, Mw 6.0,

Umbria-Marche earthquake (Marra et al., 2000; Marsan et al., 2000; Donati et al., 2001; Pischiutta et al., 2010), October 31, 2002, Mw 5.6, Molise earthquake (Massa et al., 2004) and recent April 6, 2009, Mw 6.3, Aquila earthquake (Marzorati et al., 2011).

In all of these cases the observations of damages near topographic irregularities have suggested that the morphology of the relief plays an important role in the propagation of seismic waves. So, the topographic effects are very important for seismic hazard evaluation related to many historical centres built at the top of the ridge or in correspondence of very steep hillsides (Lovati, 2011).

Boore (1972) declared that amplification involving the whole relief might be due to the resonance of the whole relief with the incident seismic-field. Bard (1982) attributed the variations of seismic motion, relatively to isolated relief, to different physical phenomena such as the interaction between incident and diffraction waves.

Experimental studies highlighted the high level of damage suffered by buildings, locate on topographic profile; also, the concentration of damage might be strongly influenced by different structural typology. In recent years, during earthquakes local site effects have been documented site effects, in these cases the empirical data pointed out that topography, in particular at the crest of a hill, might strong affect ground motion, but the topographic effects are not considered. The reason is the difficulty to separate the contribution of seismic motion at the top pf the hill might be caused by other factors: fractured rocks or fault zones. The difficult in the studies is to find a good reference site, on the top of the relief, considering that both reference site and the site on the top should be have the same geological features (Celebi, 1987; Geli at al. 1988; Chavez-Garcia et al., 1996; Chavez- Garcia et al., 1997).

The numerical models allow to reproduce the complex geometric configurations of the topographic reliefs. Many numerical methods are at present available for the computation of the seismic response of two or three dimensional topographic irregularities superimposed to a homogeneous half-space (Lovati, 2011). Some example are the *finite difference method* (Boore, 1972; Zahradnik and Urban, 1984), the *finite elements method* (Smith, 1975), the *integral equation method* (Sills,

1978), the *boundary methods* (Sanchez-Sesma et al., 1982), the *discrete wavenumber methods* (Bouchon, 1973; Bard, 1982) and the *spectral methods* (Kosloff et al., 1990).

The main features and/or parameters on which numerical model of topographic effects are based are: the shape of the relief; the physical features of ground; the shape ratio H/L, where H is the height of the relief and L is the half-width at the base; the type of incident waves (P, SH, SV or Rayleigh waves); the angle of incidence θ, measured respect to the vertical axis (Lovati, 2011).

In a recent work of Paolucci (2002) are reported some example of 3D numerical investigation of seismic site response, based on the spectral element approximation of real topographic profiles selected from the Italian geological context.

Few evidences exist about topographical site effects. The difficulty is to isolate the real entity of topographical effects and the quality of the seismic data that allow comparisons with theoretical models. Theoretical studies (Bard, 1982; Paolucci, 1999 and 2002) predict that topography affects motion at frequencies inversely proportional to the topographic feature's wavelength (width at the base of the relief).

The seismic data obtained from measurements are processed through different methodologies based on spectral analyses. Ambient seismic noise and earthquakes records can be processed with Horizontal to Vertical Spectral Ratio (HVSR). For seismic noise the technique (NHVSR) was described by Nogoshi and Igarashi (1970) and Nakamura (1989), for earthquakes by Lermo and Chavez-Garcia (1993). Borcherdt (1970) proposed the Standard Spectral Ratio (SSR) on earthquakes data and it is the ratio between the spectra calculated at a site where site effects are investigated and a reference site where there aren't site effects.

The difficult, in the case of topographic effects, is to find a good reference site, for this reason the authors used the HVSR from earthquakes and the seismic noise. Also the SSR technique, if possible, is used together. Here, the difficult is to find a reference site that is free of any site effects.

Nogoshi and Igarashi (1971) were the first to propose a method based on the use of single station microtremors. This method has become of common use only after Nakamura (1989) with the name of "Nakamura's Technique", it provides to obtain reliable ground characteristics with very simple and inexpensive noise measurements. The first articles (including Nakamura and Samizo 1989; Nakamura and Takizawa, 1990; Ohmachi et al., 1991; Nakamura et al., 1999) are all set to the simple application of the technique, without involving the theoretical aspects on which the technique is based. Also, after the Warrior – Michoacan earthquake (Mexico, 1985), it was evident that the curves obtained from measurements of noise were consistent with the observations based on seismic events (Bard, 1998). Nogoshi and Igarashi (1971) apply the normalization of the horizontal component with the aim to reduce the effects of the source. The method calculates the two spectra

of a horizontal signal recorded by a station; the two spectra then are compounds through a geometric mean or through the average Root Mean Square (RMS), to obtain a horizontal spectrum, which is used with the spectrum of the vertical component. Following their observations, Nogoshi and Igarashi (1971) observed that a NHVSR peak corresponds to the site fundamental resonance frequency under certain conditions. Nakamura (1989) stated that the NHVSR provides exactly the transfer function for the S-waves. The fundamental frequency is the frequency below which there is no significant amplification of the surface ground during a seismic events. This method is based on the hypothesis of the sedimentary plane layers.

Many studies focused their study on the theoretical basis of the method (Field and Jacob, 1993; Nakamura, 1996 and 2000; Bard, 1998; Fäh et al., 2001) and in several articles is proposed a model HVSR using the Rayleigh waves (Field and Jacob, 1993, 1995; Lachet and Bard, 1994; Bonilla et al., 1997; Bard, 1998; Konno and Ohmaci, 1998; Athanasopoulos et al. 2000; Liu et al., 2000).

The technique is compared with the results obtained from analysis of observed earthquakes, using different techniques including the SSR. Various authors found differences in the results obtained with the SSR and the NHVSR, observing instability of the value of the amplification factor (Dravinski et al., 1996; Rovelli et al. 1991; Seekins et al., 1996; Ogawa et al ., 1998). The interpretation of Nakamura of NHVSR is based on the presence of the waves in the volume and it minimizes the influence of surface waves against the thesis that connect NHVSR curves with the ellipticity of the Rayleigh curves.

2.1 Site effects in the Subequana Valley (SV) and Castelvecchio Subequo (CS)

On April 6, 2009, the central Apennines have been struck by a Mw 6.3 earthquake. The earthquake damaged the populated L'Aquila plain area and surroundings, causing destruction in L'Aquila and in tens of villages. The intensity distribution revealed an evident anomaly in the southern portion of the damage region, in the Subequana Valley (SV): here, Is=7, 6-7 and 7 were indeed attributed to three villages, Castelvecchio Subequo, Castel di Ieri and Goriano Sicoli, located among other that were affected by evidently lower damage.

In particular, Castelvecchio Subequo (CS) showed an 'anomalous' distribution of damage. This case is considered anomalous for the distance of about 40 km and the damage irregularly distributed within CS and concentrated in the uppermost portion of the old village. Geophysical investigations (ambient seismic noise and weak ground motions analyses) reveals site effects occurred at CS (Marzorati et al., 2011).

In the following chapter was analyses the Castelvecchio Subequo case, aiming at unveiling the possible cause of the anomalous MCS intensity and the irregular distribution of the damage within the village. Also, was evaluated the possible occurrence of site effects along the narrow carbonate ridge on which the village is built by means of ambient seismic noise and weak ground motions analyses.

2.1.1 Seismotectonic framework of the central Apennines

The Apennine belt formed since the Oligocene, during the Alpine-Himalayan orogenesis. The central of the chain is represented by thrust and fold systems that progressively migrated towards E and NE, displacing Meso-Cenozoic limestone sequences (Patacca et al. 2008).

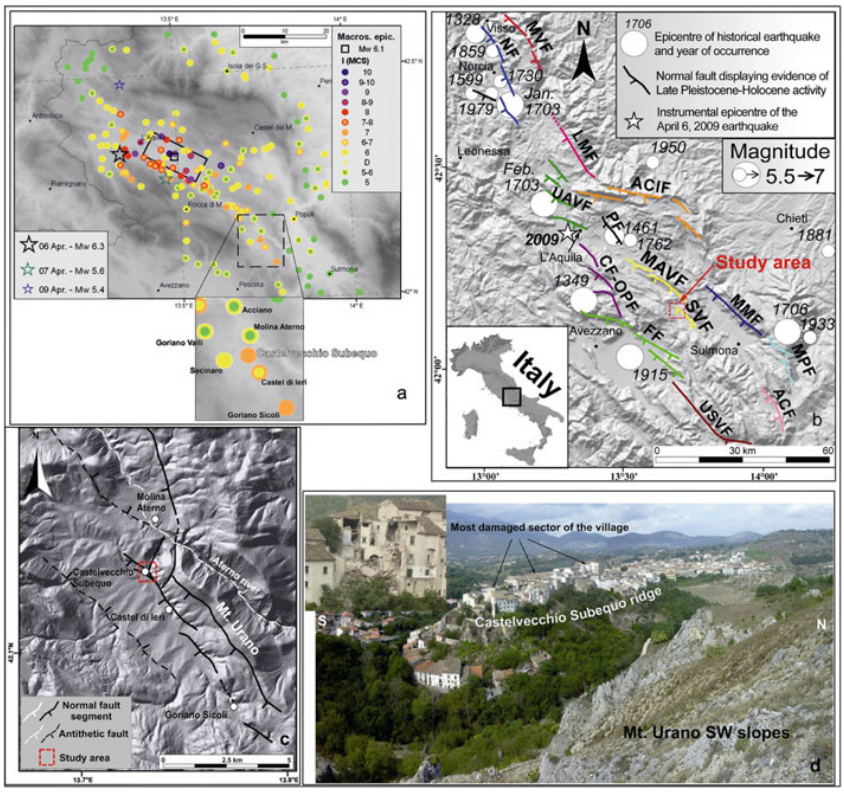

Figure1. a Intensity (Mercalli-Cancani-Sieberg scale; distribution of the 2009 L'Aquila earthquake; b Seismotectonic framework of the central Apennines (modified after Galadini et al. 2009). Faults: MVEF, Mt. Vettore; NFS, Norcia; LMF, Laga Mts.; UAVFS, upper Aterno Valley; CIFS, Campo Imperatore; CF-OPF, Campo Felice-Ovindoli-Pezza; MAVFS, middle Aterno Valley; SVF, Subequana Valley; MMF,Mt. Morrone; FF, Fucino; MPF, Maiella-Porrara; ACF, Aremogna-Cinquemiglia; USFS, upper Sangro Valley; red rectangle, the area analysed in the present work; c shaded relief of the Subequana Valley; *red* rectangle, the area under investigation; fault traces, according to Falcucci et al. (2011); d panoramic view of the Castelvecchio Subequo limestone ridge; partly collapsed edifices at the uppermost portion of the ridge, inset (from Marzorati et al., 2011).

Since the Pliocene, extensional deformation affected the central Apennines and displaced the structures inherited by the compressive tectonics (Cavinato and De Celles 1999). This tectonic phase resulted in NW–SE trending normal fault systems, paralleling the axis of the chain. The activity of these structures through the Quaternary determined the formation of several intermontane depressions, such as the Fucino, L'Aquila, Sulmona, Rieti, Norcia and Subequana basins (Galadini and Messina 2004).

Extensional deformation in the central Apennines is presently active, as witnessed by i) geological evidence of Late Pleistocene-Holocene activity along NW–SE trending normal fault systems (Fig. 1b) (Galadini and Galli 2000; Boncio et al. 2004); ii) geodetic (GPS) data, indicating an extension rate of about 3 mm/year across the chain (Devoti et al. 2008); and iii) instrumental seismicity data, which have identified earthquake focal mechanisms consistent with NW-SE normal ruptures (Pondrelli et al. 2006; Bagh et al. 2007).

The active normal faults of the central Apennines are considered as the expression at the surface of seismogenic sources, potentially responsible for earthquakes with magnitude up to 6.5–7. Some of these faults activated in historical times, causing strong seismic events, such as the 1349 (Mw 6.6), 1703 (Jan. 14; Mw 6.7), 1703 (Feb. 2; Mw 6.7) and 1915 (Mw 7.0) events (Working Group CPTI 2008) (Fig. 1b). In particular, the April 6, 2009 earthquake occurred in a sector of the central Apennines that has been already struck by several moderate-to-large magnitude earthquakes in the past. As for the 2009 seismic event, geological and geophysical investigations agreed in defining the mentioned PF as the causative fault of the earthquake. Indeed, field evidence of coseismic surface ruptures along the tectonic structure matched with the intersection with the surface of the fault modelled by means of GPS (Anzidei et al. 2009) and InSAR coseismic data (Atzori et al. 2009).

2.1.2 Geological setting of the SV

The village of Castelvecchio Subequo is located about 40–50 km SE of L'Aquila, along the eastern flank of the Subequana valley, an intermontane tectonic basin adjacent to the Aterno river valley.

The Quaternary evolution of the Subequana depression has been influenced by the activity of a normal fault system that borders the eastern side of the basin (Miccadei et al. 1997; Calamita et al. 2000; Falcucci et al. 2011), the Subequana valley normal fault system (SVF) (Fig. 1c). This tectonic element affects the SW slopes of Mt. Urano, an anticline structure related to a NE-verging thrust that displaced Meso-Cenozoic limestone and marls sequences pertaining to different paleogeographic domains (Miccadei et al. 1997; Foglio CARG 2009). The Quaternary SVF activity

led to the formation of a sedimentary trap, the Subequana basin, where a 200–300-m-thick continental sequences deposited (Bosi and Bertini 1970; Falcucci et al. 2009).

In detail, the SVF is made of two main parallel segments: an easternmost segment, detectable at the intermediate-upper sectors of the slopes and a westernmost branch, affecting the base of Mt. Urano (Falcucci et al. 2011). The latter, in turn, is made of at least three sub-segments having a dextral en-echelon arrangement (Fig. 1c). The Subequana valley (SV) is composed by different geological deposits.

The oldest are deposits in the northern part of the valley. Successively at the two structures at the base of Mt. Urano alluvial and silt deposits are deposited and then dislocated by a fault system.

The activity of the SVF during the Late Quaternary is testified by the displacement of Late Holocene deposits along the westernmost strand of the fault system, detected by means of geological field investigations and paleoseismological trenching (Falcucci et al. 2011).

In this study area is distinguished different phases of alluvial deposits in the Pleistocene. In this phase there are the two distinct alluvial basins: Subequana valley and Aterno valley. This phase is successive by tectonic deformations. Then deposits are interested the Subequana valley. The presence of the lacustrine silt is confirmed by some authors (Beneo (Carta geologica d'Italia, F° 146); Bosi and Bertini, 1970; Bagnaia et al.,1992) and they referred these deposits to a Late Pleistocene. They supposed that this sedimentation interested the Subequana valley and the lake of L'Aquila. This sedimentation is stopped when the basin is full of sediments. The close of the lake is started from north to south, in the L'Aquila zone and then in the Subequana valley, respectively. During the Pleistocene there are the deposition of some alluvial sediments. This type of structure are evident south-west of Castelvecchio Subequo.

The geological analysis conducted in the SV (Falcucci, 2011), are allowed to define 5 different lithological and morphological stratigraphic units. The first is composed by deposits of silt. These emerged diffusive in the whole basin. The visible thickness of this unit is estimated about 70-80 m. The second unit is continuative with the previous and it is composed by sandy deposits and sandy-clay deposits. Successively a carbonate unit is present with clasts. The last two units: an unit, consisting of river gravels and stratified with pebbles carbonate and the last is composed of alluvial terraces and slope deposits.

2.1.3 Geological/structural and geomechanical investigations in CS

Castelvecchio Subequo (CS) raises at about 500 m a.s.l. on a small NW–SE elongated carbonate ridge, located at the northern termination of Mt. Urano and bounded towards E and W by stream incisions, up to 20–30 m deep. The eastern incision morphologically separates the ridge from the Mt. Urano SW slopes (Fig. 1d).

Field observations indicate that the area of the old village is characterised by a complex structural setting. Indeed, the ridge is located at the northern termination of the SVF westernmost branch.

Moreover, within the area of CS, the westernmost SVF splay intersects further tectonic elements, about N–S and NNE–SSW trending, characterised by a normal-to-transtensive kinematics. These structural features, represent transfer faults that structurally and kinematically link the SVF with a further active tectonic structure, namely the Middle Aterno Valley normal fault (Galadini and Galli 2000).

Here, indeed, transpressive-to-reverse shear planes, probably related to a back-thrust outcropping at the base of the Mt. Urano slopes, have been cross-cut by shear planes related to the SVF strand (Fig. 2).

In particular, in the southernmost sector of the CS ridge, the bedrock exposed at the lowermost portion of the small relief is affected by near vertical, narrowly spaced shear planes and closed fractures (Fig. 3b).

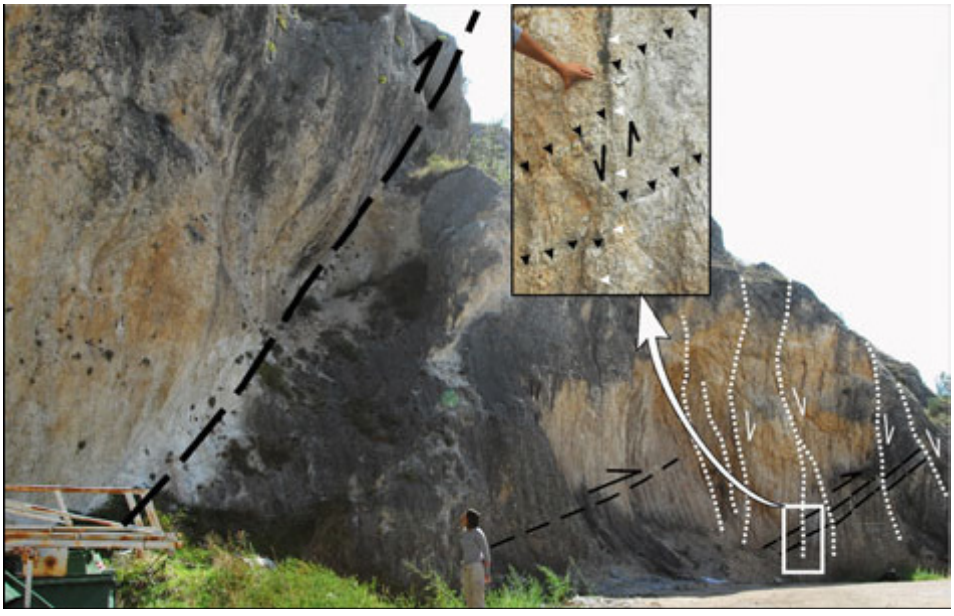

Figure 2. Reverse fault planes (*black dashed lines*), affecting the carbonate bedrock, that are crosscut by extensional shear planes (*white dotted lines*)—a close-up image is shown in inset (from Marzorati et al., 2011).

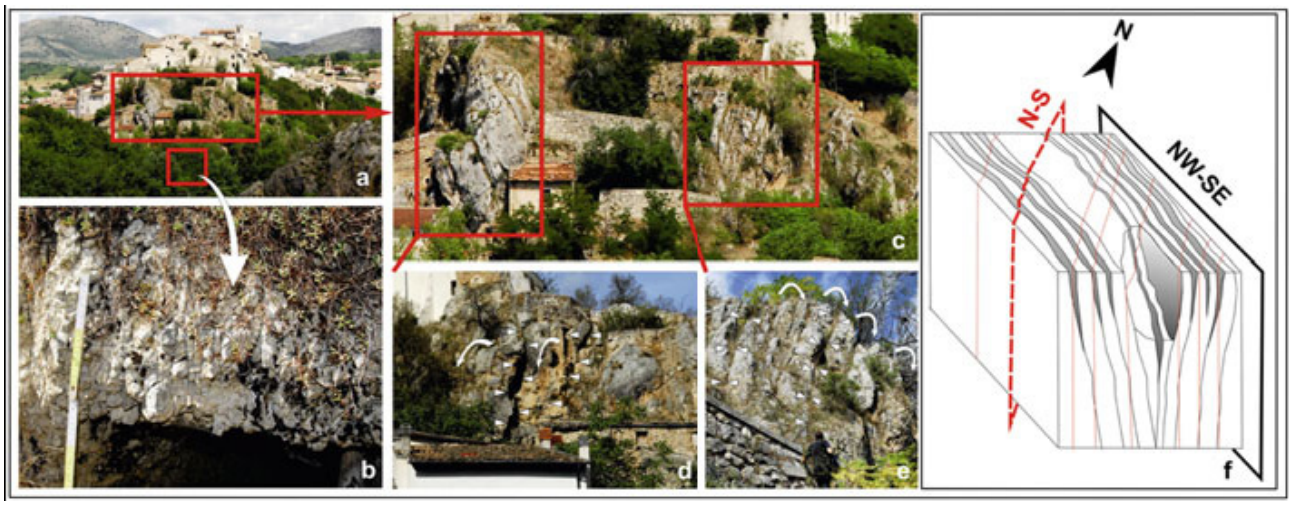

Figure 3. a Panoramic view of the southern termination of the Castelvecchio Subequo ridge; **b** close-up photograph showing narrowly spaced shear planes and closed fractures affecting the limestone bedrock at the lowermost portion of the ridge, **c** close-up image of the uppermost portion of the ridge, where opening mode discontinuities affect the carbonate bedrock; details of the open fractures (indicated by *white triangles*) detected along the western **d** and eastern **e** flanks of the ridge; *white arrows* indicate the direction of toppling of the bedrock slabs; **f** block diagram showing the main sets of fractures affecting the Castelvecchio Subequo ridge (from Marzorati et al., 2011).

In the uppermost portion of the ridge, instead, the rock mass is affected by opening mode discontinuities (Fig. 3c), open, planar parallel fractures and joints, that separate different slabs of limestone bedrock. In detail, at the uppermost sectors, these fractures have irregular spacing that ranges from tens of centimetres, along the eastern flank of the ridge, to some metres, along the western side; they are up-to-several-tens-of-cm wide; they are mainly NW–SE trending, strike parallel to the SVF segment; and opposite dip direction, towards W and E along the eastern and western flanks of the ridge, respectively (Fig. 3d, e, f).

These observations indicate that the fractures originated from antithetic and synthetic shear planes mainly related to the SVF segment and, secondarily, to the above mentioned transfer faults.

As shown by the data collected in the different geomechanical stations, the bedrock of the lowermost sectors of the rock mass is characterised by poorer geomechanical characteristics than that exposed at the uppermost part of the ridge where open fractures have been identified.

2.2 Geophysical survey in CS and SV

With the aim to study the characteristics of the Castelvecchio Subequo and the Subequana valley a campaigns of ambient seismic noise were carried out between July, 2009 and February, 2010 obtaining information about possible local amplification of the ground motion in the area of CS.

The campaigns of seismic noise are the first in the central part of the CS with two local experiment at Mt. Urano and at the school of the town and the second has interested the SV.
In this chapter were described the geophysical survey made in CS and SV.
Here was described the ambient seismic noise recordings along the CS ridge (from the basal portion to the uppermost sector), in the ancient portion of the village (Fig. 4), in the SV and the equipment for the local experiment at Mt. Urano.
Microtremors were recorded through two portable seismic stations equipped with Lennartz 5s (url: www.lennartz-electronic.de) velocimetric sensors and 24-bit Reftek 130 (url: www.reftek.com) Digital Acquisition Systems (DAS). The stations was connected with battery of 12V/12Ah/20Hr and with GPS antenna to find the coordinates of the point. The digital acquisition set the gain high to obtain the maximum resolution and the possibility to record all the seismic noise vibrations. The acquisitions were set with rate of 100 sps, the length of measurement is at least 30 minutes, the three acquisition channels (one for each component) were recorded on memory compact flash.
The aim of these seismic records is to investigate the local seismic effects. The historical part of CS is located at morphological north-south relief, length about 300 m. The relief raises about 30-40 m respect the valley.
In this phase were acquired twenty-two reliable ambient seismic noise recordings (red triangles in Fig.4) to investigate all the morphological situation, the base and the uppermost of the relief. These seismic records were performed considering the atmosphere agent and also the presence of void underground and the vehicular traffic. The records were performed outside the buildings to avoid the effects due to the vibrations of the structure.
With the seismic noise records CV84 and CV33 was investigated the most damage area and the less damage area with CVS6, CVS4 and CV30 seismic records. The ambient seismic noise measurements in CS were carried out on limestone bedrock detected within the village and on paving superposed to the bedrock. The seismic records were performed in free-field, outside the structures; in 3 cases the sensors were installed to the base of buildings to have an estimate of vibration period.
The seismic records CVS8, CV28 and CV29 were performed near the school of the CS. This area was not damage but had a particular interest for the local administration. Inside the school were performed two seismic records to the first floor to estimate the vibration period of the building.
Also the CVS7 was performed to the base of the church which bell tower was damaged by the earthquake. Three seismic records were performed also to the base of Mt. Urano: CV17, CV18 and C18B, where the pinnacles were presents. These records were performed to investigate morphological setting similar to this of the historical part of CS. The record CV17 was located to

the base of the pinnacles, the CV18 to the uppermost of one of these. In this way it was possible to investigate that these structures have own properties and mode of vibrations.

Besides, a small temporary seismic network (made of three seismic stations) was installed from September 17 to November 4, 2009 to collect earthquake waveforms. The stations were equipped with Episensor FBA accelerometers (www.kinemetrics.com), in addition to velocimetric sensor Lennartz 5s., in order to avoid the saturation of digital seismic signals due to strong ground motions. The Reftek 130 DAS recorded a continuous dataset with rate of 100 samples per second (hereafter sps).

The geometry of the temporary seismic network, shown in Figs. 4 and 5, has been defined basing on 1) geologic observations, that highlighted the different degree of fracturing of the CS ridge and the Mt. Urano SW slope, and 2) on the ambient seismic noise campaigns which showed no ground motion amplification along the Mt. Urano SW slopes and different amplification values between the base and the uppermost portion of the CS ridge.

Another geophysical survey was performed in SV. The seismic noise records performed in the SV have the aim to obtain a 1D response of the basin and to estimate the bedrock. Microtremors were recorded with the same seismic stations used in the area of CS. Where it was possible, the seismic station were underground and covered with ground to avoid the influence of wind and vegetation.

In this phase are performed 87 seismic noise recordings, which 12 are unreliable for the presence of wind, only in 3 cases the record was repeated to obtain a reliable data.

Fig. 6 shows the location of seismic noise records in the SV. This seismic campaign not covered the entire valley, because the area was inaccessible but with the seismic noise recordings made it is possible to study the basin longitudinally and transversally (Fig. 6).

The most important numbers of noise seismic records were performed in the basin in front of Castelvecchio Subequo, between Gagliano Aterno and Castel di Ieri. This is the area where it is supposed the most deepening of the bedrock by recent geological studies (Falcucci et al., 2009).

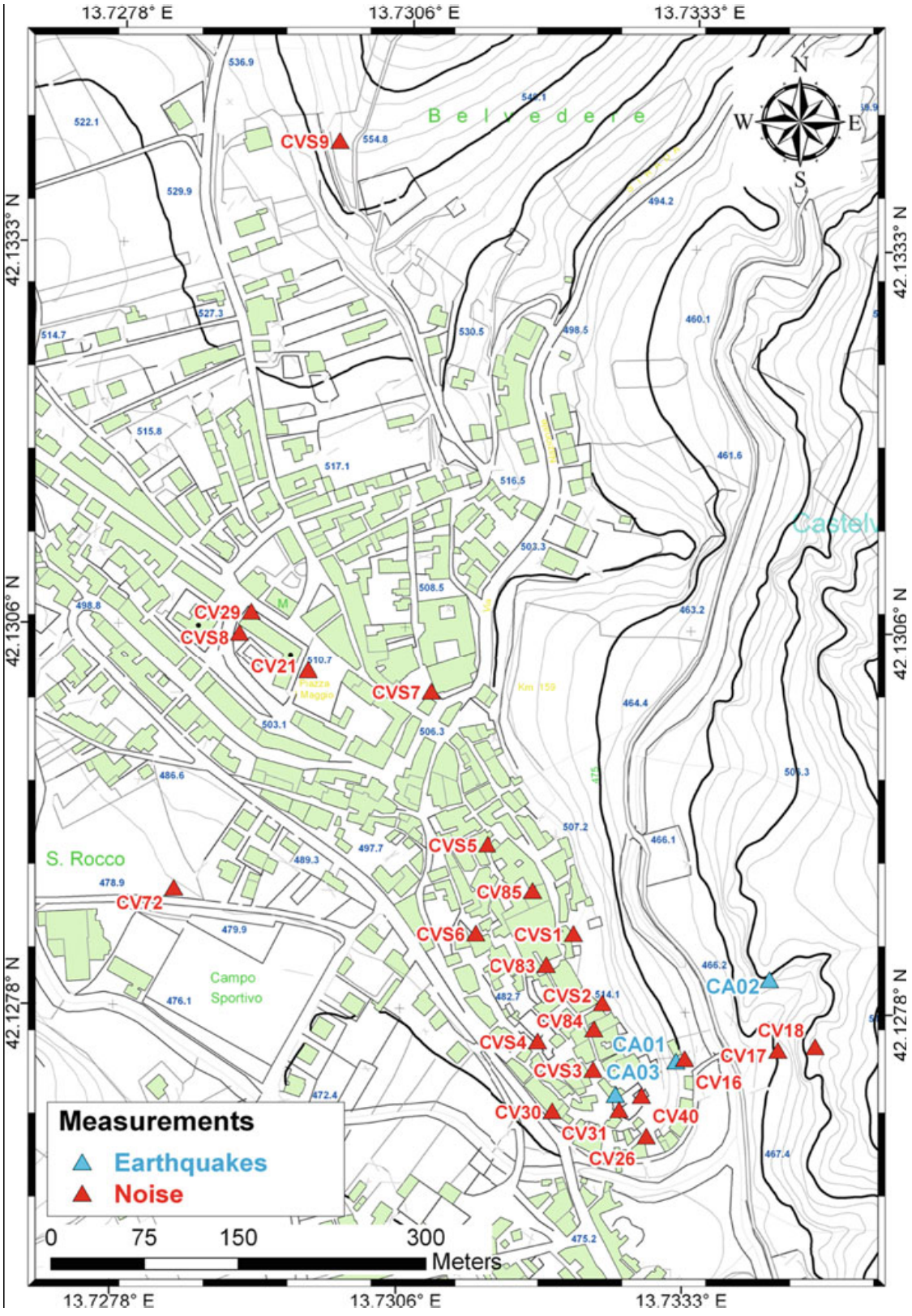

Figure 4. Red triangles: ambient seismic noise stations. Blue triangles: temporary seismic network in CS and in its hinterland. CS buildings are represented with light green polygons. Background: Carta Tecnica Regionale (1:5000) Regione Abruzzo. Blue numbers are the elevation a.m.s.l.. Green numbers are elevation relative to height contours (from Marzorati et al., 2011).

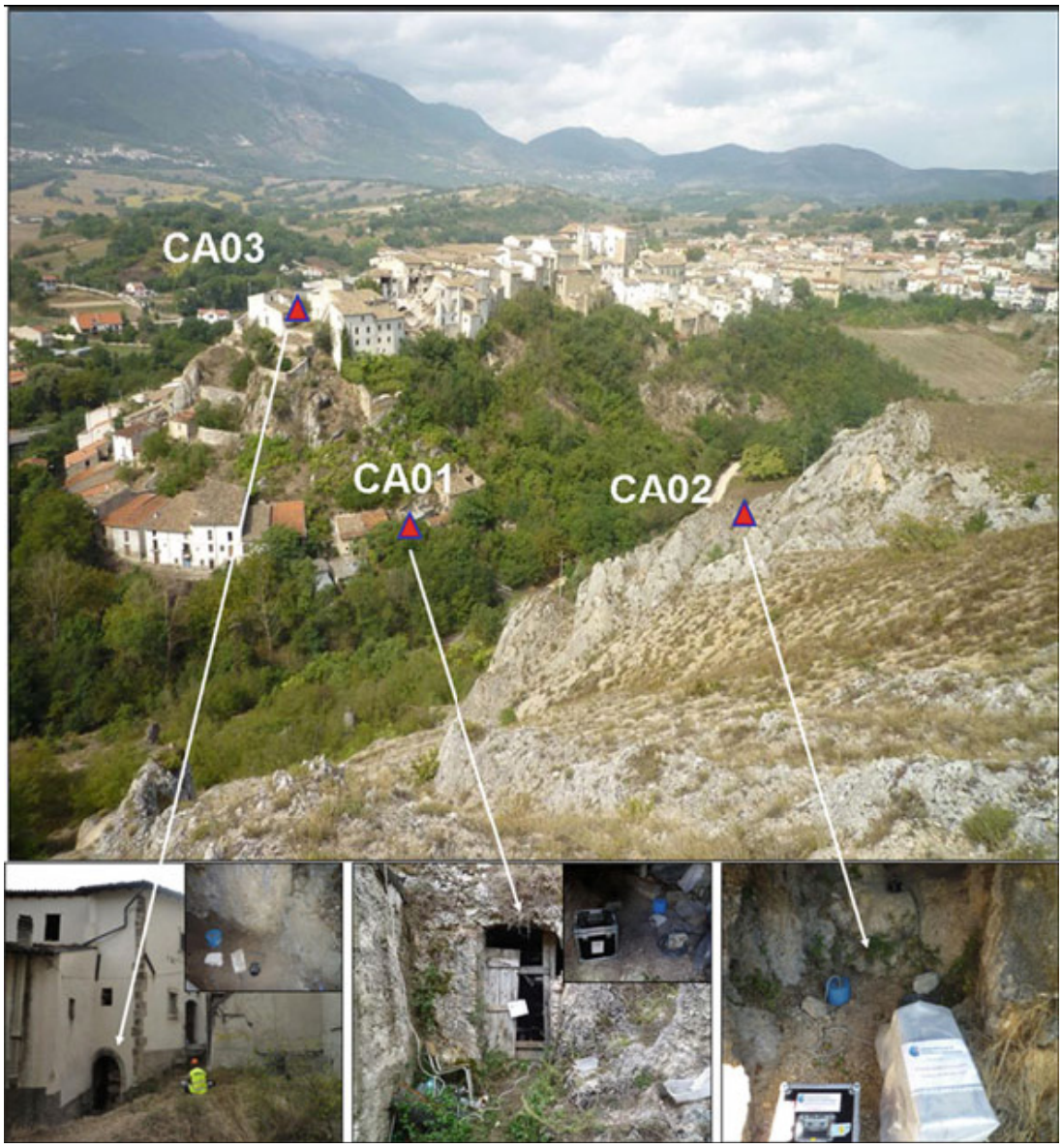

Figure 5. Panoramic view of the temporary seismic network (red triangles). CA03 is located in the historical part of CS, in the foundation floor of a building (bottom on the left); CA02 is located on the slope of Urano mountain in the natural cave; CA01 is located at the base of the relief in a cellar inside the rock outcrop (from Marzorati et al., 2011).

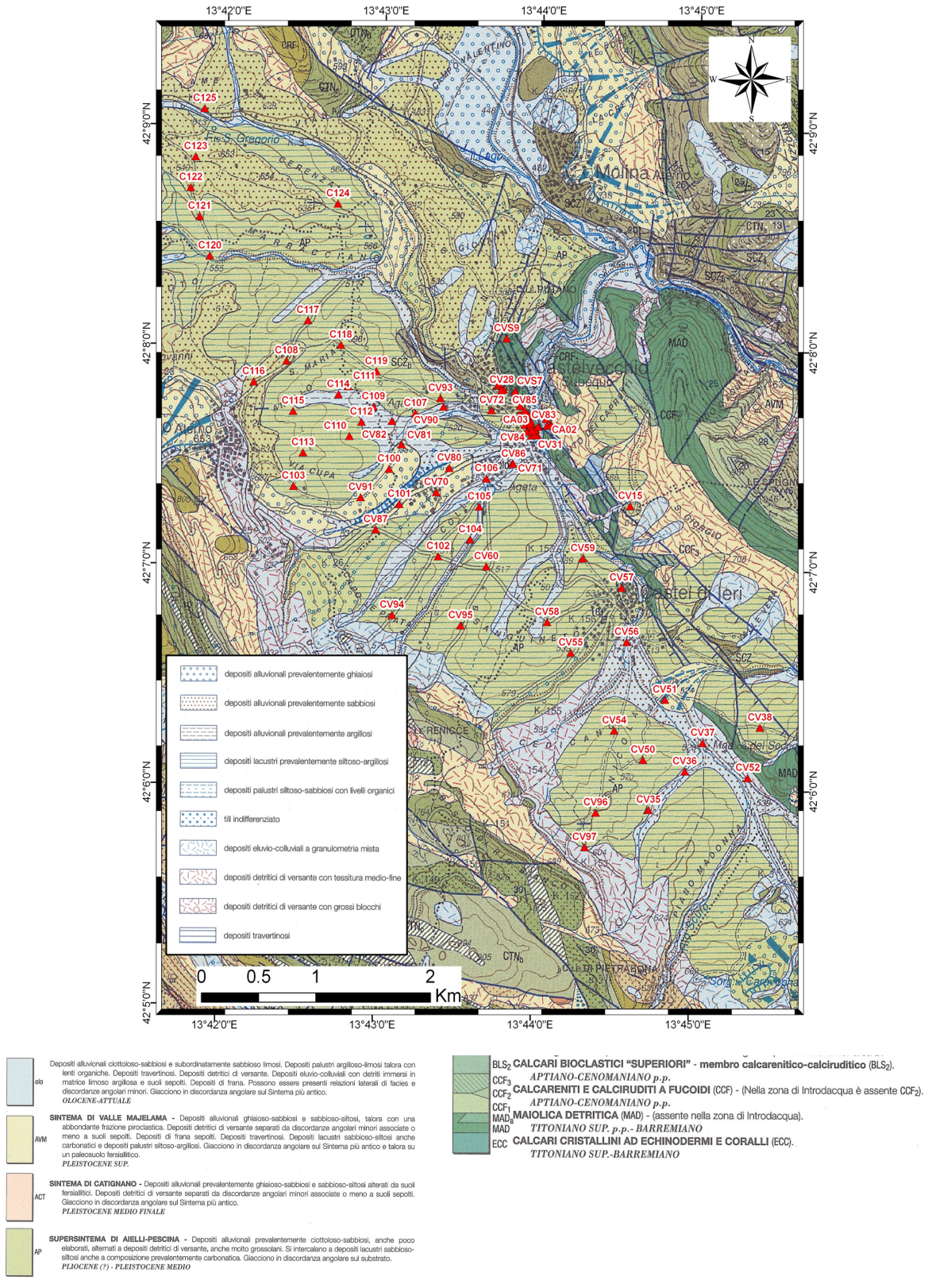

Figure 6. Map of seismic noise records in the SV. Background CARG 1:50.000, the most important geological elements are represented in figure (from Marzorati et al., 2011).

2.2.1 Ambient seismic noise: data processing and spectral ratio analysis in CS

All the ambient seismic noise records are analysed in a preliminary selection so as to eliminate the records unreliable. The programming language used is Matlab® and it allowed to display for each component of the signal the seismic trace, the Power Spectral Densities (PSD) and the spectral ratio between the horizontal and vertical component.

The ambient seismic noise recordings were manually selected in order to remove the possible traces of signal affected by disturbances and artificial transients. The waveforms were windowed in 120-s-long time series. Also, the mean, the linear trend and the instrumental response were removed from all the recordings. In Fig. 7 is a picture of the software interface developed in Matlab® language to select the reliable time series used to calculated NHVSR. This Figure showed the Power Spectral Densities (PSD, top panels), NHVSR (middle panels) and the waveforms in the analysis window (bottom panels) of three components of the seismic record. The grey curves represents the PSD and NHVSR of all analysis windows; they are useful to show the spectral shape of the distribution of the values. The example of Fig.7 shows a window with a clear disturbance in the waveform (black lines in the bottom panels). The resulting PSD and NHVSR come out from the cloud of value. This window is eliminated of the final analysis. In Fig. 8 a quiet analysis window, where PSD not present anomalies and NHVSR show a clear peak of resonance, is an example of a time series selected for the final analysis.

Same traces were affected by various disturbances; frequently disturbances are the gusts of wind. The effect is clear in the analysis of this spectral shape which the spectra was modified in all frequencies range analysed (Fig. 9).

Using the selected window of the all seismic records, it was possible to find the interval of levels of ambient seismic noise. In Fig. 10 the Probability Density Function (PDF) obtained from all the PSD of seismic noise. The PDF were calculated with the method described in McNamara and Buland (2004) and Marzorati and Bindi (2006). The PDF represent the noise levels of probability in all the records performed in the SV and in CS. In Fig. 10 the level of noise doesn't exceed the New High Noise Model (Peterson, 1993), this indicates that the disturbances are not elevated even if they are present. In fact, the noise level over 1 Hz increases for the presence of disturbances due to industrial machineries or human activities of various type. At low frequency, below 1 Hz, it is possible to note an elevated level of seismic noise on the horizontal components; this phenomena is due to the amplification of the microseismic signals for the presence of deep sediments in the basin of the SV.

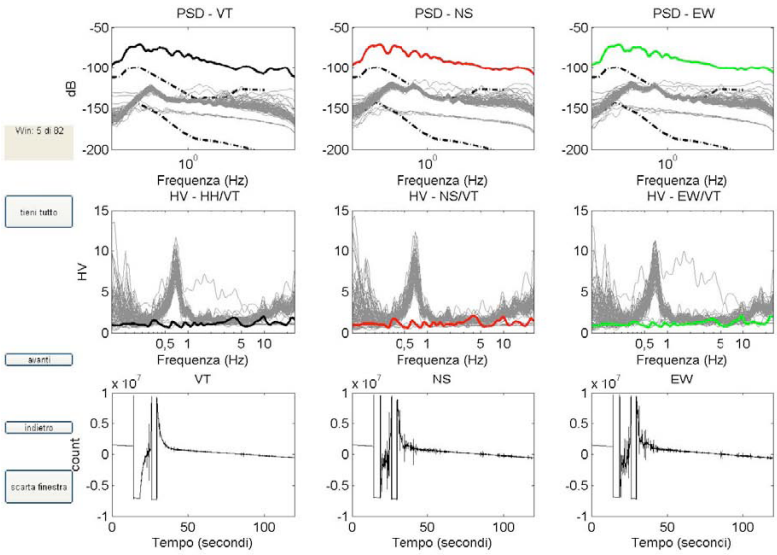

Figure 7. Matlab ® interface for the selection of windows of signal noise. Upper panels: PSD of all the windows analyzed. Middle panels: HV of all the windows analyzed. Bottom panles: window signal disturbed. Grey lines: PSD and of HV windows of the measuring signal. Black line: vertical component, red line: north-south component; green line: east-west component; black dashed: Peterson curve [Peterson, 1993] (from Marzorati et al., 2011).

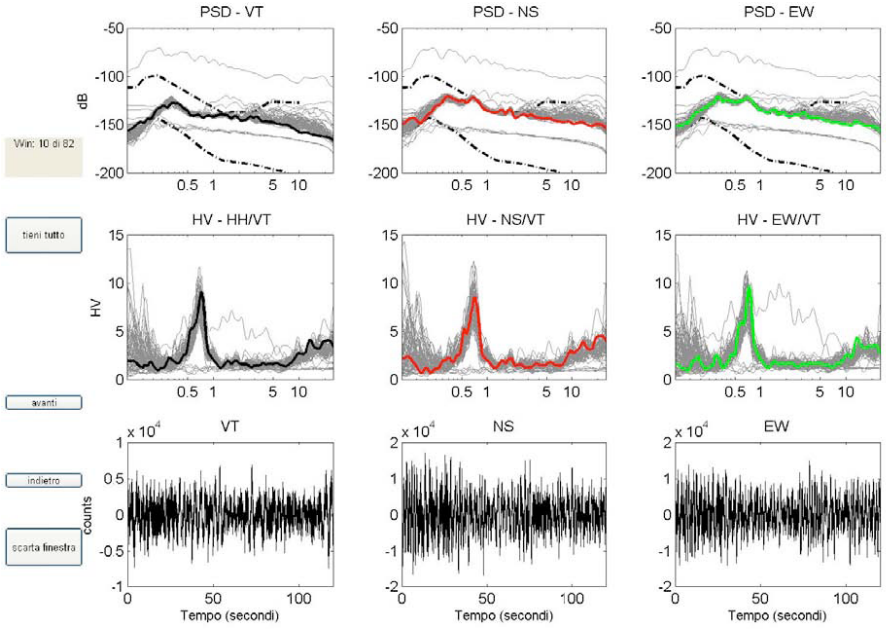

Figure 8. Matlab ® interface for the selection of windows to signal noise. In the example is given a window signal is not disturbed and considered useful for the analysis. Grey lines: PSD and spectral windows of the measuring signal. Black lines: vertical component; red lines:
north-south component, green line: component of east-west. Black dashed line: Peterson curve [Peterson, 1993] (from Marzorati et al., 2011).

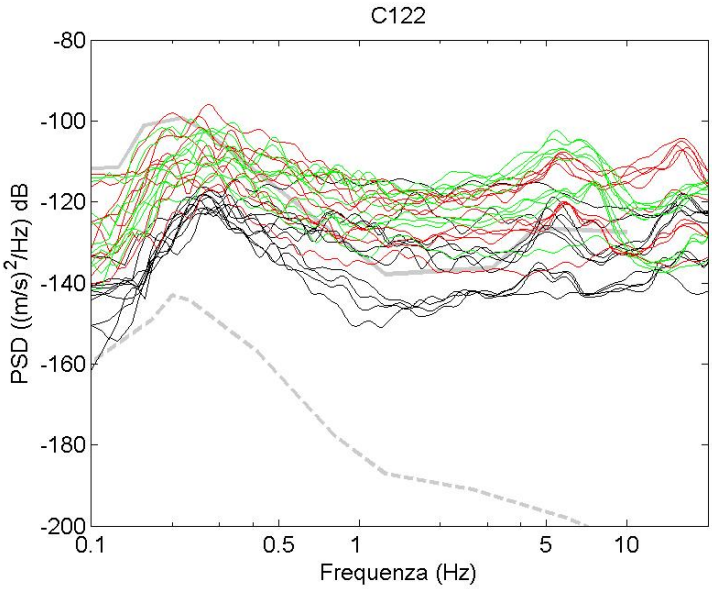

Figure 9. Power Spectral Density for the seismic record C122. is evident the present of gusts of wind. Red line: north-south component. Black line: vertical component. Green line: east- west component (from Marzorati et al., 2011).

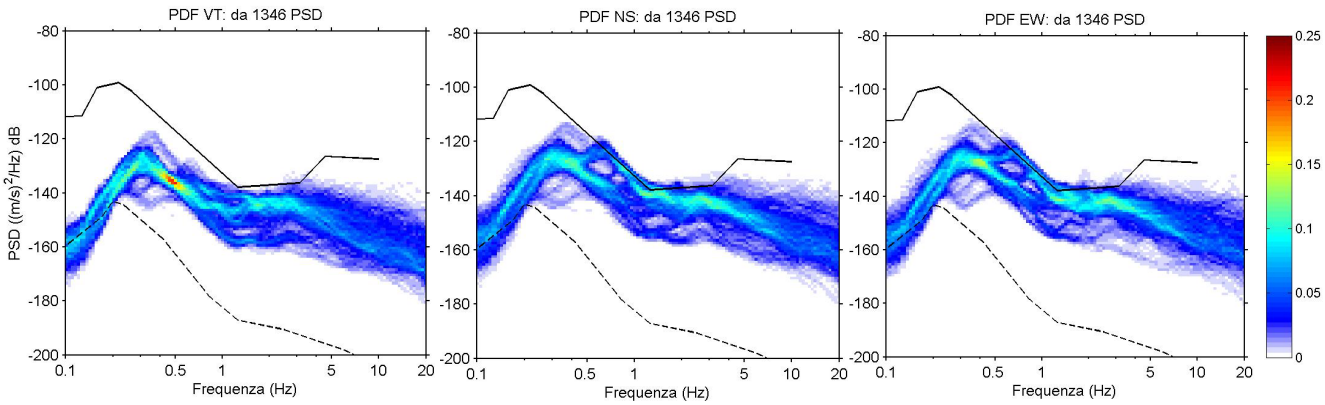

Figure 10. PDF obtained by 1346 PSD with window of 120 s for all the seismic noise records. Colour bar indicates the probability. Left: vertical component. Right: east- west component. Centre: north-south component. Black lines: Peterson curve (1993)(from Marzorati et al., 2011).

After this first analysis the seismic noise records performed in the historical part of CS were rotated between 0° and 175° (with steps of 5°) to investigate preferential directions of the amplifications.

This type of analysis is made only for the seismic data of the historical part of CS. Then, a band-pass Butterworth 4 poles filter between 0.2 and 25 Hz and a cosine taper 10% were applied to every window and the single PSD was smoothed using the Konno and Ohmachi (1998) technique (with smoothing parameter, $b = 40$).

Then, these records were analysed to compute the Horizontal to Vertical Spectral Ratio (Nogoshi and Igarashi, 1971; Nakamura 1989).

From the ambient noise recordings (NHVSR) for each considered azimuth, the ratio between the spectrum of the radial and vertical components was calculated. The resulting NHVSR was obtained by geometrical mean of the NHVSRs from all the selected signal windows.

In Fig. 9 the results of the NHVSR in terms of amplification curves and polar diagrams (amplitude-frequency-azimuth plots).

The measurements CVS4, CVS6, CVS7, performed along the western flank of the ridge, show moderate amplifications between 1 and 8Hz. In particular, CV26 and CV30, located at the base of the ridge, provided NHVSR slightly larger than 2; then, in this site there are not amplifications. These NHVSR are heterogeneous as regards the frequency of the peaks and the direction of the amplification at each site (Figs. 11-12).

As for the measurements performed along the eastern flank, the NHVSR show site amplifications with amplitudes smaller than 6(Figs. 11-12).

The CVS5, CV83, CV74, CVS2 and CVS3 point out strong amplification of ground motion of the horizontal components compared to that of the vertical components derived from the measurements performed at the uppermost portion of the ridge (Fig.12). The site amplifications appear in the frequency range 1.5–8 Hz, with larger amplitudes around 3–4 Hz. The direction of the maximum amplifications is about 70°–250° striking, perpendicular to the main axis of the ridge elongation. In particular, the NHVSR of CV40 and CV85 show amplifications in directions that are different from those of the other measurement of the UPR sector (Fig. 12).

Finally, the measurements performed in the surrounding areas of CS (CVS9, CV72, CV86, Fig. 4) and along Mt. Urano (CV18, Figs .4-13) provide NHVSR that displays no site amplification. On this basis, the Mt. Urano flank has been chosen as reference site and a seismic station was installed for the temporary network.

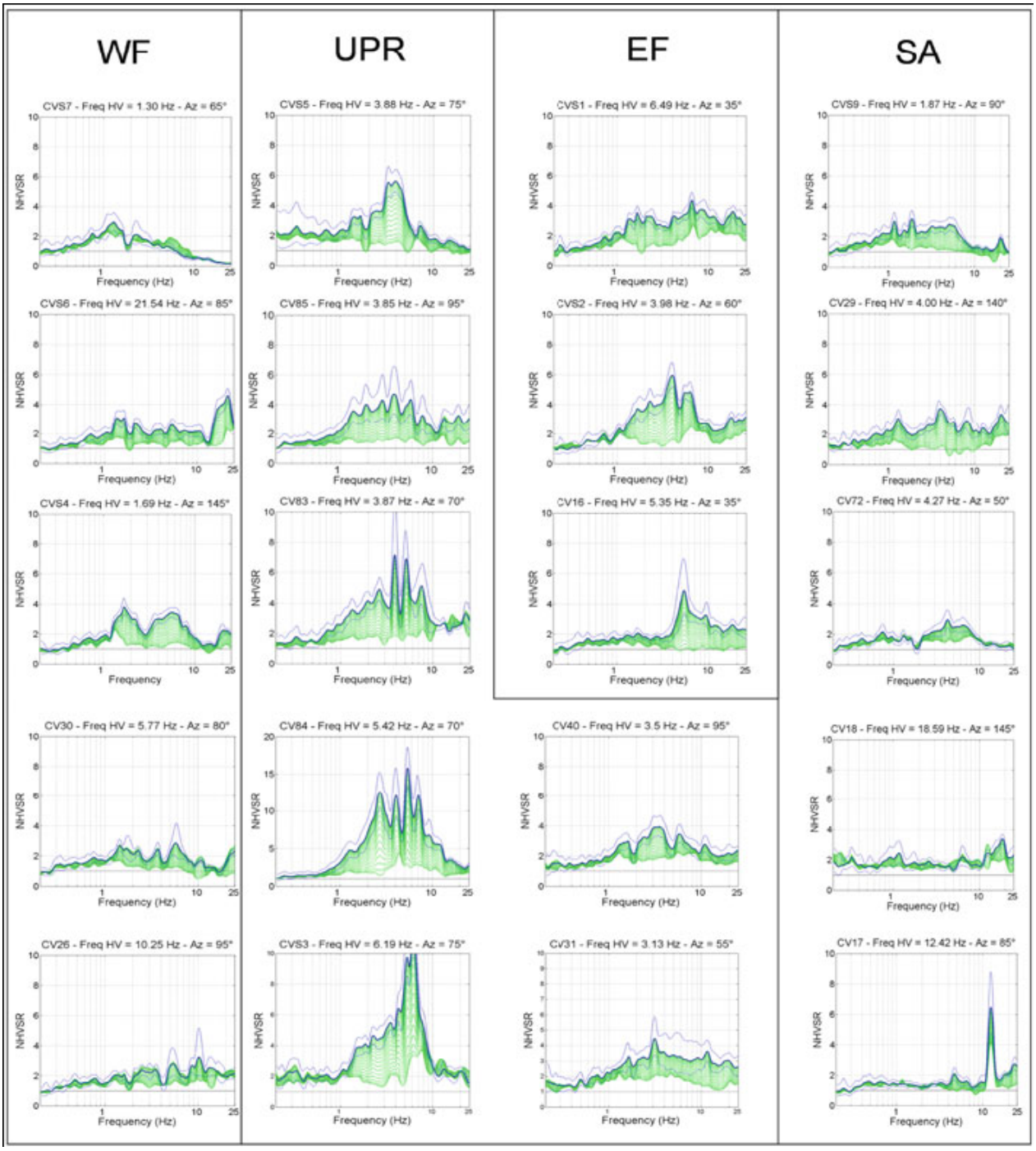

Figure 11. Summary of results about NHVSR analysis. WF: Western flank; UPR: Upper portion of the ridge; EF: Eastern flank; SA: Surrounding areas. Green lines: 36 directions from 0° to 175°. Thick blue lines: amplitudes in the maximum amplification direction. Thin blue lines: standard deviation of the amplitudes in the maximum amplification direction (from Marzorati et al., 2011).

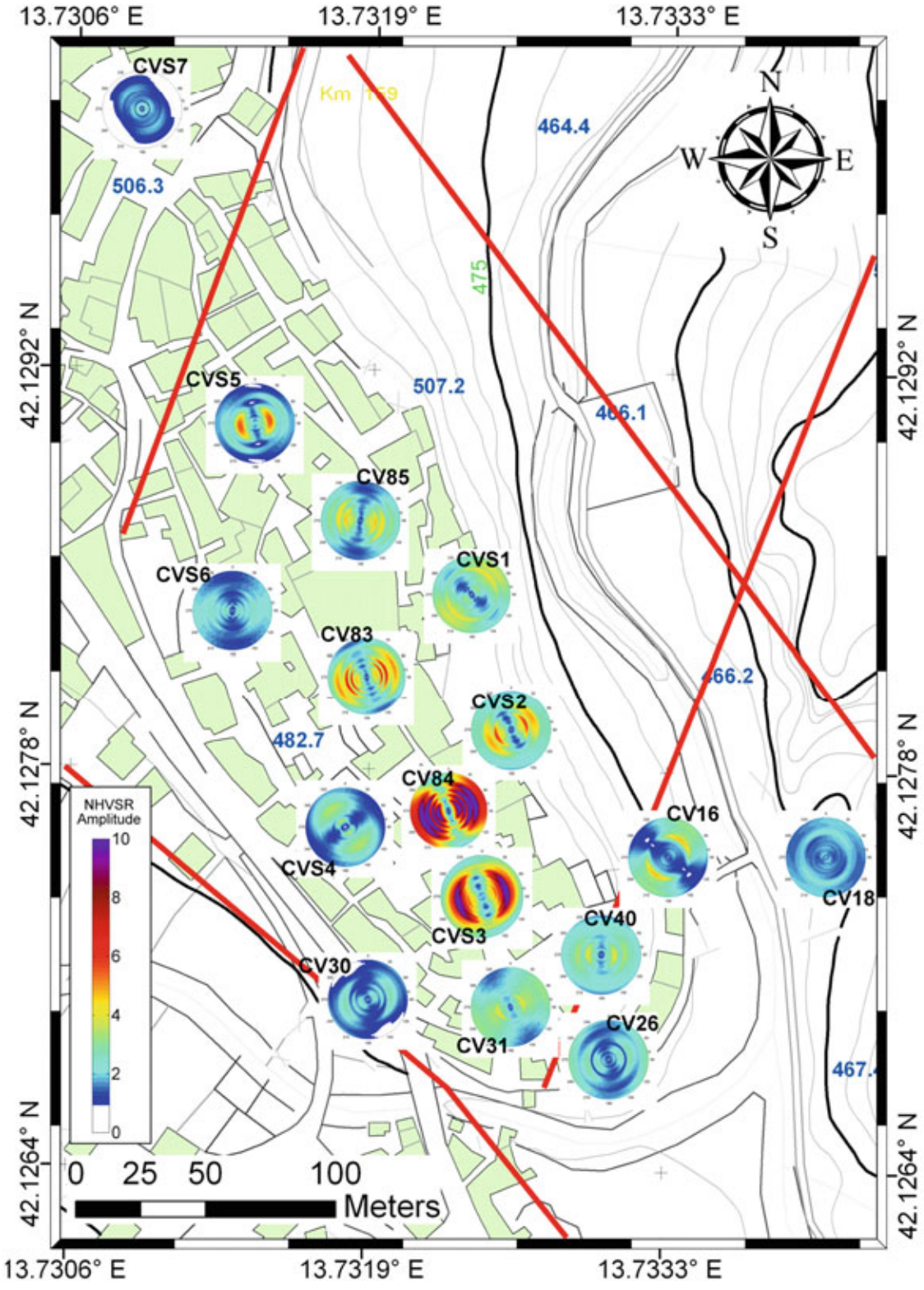

Figure 12. Summary of results about NHVSR analysis. The map shows the polar plot of NHVSR lines at each measurements site (black code). Green polygons: CS buildings. Red lines: geologic faults. Blue numbers: elevation (a.m.s.l.). Green numbers: elevation relative to height contours. Polar plot of NHVSR curves: black numbers mark degrees from the North; color bar marks the NHVSR amplitudes. Background: Carta Tecnica Regionale (1:5000) Regione Abruzzo (from Marzorati et al., 2011).

2.2.2 Temporary seismic network in CS

To complete the study of local effect in the historical part of CS, a local temporary network of three stations was installed to record earthquakes. The network was carried out between September, 2009 and November, 2009, record continuous data for 48 days. One of the seismic stations of the network was located in a reference site. Amplifications of the horizontal component respect to the vertical component were found in the upper part of the morphological relief. On the contrary at the base of Mt. Urano, near the CS, any amplifications as found for the same limestone lithotype (Fig. 13). With these hypothesis the stations were located with this criterion: a station is located in the upper most part of the morphological relief, in the historical part of CS in the foundation floor of a building (CA03); a first reference station is located at the same altitude of the station in CS on the slope of Mt. Urano (CA02) and the second reference stations at the base of the relief (CA01) (Figs. 5-14). In Table 1 there are the characteristics of the seismic stations of the temporary network, start time and stop time of the recordings, latitude, longitude and elevation.

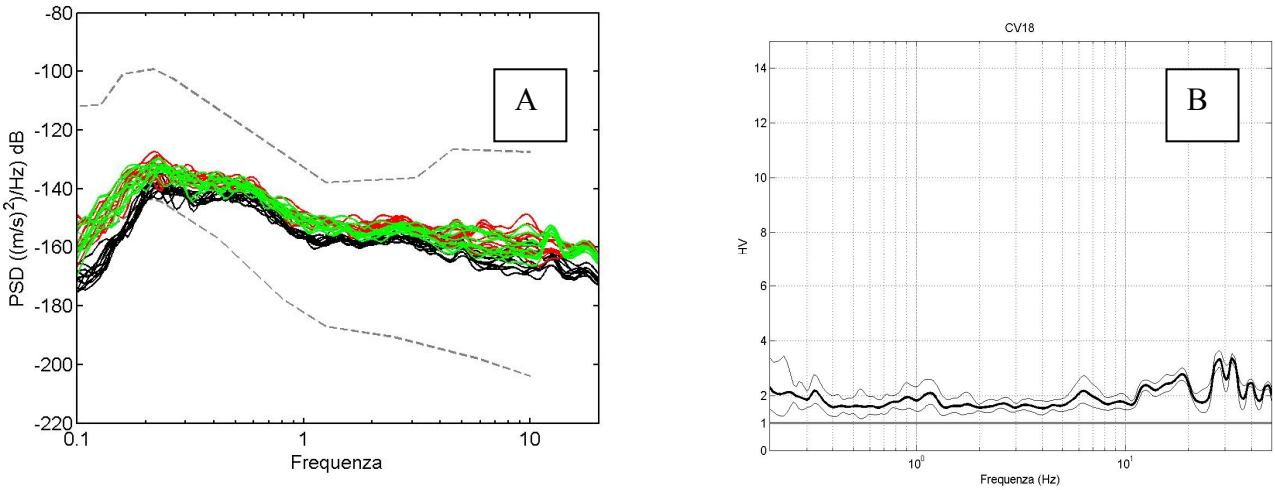

Figure 13. A PSD of the 11 noise windows selected of the CV18 record. Red line: north-south component. Black line: vertical component. Green line: east- west component. Grey line: Peterson curve (1993) (from Marzorati et al., 2011). B spectral ratio between horizontal and vertical components performed at CV18 station. This was chosen as reference site (from Marzorati et al., 2011).

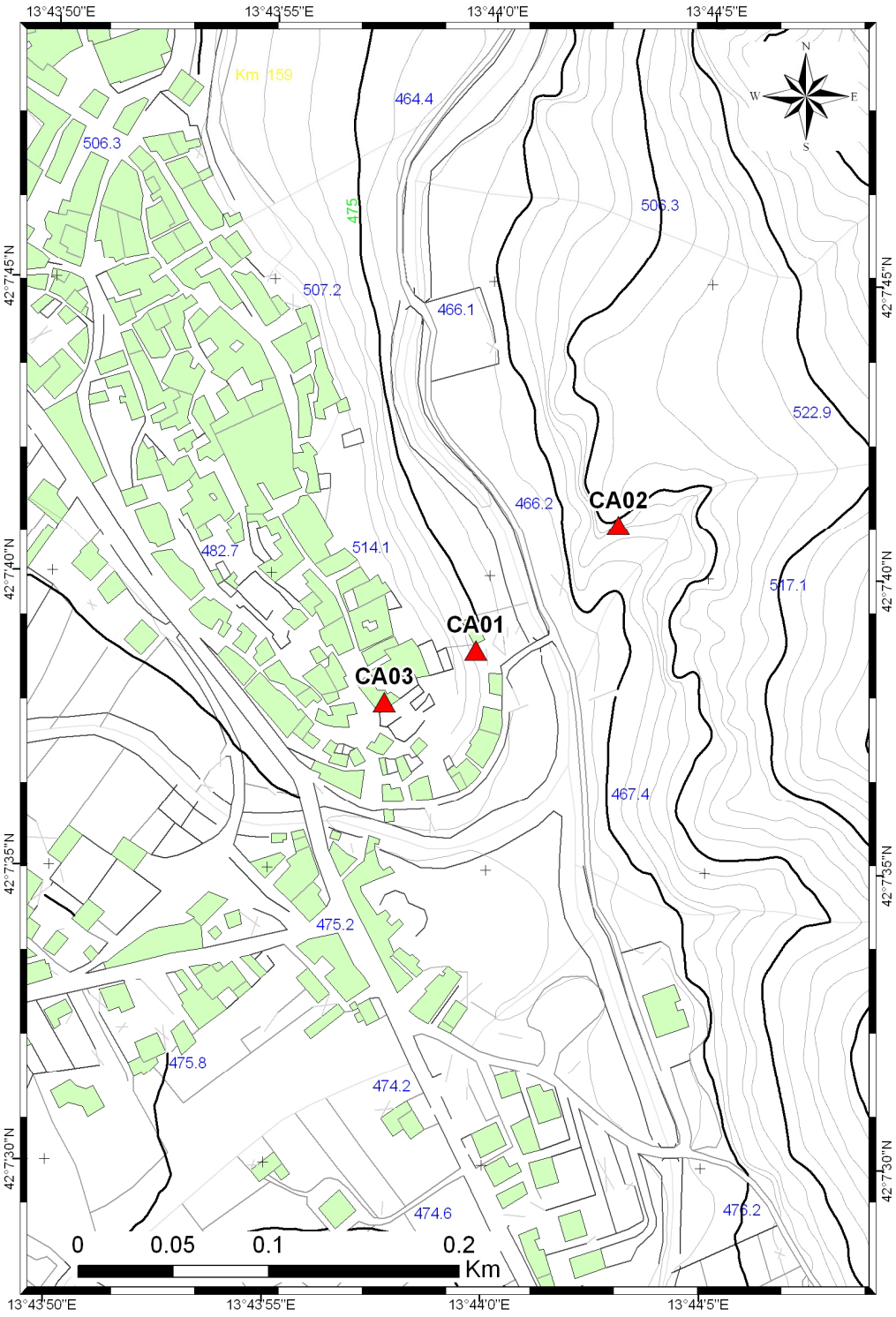

Figure 14. Temporary seismic network for the study of site effects. Background: Carta Tecnica Regionale (1:5000) Regione Lazio. Red triangles: seismic stations. Green polygons: CS buildings. Blue numbers: elevation (m.a.s.l.). Green numbers: elevation relative to height contours (from Marzorati et al., 2011).

SC	DAS.	CH 1-3 Sensor	CH 4-6 Sensor	START	STOP	LAT (°)	LON (°)	EL (m.a.s.l.)
CA01	RT130	Le3D-5s	Episensor	17-09-2009 07:04	03-11-2009 15:17	42.128079	13.733157	476
CA02	RT130	Le 3D-5s	Episensor	18-09-2009 09:38	03-11-2009 15:49	42.128683	13.734050	495
CA03	RT130	Le 3D-5s	Episensor	17-09-2009 11:44	04-11-2009 10:44	42.127830	13.732578	520

Table 1. SC: station code. DAS: type of digital acquisition system. CH: type of sensor. START : start time STOP: stop time. LAT: latitude. LON: longitude. EL: elevation, m. a. s. l.

2.2.3 Earthquake data: processing and spectral ratio analysis

With a dataset of earthquake waveforms created selecting the events from the Italian Seismological Instrumental and parametric Data-base (ISIDE, http://www.iside.rm.ingv.it) the events recorded by the seismic network are 295, 234 and 308 for CA01, CA02 and CA03 respectively.

The earthquakes are selected within an area of 100 km from CS, from September 17 to November 4, 2009. Events with magnitudes (Ml) comprised between 0.1 and 4.1 are 903. Some of these seismic events were localized NE and S of the Subequana valley.

The procedure of analysis of these events are: firstly, manual picking of the S-phase on the horizontal components and events with a low signal-to-noise ratio are removed.

The off-set, the linear trend and the instrumental response are removed from each waveform. The Horizontal to Vertical Spectral Ratio (HVSR) (Lermo and Chavez-Garcia 1993) and Standard Spectral Ratio (SSR) (Borcherdt 1970) analyses are applied to the selected dataset with the aim of obtaining an estimate of local seismic response. The spectral ratios were calculated on time-windows of 10 s from the onset of the S phase and are applied a band-pass Butterworth filter with 4 poles between 0.2–25Hz and a 10% cosine tapering.

Then, the FFT of the signal window was calculated and smoothed with Konno–Ohmachi technique (as for the NHVSR).

For each seismic event the spectra are divided in order to obtain HVSR and SSR. Then, the north-south and east-west spectra are divided by the vertical spectrum to obtain a HVSR. Similarly, the horizontal and vertical spectra of CA03 are divided by the horizontal and vertical spectra of CA02 and CA01, respectively, to obtain a SSR. Moreover, the spectra of CA01 is divided by the spectra of CA02.

Finally, a geometric mean of all events spectral ratios is considered to obtain HVSR and SSR at each site. The results obtained from the HVSR analysis are described in Fig. 15.

CA02 is the reference station, its HVSR has a flat trend (Fig. 15 bottom). The station has been installed at the lowermost portion of Mt. Urano ridge where no significant amplification, due to topographic effect, are expected. On the contrary, for the stations CA01, at the base, and CA03, at the top of the ridge, the HVSR show significant amplifications (Fig. 15).

In both cases, the larger amplification occur on the EW component (Fig. 15 middle and top). At CA01 station, the EW component is amplified in the frequency range 5–8Hz with respect to the vertical component while, HVSR of CA03 station is greater than 2 between 1 and 8Hz, and the maximum amplification appears around 3Hz.

Then, SSRs are calculated for the three components of the signal (Fig. 16). The station CA03 is compared with CA02 and CA01 stations, also the CA01 station is divided by the CA02 station.

These analyses indicate the lack of amplifications on the NS and vertical components for CA03 and CA01 stations with respect to the reference station CA02. In contrast, clear amplifications emerge on the EW component.

For the EW horizontal component, the SSR between CA03 and CA02 shows amplification peaks between 2 and 4Hz with amplitudes that reach the value of 3; SSR between CA01 andCA02 shows amplifications between 5–8Hz and finally SSR between (CA03) and (CA01) shows amplification at 3Hz.

The waveforms of earthquakes of magnitude 4.1, 3.5 and 2.5 recorded by the stations of the network are showed in Fig. 17. The 2–4Hz band-pass filtered waveforms (red line) overlap the original waveforms (black line). The CA03 station amplitudes are larger than those of the other two stations in the frequency band and there is a clear effect on the signal duration which is extended by a few tens of seconds.

These considerations are confirmed by the analysis of the ground motion and HVSR (Fig. 17) related to an earthquake of Ml 2.4 on 17 July 2009 recorded during the seismic noise measurements at CVS5 and CVS6 stations (Fig. 4).

CVS5 was located in the uppermost portion of the ridge and CVS6 on the western flank near the CVS5 but in lower elevation. The HVSR analysis show remarkable amplification differences at CVS5 and CVS6 stations (Fig. 17).

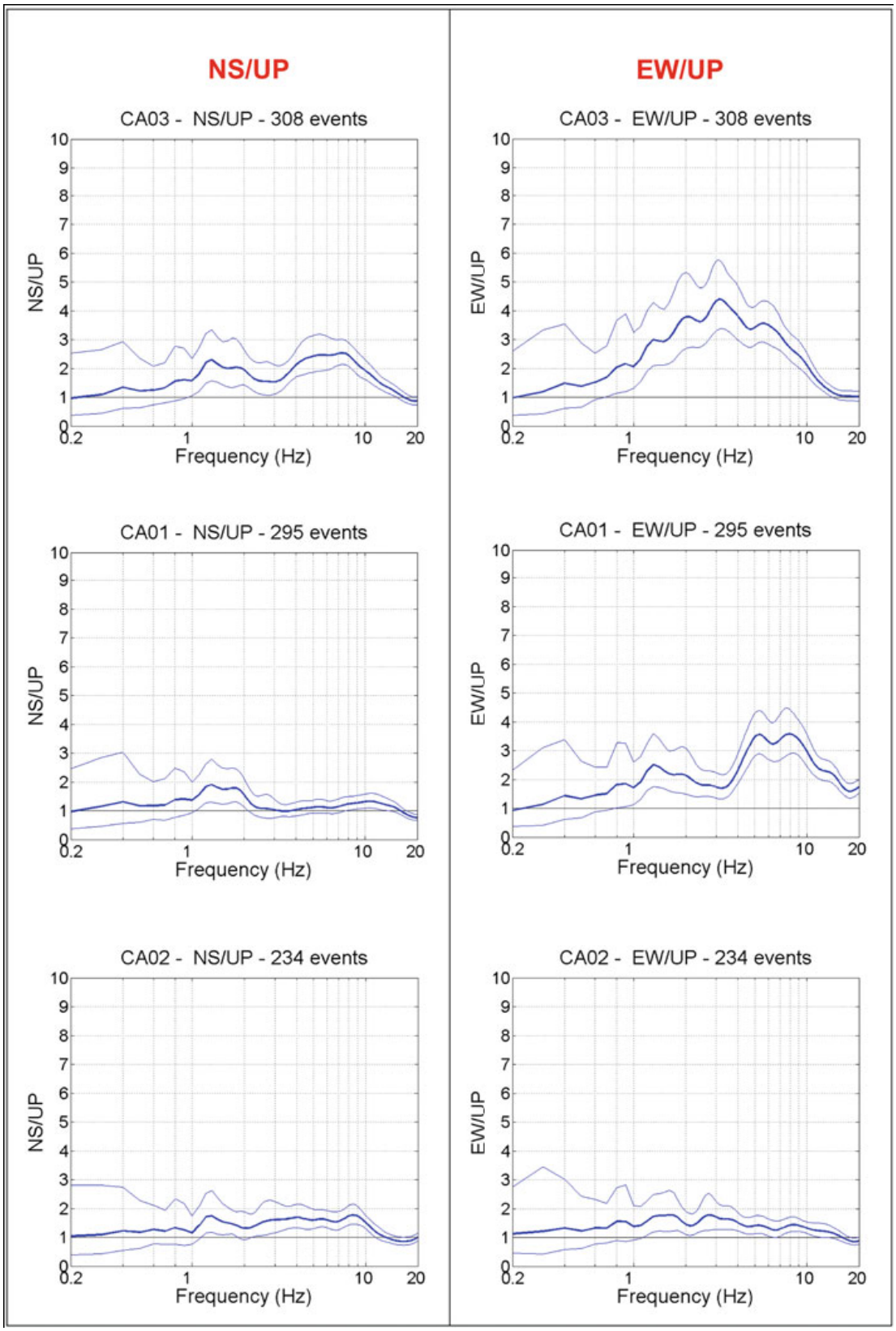

Figure 15. Summary of results about earthquake HVSR analysis. NS/UP: HVSR between north–south component and the vertical one. EW/UP: HVSR between east–west component and the vertical one. Thick blue-line: HVSR geometrical average; thin blue lines: HVSR standard deviation. Black titles: station code, HVSR type, number of seismic events used for HVSR analysis (from Marzorati et al., 2011).

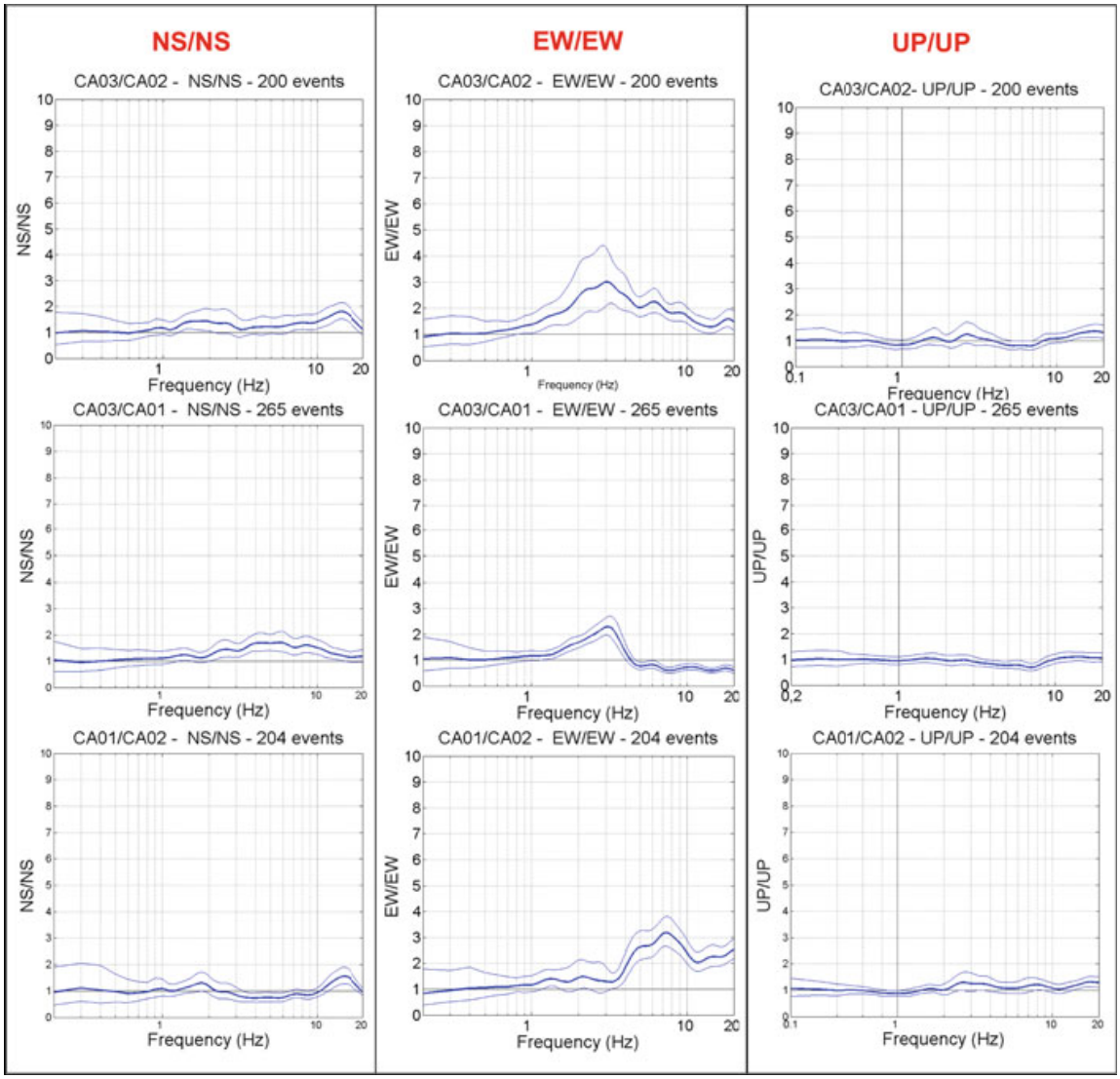

Figure 16. Summary of results about earthquake SSR analysis. EW/EW: SSR between east–west components. NS/NS: SSR between north–south components. UP/UP: SSR between vertical components. Thick blue line: SSR geometrical average; thin blue line: SSR standard deviation. Black titles: analysed station code on reference station code, SSR type, number of seismic events used for SSR analysis (from Marzorati et al., 2011).

The CVS5 HVSR shows a polarization of the horizontal amplification around 75°N oriented (Fig. 17) in the whole frequency range (1–10 Hz); the HVSR shows also remarkable amplifications at about 4Hz. While, CVS6 HVSR shows moderate amplifications in different directions. The amplification of earthquake recorded at CVS5 and CVS6 confirm the outcomes of the analyses of the seismic events recorded by the temporary seismic network (CA03, CA02 and CA01 stations). The observation highlights the heterogeneity of the ridge response, composed by amplifications in area near site without anomalies.

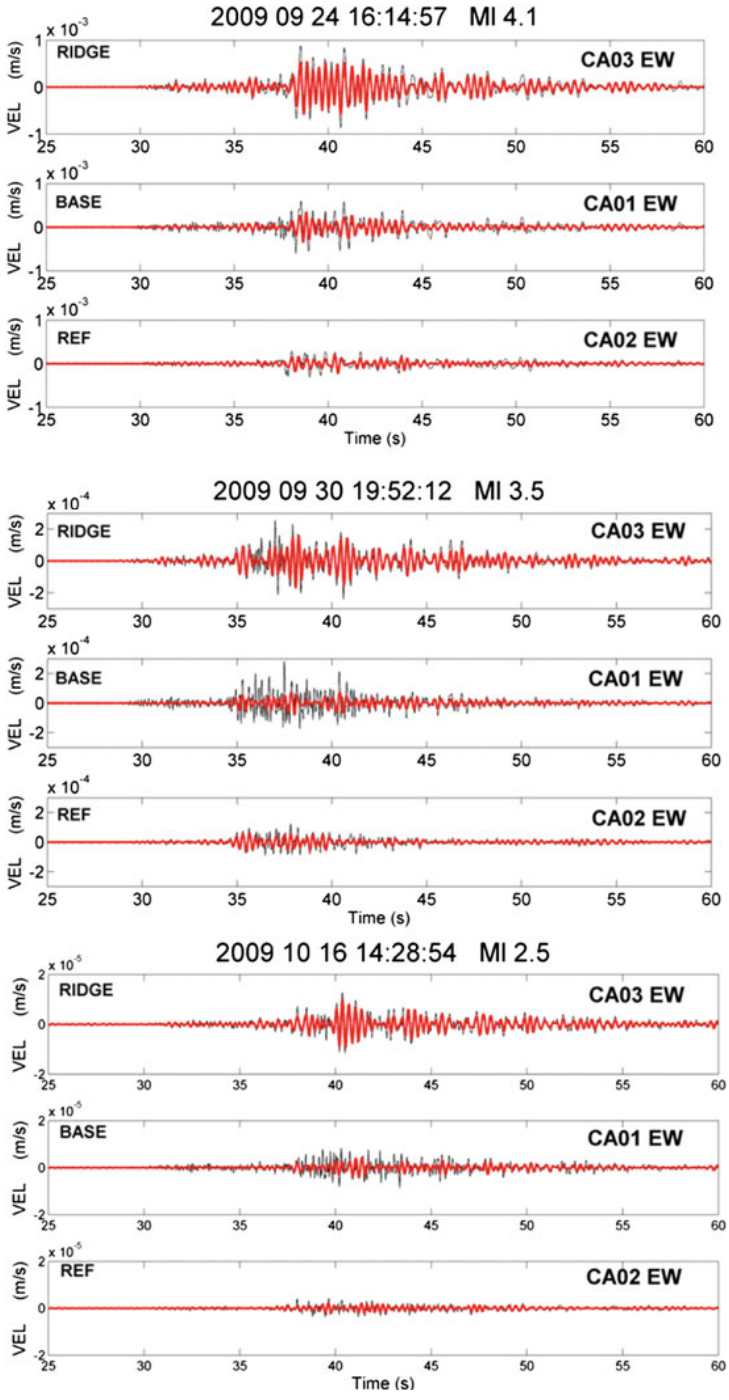

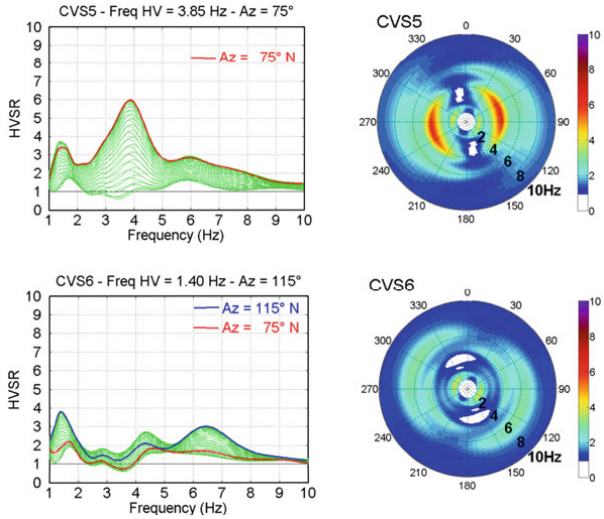

Figure 17. Left : East–West (EW) waveforms of earthquakes recorded at CA03, CA01, CA02 stations. Black titles: origin time and magnitude of the seismic event. RIDGE: station at the ridge of the relief; BASE: station at the base of the relief; REF: reference station on the slope of the Urano mountain. Black line: original waveform. Red line: band-pass filtered waveform from 2 to 4Hz.

Right: HVSR of the earthquake of Ml 2.4 on July 2009. Top: HVSR at CVS5 station. Bottom: HVSR at CVS6 station. Black titles: station code, frequency (Freq HV) and azimuth (Az) of maximum HVSR amplitude. Red lines: HVSR 75°N direction. Blue line: HVSR 115°N direction. Polar plot of NHVSR curves: black numbers mark degrees from the North; inner black numbers: represent the NHVSR frequency (Hz); color bar: marks the NHVSR amplitudes (from Marzorati et al., 2011).

2.2.4 Investigations at the base of Mt. Urano

Seismic noise measurements are performed to estimate the seismic response of the pinnacles (CV17 and CV18 in Fig. 18).

The seismic records were performed at pinnacles of Mt. Urano: CV17 and CV18 , where the pinnacles were presents. These records were performed to investigate morphological setting similar to this of the historical part of CS. The record CV17 was located to the base of the pinnacles, the CV18 to the uppermost of one of these. In Fig. 19 HVSR related to these two seismic noise records. HVSRs don't present clear peaks, the peak (10.5 Hz) present at HVSR CV17 station is due to the present of industry near the structural element. This analysis allows to define that at the base of the pinnacles there is not amplification. The geological characteristics of this structure are similar to those of the rock at the base of CS. There is not presence of amplification and fracturing as the base of the village. So, it is possible suppose that the amplifications at CS are due to rock particular conditions rather than the morphology of the rock outcrop.

Figure 18. Pinnacles near the CS village and the location of the seismic stations: CV17, at the base, and CV18, in the upper part of the geological structure.

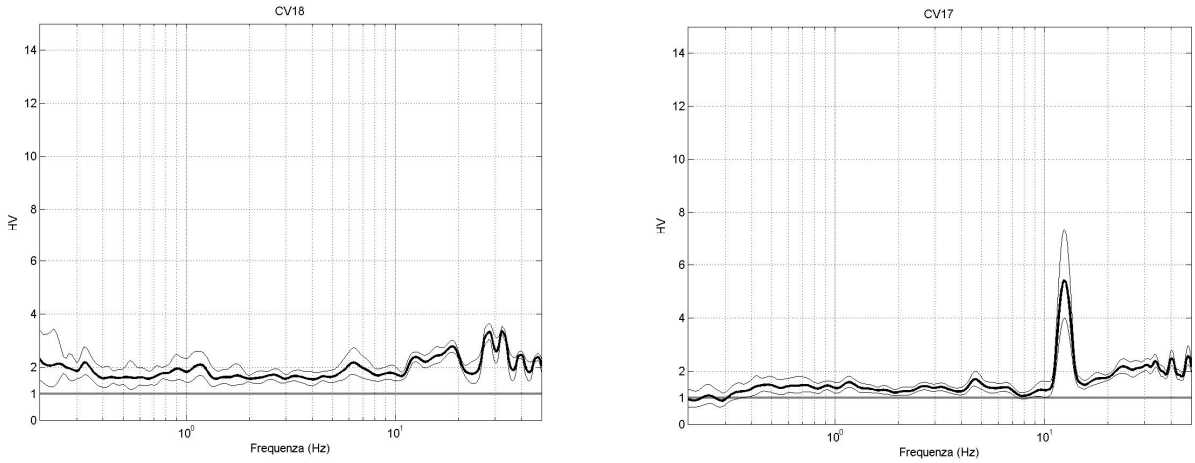

Figure 19. HVSR of the CV17 and CV18 seismic stations. Flat HVSR for CV18 station, anthropic peak at 10.5 Hz for HVSR of CV17.

2.2.5 Discussion on the results of investigation in CS

After the April 6, 2009 L'Aquila seismic event (Mw 6.3), many villages have an 'anomalous' level of damage. CS, located at about 40 km from the earthquake source, revealed an high degree of damage. The damage was distributed irregularly within CS and concentrated in the uppermost portion of the village, the old historical part.

The seismic campaigns performed at CS allowed to show an evident heterogeneity for the amplifications within the village and the seismic noise temporary campaign allows an hypothetic reconstruction of the SV with the different depth of bedrock. Also, the seismic noise data derived from three temporary seismic stations of the seismic network are added to the seismic data recorded in the historical part of CV. The geological and structural surveys performed with geophysical investigations add to reveal the site effect at CS.

In particular, the amplifications of the horizontal components along the CS ridge, with local variations of the frequency bands and amplitudes, have ranging between 1 and 15 Hz. In the surrounding areas, instead, no ground motion amplification has been detected (Figs. 12-13).

The largest amplifications of the horizontal components occur at the uppermost portion of the ridge, perpendicularly to its major elongation axis.

The HVSR and SSR, calculated with seismic data of temporary network confirm the amplification detected by NHVSRs, with amplifications between 1 and 7Hz.

The first hypothesis was that the topographic effect was the main factor that influences local site effects along small and narrow mountain ridges (Géli and Bard 1988; Massa et al. 2010). It must be noted that topographic effects involve the whole relief and is due to the fundamental frequency of

resonance of ridges (Faccioli et al. 2002). The seismic measurements showed an increase of the amplification amplitude from the base to the top of the ridge. These two seismological features are clearly visible also in many cases: for example in the case of Castelnuovo village, severely damaged by the April 6, 2009 earthquake (Gallipoli et al. 2009). Nevertheless, the marked heterogeneities concerning frequency, amplitude and polarization in the local seismic response of the CS ridge suggest that other causes have to be invoked to explain the observed ground motion amplification.

The results of geological investigations have shown that the limestone bedrock of the CS ridge is affected by different deformation between the lowermost and the uppermost sectors. These analyses reveal that the lowermost portion of the rock mass is characterised by deformation, with vertical, narrowly spaced shear planes and closed fractures, related to the main tectonic features that affect the CS area (Marzorati et al., 2010).

The uppermost portions of the ridge is characterised by rock slabs separated by moderately spaced joints and fractures. This characteristics allow to hypothesise that the heterogeneity of the local seismic response is related to the structural characteristics of the CS ridge. Significant ground motion amplification has not been identified at the lowermost portions of the rock mass. ground motion amplifications strongly increase at the uppermost portion of the ridge and displays a NE–SW orientation. No evident correlation n with the trend of the structural features is seen (Fig. 19 b–e). The described structural setting and the morphological characteristics of the relief, have favoured the spreading of the fractures. This is one of the main factors that contributes to the ground motion amplification in the uppermost sector of the CS.

This interpretation is also confirmed by the data obtained by the temporary seismic network. The Mt. Urano slopes (station CA02), is affected by closed joints (Fig. 19e, stations CS1-CV18). On the contrary, at station CS1, limestone bedrock is affected by pervasive ad intense deformation. Station CA03, installed at the top of the ridge, showed clear evidence of ground motion amplification perpendicular to the trend of the open fractures (Fig. 19a, CS5-CVS3).

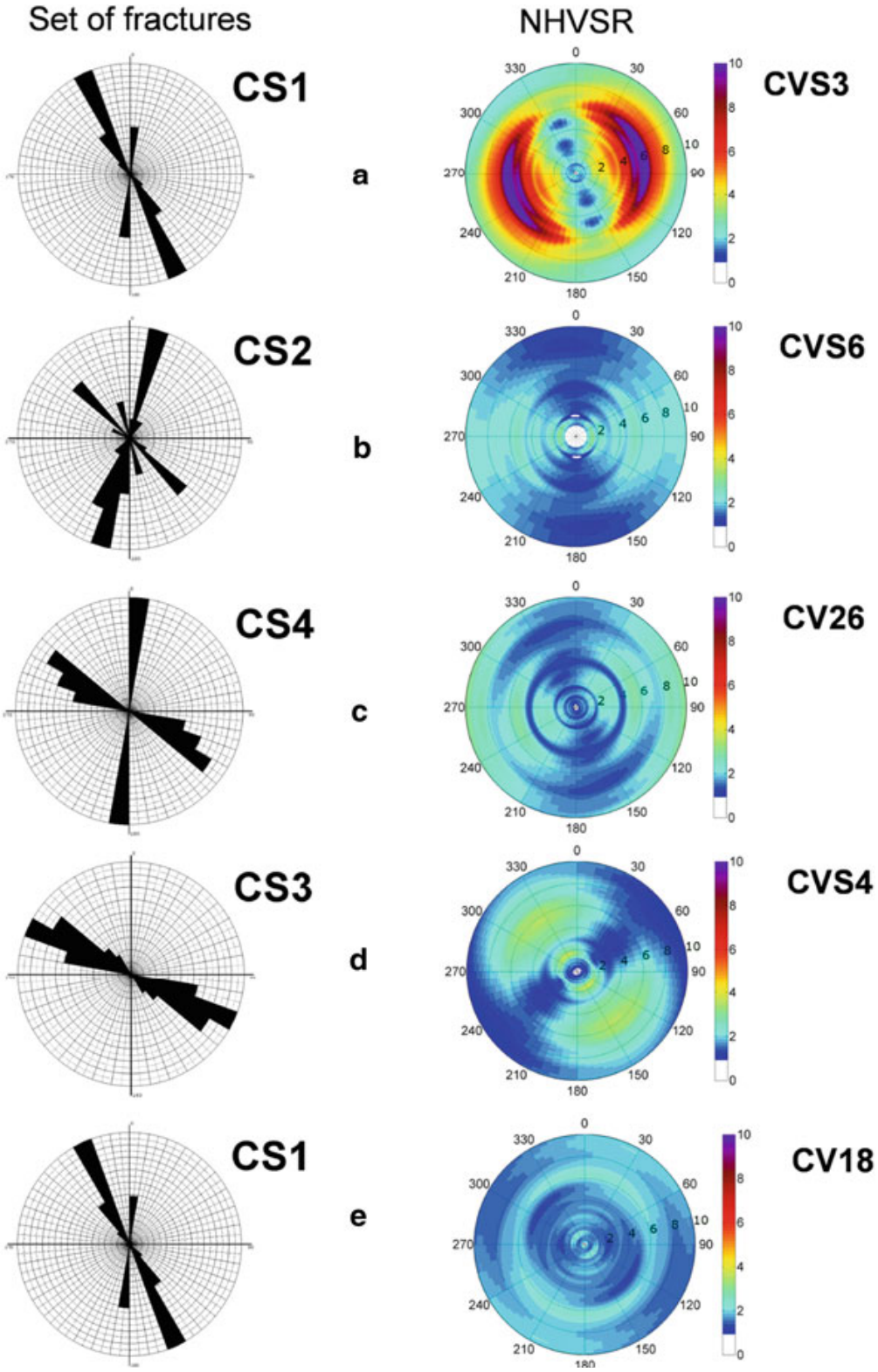

Figure 19. Structural discontinuities versus amplification directions. Left panels: rose diagrams. Right panels: polar plot of NHVSR curves. Outer black numbers: mark degrees from the North. Color bar: marks the NHVSR amplitudes (from Marzorati et al., 2011).

2.2.6 Analysis in the school of CS

Seismic noise measurements are performed to estimate the seismic response of the school of CS (CVS8 and CV29 in Fig.4).

Three seismic noise records are performed on school area. Two records investigate the amplification of the ground at the base of school building and in the garden. The last measurement carried out at the first floor of the school building to find the mode of vibration of the structure.

The results are elaborated with the same processing of the seismic noise records described before. Then, the results of the NHVSR allow to define that in the outside of the school there is not resonance frequency peak (base and garden, Fig. 20). The evident frequency peak is present in the record performed at the first floor at 5.5 Hz. This denote a fundamental mode of vibration of the school; likely below the school is present bedrock. The analysis exclude value of ground resonance frequency near the fundamental frequency of building vibration.

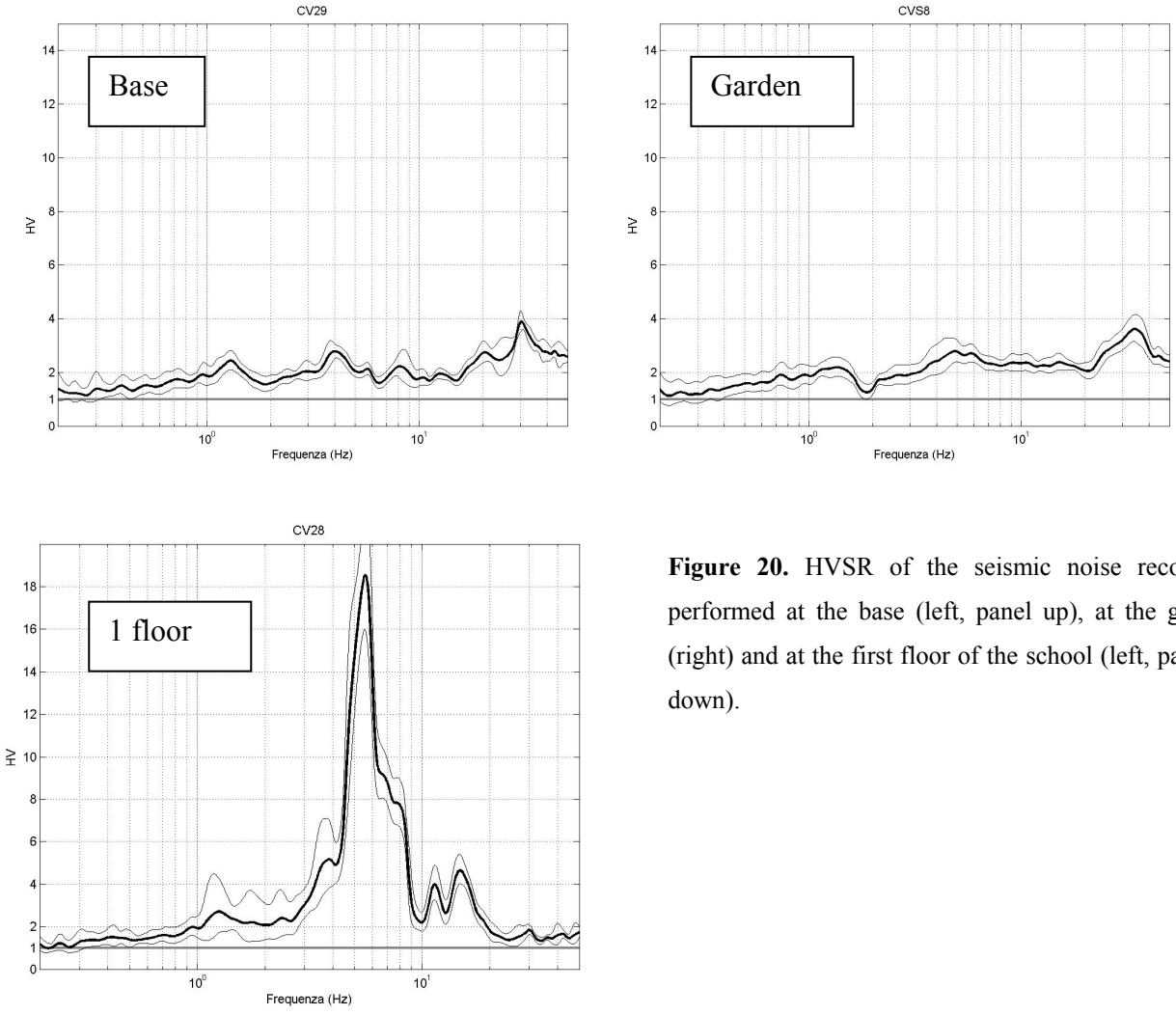

Figure 20. HVSR of the seismic noise records performed at the base (left, panel up), at the gym (right) and at the first floor of the school (left, panel down).

2.2.7 Seismic amplifications in SV

Ambient seismic noise is always present and it contains information about characteristics of the ground. The seismic noise is generated by human and natural sources located at few meters up to same kilometres. Seismic stations record always seismic noise. Human sources are characterised by high frequency (> 1Hz), this includes cars, industries as noise sources. The noise varies with human activity during the day. Natural sources are characterised by a low frequency (<1Hz). The sources are waves, sea storm, wind ecc. The natural noise varies with seasonal cycles (summer-winter).
The resonance frequency f_0 of the sedimentary cover is described as the maximum of the H/V ratio, average spectral amplitudes of horizontal (H) and vertical (V) noise components (Lachet and Bard, 1994; Tokimatsu, 1997; Bard, 1999; Nakamura, 2000; Fäh et al., 2001; SESAME European project, 2005). This parameter provides information on the ratio between the velocity V_a in the sedimentary cover and its thickness H:

$f_0 = V_a/4H$

This property is used to infer thickness of recent sedimentary cover from passive seismic measurements (Yamanaka et al., 1994; Ibs-von Seht and Wohlenberg, 1999).
For example this approach was used to provide an estimate of the subsurface geometry of the seismic bedrock in the Gubbio area (Fiorini et al., 2007). A seismic campaign of noise measurements were performed with light instrumental tool (url: http://www.tromino.it/). The seismic signal was corrected (base-line removed, tapered, smoothed) and the H/V ratio was computed for each frequency. The spectral ratio were analysed in term of time stability and directionality. The H/V spectral ratios gave evident peaks, some of these due to impulsive or anthropic sources. The peak of frequencies and their amplitude A_0 were computed averaging all the frequency/amplitude values corresponding to the maximum value of the H/V ratio in each time window. The peaks were analysed to exclude industrial origin, wind, presence of buildings or bad sensor coupling. If the measurement was unclear the record was repeated. In the case where only a single peak was found, f_0 was considered the fundamental frequency of the site when another peak was present, it was interpreted as a natural resonance frequency. All the curves with no significant peak were considered ‘flat’. For this case study 90 seismic measurements were performed. The results obtained with geophysical survey were associated with the geological analysis of the area.
The H/V ratios results are in good agreement with the geological data (Fig. 21).

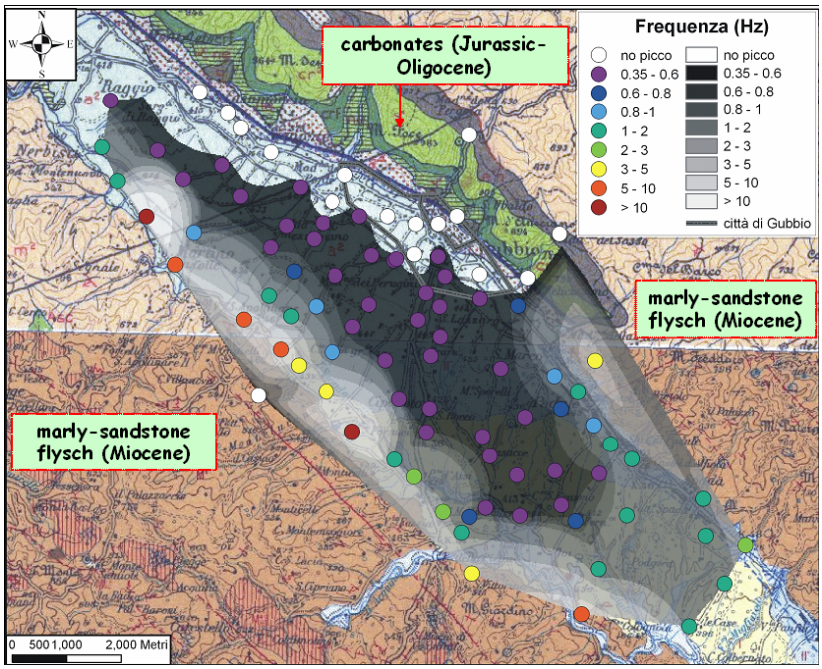

Figure 21. H/V spectral ratio measurements location site. Colours indicate the estimated value of the local fundamental resonance frequency. The contour is superimposed to the Geological map of the area (from Fiorini et al., 2007).

The results showed that the lowest resonance frequencies was obtained along the alluvial basin (< 0.5 Hz); f_0 increase near the boundaries of the plain. In the northernmost part of the plain (Gubbio old centre) the H/V ratios indicate the absence of resonance peaks.

The area with no-resonance correspond to the area with carbonatic breccias, but the alluvial fans dominate. The Vs velocity is high respect to sediments of the alluvial basin. The low values of f_0 indicate deep sedimentary cover (hundreds of meters).

Then, the active and the passive seismic surveys give an indication about the maximum depths of the order of 500-600 m from the surface. With the aim to construct the bedrock profile of the basin, the value of f_0 is deduced from H/V ratios. The depth of the bedrock is simply related with f_0 and H is obtained with:

$$H \approx a f_0^x$$

where a and x are empirical parameters determined by the regression analysis of experimental data, following Ibs-von Seht and Wohlenberg (1999). In this case the dataset is used for the determination of a and x value, considering f_0 estimated. The measured and computed profile suggests that this relationship can be used to constrain the bedrock profile from f_0 estimated. The results expected since the Vs profile indicated a different Vs pattern near the surface (H<100m) and

at depth. This results underline that the relationship considered is 'equivalent' of the more complex pattern in Fig. 22 and does not correspond to any realistic Vs profile (Fiorini et al., 2007).

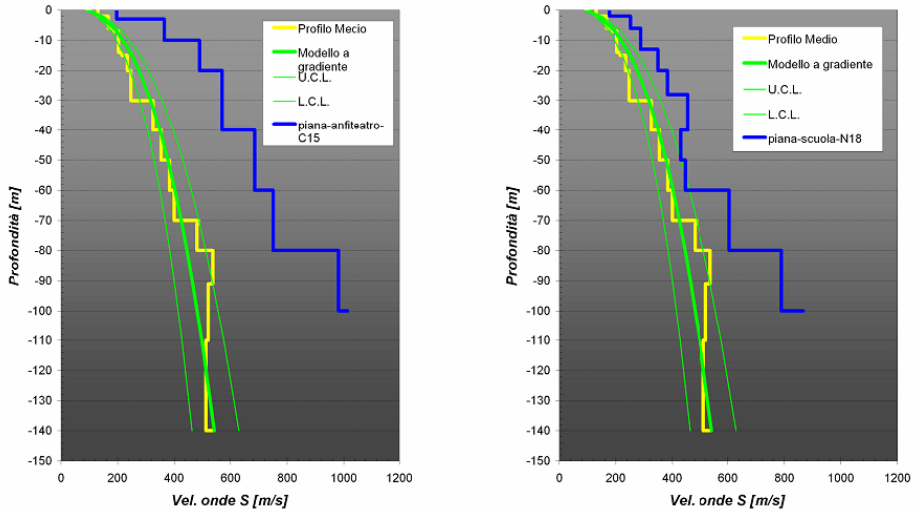

Figure 22. blue line: Vs velocity profiles obtained at two sites located in correspondence of the carbonatic debris and alluvial fans near the Gubbio downtown (from Fiorini et al., 2007).

D'Amico et al.(2008) using ambient seismic noise measurements and borehole data to characterize the Plio-Quaternary sedimentary basin underlying the city of Florence(Italy).

They considered ambient seismic measurements to calculated seismic noise horizontal to vertical spectra spectral ratio with the HVSR technique. The aim is to map the fundamental resonance frequency of the sedimentary cover to verify changes of the ground seismic response over the urban area related to variability of surface and subsurface geology. The S-waves velocities are obtained from array noise recordings and direct measurements of the sediments thickness at borehole sites. To analysis the site effects (Pitilakis, 2004) they investigated the fundamental resonance frequency of sediments, the relevant Vs profile and the depth of seismic bedrock. The frequency range considered is 0.1-20 Hz. The frequency peak and the amplitude were computed by averaging all the amplitude/frequency values of the HVSR maximum in each window (D'Amico et al., 2004). In the northwestern and eastern sectors of the urban territory the range of values is 0.9-3 Hz, the higher values are in proximity of the southern hills. The lower frequencies (1-5 Hz) were measured at sites of fluvio-lacustrine deposits. The HVSR peak frequencies are in general agreement with the topography of the rock basement. The low/high resonance frequency areas corresponding to deep/shallow bedrock zones.

In the case of SV, the aim is to construct the bedrock profile of the valley through a campaign of seismic noise and their analysis with HVSR technique. The fundamental frequency (f_0) of vibration of the ground is obtained with the analysis with seismic noise.

The deposits of the SV consists mainly of silt and lacustrine deposits similar to the basin of L'Aquila. Geotechnical survey (Gruppo di Lavoro MS–AQ (2010) Microzonazione sismica per la ricostruzione dell'area aquilana) estimate the Vs of this lithology at 600 m/s, for sediments of some meters (Fig. 23). In Fig. 23 the velocity is about 580-600 m/s between 100-200 m depth.

In Fig. 24 the seismic noise records. The seismic noise records reliable are 23 in the Fig 24 with their frequency (red number). For example, in Fig. 15 the f_0 is estimated at 0.83 Hz.

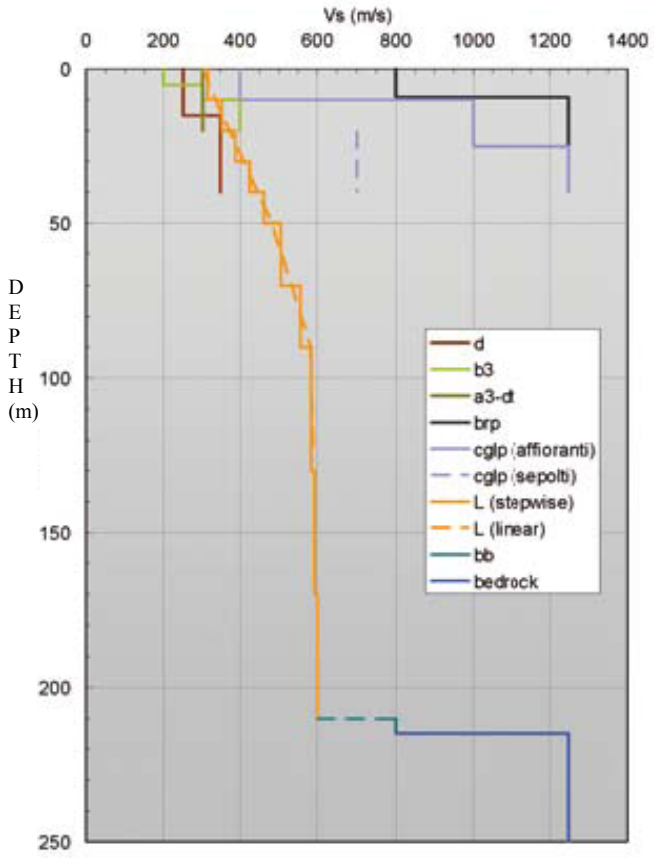

Figure 23. Velocity profile of ground for the Macroarea 4 (from Gruppo di Lavoro MS–AQ (2010) Microzonazione sismica per la ricostruzione dell'area aquilana)

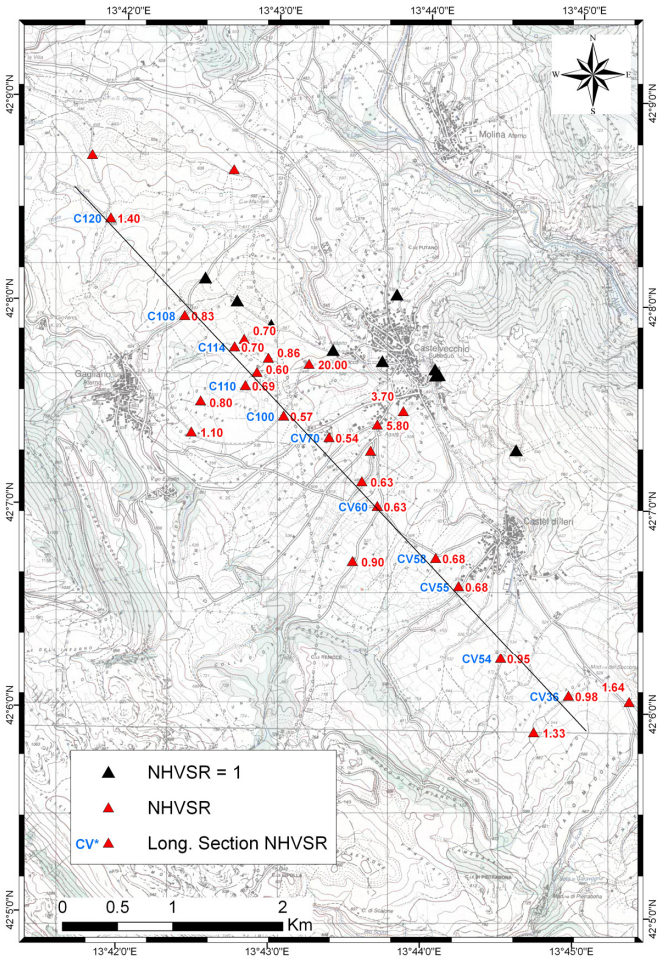

Figure 24. Location of the ambient seismic noise records. Red triangles: noise measurement. Black triangles: flat HVSR. Red number: HVSR frequency peak. Blue letters: station name. Black line: section line. Background: Carta Tecnica Regionale, Regione Abruzzo.

HVSR are performed for the seismic noise records in SV, the results can be grouped in three different cases:

- 1.flat HVSR at CV93 (Fig. 16 A);
- 2.presence of broad-band peak but not evident at CV82 (Fig. 16 B);
- 3.presence of an evident frequency peak at C100 (Fig. 16 C).

A flat HVSR results at the stations CVS9, CV15, CV17, CV18, CV72, CV71,CV93, C117, C118 and C119 (blue circles in Fig. 25). The seismic noise record, in this case, was performed directly on the bedrock or on a sedimentary layer, but very thin because the HVSR in this case has not frequency peak.

In the second case, the stations CV37, CV51, CV52, CV56, CV59, CV81, CV82, C105 and C111 (red circles in Fig. 25) present a broad-band peak, but not evident. These stations are located on the eastern basin edge, where it is a fault scarp described in the Falcucci et al. (2010).

In the third case, the stations selected are in Fig. 24. They present a clear peak of amplification. These stations are located in the SV, the zone is flat or with little slope. This characteristic allows to suppose that the horizontal sublayers and the present of a high layer of sediments.

In Fig. 26 an example of the trend of the SV suppose with the characteristics of the ambient seismic noise records described previous.

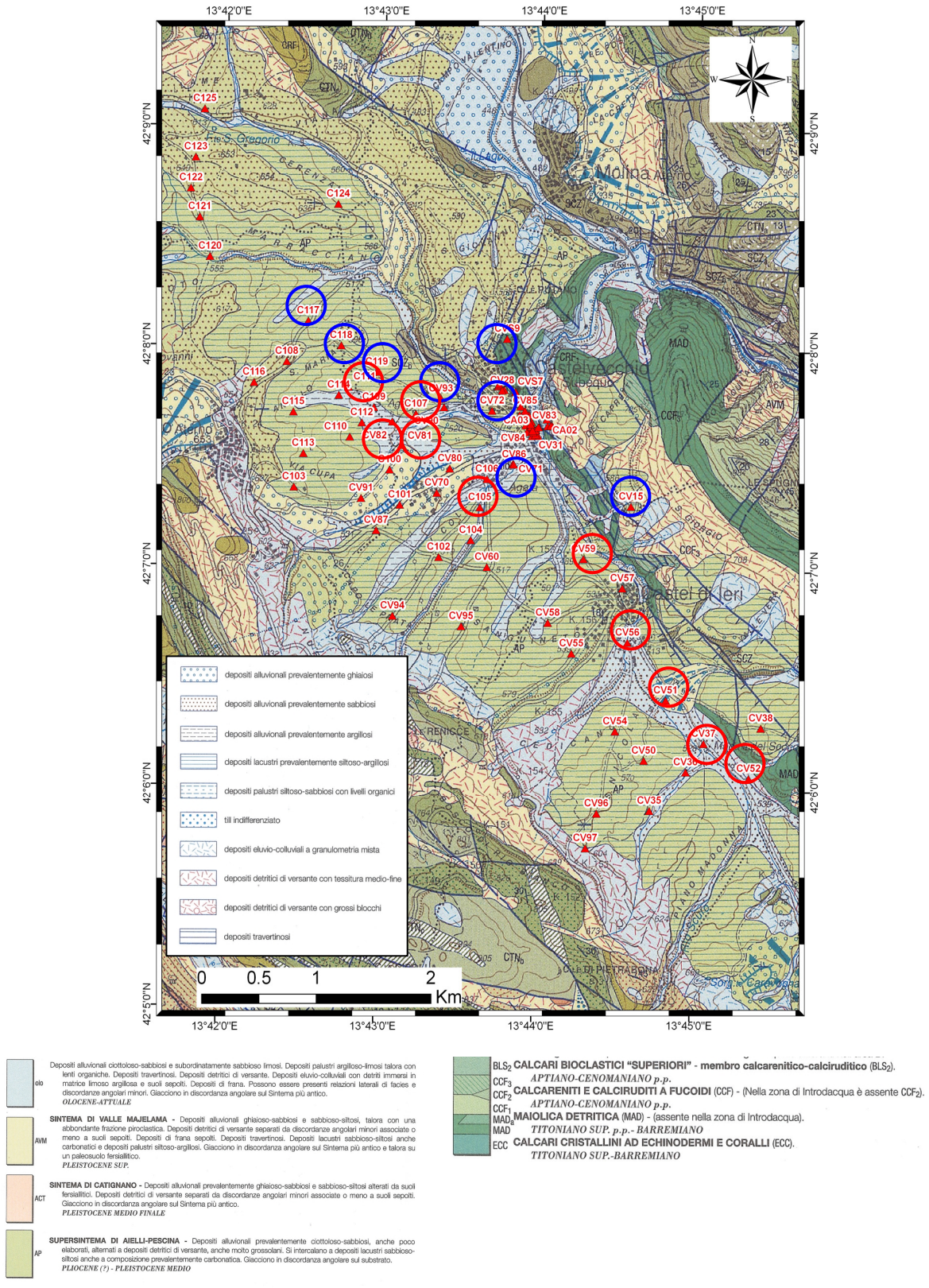

olo — Depositi alluvionali ciottoloso-sabbiosi e subordinatamente sabbioso limosi. Depositi palustri argilloso-limosi talora con lenti organiche. Depositi travertinosi. Depositi detritici di versante. Depositi eluvio-colluviali con detriti immersi in matrice limoso argillosa e suoli sepolti. Depositi di frana. Possono essere presenti relazioni laterali di facies e discordanze angolari minori. Giacciono in discordanza angolare sul Sintema più antico.
OLOCENE-ATTUALE

AVM — **SINTEMA DI VALLE MAJELAMA** - Depositi alluvionali ghiaioso-sabbiosi e sabbioso-siltosi, talora con una abbondante frazione piroclastica. Depositi detritici di versante separati da discordanze angolari minori associate o meno a suoli sepolti. Depositi di frana sepolti. Depositi travertinosi. Depositi lacustri sabbioso-siltosi anche carbonatici e depositi palustri siltoso-argillosi. Giacciono in discordanza angolare sul Sintema più antico e talora su un paleosuolo fersiallitico.
PLEISTOCENE SUP.

ACT — **SINTEMA DI CATIGNANO** - Depositi alluvionali prevalentemente ghiaioso-sabbiosi e sabbioso-siltosi alterati da suoli fersiallitici. Depositi detritici di versante separati da discordanze angolari minori associate o meno a suoli sepolti. Giacciono in discordanza angolare sul Sintema più antico.
PLEISTOCENE MEDIO FINALE

AP — **SUPERSINTEMA DI AIELLI-PESCINA** - Depositi alluvionali prevalentemente ciottoloso-sabbiosi, anche poco elaborati, alternati a depositi detritici di versante, anche molto grossolani. Si intercalano a depositi lacustri sabbioso-siltosi anche a composizione prevalentemente carbonatica. Giacciono in discordanza angolare sul substrato.
PLIOCENE (?) - PLEISTOCENE MEDIO

BLS_2 **CALCARI BIOCLASTICI "SUPERIORI" - membro calcarenitico-calciruditico** (BLS_2).
CCF_3 *APTIANO-CENOMANIANO p.p.*
CCF_2 **CALCARENITI E CALCIRUDITI A FUCOIDI** (CCF) - (Nella zona di Introdacqua è assente CCF_2).
CCF_1 *APTIANO-CENOMANIANO p.p.*
MAD_2 **MAIOLICA DETRITICA** (MAD) - (assente nella zona di Introdacqua).
MAD *TITONIANO SUP. p.p.- BARREMIANO*
ECC **CALCARI CRISTALLINI AD ECHINODERMI E CORALLI** (ECC).
TITONIANO SUP.-BARREMIANO

Figure 25. Noise measurements in SV. Red circle: broad band NHVSR peaks. Blue circles: flat NHVSR.

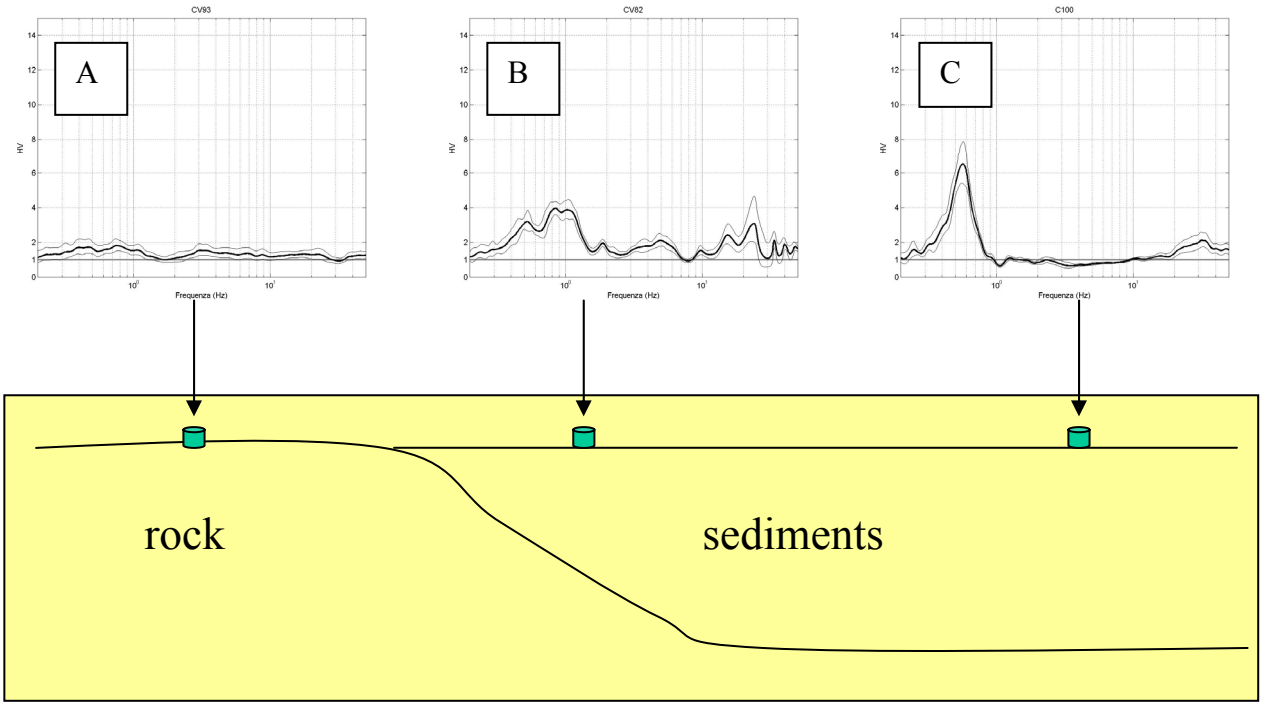

Figure 26. HVSR that represent the three situations found in the analysis of the seismic noise records in the SV. A: HVRS flat at CV93; B: presence of broad-band peaks at CV82; C: presence of evident frequency peak at C100.

In Fig. 27 show an example of two different seismic records, CV93 record performed in CS (Fig. 6), with a flat HVSR and C100 record (Fig.6) performed in SV with an evident peak between 0.5 and 0.6 Hz. The depth calculated for these two different records show that in the first case the seismic station is located at rock, in the second case the seismic station is located at sediments. The depth of the bedrock in the first case is 0 m. and in the second case is about 250 m, value supposed in Falcucci et al. (2011).

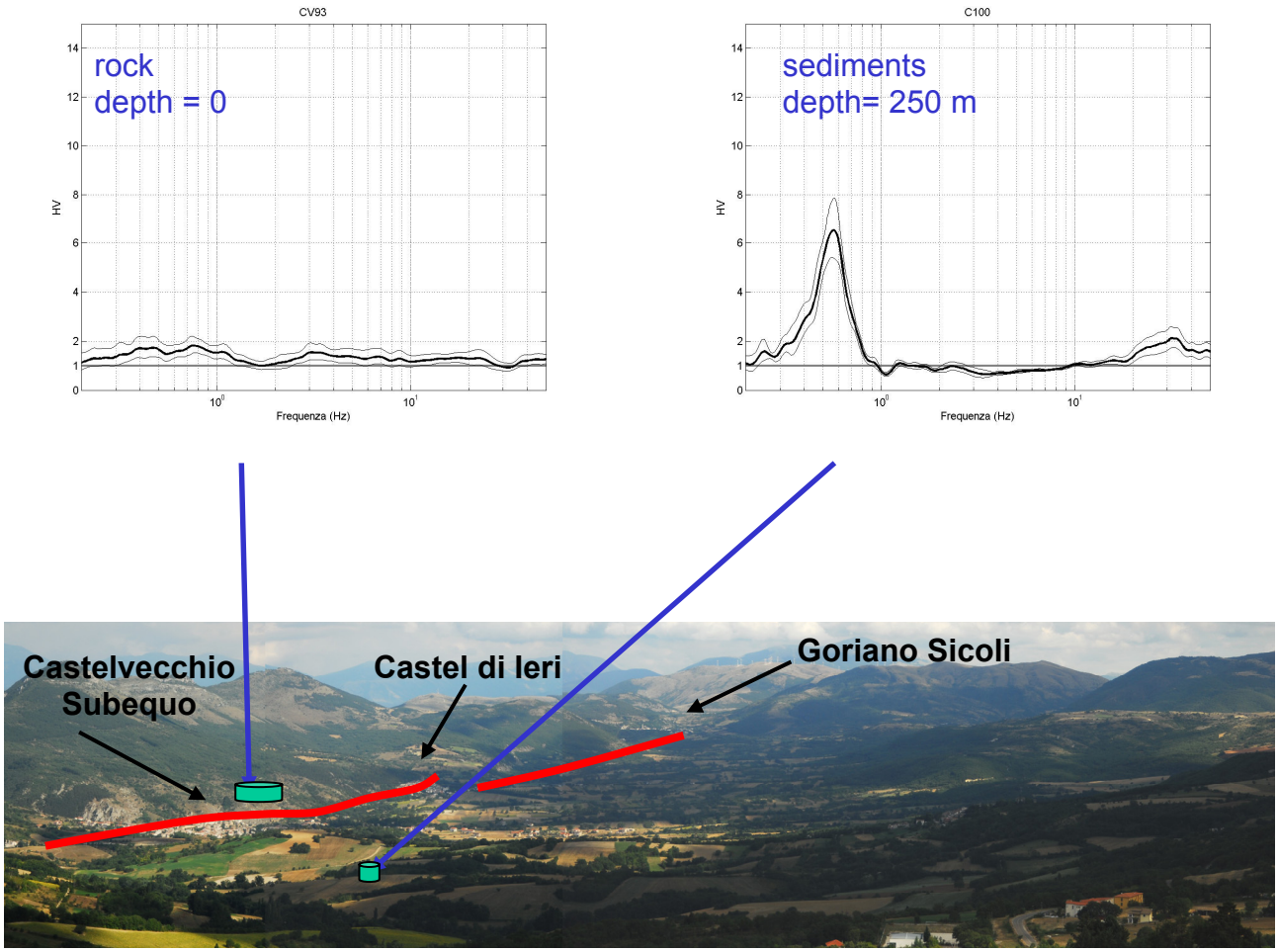

Figure 27. HVSR of CV93 and C100 seismic records and image of the SV with the towns of Castelvecchio Subequo, Castel di Ieri and Goriano Sicoli. Red line: fault. Green balls: location of the seismic stations.

For all seismic records are calculated the Fo and the corresponding depth of the bedrock. With these data it is possible to obtain an hypothetic reconstruction of the SV where it is evident the deepening of the bedrock. The most value of deepening of the sediments is 312 m (black area in Fig. 28), in the area in front of CS (Fig. 28). In Fig. 29, representation with the topography of the area. Under the topography (black line with triangles) the trend of the ground (black line with points). This trend is obtained with seismic noise records (triangles in Fig. 29). The greatest depth is evident under CS and the depth is less under Castel di ieri (Fig.29).

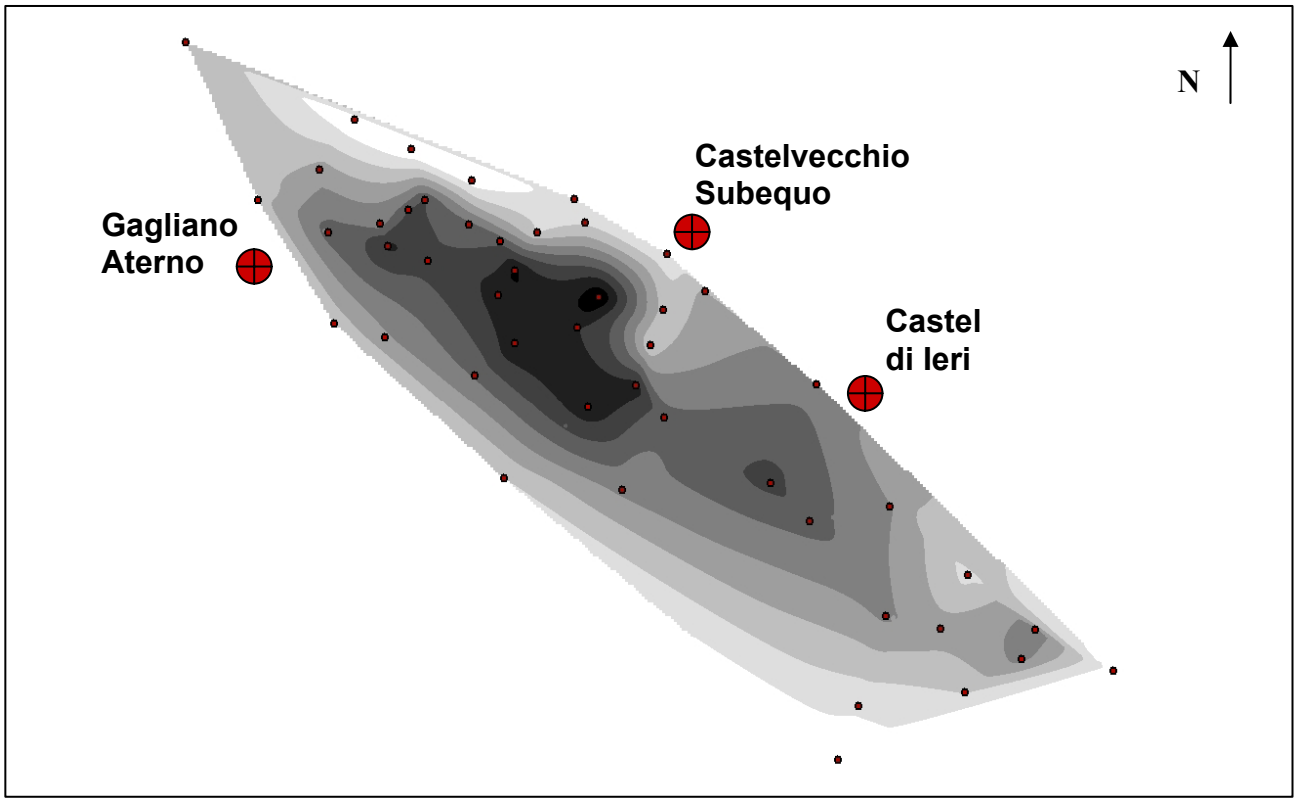

Figure28. Hypothetic reconstruction of the SV. The values of depth are obtained from HVSR. Red little circles: the localization of the seismic noise records. Red circles: location of the CS, Gagliano Aterno and Castel di Ieri. The different colour scale indicate the different depth of the sediment (white to black, more superficial and deeper, respectively).

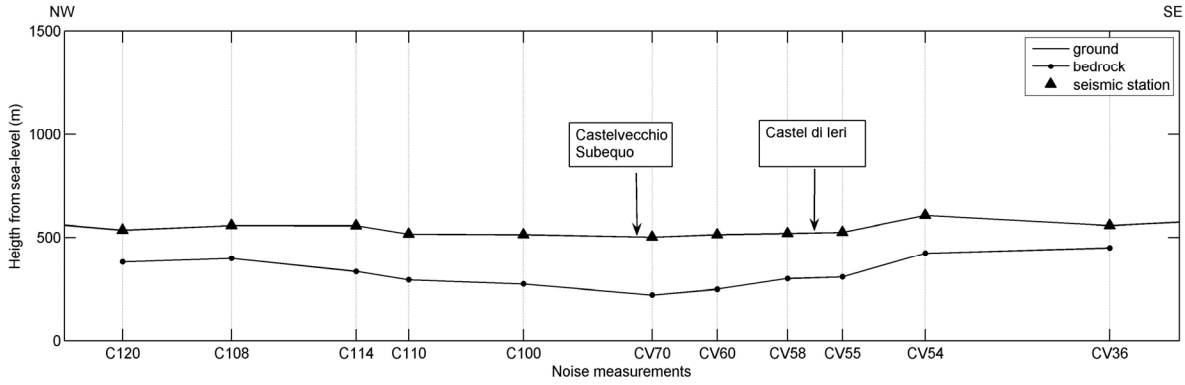

Figure 19. Trend of the ground (black line with points) under the topography (black line with triangles). Triangles: seismic stations. X axis: seismic station location. Y axis: height from sea level (m).

Chapter 3.
Cross-correlation of the seismic noise

3.1 Green Function: Mathematical Approach

The seismic Time Domain Green's Function (TDGF) between two stations is estimated from the measured response from an active controlled source or using seismic sources of opportunity (Sabra et al., 2005). Also, coherent deterministic arrival-times can be extracted from the time derivative of the time averaged ambient noise cross-correlation function (NCF) between the receivers. Large and dense network of broadband seismic stations are used for earthquake monitoring and they measure ambient noise continuously. The TDGF estimate emerges from these correlations that contain noise sources whose field passes through receivers. Evidences of this results has been presented in helioseismology (Rickett and Claerbout, 1999), ultrasonics (Lobkis and Weaver, 2001; Weaver and Lobkis, 2003; Larose et al., 2004; Malcom et al., 2004; Weaver and Lobkis, 2004), underwater acoustics (Roux et al., 2004; Sabra et al., 2005a) and in seismology (Shapiro and Campillo, 2004).
The NCF C of the traces at two receivers separated by distance L is zero for $|t| > L/c$ (no wave can travel slower than c, sound speed) in a spatially uniform broadband noise distribution in a uniform medium; while non-continuous at $t = \pm L/c$ and continuous for $|t| < L/c$ (waves originating from broadside will appear to travel faster than c). Thus the derivative of the NCF is

$$\frac{dC}{dt} \approx -\frac{\delta(t + L/c)}{L} + \frac{\delta(t + L/c)}{L} \qquad (1)$$

Then was constructed a relationship for the time-derivative of the ambient noise cross correlation C_{ij} between two stations (the first located at r_1 recording component i and the second located at r_2, recording component j) to the TDGF G_{ij} (r_1 ; r_2 ; t)

$$\frac{dC_{ij}}{dt} \approx -G_{ij}(r_1; r_2, t) + G_{ij}(r_2; r_1, -t) \qquad (2)$$

The TDGF G_{ij} (r_1 ; r_2 ; t) relates a unit concentrated impulse displacement in direction i at r_1 to the displacement response in direction j at receiver r_2.
In equation (1) the terms are respectively: 1) the TDGF which comes from noise events that propagate from station 1 to 2 and yields a positive correlation time-delay t and 2) the time-reversed TDGF which comes from noise events that propagate from station 2 to 1 and yields a negative correlation time-delay $-t$. For a uniform noise source distribution surrounding the stations, the

derivative of the NCF will be a symmetric function because ambient noise sources are distributed on both sides of the station pair.

The cross correlation C_{ij} is computed from the observed fields $v_i(r_1, t)$ and $v_j(r_2, t)$ by integration over the whole observation period T

$$C_{ij}(1,2,t) = \int_0^T v_i(r_1,\tau) v_j(r_2,\tau+t) d\tau \tag{3}$$

The ambient noise recorded on seismic stations has a small bandwidth. The derivative improves the higher frequencies in the derived TDGF usually enhance noise.

Other researches used a similar form to equation (1), but they used the cross-correlation instead of the derivative.

For example in Campillo and Paul (2003) velocity variations of seismic waves with depth can be derived from arrival times or from the dispersion properties of coherent surface waves. One difficulty with this technique is that it requires energetic sources such as explosions or earthquakes. They noted that the use of field-to-field correlation to retrieve the Green function is a valid approach such as in the favourable conditions but also with natural signal (earthquakes). In seismology, the coda waves, which make up the later part of the signals, are the result of the scattering from small-scale heterogeneities in the lithosphere; but the physics of the coda waves cannot be fully understood with classical ray theory (Aki et al., 1975; Sato et al., 1998). Multiple scattering plays a prominent part in the seismic coda, and seismologists have made use of the radiative transfer theory to model the coda intensity (Wu et al., 1988; Margerin et al., 1999).

They used the coherence of diffuse waves to retrieve direct waves between two stations at Earth's surface. In this case the cross-correlation function between the wave fields produced by a single source at two points is averaged over the source location. Assuming a modal representation of the wave field, the spatially correlation is an approximation of the Green function between the observation points. Considering a time window delayed from the first arrival for the waves to have become diffuse as a result of scattering, the displacement u at location R and time t in the form of its expansion in the functions Φ^n of the elastic medium results

$$u(R,t) = \sum_n \varepsilon_n \Phi^n(R) \exp(-i\Omega_n t) \tag{4}$$

where the Ω_n are the frequencies and ε_n are independent variables. The expression of the cross-correlation of the displacement at two different locations is close to the Green function between two stations.

Shapiro and Campillo (2004) considered the alternative method proposed by Campillo and Paul (2003) and supposed that a diffuse wavefields are composed of waves with random amplitudes and phases and contain information that can be extracted by cross-correlations between the two receivers. In this case a simple demonstration is based on a modal representation of a diffuse wavefield inside an elastic body (the Earth)

$$\phi(x,t) = \sum_n a_n u_n(x) e^{iw_n t} \tag{5}$$

where x is the position, t is the time, u_n and w_n are functions and frequencies of the body and a_n are modal excitation functions. An important property of the diffuse field is that the modal amplitudes are variables

$$\left\langle a_n a_m^* \right\rangle = \delta_{nm} F(\omega_n) \tag{6}$$

where $F(\omega)$is the spectral energy density. The correlation between the fields at locations x and y becomes

$$C(x,y,\tau) = \sum_n F(\omega_n) u_n(x) u_n(y) e^{-i\omega_n \tau} \tag{7}$$

The equation (7) differs only by amplitude factor F from the actual Green function between two points (x, y). This is a very important application: the Green function can be extracted from the diffuse field with a simple field-to-field correlation taken over long time.

Also Stehly et al., 2006, applied the idea of using random noise to reconstruct the Green function. In case of a homogeneous distribution of noise source, the cross-correlation is nearly symmetric in amplitude and in arrival time and its positive and negative parts correspond to the Green function of the medium and its anticausal counterpart. In practice, the casual and anticausal parts of the cross-correlation may differ in amplitude. This different amplitude depends on the energy flux of the waves travelling between stations. In the case of perfectly isotropic distribution of sources , the energy between the two stations is the same in both directions and the cross-correlation is

symmetric; but in other cases, the energy propagating is different between the stations. The resulting cross-correlation is not symmetric in amplitude. This case has an important consequence, the asymmetry of the cross-correlation can be used to measure the main direction of the energy flux.

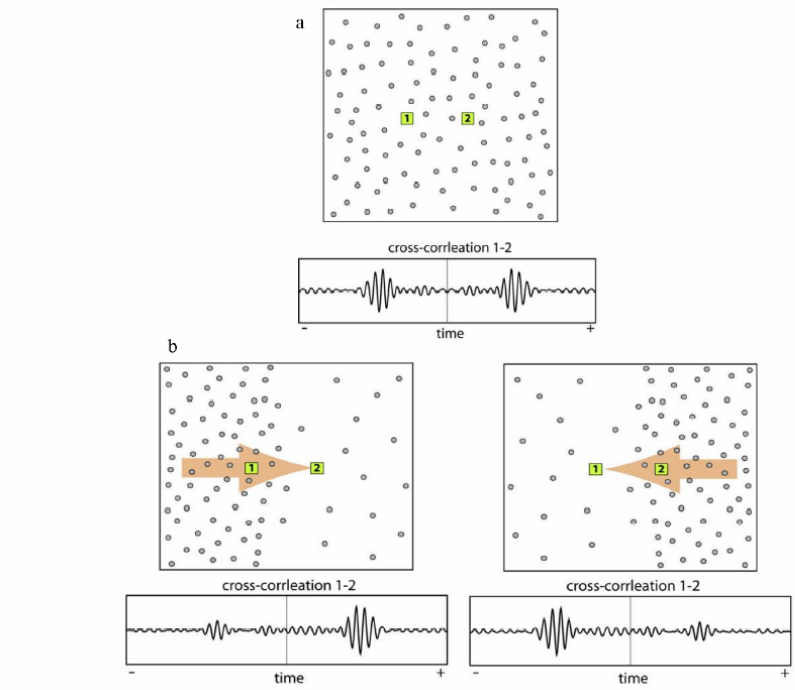

Figure 1. Illustration of the effects of noise sources distributions. (a) symmetric cross-correlation obtain when the noise sources are equally distributed. (b) asymmetric cross-correlation associated with unequal sources distribution (Stehly et al., 2006).

In the last cases the sources were randomly located and active in any time, but these are a particular conditions. A demonstration of the link between the Green's functions and the cross-correlations can be made without assumptions about noise sources location and activation time. Sanchez-Sesma and Campillo (2006) consider an isotropic distribution of P and S waves in an elastic medium. They supposed that the azimuthal average of the cross-correlation of motion between two points is proportional to the imaginary part of the Green's tensor between these points. These results show that equipartition is a necessary condition to retrieve the exact Green's function from correlations of the elastic field.

Weaver and Lobkis (2004) used an integral representation approach to study the problem of the heterogeneous region in an open medium. The property is expressed in the spectral theory of scattering that shows that the properties obtained in the simplest case of a homogeneous medium are valid in presence of heterogeneities.

3.2 Multi Window Cross-Spectrum technique (MWCS)

Stress field variations in time modify the elastic behaviour of the Earth's crust and they can be recovered through the analysis of the Earth's seismic response and temporal evolution. There are many studies of waveform variations in space and time to understanding the dynamic behaviour of the crust. Particular interest are tectonically and volcanically active regions in which stress changes are frequent and may precede earthquakes and volcanic eruptions. Initially all studies focused on coda waves, their amplitude and a possible application in the forecasting of volcanic activity. The analysis of Poupinet et al. (1984) gave a new approach which led to the detection of relative variations in velocity. At the same way, the seismic coda wave interferometry technique developed by Snieder et al. (2002) confirmed the existence of detectable precursory crustal change. These techniques are practicable in cases where records of earthquake doublets are available, seismic noise became popular study argument thanks to these recent studies. This is due to the possibility of retrieving seismic Green's functions from the cross-correlation of records of a random seismic wavefield taken at various locations within the interest area (Lobkis and Weaver, 2001; Weaver and Lobkis, 2001; Campillo and Paul, 2003; Shapiro and Campillo, 2004; Sabra et al. 2005; Shapiro et al. 2005). Seismic noise is recorded continuously and it does not depend on earthquake sources. The idea for monitoring the evolution of seismic velocities using seismic noise is to compare 'current' function, that represents the situation at a given time period, to 'reference' functions, that represents an average background state of the studied media. The noise cross correlation reflect variations of the elastic properties in the propagating medium.

In a seismogram or in a correlation function, the delay accumulates linearly with the lapse time when the wave speed changes homogeneously within the medium. This makes the use of coda waves particularly suited to measure temporal variations.

The first method was known as coda wave interferometry, and the theory was described by Snieder (2006), later evolved to Passive Image Interferometry (Sens-Schönfelder and Wegler, 2006; Wegler et al., 2009) for noise sequence cross-correlations. The second method named Moving Window Cross Spectral Analysis (MWCS) by Ratdomopurbo and Poupinet (1995) has the advantage of operating in the frequency domain. Clarke et al. (2011), in their study, assess the accuracy of the velocity variations measured from noise cross-correlations with MWCS technique and how this accuracy depends on the quality of the reconstructed cross correlation function. This analysis is applied to time-series which are computed by cross-correlating the noise sequences recorded at two different seismic stations, for all possible stations pairs.

As regards the first method, temporal changes in Earth's structure, for example earthquakes, have been observed on the basis of the attenuation of coda waves, on the arrival times of the directly arriving waves, on velocity changes inferred from later arriving waves and on changes in seismic anisotropy. In their study Snieder et al. (2002a) introduced coda wave interferometry method where multiply scattered waves are used to detect temporal changes in a medium by using the scattering medium as an interferometer (Fig. 2). In coda wave interferometry method, one records multiply scattered waves at a limited number of receivers to infer changes in the medium over time. Through this method Snieder et al. (2002a) determined the nonlinear dependence of the seismic velocity in granite on temperature and the associated acoustic emissions. This technique can be used also in the warning mode, in order to detect the presence of temporal changes in the medium, or in diagnostic mode, where the temporal change in the medium is quantified (Snieder et al., 2002a).

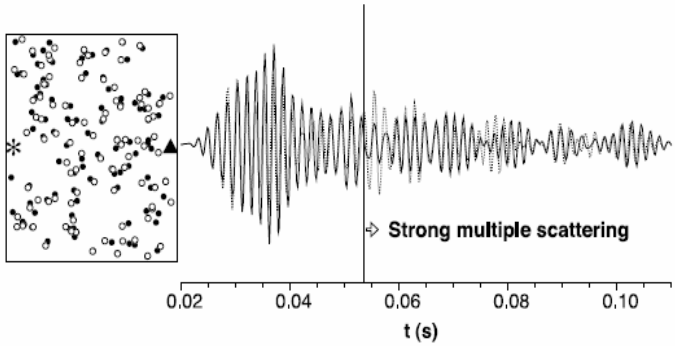

Figure 2. Location of 100 scattered before and after the perturbation (filled and open circles) with the source (asterisk) and receiver location (triangle). The waveforms recorded before and after the perturbation at the receiver are shown on the right with a solid and dashed line (from Snieder et al., 2002a).

The MWCS analysis was proposed for the first time by Poupinet et al. (1984) to recover the relative velocity variation between earthquake doublets.

Events with similar waveforms are observed and they seem to originate from the same location. Moreover, if the seismograms of the doublets are identical, the source processes are identical and also the medium properties are also invariant. Poupinet et al. (1984) selected doublets that occur on different dates to search possible temporal variations of crustal properties. In this study they analysis two events located on the section of the Calaveras fault that ruptured during the M=5.9 Coyote Lake earthquake of August 6, 1979. To process these signals a window (1.2 s) with 50% cosine taper is moved along the length of each seismograms and the Fourier transform of the two seismograms is estimated. The delay between two signals is evaluated in the frequency domain with a cross-correlation method. At first, the traces are aligned to the nearest sample to avoid bias in the delay estimation. The Fourier transform are computed and the cross spectrum is defined by

$$S_i(f) = A2^*_i(f)A1_i(f)$$

where the asterisk denotes the complex conjugate. So the coherence is calculated from smoothed spectra ($A1_i$, $A2_i$) and cross spectrum S_i:

$$C_1(f) = \frac{S_i^2(f)}{A1_i(f)A2_i(f)}$$

The phase $\Phi(f)$ of the cross spectrum in obtained from the complex valued $S_i(f)$ (Fig. 3).

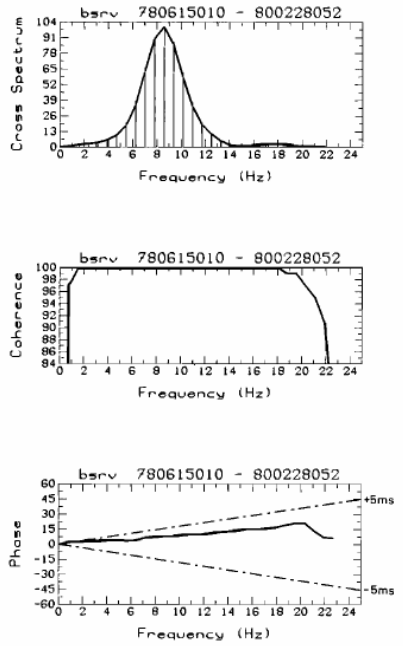

Figure 3. Cross spectrum, coherence and phase of the cross spectrum for seismograms (from Poupinet et al., 1984).

The time delay δi between the windowed signals is obtained by fitting a line, starting at the origin, to the phase of the cross-spectrum $\Phi(f)=2\pi\delta_i f$, where the phase Φ is expressed in radians.

Also they assess the uncertainties introduced during the data acquisition process; the observed changes could be caused by a variation of the instrumental delays in the seismic system. Moreover, there are two different classes of possible errors. The first class consists of errors that vary along the seismogram; the second class corresponds to errors that are constant over the time span of the seismogram and modify the absolute value of the delay.

The S velocity change in the crust in a volume between the source and receiver during the time interval between the events of the doublet. Waves travelling in this volume will be delayed in proportion to their total travel time. The velocity changed $\Delta Vs/Vs$ is given by the slope of $\delta(t)$

$d\delta/dt = -\Delta Vs/Vs$

$\Delta Vs/Vs$ was computed by fitting a line to $\delta(t)$, from the origin time. They interpreted this variation as a *S* velocity decrease.

In this study they have presented a technique that improves the precision in measuring temporal variations of the velocity of body waves using data from microearthquakes networks. The time delay $\delta(t)$ is plotted as a function of the running time along the seismogram and they calculated the fractional change in S velocity from the slope of $\delta(t)$. A change of S velocity is found in a small region near the rupture zone. This may reflect a decrease in stress or a change of crustal properties in the region.

In summary, this technique can be easily applied to data from seismographic networks that provide the time base sufficiently stable.

Another study case was proposed by Ratdomopurbo et Poupinet (1995) where they monitored the velocity variations of Mt. Merapi (Indonesia) using the MWCS technique. In this case the high level of seismic activity is a precursor to an impending eruption. In this study they used doublets to monitoring temporal velocity variations. Doublets or multiplets are frequently observed on volcanoes (Okada et al., 1981; Fremont and Malone, 1987). Their similarity indicates that sources are spatially near. Doublets study is a precise method to detect small temporal changes in physical properties in the medium traversed by seismic waves.

To know their location, they stacked all traces in each stations and determined the hypocenter of the stacked event. This technique improves significantly the S/N ratio and it makes phase arrival picking easier. The aim of this work is to detect any change in the waveforms of the seismograms of a doublet. At first the seismograms are aligned with a precision of one sample. In a window, the phase spectrum Φ of the cross-correlation between two events is linearly proportional to the frequency f and to the time delay between the two signals Δt: $\Phi(f)=2\pi\Delta tf$.

The delay Δt between the traces can be computed from the slope b of the phase of the cross-correlation (Poupinet et al., 1984), $\Delta t=b/(2\pi)$. The MWCS analysis is applied to the entire seismograms recorded at the summit located near the crater to find velocity variations. They computed the time delay between the two seismograms for each window starting from the P wave arrival until the end of the coda (Fig. 4).

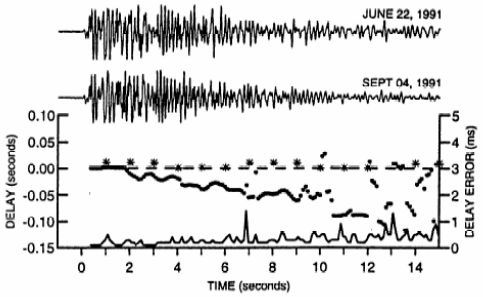

Figure 3. Example of the computation of the delay between the seismograms of the two events aligned on the P wave arrival time. The slope of the time delay is proportional to the S-velocity change $-\Delta V/V$. Stars are the delay of the PPS clock signal. Errors in delay calculation are presented in the lowermost line graph (right scale) (from Ratdomopurbo et al., 1995).

Considering a doublet, two earthquakes occurring at different dates and at the same hypocenter, they found that $\Delta t=-(\Delta V/V)$; This relationship means that the fractional change in velocity is equal to the slope of the time delay in the coda. A decrease in delay time along the seismogram indicated an increase in velocity. The slope is calculated using a coherence weighted linear regression.

These results showed that the precursory period can be divided into two periods: in the first period the velocity was stable and in the second period there was a continuous increase in seismic velocity. The velocity change is probably related to a pressure change within the magma chamber and in the conduits. An eruption usually results from an increase of pressure inside the magma chamber; pressure is at least higher than lithostatic pressure. Seismic velocity and anisotropy in cracked rocks is dependent on stress.

Another possibility is that the coda is composed of several reflected waves. Therefore, time delay variation could result from a velocity change in a restricted zone located between source-receiver and the reflectors.

At the end, they supposed that the velocity increase was located close to the magma chamber. The velocity variation might be due to the change in the state of the magmatic fluid.

The processing of temporal multiplets by the MWCS technique provides a means to measure temporal variations of seismic velocity inside a volcano. The results showed that S velocity had changed eight months before the eruption, so it may be used as a long term precursor to an eruption.

Based on previous studies, more analysis were performed in the last years.

Information about the stress variations in deeper parts of continental faults can be obtained by studying source properties of microearthquakes. Changes in seismic velocities measured by using

repeated natural and active seismic sources can provide information about rock damage and healing at depth after large earthquakes or stress changes in seismogenic zones.

The limitation of these measurements is the episodic nature of their seismic sources.

Clarke et al. (2011) investigate the sensitivity of the MWCS applying it to microseismic noise cross-correlations which have been perturbed by small velocity variations. They used the noise cross-correlations computed from seismic stations of the Piton de la Fournaise volcano network. They study the convergence of the cross-correlations functions and their fluctuations in the time and frequency domains; applied the MWCS to the cross-correlation functions and compare these velocity variations with known value.

In this method signal was reconstructed from cross-correlations of continuous seismic records generated by repeatable seismic source. In case of well distributed noise, the sources are close to point forces and the cross-correlations functions can be considered as Green's functions (Weaver and Lobkis, 2001; Shapiro and Campillo, 2004; Sabra et al., 2005; Shapiro et al., 2005). The idea of this method is that the noise cross correlations computed from time windows can be analysed similar to records from earthquake doublets. The preliminary step is to built one reference and several current cross-correlations. Then the continuous noise sequence was cut in short sequences and a number of single cross-correlation functions was stacked. The reference and current functions are defined by the number of cross-correlation functions; the fundamental requirement is that $N_{ref} >> N_{cur}$, because the reference is representative of a background value and the current contains information on the actual state of the crust. In long time series it is possible to compare a single reference cross-correlation with subsequent current functions. The Reference Cross-Correlation (CC^R) for a pair of stations is obtained from stacking all cross-correlations for this pair of stations. The Current Cross-Correlation (CC^C) are obtained from stacking a set of cross-correlations.

For any couple of reference and current functions the first step is the computation of the time-delay between the two signal within an overlapping window, this operation was computed in the spectral domain. In particular the first step is the calculation of the delay-time, δt, between two cross-correlation functions within a series of overlapping lag-time windows. A single cross-correlation function is divided into N_w windows. The window length, the overlap and windows depend on the frequency content and on the SNR of the cross-correlation functions considered. In Fig.5 an example of a windowed pair of cross-correlation function.

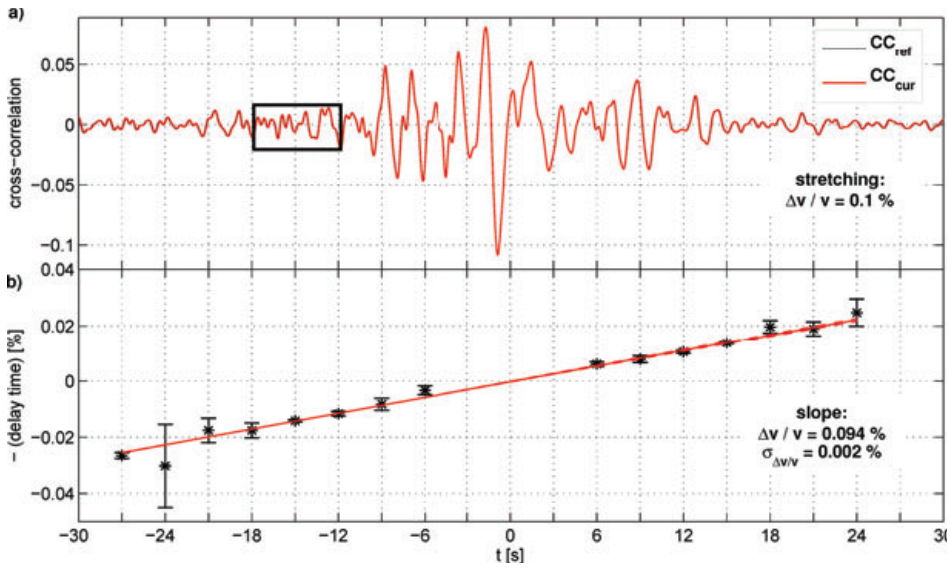

Figure 5. (a) A pair of a real reference (from Piton de la Fournaise) and a synthetic current cross-correlation, along the time interval between −30 and 30 s. The current function is generated by stretching the reference by 0.1 per cent. The black rectangle delimits one of the windows used in the analysis (6s long, sliding 3s). (b) The second step in the MWCS analysis: a linear regression through weighted least-squares over the time delays that have been computed during the first step. Each time-delay is associated with the mean time in its sliding window. The red line is the fitted slope and the dotted lines highlight the error margins (from Clarke et al., 2011).

The cross-spectrum, X(ν), between the two windowed time-series is calculated as

$$X(\nu) = F_{ref}(\nu) \cdot F^*_{cur}(\nu)$$

where $F_{ref}(\nu)$ and $F_{cur}(\nu)$ are Fourier-transformed representations of the windowed time-series, ν is the frequency in Hz and the asterisk denotes complex conjugation.

The time shift, δt_i (*i* for the *i*th window), between two signals is estimated from the slope of a linear regression of the samples within the frequency range of interest (Fig. 6).

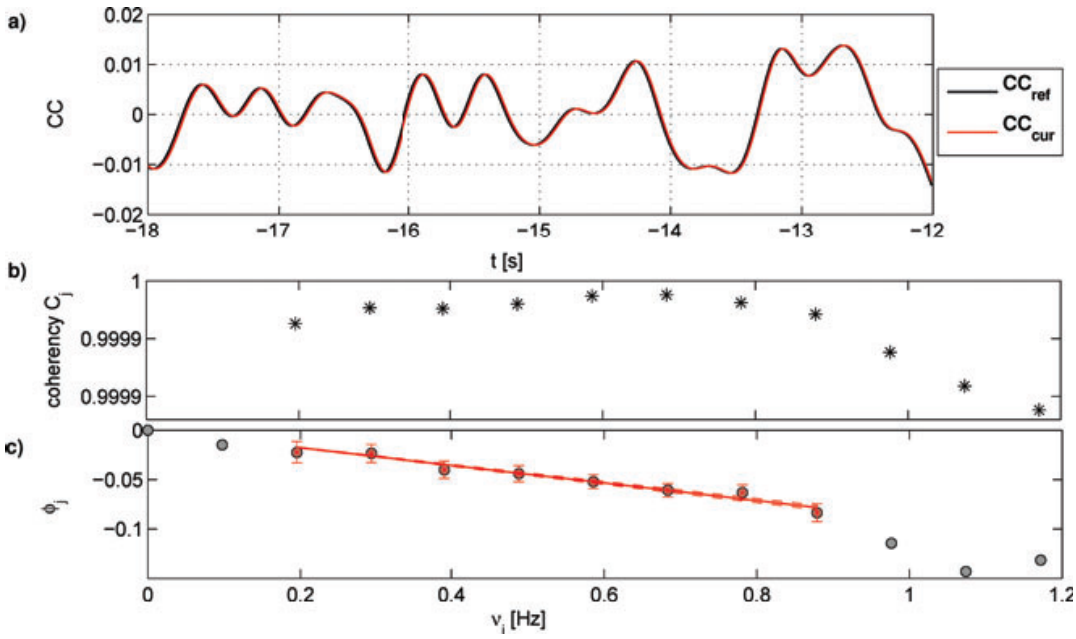

Figure 6. Example of how a delay-time is measured between two windowed cross-correlations. (a) Zoom-in of the two cross-correlations within a single lag-time window (black rectangle in Fig. 2, panel a). (b) Coherency calculated for the two windowed signals at all frequencies. (c) Linear regression for the phase displacement along the frequencies of interest (0.2 to 0.9 Hz), which have been marked with red asterisks and error bars ($1/w2j$) (from Clarke et al, 2011).

The latter is the evaluation of the relative velocity variation associated to the current function. Here the hypothesis is that the seismic wave propagation velocity is perturbed homogeneously in the studied area. With this assumption, the resulting seismic velocity perturbation δv/v in the region will be also homogeneous and be manifested as a stretching – δt /t of the current cross-correlation function relative to the reference function. This stretching is constant over t and is numerically the opposite of the velocity perturbation (Poupinet et al., 1984)

$$\frac{\delta t}{t} = -\frac{\delta v}{v}$$

To recover δv/v they apply a linear regression to the N_w delay-time measurements: $\delta t_i = a + b t_i$, where *a* coefficient represents a possible instrumental drift and *b* corresponds to the relative time variation δt /t.

This second step involves the evaluation of the trend, δt /t, of the delay-time estimates for the length of the signals. The slope of this linear regression indicates the relative homogeneous velocity perturbation of the current cross-correlation respects to the reference cross-correlation.

An example where was applied the MWCS technique was described in Zaccarelli et al. (2011). They analysed cross-correlation of more than two years of continuous seismic records and they includes the 2009 L'Aquila earthquake and used the MWCS technique based on seismic noise.

They re-sampled time series recorded at the stations in order to obtain a perfect time synchronization and filled gaps with a linear interpolation. Then, the vertical components of the seismograms was processed by whitening between 0.1-1 Hz and by normalizing their amplitude through a one-bit normalization. In this way the contributions arising from transient phenomena were reduced in time and frequencies domains. Finally they calculated the cross-correlations between stations for every hours.

The reference cross-correlation is obtain from stacking all cross-correlations for this pair of stations; the current cross-correlations are obtained from stacking a small sub-set of cross-correlations representative of the period of time. The different lengths between days was tested from 10 to 100 days to find an optimal stacking duration for the current function. For each sampled stacking length, the CC^C was computed applying moving window shifted by two days. Then, the correlation coefficient was calculated between the reference function CC^R and every CC^C. The correlation coefficient defines the similarity between the current cross correlation and the reference for a given stacking length (Fig. 7).

The degree of similarity increases rapidly for a short stacking duration and then it tends to stabilize.

It was selected a value of 50 days as stacking length for computing the current correlation functions.

To obtain a representative valuation of the interested crustal volume, the single delays measured from a single station are merged together. The median value of the delays was calculated for every window and was estimated $\frac{\Delta v}{v}$ for the entire volume of the region selected. During this analysis was removed the central part of the cross correlation containing direct waves (group velocities estimated faster than 2.5 km/s), because they may be sensitive to the changing position of the noise source (Froment et al., 2010). Velocity variations were computed by taking into account the coda of the cross-correlation up to a length of 60 seconds where the signal decreases to value close to the noise levels.

Then, they applied the MWCS technique to measure the apparent velocity variations between the perturbed cross-correlations and the original CC^R. They performed the analysis in three different frequency bands: 0.1-1; 0.1-0.6; 0.5-1 Hz. The results for the different frequency band are presented in Fig.8, where velocity decrease at the time of occurrence of the L'Aquila main shock. The velocity amplitude is largest frequencies higher than 0.5 Hz and decreases at lower ones. This indicates that a large part of their variations have their origin within the shallow crustal layers. The results presented in their study show that the L'Aquila main shock caused a detectable reduction of

seismic velocities, but this study has not the time resolution required to identify possible short-term precursory variations and to separate them from the co-seismic effect.

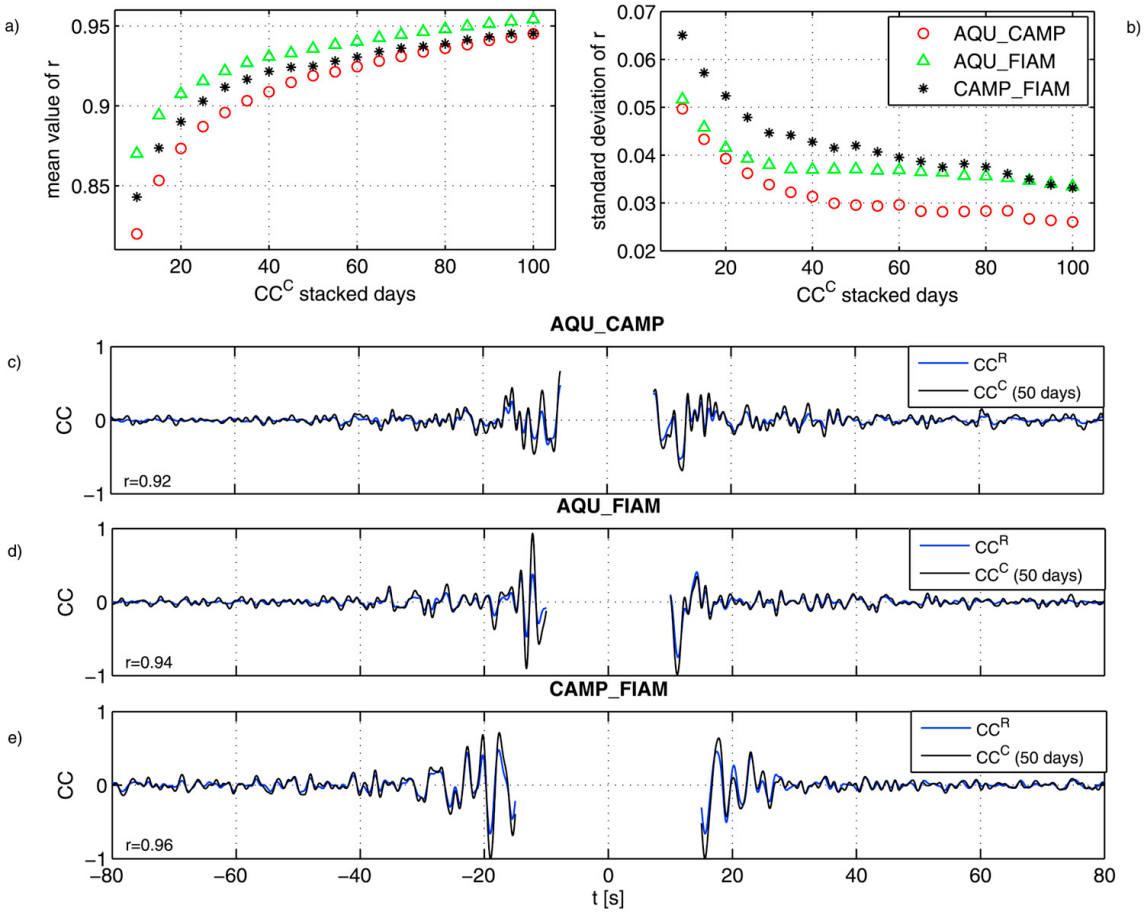

Figure 7. (a) mean and (b) standard deviation values of the correlation coefficients between CC^C and CC^R as a function of number of days used to construct the current correlation functions CC^C. (c, d, e) reference cross-correlation functions (blue) with an example of 50 days current function (black) for three couples of stations. Respective correlation coefficients *r* (from Zaccarelli et al., 2011).

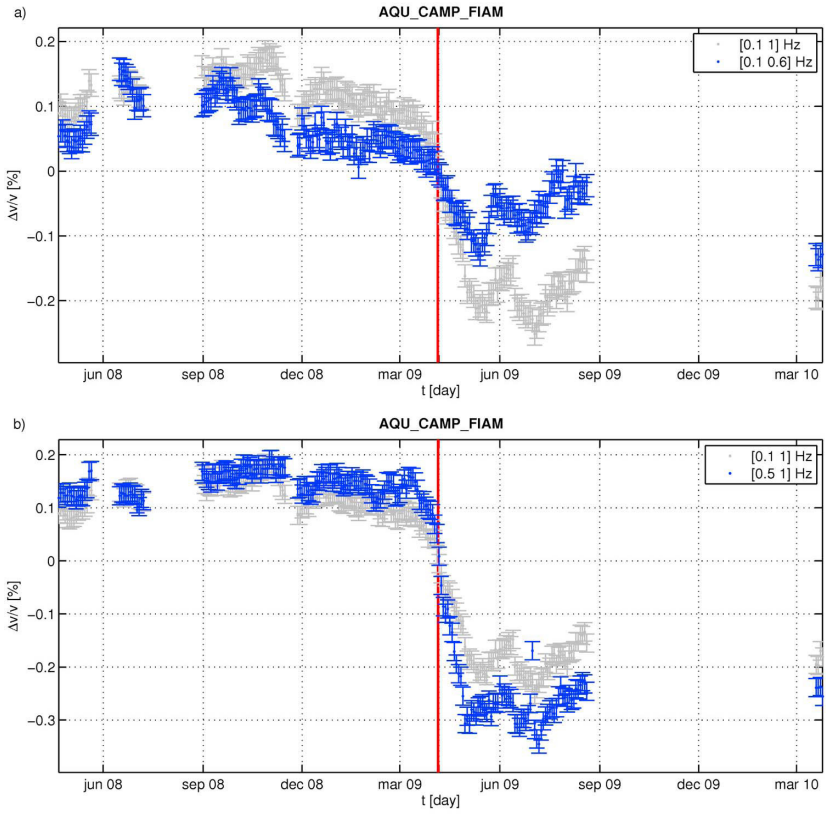

Figure 8. Velocity variations measured from cross-correlations of seismic noise recorded at three stations (gap correspond to periods when the stations were not operating simultaneously). Vertical bars indicate the uncertainties of the measurements. The vertical red line corresponds to the L'Aquila main shock (from Zaccarelli et al., 2011).

Brenguier et al. (2008a) used measurements of ambient seismic noise to recover velocities variations of the crust. They noted that seismic velocity changed and nonvolcanic tremor activity in the Parkfield area in California revealed that large earthquakes induce long term perturbations of crustal properties in the San Andrea fault zone. The 2003 San Simeon and 2004 Parkfield earthquakes reduced seismic velocity that were measured from correlations of the ambient seismic noise. They used more than 5 years of continuous seismic data, for every possible pair combination of stations, they computed the daily cross correlation seismic noise using the procedure described in Brenguier et al., (2007). A reference Green function was computed for each station pair by stacking the daily cross correlations for the entire period. The velocity changes were then determined by measuring time delays between the reference Green function and 30 day stacks of cross correlation in different frequency range. If the medium is homogeneous relative seismic velocity change, $\Delta v/v$, the relative travel time shift ($\Delta\tau/\tau$)between a perturbed and reference Green function is independent of the time lapse (τ) at which it is measured and $\Delta v/v = -\Delta\tau/\tau$ = constant. When computing a local shift, $\Delta\tau$, between the reference and a chosen cross-correlation function in a short window centered at time τ, they expected that $\Delta\tau$ should be a linear function of τ. Measuring the slope of the travel

shifts $\Delta\tau$ as a function of the time τ, it is possible estimated the relative time perturbation ($\Delta\tau/\tau$), which is the opposite value of the medium's relative velocity change ($\Delta v/v$) (Fig. 9).

The seasonal variations, seen in Figure 2, mainly affect the direct waves and there is no differential time measurements for these waves. After the San Simeon earthquake, the seismic velocity decreased by 0.04%. The velocity change may be related to co-seismic damage in the shallow layers caused by strong ground shaking; 7 months after the quake, velocities in the Parkfield area appears returned to their pre-earthquakes levels. Immediately after the Parkfield earthquake, velocities decreased by 0.08% and post seismic velocities remained low for almost 3 years (Fig.10). The hypothesis is that the evolution of the observed seismic velocity changes after the Parkfield earthquake was governed by the stress relaxation within deeper parts of the fault zone and it was supported by the observations of nonvolcanic tremors. After the Parkfield earthquake, tremor activity remained elevated and has yet to return to its pre-event level similarly to the seismic velocity changes.

Differences in the evolution of seismic velocities after two earthquakes indicate that two different mechanisms may be responsible of the changes in crustal properties: damage of shallow layers and fault zone caused by strong ground shaking and co-seismic stress change followed by the post-seismic relaxation. These results demonstrate that measuring small velocities perturbations from correlation from seismic noise can be a useful tool for studying time evolution of the stress regime near seismogenic faults.

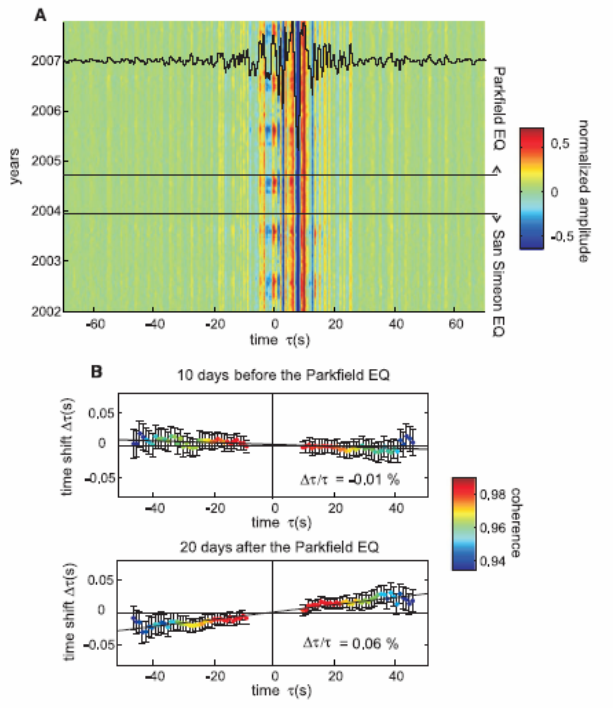

Figure 9. (A) thirty day stacked cross correlation functions. Back curve represents the reference stacked cross correlation function. (B) time shifts averaged over 91 receiver pairs and coherence measured between the reference stacked and 30-day stacked cross-correlation functions (frequency 0.1-0.9 Hz) (from Brenguier et al., 2008a).

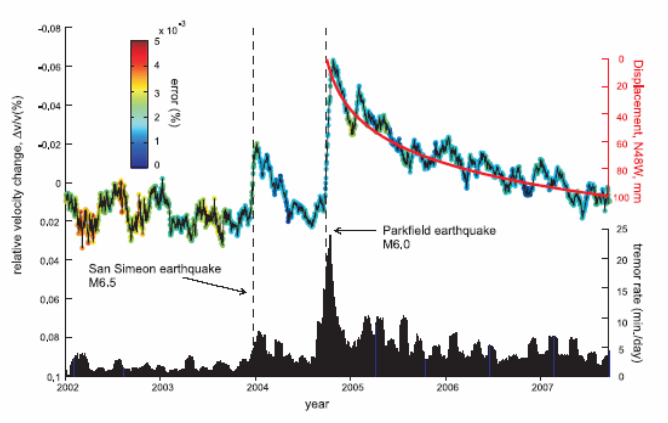

Figure 10. seismic velocity changes, surface displacements from GPS and tremor activity near Parkfield. Red curve represents the post-seismic fault-parallel displacements along the San Andreas fault (from Brenguier et al., 2008a).

The seismic ambient noise data processing procedure for estimate Rayleigh wave Green functions from ambient seismic noise has largely used and stabilized. The procedure that Bensen et al (2007) proposed is flexible and applicable to a variety of settings and it was divided into four phases: single station data preparation; cross-correlation and temporal stacking; measurement of dispersion curves and quality control. Here were described the first two phases (Fig.11).

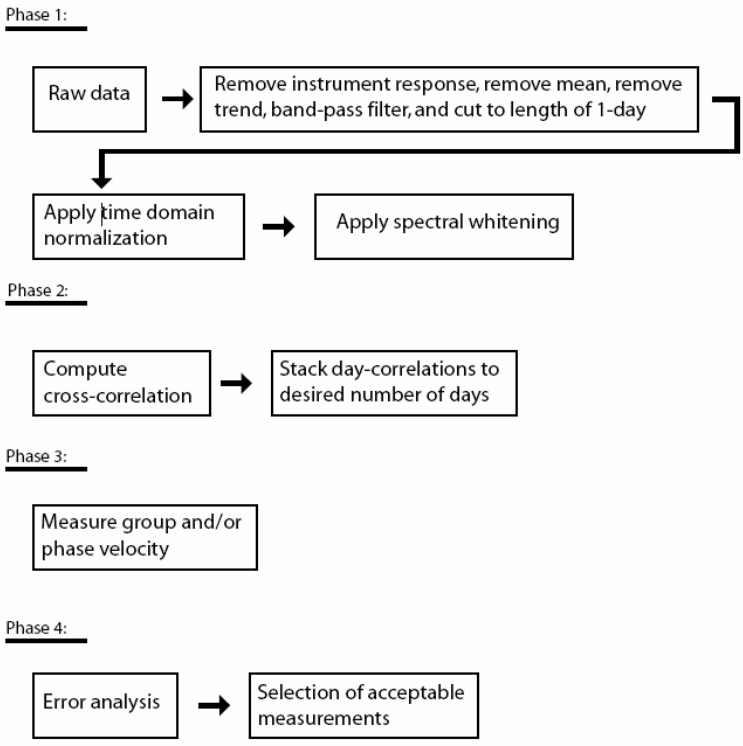

Figure 11. Representation of the data processing scheme. (from Bensen et al., 2007)

The first phase of data processing is to accentuate broad-band ambient noise to remove earthquake signals and instruments irregularities that tend to cover the ambient seismic noise. This first phase consists of these steps: removal of instrument response, de-meaning, de-trending and bandpass

filtering the seismogram, time domain normalization and spectral whitening. This procedure was applied to a single day of data.

Temporal normalization is the first most important step in data preparation. This procedure is applied to reduce the effects on the cross correlation of earthquakes, instrumental irregularities and non-stationary noise source near the stations. Earthquakes are the most significant impediments to automated the noise data processing. For this reason Bensen et al.(2007) have considered different methods to identify and remove the earthquakes and other contaminants from seismic data. The first and most aggressive method is called 'one-bit normalization'; which retains only the sign of the raw signal by replacing positive amplitudes with 1 and negative amplitude with -1. This method has been used in a number of early seismic studies of coda waves and ambient noise (Campillo and Paul 2003; Shapiro and Campillo 2004; Shapiro et al. 2005). The second method (employed for example by Sabra et al. 2005a) involves the application of a clipping threshold equal to the rms amplitude of the signal. The third method involves automated event detection and removal in which 30 minutes of the waveform are set to zero if the amplitude of the waveform is above a critical threshold. The fourth method is the running absolute mean normalization. This method computes the running average of the absolute value of the waveform in a normalization time window of fixed length and weights the waveform at the centre of the window by the inverse of this average. It is possible to compute the normalization weight for the time point *n* as:

$$\omega_n = \frac{1}{2N+1} \sum_{j=n-N}^{n+N} |d_j| \qquad (1)$$

d_j discrete time series and the normalized datum (d_n) becomes $\tilde{d}_n = d_n / \omega_n$.

The width of the window is (2N+1) and determines how much amplitude information is retained. A one sample window (N=0) is equivalent to one bit normalization. Bensen at al. tested various time window widths and find that about half the maximum period of the bandpass filter works well and this length can be varied and produce similar results (Fig. 12 panel (e)).

Finally, the water level normalization in which any amplitude above a specified multiple of the daily rms amplitude is down-weighted (Fig. 12 panel (f)).

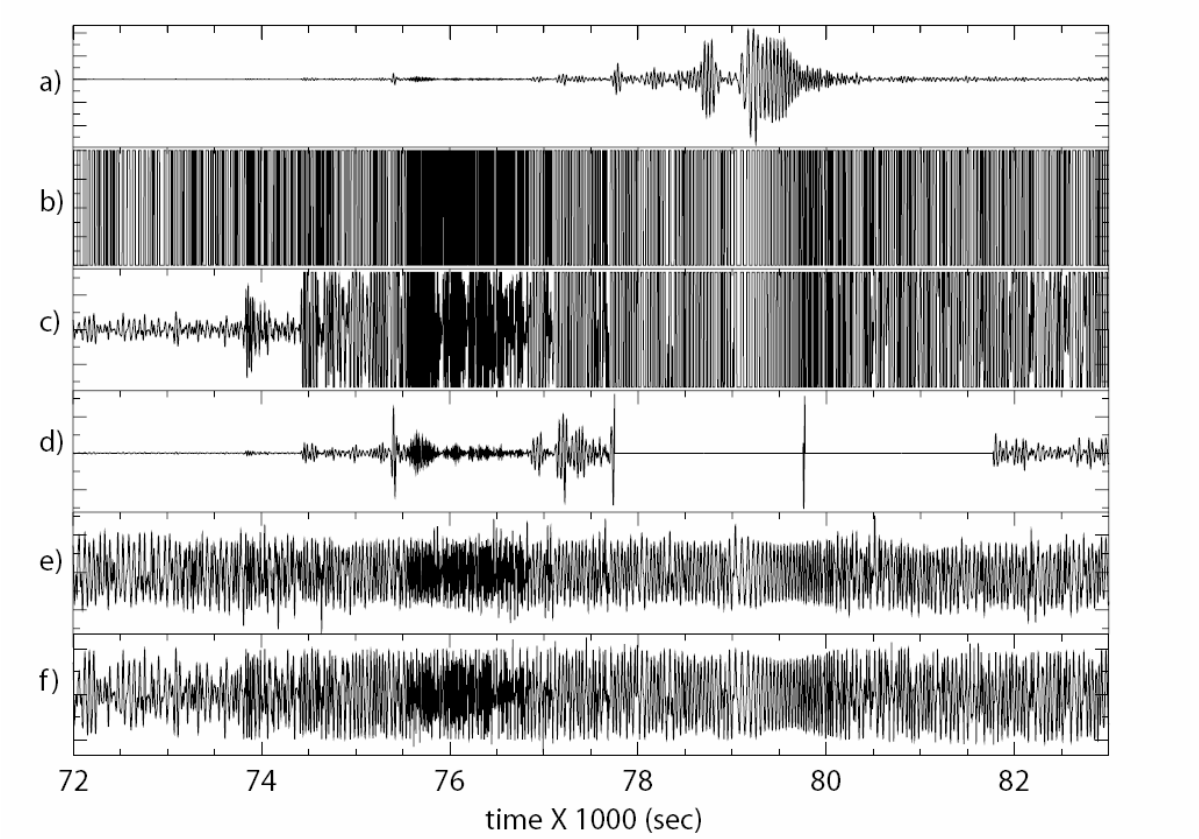

Figure 12. Waveforms displaying examples of the five types of time-domain normalization tested. (from Bensen et al. 2007)

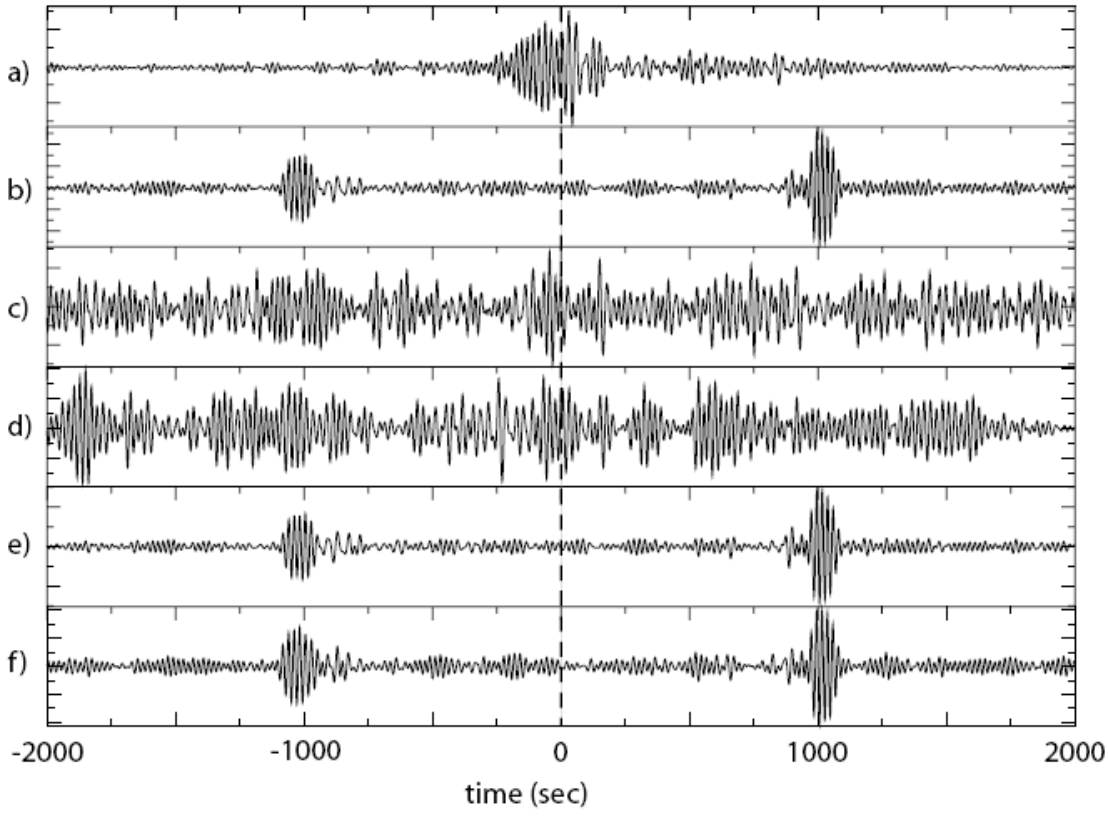

Figure 3. Example of twelve month cross correlations between two stations (ANMO-HRV) for the time domain normalization method. (from Bensen et al. 2007)

Fig. 13 shows one year long cross correlations, band-pass filtered between 20 s and 100 s period, using each of these methods of time-domain normalization. The raw data (Fig. 13 panel a), the clipped waveform method (Fig. 13 panel c) and the automated event detection method (Fig. 13 panel d) produce noisy cross correlations. While, the one bit normalization (Fig. 13 panel b), the running mean normalization (Fig. 13 panel e) and the water level normalization method (Fig. 13 panel f) produce relatively high SNR waveforms that show arrival time at nearly the same time. The one-bit and the running-mean normalizations are nearly identical. Also the water level method allows to recover the meaningful results and the running absolute mean method provides a small enhancement to SNR values above one-bit normalization at all periods and a more significant improvement over the water-level normalization. Bensen et al.(2007) preferred running absolute-mean normalization because this method is flexible and adaptable to the data.

Ambient noise is not flat in the frequency domain, but is peaked near the primary and secondary microseisms.

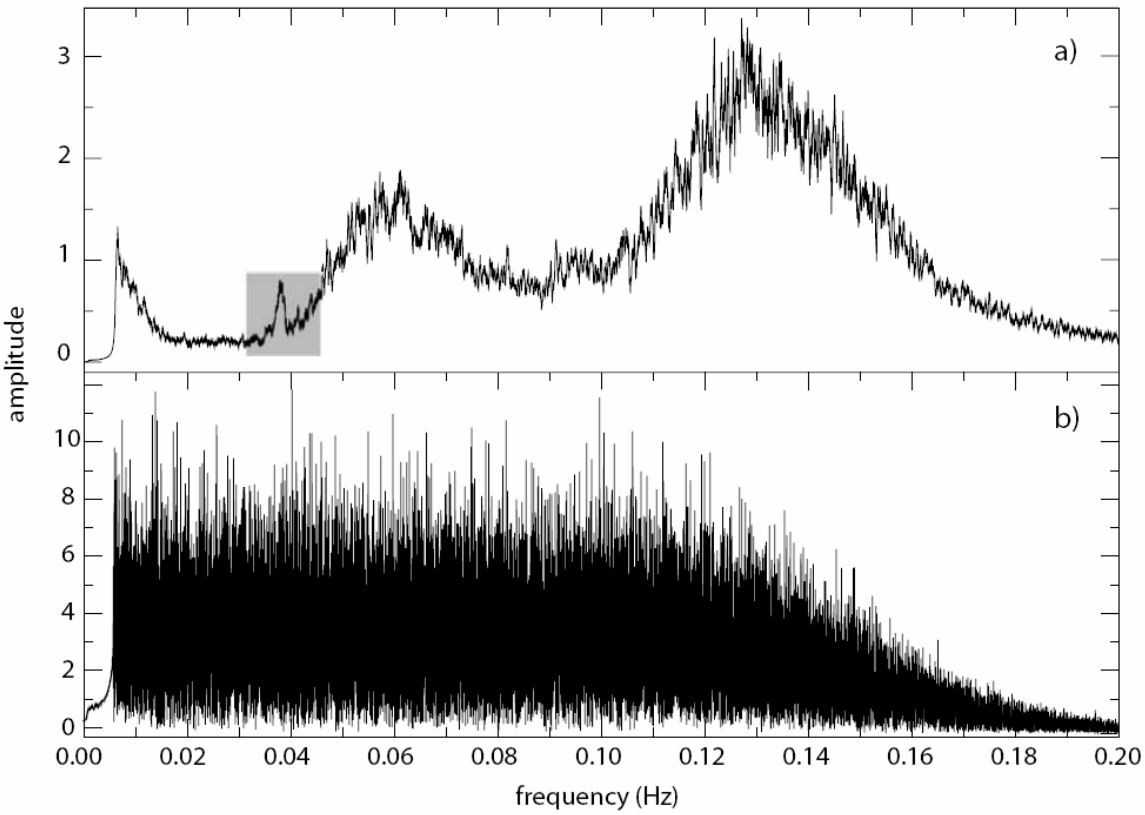

Figure 14. Raw (a) and spectrally whitened (b) amplitude spectra for 1 sample per second vertical component data at station HRV. The shaded box indicates the location of the 26 s period signal originating from the Gulf of Guinea. (from Bensen et al., 2007)

Primary and secondary microseisms as well as Earth hum signatures can be seen in Fig. 14, where the record was bandpass filtered between 7 and 150 s period. There is also a smaller peak near 26 s that is caused by a persistent narrow band noise source in the Gulf of Guinea (Shapiro et al., 2006). Without the temporal normalization the 26 s resonance typically is not seen. Inversely weighting the complex spectrum by a smoothed version of the amplitude spectrum produces the normalized or whitened spectrum (Fig. 14 panel b).

The signal at 26 s is seasonal, as documented by Holcomb (1998), and it is much stronger in the northern summer than in the winter. The effects of the 26 s resonance is reduced if the spectral normalization has been applied. In many cases the spectral whitening is sufficient to eliminate the 26 s peak from the cross-correlations. Then, spectral normalization seems to reduce to reduce broad imbalances in single station spectra to aid in the production of a broad-band dispersion measurement.

Fig. 15 (a) and (b) show the cross correlation between stations CCM and SSPA for spectrally unwhitened and whitened data taken during the northen spring. Fig. 15 (c) and (d) display the amplitude spectra of the unwhitened and whitened cross correlations. Without the whitening, Fig.

15 (c) shows that the resulting cross-correlations is dominated by signals in the microseism band, from 15 to 17 s. In Fig. 15 (d), the cross correlation amplitude spectrum is shaped with the longer periods having higher amplitudes than the shorter periods. Additional whitening of the cross-correlation prior to dispersion measurement is an added option.

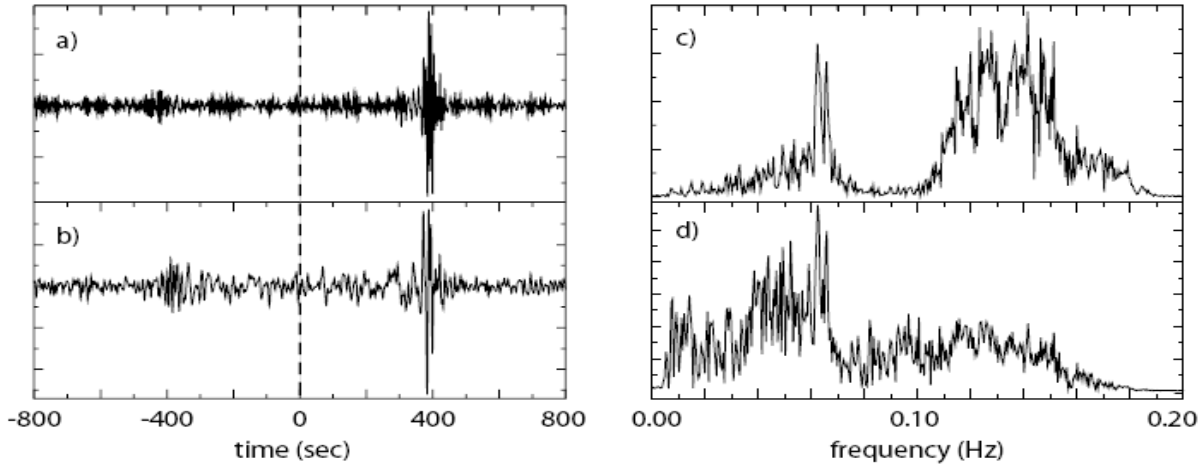

Figure 15. Comparison of cross correlation with and without spectral whitening from the stations CCM and SSPA. (a) Cross-correlation without spectral whitening. (b) Cross-correlation with spectral whitening. (c) and (d) amplitude spectrum of the waveform respectively (a) and (b) (from Bensen et al., 2007).

The second step in the data processing is cross-correlation and stacking.

Cross correlation is performed daily in the frequency domain. The cross correlation, in time domain, are stacked. So the stack corresponds to longer time series.

The stacking can be done in the frequency domain which would save the inverse transform. The length of the cross-correlations depend on the group speeds of the waves and the longer interstation distance. The positive lag part is called the 'causal' signal and the negative lag part the 'acausal' signal. If source of ambient noise are distributed homogeneously in azimuth, the causal and acausal signal would be identical. Asymmetry in amplitude and spectral content is typically observed, which indicates differences in the source process and distance to the source. It is possible to compress the two-sided signal into a one-sided signal by averaging the casual and acasual part; this is the 'symmetric' signal or component.

Stacking over long time series improves Signal to Noise Ratio (SNR).

Fig. 16 displays cross correlation of different time-series. The casual and acasual part signals are seen to emerge as the time series length increases in both of the period bands that are displayed in Fig. 16 (a) and (b).

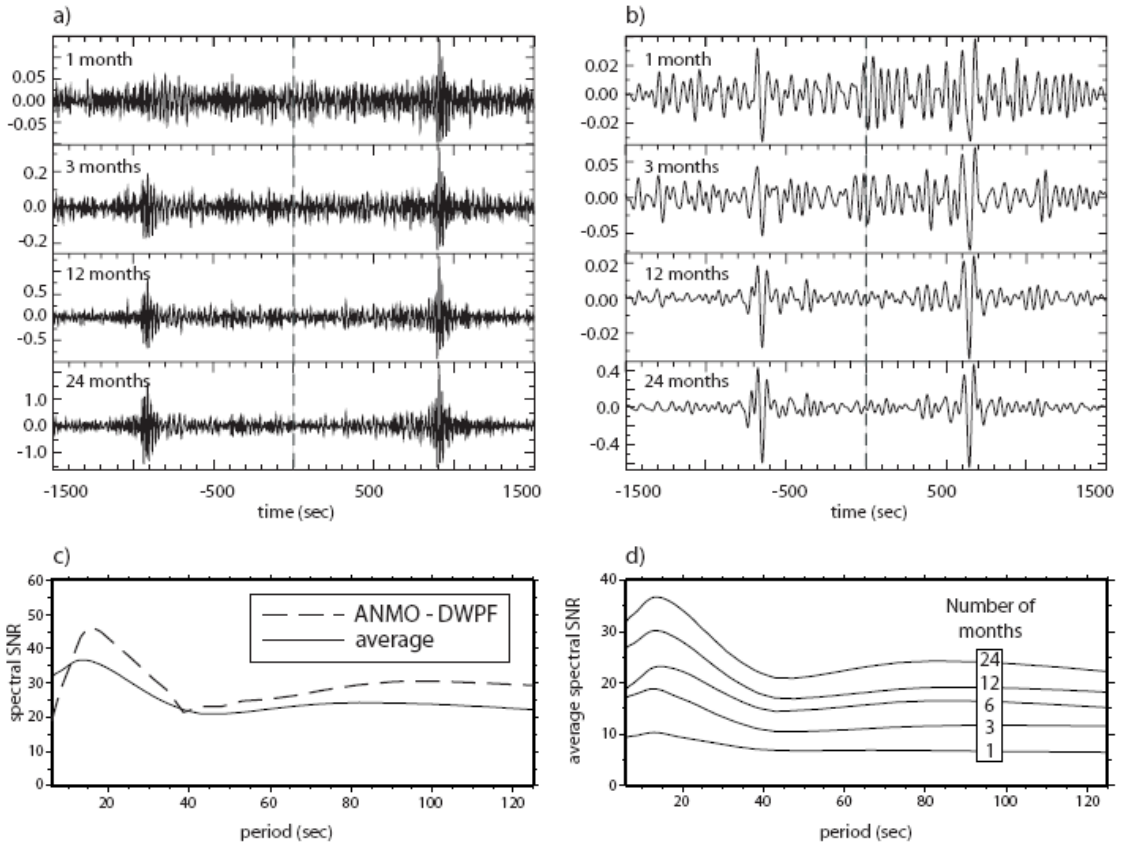

Figure 16. Cross correlation between stations ANMO-DWPF is presented in a and b, and it is also presented with a dashed line in c. In d how the spectral SNR increases with time series length (from Bensen et al., 2007).

Measurements of the frequency dependence of the SNR are useful to quantify observations of the emergence of the signals with increasing time-series length. Fig 17 shows the way of which the frequency dependence can be measured. In this case it is performed a series of bandpass filters centred on a discrete grid of frequencies and it is measured the peak in the time domain. This is a spectral SNR measurement; in fact it is a measurements of SNR in the time domain. It is spectral only in the sense that the measurements are a function of frequency. This spectral SNR, which takes the ratio of signal to trailing noise, is a measure of the signal levels, as the trailing noise is not dependent on signal generated noise. Also, it is possible define the ratio of signal to leading noise, which is dependent on signal-generated noise (Fig 16).

Fig 18 is an example of how the SNR depends on time series length computed.

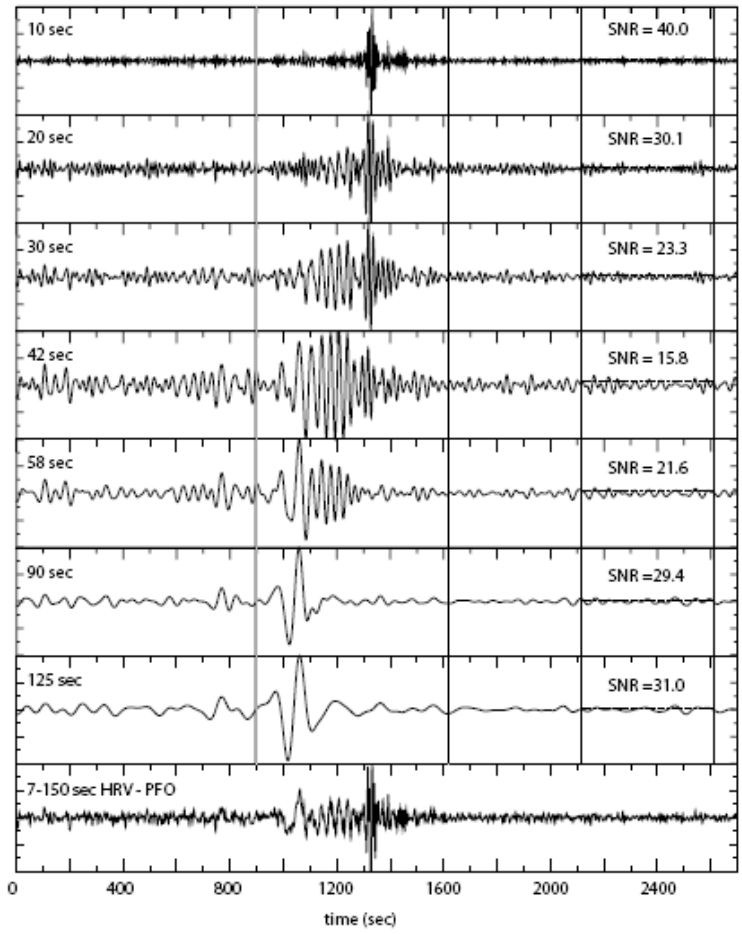

Figure 17. Waveforms are centred on the period indicated at the left hand side in each panel. The SNR is defined as the ratio of the peak within the signal window and rms noise in the noise window (from Bensen et al., 2007)

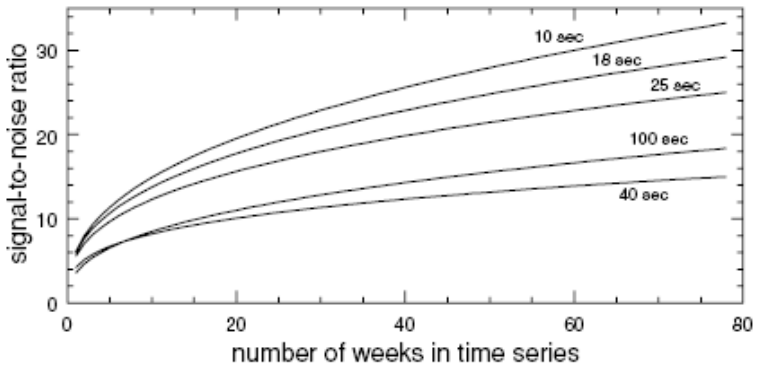

Figure 18. Emergence of the time signal with time series length. It is showed the fit power law rather than the raw data, SNR = $At^{1/n}$, where A and n are period dependent (from Bensen et al., 2007).

3.3 Applications of the MWCS technique in the Alto Tiberina Valley

In this study was used the recently proposed Multi Window Cross-Spectrum technique based on ambient seismic noise processing. The idea of this method is to use signals reconstructed from repeated cross-correlations of continuous seismic records as a virtual seismograms generated by repeatable sources.

In particular case of well distributed noise, the reconstructed virtual sources are close to point forces and the cross-correlations functions can be considered as Green function (Weaver and Lobkis, 2001; Shapiro and Campillo, 2004; Sabra et al., 2005; Shapiro et al., 2005).

The change of the travel times measured from the noise cross-correlations reflect variations of the elastic properties in the propagating media (Clarke et al., 2011). The delay accumulates linearly with the delay time when the wave speed changes homogeneously within the medium.

The MWCS was performed in the region of the Alto Tiberina Valley (ATV) (central Italy) and is evaluated considering cross-correlations of more than one years of continuous ambient seismic noise records. During the study period, seismic stations operated in continuous mode and they recorded an earthquake on April 15, 2010 01:45:36 UTC (Ml 3.8) (url: http://iside.rm.ingv.it/). The event was followed by a seismic sequence characterized by a migration of seismicity forward North-West (Fig. 19, red circles) (Amato et al., 2010).

Considering the whole period of the analysis (November 2009 – December 2010) the seismic network collected a data set with Ml ranging from 0 to 3.8.

The MWCS technique was applied in this region to evaluate the possibility to find velocity variations during a seismic sequence with little seismic events. On the contrary, in literature, this technique was applied in the cases of strong earthquakes.

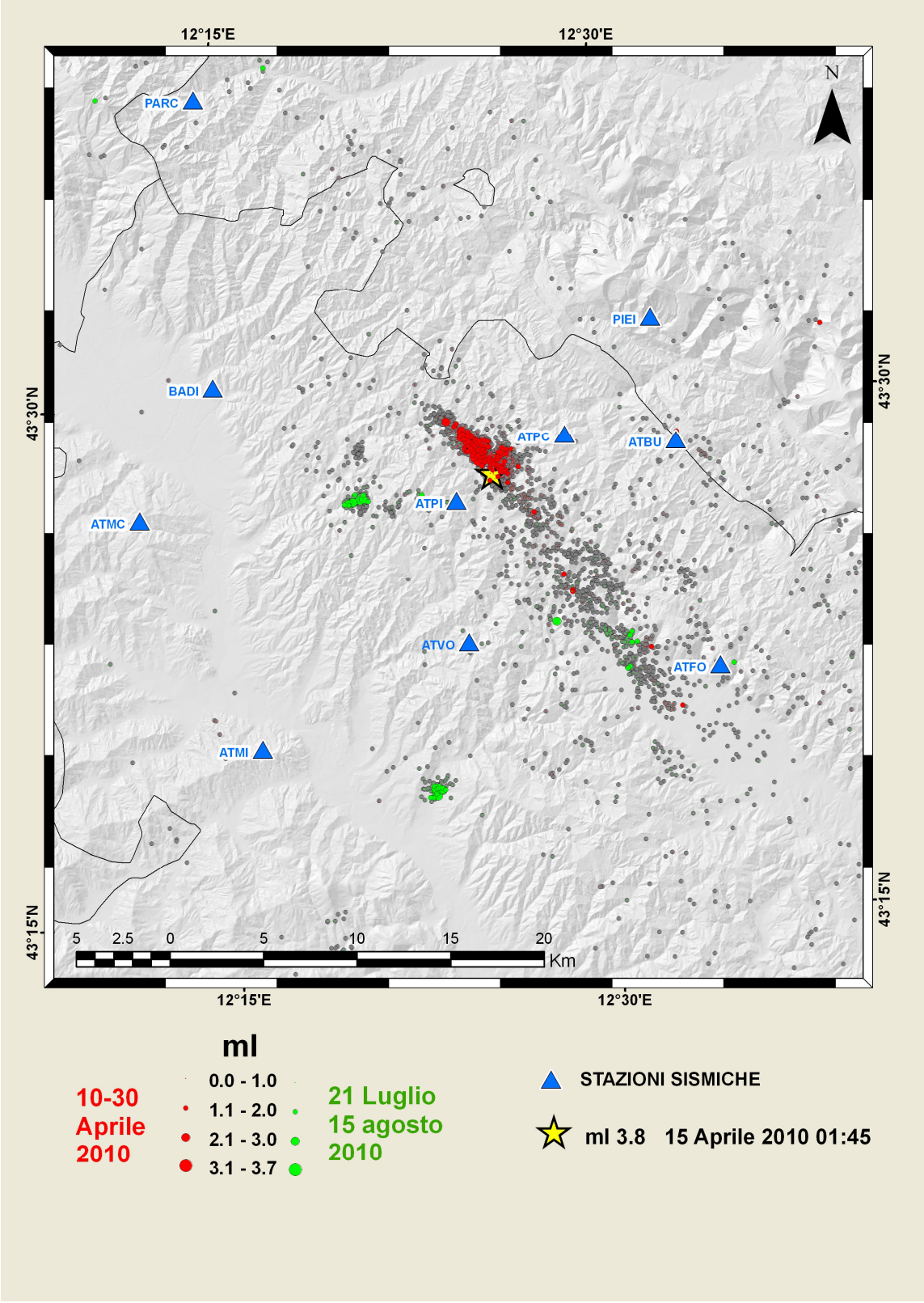

Figure19 . Seismicity of the Alto Tiberina Valley. Grey circles: seismicity from November 2009 to December 2010. Red circles: seismicity from 10 to 30 April 2010. Green circles: seismicity from 21 July to 15 August 2010. Blue triangles: seismic stations. Yellow star: mainshock of seismic sequence on April 2010.

3.3.1.Seismic monitoring of the central eastern Italy

The seismic monitoring of the entire Italian territory was one of the most important work of the Istituto Nazionale di Geofisica e Vulcanologia (INGV). The constant developments technology implemented in recent years have made a significant improvement in both quality and quantity monitoring.

INGV operates two large seismological networks: the Italian National Seismic Network (INSN) and the Mediterranean Very Broadband Seismographic Network MedNet (url: http://mednet.rm.ingv.it/). The INSN consists of more than 250 stations with various characteristics (Delladio, 2011). MedNet consists of 22 very broadband stations distributed over the Euro-Mediterranean area with 13 of them located in Italy (Mazza et al., 2008).

In addition there are many other regional local networks. For example, there are the network of INGV Osservatorio Vesuviano, network of Western Sicily and Eolie Islands of INGV-Catania department, network of North-West Italy of the University of Genova (Pasta et al., 2011), broadband network of North-East Italy (Pesaresi et al., 2011), network of Mugello, network of Marche Region, network of Alta Val Tiberina (Cattaneo et al., 2011) and many others.

In case of seismic emergency, the data of permanent network are integrated with data of temporally network. Standard reference for a seismic stations, independently of instrument type, is actually constituted of a digital acquisition at 24 bit, a velocimetric sensor at three components, Broad Band (BB) or Very Broad Band (VBB), an accelerometric sensor (Strong Motion) at three components, acquisition system GPS and data transmission system. There is not a standard mode for national network.

The temporally network of CNT is divided in emergency and experiments network.

The emergency network are of two type, the first is a seismic network of stand-alone stations. It is composed by 8 stations of rapidly installation with a velocimetric and accelerometric sensors. This temporally network is an integration at RSN stations to study the seismicity of an area struck by an earthquake.

The second network is computed by three complete stations (sensor and digital acquisition, GPS system and battery). Finally there are also 44 stations stand-alone used usually for scientific experiments or in case of emergency (Delladio, 2011).

INGV operates in the ATV area with a two principal seismological networks. Besides INSN stations, other seismic stations were installed in the framework of the project FIRB-Airplane (‘Piattaforma di ricerca multidisciplinare su terremoti e vulcani’). From the second half of the year

2009 about 20 seismic stations were installed in the study area and surrounding and their continuous seismic data were transmitted to the acquisition centre of Ancona with network Wi-Fi Hyperlan (Monachesi et al., 2010).

The stations were equipped with velocimetric seismic sensors Trillium 40s (url: (http://www.nanometrics.ca/) or Lennartz LE-3D 5s (url: www.lennartz-electronic.de) coupled with Gaia 2 (Rao et al., 2010). In Table 1 are described the seismic stations in the ATV area used in this study.

STATION	LAT	LONG	ALTITUDE (m a.s.l.)	SENSOR	DATA LOGGER	START TIME
ATBU	43.4757	12.5482	1000	LE3D-5S-VEL	GAIA2-FS-10-VP	01/11/2009
ATMI	43.3341	12.2680	581	TRILLIUM-40S VEL	GAIA2-FS-16-VPP	24/11/2009
ATVO	43.3821	12.4066	630	TRILLIUM-40S VEL	GAIA2-FS-16-VPP	20/11/2009
ATPC	43.4807	12.4570	810	TRILLIUM-40S VEL	GAIA2-FS-16-VPP	22/04/2009
ATPI	43.4506	12.4022	649	LE3D-5S-VEL	GAIA2-FS-10-VP	22/04/2009
ATFO	43.3666	12.5715	960	TRILLIUM-40S VEL	GAIA2-FS-16-VPP	01/09/2009
ATMC	43.4468	12.1928	740	LE3D-5S-VEL	GAIA2-FS-10-VP	01/11/2009
BADI	43.5096	12.2443	430	LE3D-5S-VEL	GAIA2-FS-16-VPP	01/01/2010
PARC	43.6486	12.2386	580	TRILLIUM-40S VEL	GAIA2-FS-16-VPP	01/09/2009
PIEI	43.5356	12.5350	665	TRILLIUM-40S VEL	GAIA2-FS-16-VPP	01/10/2009

Table 1. Seismic stations used in this study with their technical characteristics (from http://iside.rm.ingv.it)

The INGV- Ancona team manage the seismic data acquisition from some seismic stations of national seismic network of CNT, Rete Sismometrica Marchigiana (RSM), AVT network and seismic network of Umbria region. Seismic data are acquired by 58 stations real-time (for the year 2010) and 13 dial-up stations.

In particular, Ancona acquisition centre acquired directly seismic data for 28 seismic stations and seismic signal is send to CNT-Rome with dedicated ITC/IP line, also with the same dedicated ITC/IP line, the signal of INSN stations is received directly from central acquisition center of Rome.

The stations are equipped with various instruments. The digital recorders are GAIA1 and GAIA2, Trident / Cygnus, HDR24 and Lennartz Mars88/MC/RC. Sensors are: Trillium 40-120-240s; Lennartz LE3D- 5s/1s lite/BH, Mark L4-3D, Episensor ES-T. The data acquisition system is based on Seiscomp3 (www.seiscomp3.org), while for the detection of events Earthworm system is used.

In Fig. 2 is represented the complex communication system among stations and the INGV-Ancona centre acquisition. In the Marche region is operative a telecommunication service Marche-Way (yellow line in Fig. 20) managed by Department of Civil Protection of Marche region (DPCM) and Arscomm group (url: www.arscomm.it) for the transmission of continuous seismic data (Monachesi et al., 2010).

The HIPERLAN Wi-Fi network (red line in Fig.20) is connected with Marche-Way; this infrastructure allows to receive the seismic signal of the ATV local network in real time at Ancona center.

INGV-Ancona and the DPCM collaborate for monitoring the seismicity of central-eastern Italy. Using a specific software called Netscout (url: www.arscomm.com) it is possible to control the functioning of seismic stations. Also, it is possible to control if the seismic stations are active. Sometimes it happens that stations and connections are active, but the signal is not integer or continuous. For this reason the INGV Ancona team controls the presence of gaps in continuous seismic signals with software Pascall and with procedures developed in programming language Matlab® (Monachesi et al., 2011).

In Ancona centre of the CNT same applications control the performance of the system monitoring. In particular, are checked: 1) the functioning of radio and ethernet system; 2) the status of stations and number of satellites received by the GPS equipment, 3) the seismic signal and the gaps of continuous signal, and 4) the levels of background noise and quality of the seismic signal.

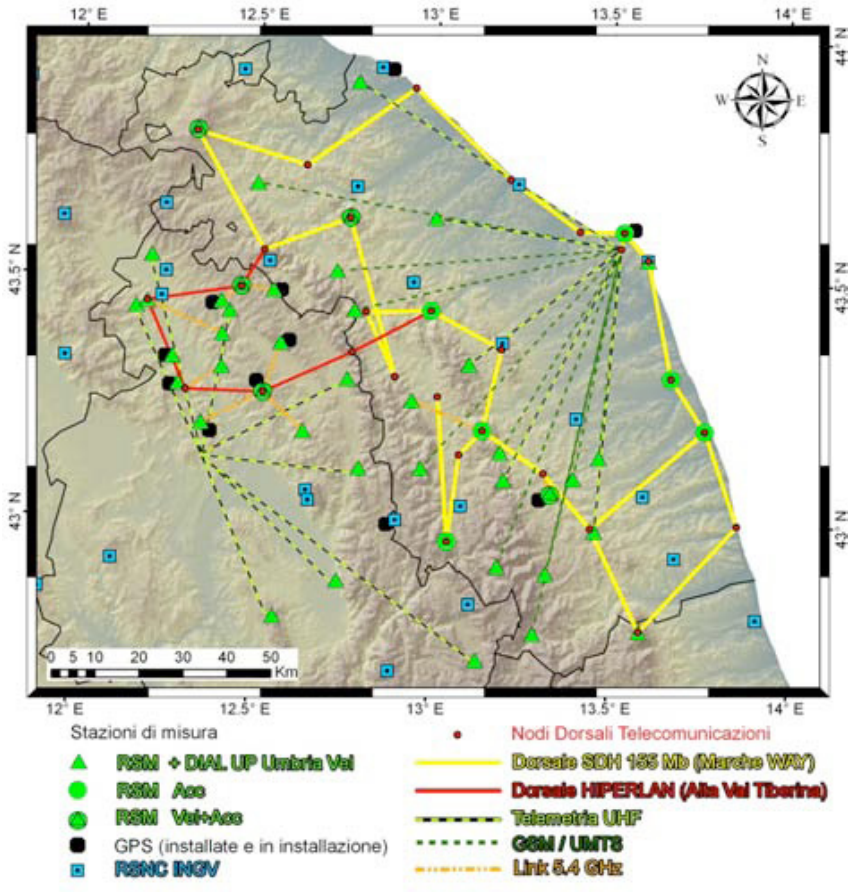

Figure 20. Acquisition of seismic data at INGV-Ancona data acquisition centre (from D'Alema et al., 2011)

3.3.2 Dataset and processing of the seismic noise signal

A fundamental step for seismological analysis consists of data processing.

In particular, this part describes in detail data processing procedures applied to seismic data recorded by digital instruments of seismic networks in ATV area.

The seismic data recorded by digital instruments were processing to obtain a data set of seismic noise data continuous, without gaps. The absence of gaps, in particular, is important for the calculations of cross-correlation functions. This operation is possible only with continuous seismic data.

The seismic data were available through the European Integrated Data Archive (EIDA). EIDA is an archive of waveform broad band data from european broad band seismic stations available from INGV and many others European Institutions.

In this work the seismic data were directly organized at Ancona acquisition centre with Seed-link protocol in Only SEED Volumes (Mini-SEED) format. MSEED format is defined at http://www.iris.edu/manuals/SEEDManual_V2.4.pdf.

The data were automatically archived in a server. The system allows to organize the file in an archive, structured in the followed way:

seiscomp/acquisition/archive/YYYY/NET/STATION/CHN.D/mseed file

where 'seiscomp' is the software to manage the seismic data, 'acquisition' and archive are subfolders, YYYY is the year of acquisition, NET is the seismic network code, STATION is the name of station, CHN is the type of station and D code indicates the length of the file (D: daily file) and then the file in mseed format.
The term MSEED has come to be used to identify SEED data records with some of the associated control header information.
The MSEED format contains digital seismic data organized in little packets; some packets can be lost. Seismic stations transmit at server centre seismic data in different ways: WiFi, satellite, radio modem or umts router. In this way the seismic data arrived at server centre but some packets are loose during the transmission. In this study was used particular softwares that allow to reconstruct continuous time series from the series which containing gaps.
The evaluation of this particular aspect was realized with Passcal (url: http://www.passcal.nmt.edu) applications that allows the change from the MSEED format to the SAC format. SAC is a general purpose interactive program designed for the study of sequential signals, especially time series data (url: http://www.iris.edu/manuals/sac/SAC_Home_Main.html).
The MSEED file is daily and continuous and it is transformed in SAC file divided in many files without gaps.
The used Passcal applications are:

- SDRSPLIT, this script allows to divide a single daily file MSEED in many files in case of the presence of temporal gaps. It allows to obtain many files without gaps.
- MS2SAC, this second step allows to convert every single MSEED file to the correspondent Seismic Analysis Code (SAC) file.

Hereafter an example of the Passcal software. IV.INTR..HHZ.D.2009.090 is the name of the MSEED file archived in the data server, where IV is the acronym of seismic network (in this case IV represents INGV), INTR is the station name, HHZ the sensor type and the component (HH for broad-band sensor and sampling >80 Hz, Z for up (http://colossus.iris.washington.edu), D code indicates the length of the file (D: daily file), 2009 is the year and 090 is the number of julian day.
In Fig. 21 are described all the steps from MSEED format to SAC format.

SDRSPLIT software divides MSEED file if is present a temporal gap; in this example the first created file is INTR.IV.HHZ..D.2009.090.000003. The second created file is INTR.IV.HHZ..D.2009.090.133225. The first file starts at about 00:00:03 UTC, the second file starts at about 13:32:25 UTC. After the end of the first file there is a temporal gap in the seismic data and the original MSEED file is so separated in two MSEED files.
The MS2SAC script convert the MSEED files in SAC file. INTR.IV.HHZ.D.2009.090.000003.sac is the name of the file that contains the same characteristics of MSEED file but in SAC format.

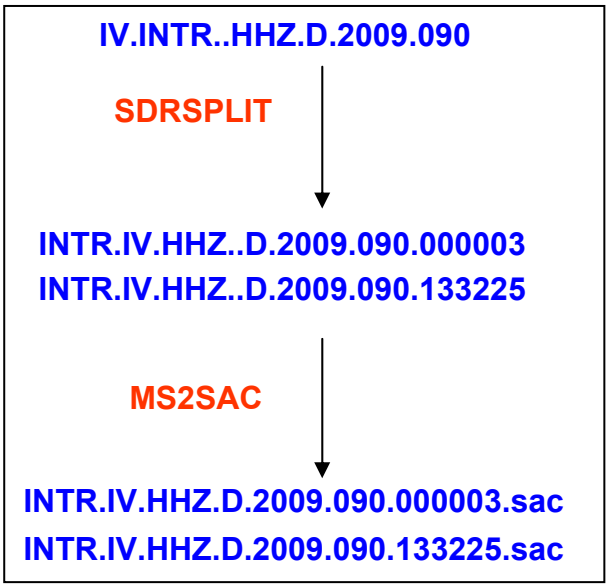

Figure 21. Steps from MSEED format to SAC format .

The next step is to convert the seismic data in a Matlab® format, because all the analysis were performed using the programming language Matlab® (url: www.mathworks.com)
Before to convert SAC file in Matlab format, the name of seismic data were organized in a format required in input by the MWCS scripts. These scripts were provided and developed by Dott. Zaccarelli Lucia at Institute du Physique du Globe de Paris (IPGP).
The name of a single SAC file was transformed in a new format.
Original format name is:
STAZ.IV.CHN..D.YYYY.JJJ.HHMMSS.sac

and it is transformed in:
YYYYMMDDHHMMSS.STAZ.CHN.sac

where YYYY is the numerical value for the year, MM is the month, DD is the day, HHMMSS is the expression for the hour, minutes and seconds, STAZ is the abbreviation for the station name, CHN is the abbreviation that indicates the type of sensor (http://colossus.iris.washington.edu).
The new name of the file is obtained inserting the 'julian2greg' function (http://www.mathworks.com/matlabcentral/fileexchange/11410-julian2greg).
In this function it is possible to convert the date from 'Julian' format to 'Gregorian' format, the statement of the format is:

[a,b,c]=julian2greg(jday)

where *a, b* and *c* correspond in Gregorian date to year, month and day, *jday* is the Julian day.
Julian date corresponds to a number of days from the first day of the year, while Gregorian date is the date in an ordinary format (for example 1 January).
When the names of the SAC file are transformed, the name was assembled and were regrouped in a fold with the same station name.
Each SAC file was transformed in MAT file for each days. Using the programme language Matlab® the file SAC was read with the 'leggibinarysac.m' function (see the function code in Appendix B). The header SAC information and values of waveform (see the Appendix C for SAC format) are associated to Matlab file format.

One of the most important step in the seismic data analysis is the preprocessing of seismic records. Raw data are generally elaborated through the following steps:

- 1. mean removal;
- 2. filtering;
- 3. instrument correction.

1. The mean of the whole record is removed from the trace in order to discard an offset that represents a shifting from zero-line and to obtain a zero-mean value of the signal (Fig. 22).

Trace= trace-mean(trace)

trace indicates the vector of the values of the raw data and 'mean' is the Matlab® function that calculates the arithmetic mean of a set of values.

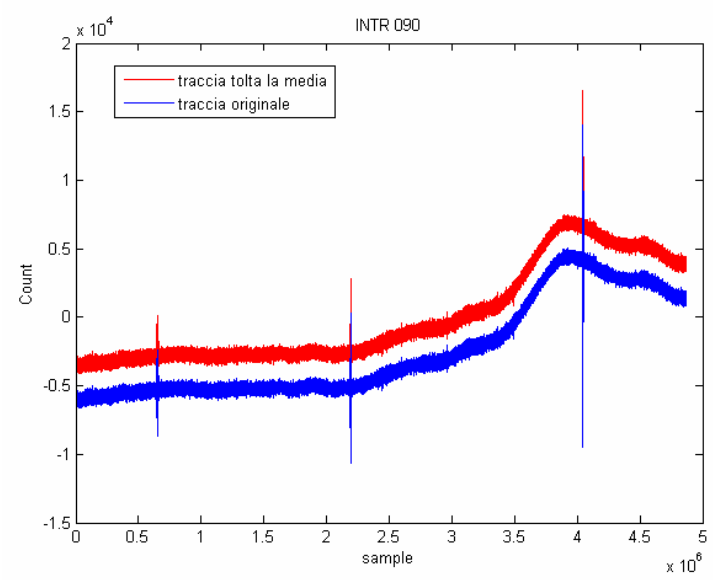

Figure 22. Blue line: original waveform. Red line: waveform after the removal of the mean.

2. A filter is a function indifferently applied both in time domain and in frequency domain by multiplying the filter function with the Fourier amplitude spectrum of the time history. There are many filter types such as Ormsby, elliptical, Butterworth (Converse and Brady, 1992).

In this study was used a band-bass filter of type butterworth and the frequency range was 0.025-25 Hz, in order to eliminate the low frequencies which are caused by temperature and pressure variations (Fig. 23).

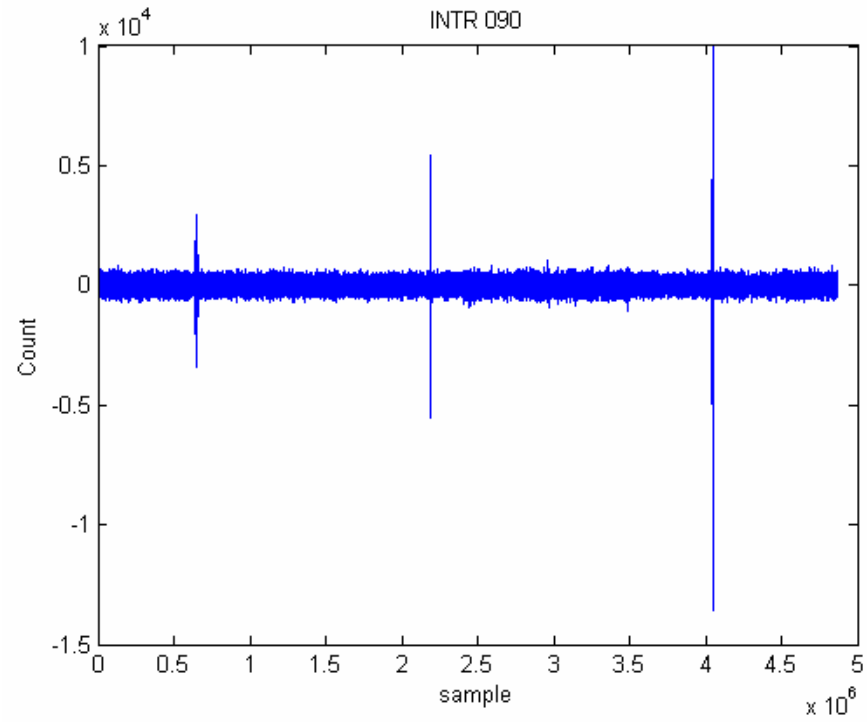

Figure 23. Blue line: waveform after band-pass filtering between 0.025 and 25 Hz.

3. The instrument correction was performed with the file of poles and zeros (hereafter paz) downloaded by the web portal ISIDE in the section 'Stations' (url: http://iside.rm.ingv.it/). At this web site it is possible to find for each station these files, that allow to correct the waveform of the instrumental response.
An example of paz file is:

20091124_0000.NOW.IV.ATMI.HHZ.paz

```
NETWORK   (KNETWK): IV
* STATION   (KSTNM ): ATMI
* COMPONENT (KCMPNM): HHZ
* LOCATION  (KHOLE ):
* START             : 2009,328
* END               : 9999,000
* CREATION          : 2012,16
* INPUT UNIT        : METER
* OUTPUT UNIT       : COUNT

CONSTANT 1.164267e+14
ZEROS 3
0.000000 0.000000
0.000000 0.000000
0.000000 0.000000
POLES 4
-172.789993 -262.369995
-0.111100 -0.111100
-172.789993 262.369995
-0.111100 0.111100
```

The constant of instrument CONSTANT is a conversion factor between counts and ground motion unit. In this example the paz file INPUT UNIT is meter and OUTPUT UNIT is count. To correct the data set of velocimetric waveforms, used in this study, is necessary to eliminate a zero and to divide by 'CONSTANT'. In this way an original waveform in count unit is transformed in m/s and corrected for instrumental response.

After the preprocessing of the raw data the following steps are performed in the programming language Matlab®:

- collect all files for each day,
- calculate the time series synchronization (FFT-shift),

- filling the gap with linear interpolation.

All Matlab® files of each day are archived in day-folder.

Then the time series is synchronized through the operation of Fast Fourier Transform (FFT) shifting. The FFT shifting allows to shift the sampling of the original seismic file to new defined sampling. The re-sampled time series is obtained with:

$$Z(t) = ifft(fft(F(t)) * e^{(\Delta t)})$$

Where Z(t) is the re-sampled time series; F(t) is the original time series; Δt is the shift between original and final sampling; fft is the FFT function; ifft is the Inverse FFT function.

The waveform of the data set are sampled at 100 sps. The first sample for a daily file must be at time 00:00:00,00, the second sample at 00:00:00,01, the third at 00:00:00,02 and so on.

When the seismic station starts it happens in a casual moment because the setting of stations doesn't allow the start at a definite instant. Often, the beginning of the start time is not at 00:00:00,00 but it is shifted by a fraction of hundredth of second.

Next, it is performed the linear interpolation. The linear interpolation allows to fill gaps of the seismic data between files. A time series with linear trend is created from the last value of the file and the first value of the next file.

After these operations is constructed a daily Mat file of 86400*100 samples. There are two principal cases: 1, the first original file for each day begins after time 00:00:00; 2, the last file ends after time 00:00:00 of the next day. So, in the first case there is an initial gap between the start time and the beginning of the first file of the day; this interval is filled with zeros. In the second case, when the last file of the day ended after the time 00:00:00 of the next day, the samples that exceed this time are cut and joined to the daily file of the next day.

So the daily file begin at the 00:00:00, 00 and ended at 23:59:59,99. Finally, the daily files are divided in 24 hourly files and they are used to calculate the cross-correlation.

3.3.3 Cross-correlation and estimate of the velocity variation

Cross-correlation is compute between pairs of stations for every hour of the available recordings; hourly files are used to avoid the computer memory overload during the computation of cross-correlations.

Before to cross-correlating seismic file there are the following steps:

- 1. control about the existence of hourly file;
- 2. spectral whitening;
- 3. normalization (one-bit normalization).

1)If the hourly waveform of the first station has not corresponding waveform in the data of the second station, the cross-correlation is set to zero. This is a gap in the computation of cross-correlation stack.

2)The spectral whitening is the equalisation of the frequency content of the seismic signal in a specified frequency band. In this study the operation of whitening is computed between 0.1, lower frequency, and 1 Hz, higher frequency. The whitening is the reconstruction of the spectral amplitudes with a function defined before. The original spectrum (blue in Fig.24), obtained with the FFT function, is used to construct the following equalized spectrum (ES):

$$ES = \begin{cases} \cos(\frac{\pi}{2} : \pi)^2 e^{(i\theta)} & \text{from 0 to 1 Hz} \\ 1e^{(i\theta)} & \text{from 0.1 to 1 Hz} \\ \cos(0 : \frac{\pi}{2})^2 e^{(i\theta)} & \text{from 1 to Nqf Hz} \end{cases}$$

where $\cos(\frac{\pi}{2} : \pi)$ is the cosine function calculated from π/2 to π, $\cos(0 : \frac{\pi}{2})$ is the cosine function calculated from 0 to π/2, θ is the phase spectrum in the frequency band [0, 1], [0.1, 1] and [1, Nqf], respectively and Nqf is the Nyquist frequency.

In Fig. 6 is showed the resulting equalized spectrum (red line).

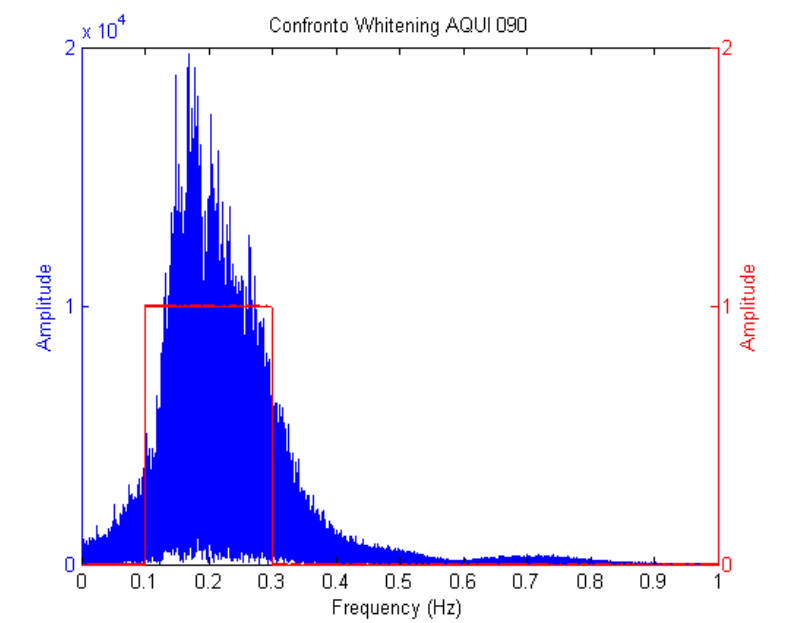

Figure 24. Spectral Whitening. Blue: original spectrum. Red: Spectrum after the whitening

3)Successively, was performed the operation of normalization. The normalization function can be chosen among different type: the one-bit normalization, the clipped waveforms method and running absolute mean normalization. One-bit normalization is choose considered Clarke et al., (2011) and Zaccarelli et al., (2011). In Fig. 25 is showed the result of the one-bit normalization.

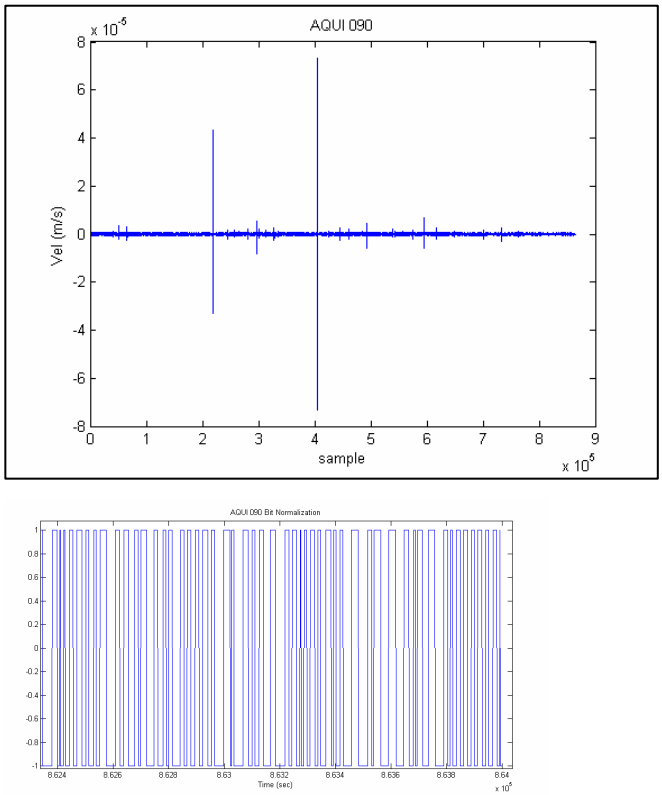

Figure 25. Top: Original waveform. Bottom: waveform after one-bit normalisation

After the control about seismic files, spectral whitening and normalization are calculated the cross-correlation functions.

Cross-correlations are used to compute MWCS technique described in chapter 3.2.

The cross-correlation represents the level of resemblance between two signals as function of a temporal moving applied to one of the signals.

In the programme language Matlab® the cross-correlation coefficient can be obtained with *xcorr* function.

The results of these operations is a hourly cross-correlation functions between all selected stations.

The hourly cross-correlations are used to calculate the current (CC^C)and the reference (CC^R) cross-correlation.

The first is the cross-correlation computing in a determined interval of days, while the second is the cross-correlation computing to the whole period of dataset, in this case 14 months.

The current cross-correlation is a stack of a subset of available cross-correlations. The reference cross-correlation is the stack of the all available cross-correlations in the whole time interval selected. In this study the reference cross-correlation is calculated with the seismic data from November 2009 to December 2010. The stack is performed in time domain.

An important parameter in the MWCS technique is the number of days useful to compute the stack of the CC^C. In fact, the stack is calculated with the aim to emphasize the coherent signal.

When the number of days of the stack increases, the SNR between the signal and the noise of the cross-correlation increases. In the Fig.26 cross-correlations of stations pairs of ATMI-PIEI are stacked for 10, 35 and 50 days. It is possible to note that the '50 days' stack presents a noise level less than the noise level of '10 days' stack. The different between stack of 10 days and stack of 50 days are evident in the coda of the cross-correlation.

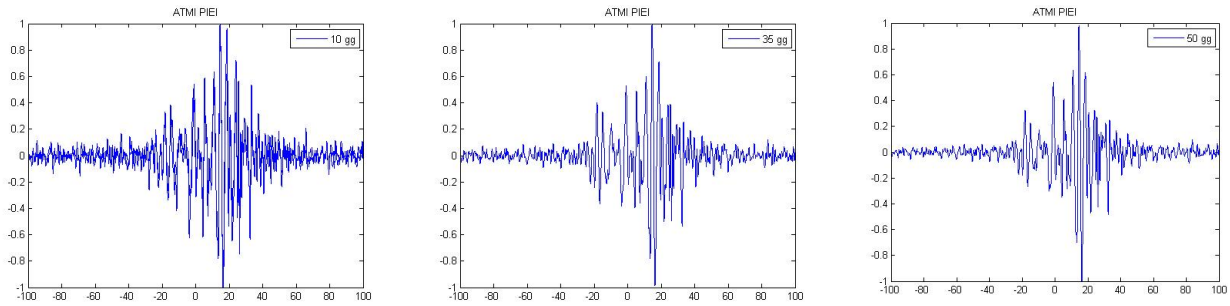

Figure 26. Example for different stack (10-35-50 days) for ATMI-PIEI stations pair cross-correlations.

The stacks are tested from 10 to 55 days to find an optimal duration for the CC^C.

Also, the cross-correlation coefficient, obtained between CC^C and CC^R, is evaluated as in Zaccarelli et al. (2011). The coefficient indicates the similarity of the CC^C and CC^R. The change of the curve that represent different stacks and the cross-correlation coefficient allows to choice the number of days for the stack for the CC^C. Fig. 27 represented three examples of coefficient curve for the stations pairs ATMI-PIEI, ATPC-PARC and ATFO-PARC. For all the examples the curve increases with the number of days of the stack. For the pair ATFO-PARC the coefficient values are the lowest and uncertainties are the larger than the other cases. The values are acceptable when the slope of the curve don't change and the coefficient of cross-correlation is elevated. Evaluated all stations pairs, the accepted parameters for the analysis are the coefficient >= at 0.85 and the number of days for the stack = 35.

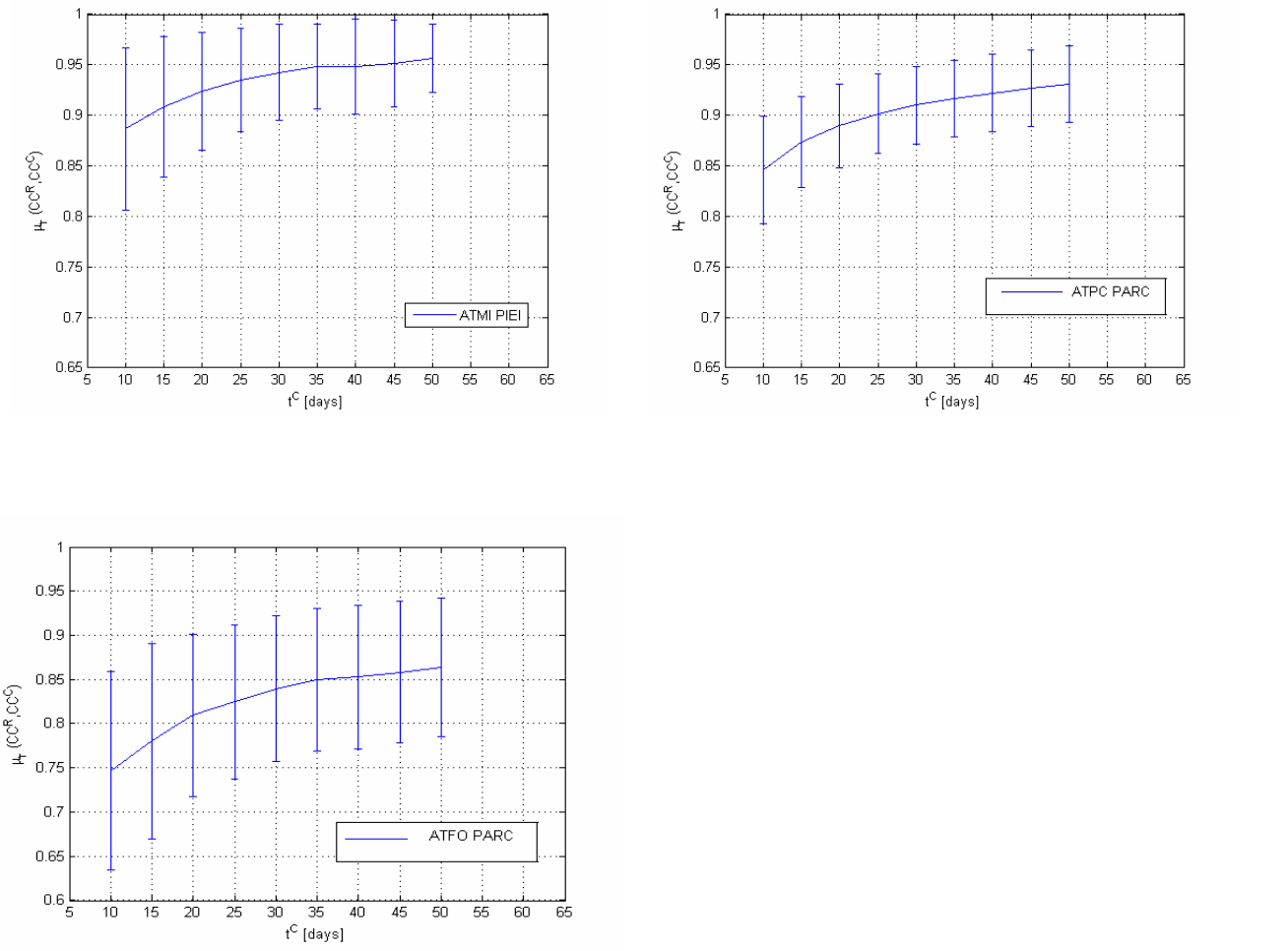

Figure 27. blue line: stack curves for ATMI-PIEI, ATPC-PARC and ATFO-PARC stations (stations name in right panel) from 10 to 5o days. The vertical blue line are standard deviation referred to the number of stack.

The most important step of the MWCS technique is the comparison between the CC^C and CC^R . The comparison is calculated in the coda of the cross-correlations because the central part contains direct waves and they may be sensitive to the sources of the seismic noise (Froment et al., 2010). Even the last segment of the coda is cut, because the signal amplitudes of the cross-correlation are similar to noise level. Then, it is necessary to eliminate some seconds of the cross-correlations from the 0 s lag. This parameter is called 'tout' and it is calculated considering a seismic velocity of the superficial waves equal to 2,5 Km/s as in Zaccarelli et al.(2011). 'Tout' is the ratio between stations pair distance (in km) and velocity (in km/s). For example for a stations pair distant 25 km, the removed signal is 10 s from the 0s lag for the casual part and 10 s for the acasual part of the cross-correlation. The 'tout' = 10 s is the value chosen for the analysis because it allows to eliminate the most energetic signal of the cross-correlation for all the stations pairs.

Another parameter 'time interval' indicates the maximum lag of the delay time calculation between the CC^C and CC^R. This operation cut the extreme segment of the cross-correlation coda where the results of the analysis are not reliable for the high level of noise. The time interval selected for the analyses is 35 s in the casual part and 35 s in the acasual part.

The MWCS technique is performed in the cross- correlation segment between 'tout' and 'interval'.

The parameters of the MWCS technique are the length of the analysis window and the overlap between two consecutive windows. The length of the analysis window is 8 s with an overlap of 1 s. For each analysis window, the cross spectrum (*S(f)*)is defined by

$$S(f) = F_{ref}(f) \cdot F_{cur}{}^*(f)$$

where F_{ref} and F_{cur} are Fourier transform of the windowed time series, f is frequency in Hz and the asterisk denotes the complex conjugate.

The similarity between the two windowed time series is assessed using the coherence C(f) (Fig.28 middle panel):

$$C(f) = \frac{\overline{|S(f)|}}{\sqrt{\overline{|F_{ref}(f)|^2} \cdot \overline{|F_{cur}(f)|^2}}}$$

where the overlines indicate smoothing. The time delay Δt between the two cross-correlation is obtained by fitting a phase value with a line because phase ϕ_j is linearly proportional to frequency (Fig. 28 bottom pane):

$$\phi_j = m \cdot f_j$$

then

$$m = 2\pi\delta t$$

The velocity change is given by the slope of Δt (Clarke et al., 2011):

$d\Delta t/\Delta t = -\Delta Vs/Vs$

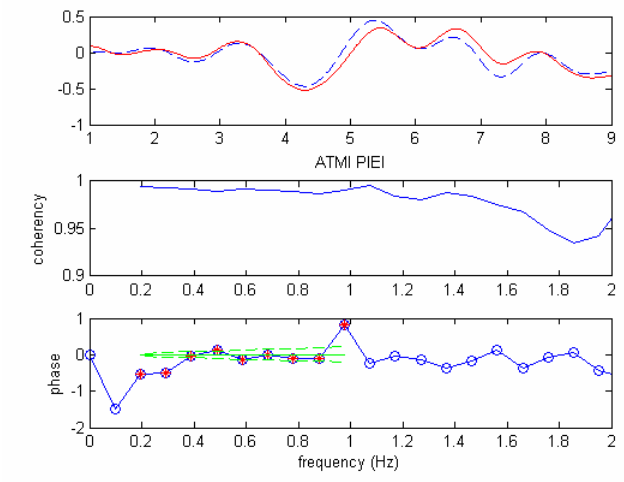

Figure 28. The panel (a) shoes the trend of the current and reference cross-correlation. (b) trend of the coherence for this window, the value can range between 0 (minimal coherence) and 1 (maximum coherence). (c) phase of the cross spectrum.

If a stress field perturbation acts homogeneously over the area the resulting seismic velocity variation ΔV/V is a stretching -Δt/t of the CC_C relative to CC_R. The stretching is constant over t and it is the opposite of the velocity variation (Poupinet et al., 1984):

$\Delta t / t = -\Delta Vs / Vs$

A linear regression to the delay time measurement (Fig. 29) is applied to recover velocity variation ΔV/V.

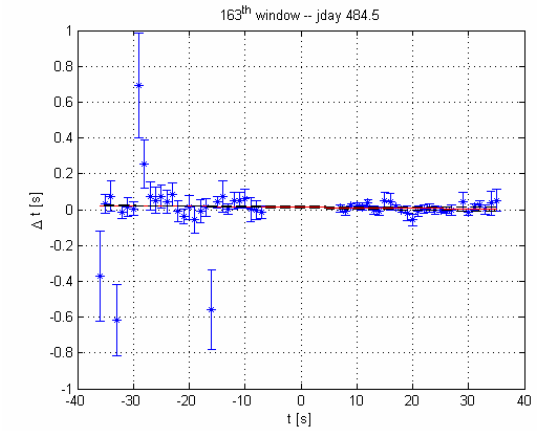

Figure 29. Example of window referred to a day of the interval. The number of the window and the day is indicates over the figures.

A ΔV/V is calculated between CC_R and CC_C obtained from stack of 35 daily cross-correlation. The next stack of 35 daily cross-correlation is performed shifting the start of the stack by one day.
In this way the velocity variations are represented by a time series similar to Fig. 30.

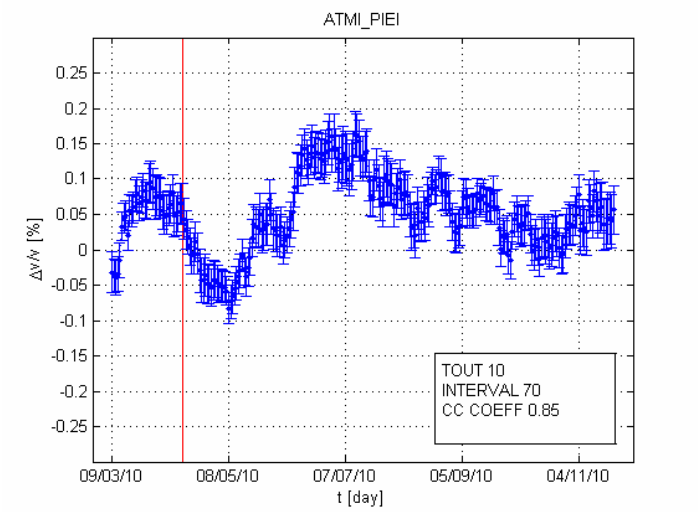

Figure 30. Example of velocity variations for the ATMI-PIEI pair.

The described procedure was applied to 26 stations pairs in ATV area (Fig.31).
The location of the stations is very different and it can interested the seismic fault zone, but sometimes they are only near the seismic zone of the seismic sequence on April 2010.
These are the case in which seismic data don't exist in time interval of analysis. Besides, some seismic data are eliminated during MWCS analysis.
With the aim to obtain velocity variation representative of the entire crustal volume in the study area, the time delays Δt_i (I number of stations pairs) from many stations pairs are merged together. The merged delay is the median value of the Δt_i and it is insert an estimate of ΔV/V of the entire area.
The test is made to combine the higher number of different stations pairs to find the most complete and exhaustive velocity variation.

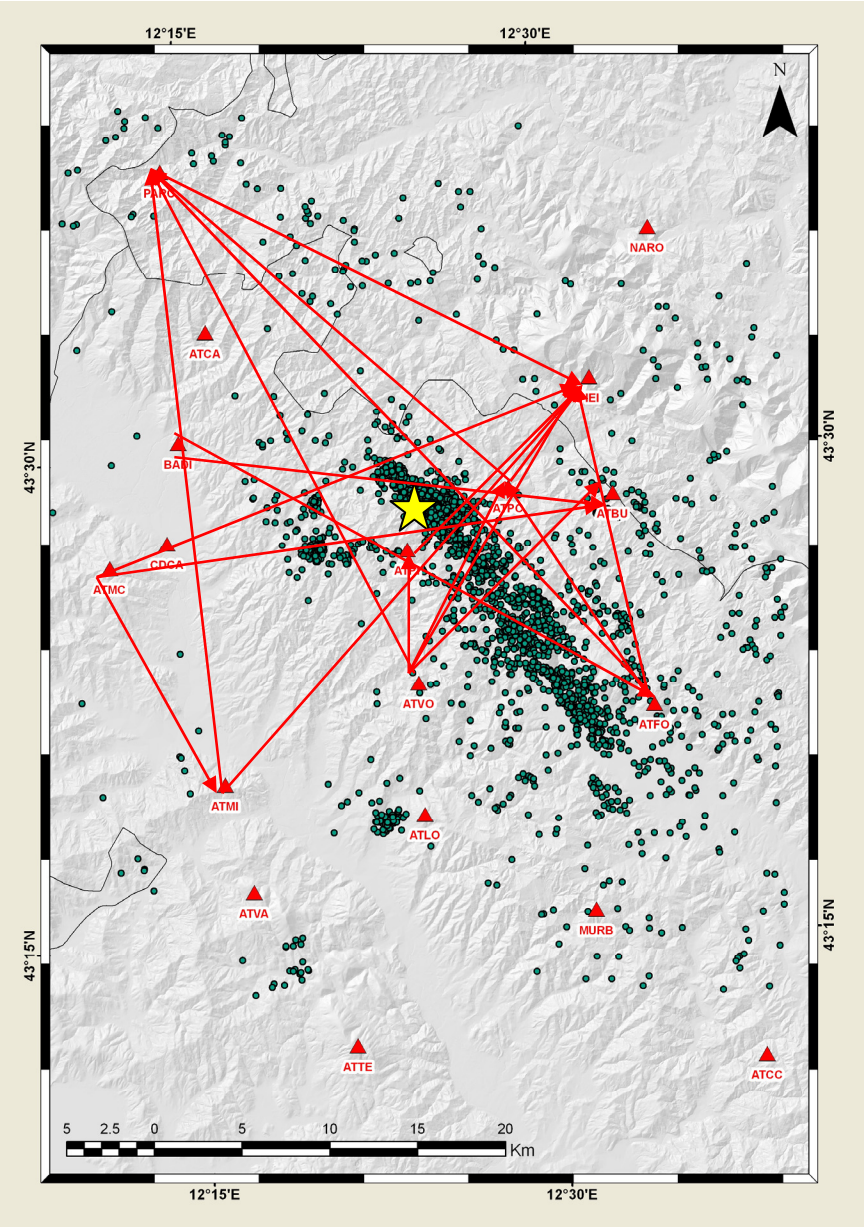

Figure 31. Localization map of stations and all possible combinations (red line). Yellow star indicates the event on 15 April, 2010. The green circles the events during the study period.

Fig.32A is an example when are used seven stations pairs and corresponding velocity variation is not continuous. There is a gap of some weeks between July and August and also they don't permit to see any variation before the sequence in April 2010. In fact, in this period there are few data and the variation starts only some days before the event on 15 April (red line in Fig. 14). In Fig.32B four stations pairs are used; there is only a little gap in the last part of the period and also before the sequence is not possible to see variation. Different case in Fig.32C, where only five stations pairs are used and where there aren't gaps and the velocity variation is present before the sequence, because the seismic data start a month before.

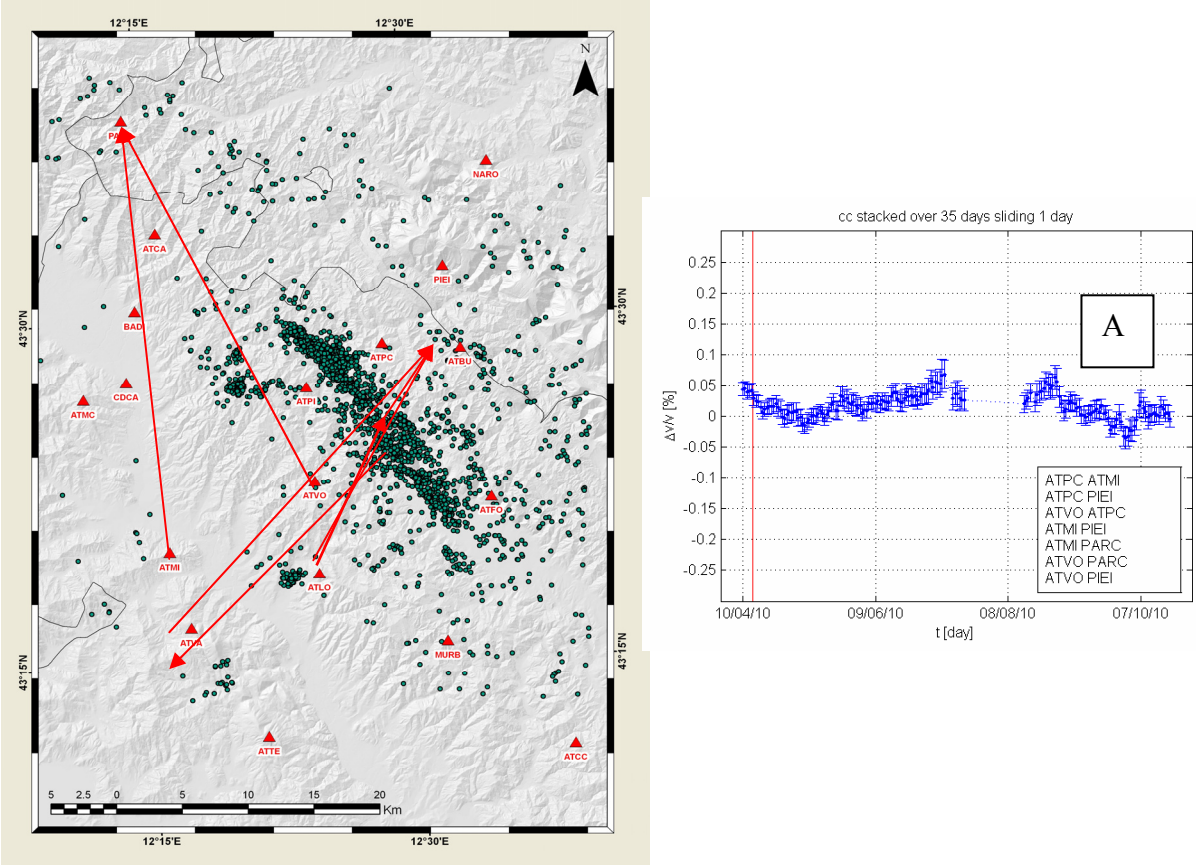

Figure 32. Left: Station pairs. Right: Velocity Variations

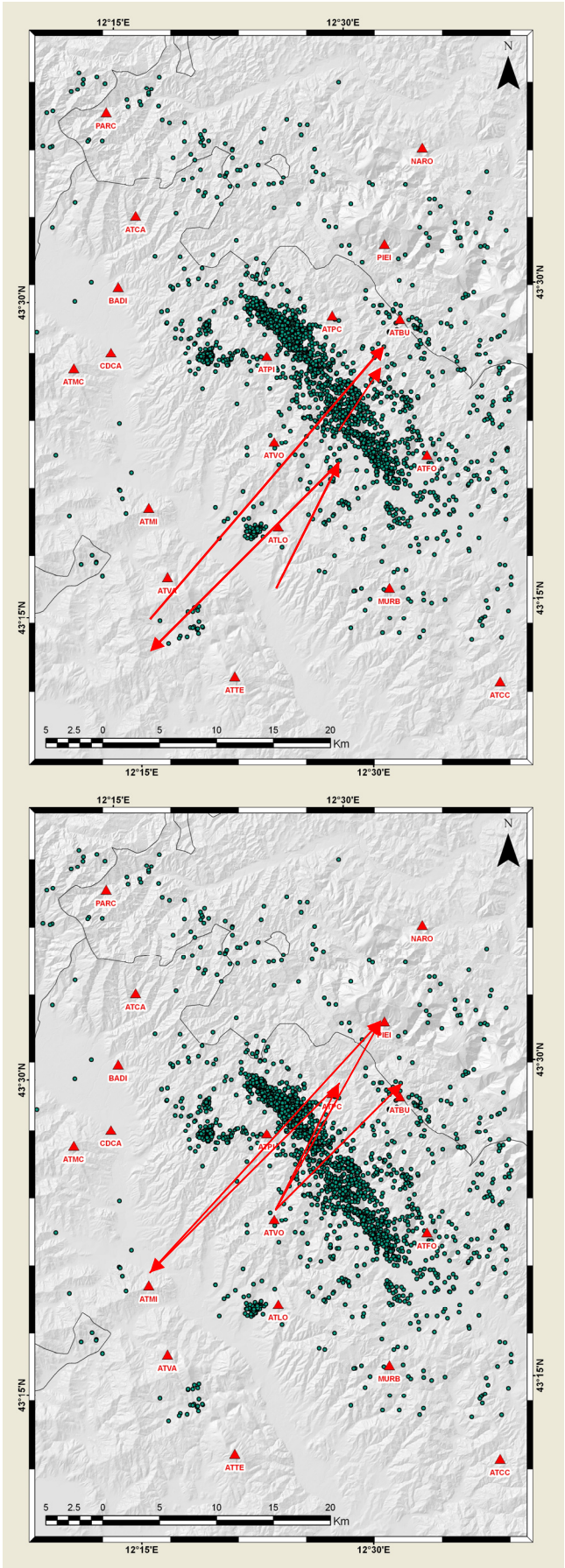

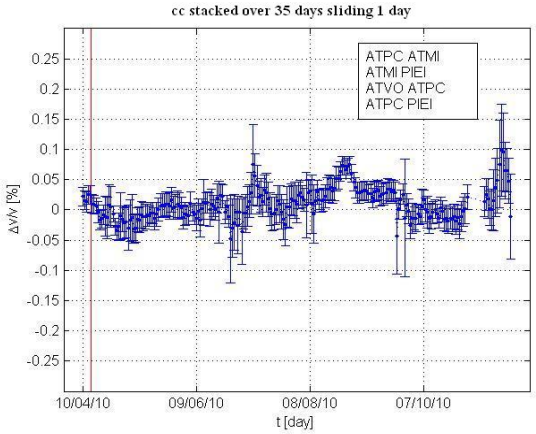

B

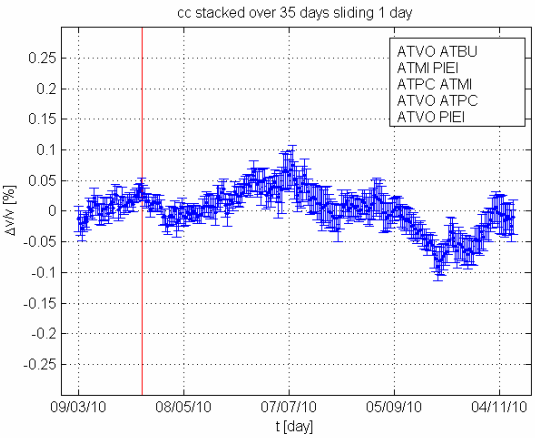

C

Figure 32. Continue…

3.3.4 Seismotectonic framework of the Umbria-Marche region

The area studied in this work is the Alto Tiberina. This area is located in Central Italy and it is considered an active seismic zone. In the past it was struck by many earthquakes. The area is characterized by a principal geological fault, the Alto Tiberina Fault (ATF), and many others little geological structures that are related with the principal. These secondary structures are synthetic and antithetic faults respect to the ATF. In this chapter is described the seismicity and the geological setting of this area.

Many studies were conducted in Central Italy, in particular in the Alto Tiberina Area. This area was struck by sequences of moderate magnitude earthquakes during the years and it has been affected by a seismic sequences.

At present, the active area is located in the inner zone of the Umbria-Marche Apennines struck by strongest historical and instrumental earthquakes. In the past 40 years, some seismic sequences have occurred in this region: the 1979 Norcia earthquake (Deschamps et al., 1984), the 1984 Gubbio sequence (Haessler et al., 1988), the 1997 Colfiorito multiple main shock sequence (Chiaraluce et al. 2004) and the 1998 Gualdo Tadino sequence (Ciaccio et al., 2005).

Historical records showed that large earthquakes, at least in the past 700 years, have not affected the Colfiorito area. The only earthquake documented in catalog to occur in this area is an event that struck Serravalle di Chienti and Nocera Umbra in the 1279. It appeared to have occurred close the northernmost portion of the 1997 epicentral area. Important sequence occurred in 1703, with a maximum intensity of XI (Mercalli-Cancani-Seeberg [MCS] scale), and in 1730 with a maximum MCS intensity of X.

Similar to the 1997 sequence, both 1703 and 1730 sequences did not have a single strong mainshock followed by aftershocks but were characterized by a few strong shocks of similar size.

The 1703 sequence had two mainshocks, which ruptured two adjacent zones of the belt, this is similar to what happened in 1997 with two shocks. The 1730 sequence had two shocks of similar magnitude and time lag similar to that elapsed between the two mainshocks of the 1997. Some months after in 1730 another seismic event struck the Gubbio area. It is interesting to note that the 1997 event was followed by 1998 Gauldo Tadino earthquake.

Recent analysis about the seismicity of the area does not reveal this peculiarity. The earthquakes with M>5 (1979 Norcia earthquake, Ms 5.8, and 1984 Gubbio earthquake , Ms 5.3) had a single mainshocks followed by aftershocks; the earthquakes with magnitude larger than 4.3 have a sequence of aftershocks (Perugia, 1993, Massa Martana 1998) a few months before the sequence of

Colfiorito. Chiaraluce et al. (2004) declared that the analysis of seismicity of the past 20 years does not show any complex and prolonged seismic sequences with multiple shocks.

Chiaraluce et al. (2004) investigated some aspects about the sequence of 1997; they used the earthquake locations to investigate the details of the seismic sequence and to compute aftershock fault-plane solutions. Also they investigated the tectonic setting of this portion of the Apennines and the kinematics of the normal faults that rupture during the sequence and the complexity of the sequence of 1997 and its relation to the former seismicity of the region.
A long sequence of moderate magnitude earthquakes ($5<M_w<6$) struck central Italy in September and October 1997. Three mainshocks (which occurred on 26 September at 00:33 and 09:40 GMT and on 14 October) occurred on distinct 5 to 10 km long fault segments, adjacent and slightly offset between each other, the sequence occurred during a month on a seismogenic volume expanding for near 60 km along the Apennines (Fig. 33).
The epicentral area of the 26 September shocks corresponded to the intramountain basin of Colfiorito. The highest intensities (VIII-IX degree MCS scale) were recorded in small villages located around the basin. A few hours after these two shocks a dense seismic array was deployed in the epicentral area (Cattaneo et al., 2000). The analysis of seismic data recorded by the temporally network have shown that the shocks ruptured normal fault segments parallel to the trend of the Apennines mountain belt (NO-SE); the rupture were shallow and dip to the SE at relatively low angles. The analysis of strong motion and broadband seismic data revealed clear evidence of rupture directivity during the largest shocks of the sequence.
Chiaraluce et al. (2003) investigated the distribution of the seismicity of the 1997 Umbria-Marche sequence and the complex faults system. Seismicity of the area showed a clear migration (northwest-southeast) of the main fault corresponding to the Apennines orientation. All seismic sequences (1703, 1730, 1747-1751) are characterized by multiple ruptures in shorts time intervals. This complex behaviour of faulting could be due to the heterogeneity in the crust of the central northern Apennines, characterized by fold and thrust structures. According to the results of this study some authors suggested the presence of a regional normal fault dipping at low angle to the northeast, named ‘Alto Tiberina Fault’.
Chiaraluce et al. (2007) presented seismological evidence for microseismicity associated with active slip along a long-angle normal fault (hereafter LANF, normal fault dipping less than 30°). They documented the geometry and features of the Alto Tiberina Fault by seismological data collected during the 2000-2001 seismic survey (Fig. 34).

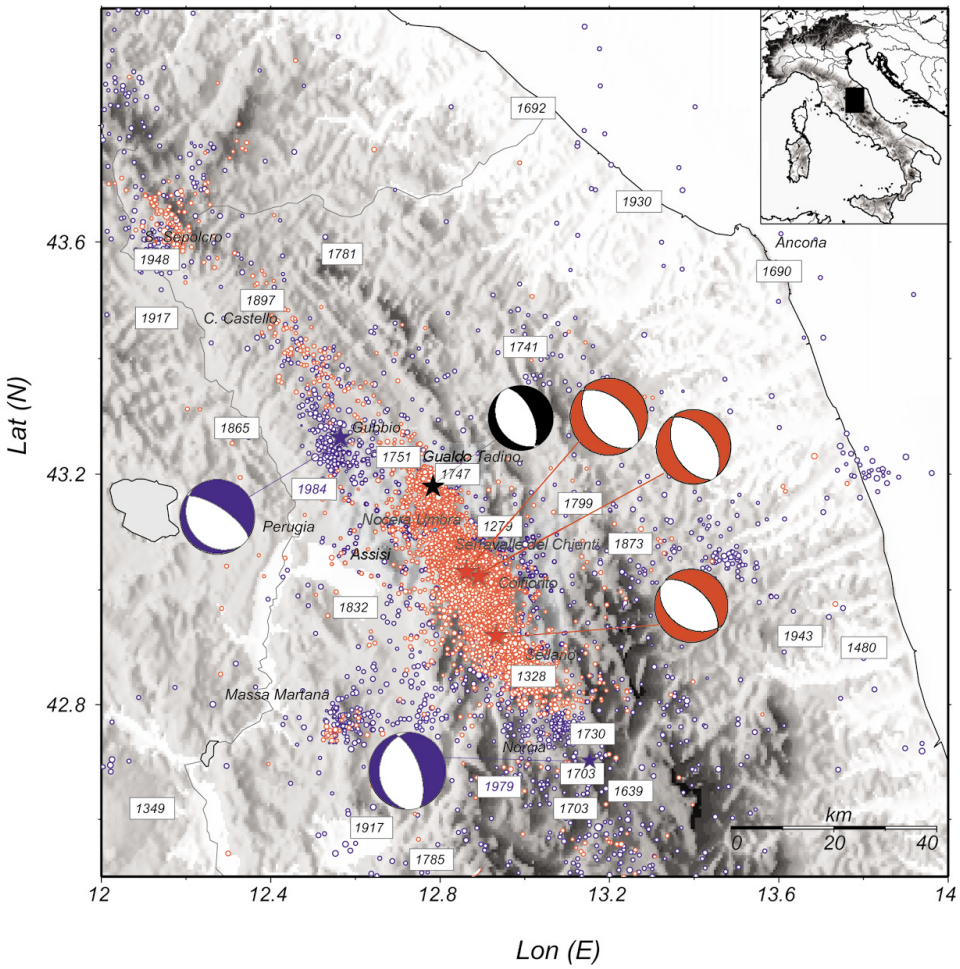

Figure 33. Map of seismicity of the Umbria–Marche sector of the Apennines. Blue and red symbols show the distribution of epicenters before and after 26 September 1997, respectively. The red focal mechanisms are those of the three largest shocks of the 1997 sequence whose epicenters are shown by the stars. Blue fault-plane solutions are those of the mainshocks of two recent seismic sequences that occurred in 1979 and 1984 in Valnerina and Gubbio, respectively (Deschamps et al., 1984; Haessler et al., 1988). The white rectangles show the distribution of historical seismicity (Boschi et al., 1995) in the area. Plotted in black are the location (star) and the focal mechanism of the Gualto Tadino event that occurred on 3 April 1998, a few months after the beginning of the sequence (Chiaraluce et al., 2004).

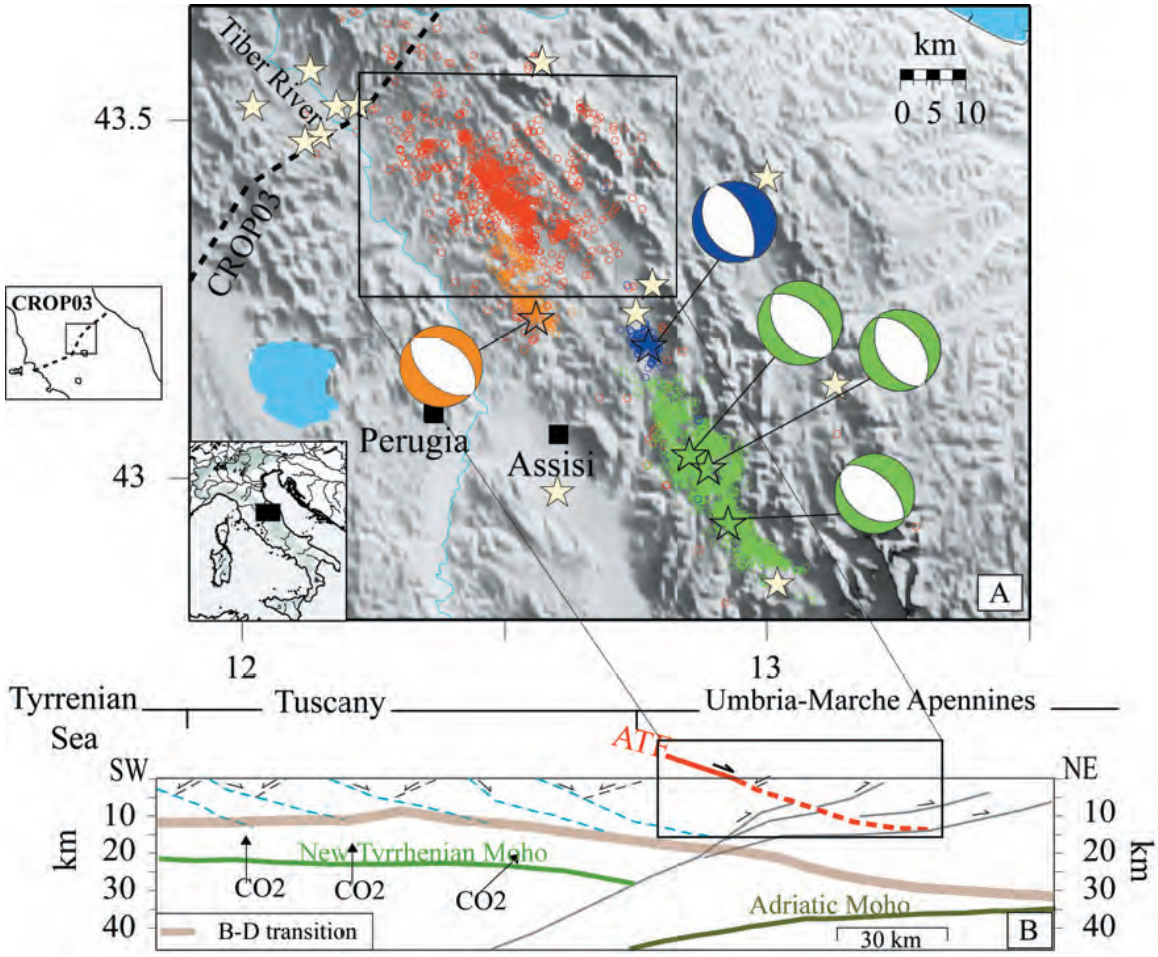

Figure 34. (A) distribution of seismicity in the northern Apennines. The strongest historical earthquakes are located with stars. Red symbols show epicenters of the earthquakes recorded during the 2000-2001 seismic survey; orange and blue symbols indicate the aftershocks of the 1984 Gubbio (Mw 5.1)and the 1998 Gualdo Tadino (Mw 5.1) earthquakes; green symbols indicate the seismicity during the 1997 Colfiorito sequence. (B) crustal-scale section cross section interpretation of the seismic profile running from the Tyrrhenian to the Adriatic coasts. The ATF is drawn in red, the brittle-ductile transition is indicated with light grey curve (Chiaraluce et al, 2007).

The aim of the study was to provide the location and the geometry of seismic sources located along this active portion of the northern Apennines. The seismic network recorded nearly 2000 earthquakes with Ml<3.1 which represents the background seismicity of the area.

They analyzed two different data sets (seismicity and seismic reflection profile). The data sets showed the same regional scale eastward dipping low-angle fault (Figure 35 A). The seismicity is elongated in the Apennines direction (NNW) for 60 Km parallel to the strike of the normal faults in the area (Figure 35 B). Also the earthquake distribution defined a volume confined at depth by a nearly planar surface dipping E-NE at low angles. This plane separates the active hanging wall block from a completely aseismic footwall. The major NNW trending structure is associated with microseismic activity from 3-4 km to 16 km depth.

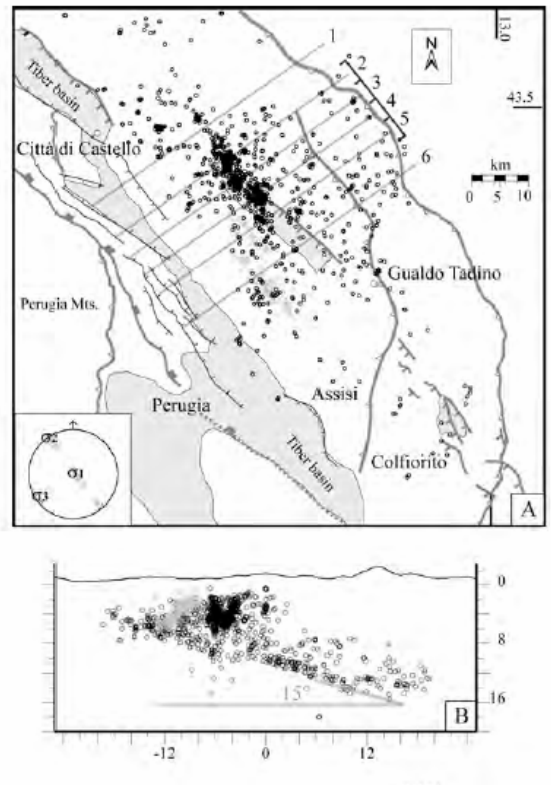

Figure 35. Earthquakes localization and distribution of the seismicity of the area (A). Earthquakes distribution that defines the planar surface dipping E_NE at low angle (15°) (B) (Chiaraluce et al., 2007).

The alignment of the hypocenters in the hanging wall highlights two minor faults. The first structure is a 5 km long and the second structure is a high-angle fault which merges at the surface with the Gubbio normal fault.

In conclusion in this study they analysed the seismicity associated with an active long-angle normal fault situated in the northern Apennines. The integration with geological observations, seismic reflection profiles and seismicity defined an east dipping low-angle normal fault 60 km long and 40 km wide, identified with the ATF the major structure of the area.

De Luca et al.(2009) described the seismicity of the Northern Apennines between 2002 and 2006. The aim is to determine the geometry and kinematics of the crustal and the seismicity that affected the Northern Apennines area. The Neogene to Quaternary evolution has been controlled by eastward retreat of a west directed subducting slab that caused the eastward migration of the thrust fronts and of the extension in the Tyrrhenian side. During the 1997 Umbria-Marche seismic sequence antithetic normal faults were activated, with no evidence of activity on the ATF. The trend of the crustal seismicity confirms what found by other authors and adding some details to the general picture. The shallow seismicity appears to be concentrated in a narrow band following the trend of the Apennines. The main NW-SE region is separated by areas of lower seismic activity (Fig. 36). In the central-southern region (boxes GH, IJ and KL in Fig 36) there is a more diffuse

seismicity in the eastern sector, also in the western area. In the northern sector (boxes AB, CD and EF in Fig 36) the western area appears almost aseismic, while a diffuse activity characterizes the Adriatic region. The deeper seismicity (25-80 km) is spread in the Adriatic region and tends to cluster below the Apennines, whereas no deeper earthquakes occur in the western. The two northernmost sections (AB and CD in Fig. 36) show similar characteristics and some clusters of deeper seismicity in the eastern sector. The central sector (EF and GH in Fig. 36) show a rather different trend: the shallow seismicity exhibits a gentle (~ 20°) deepening from west to east, between 5 to 15 km depth, in agreement with what proposed previous studies related to the geometry of the ATF (see Chiaraluce et al., 2007).

Complementary to the evidence of east-deepening seismicity in the upper crust, they find clear evidence that the deeper seismicity shows an opposite dip, from 30 to 70 km depth. The two clusters are separated, the dip of this feature appears to change from about 20°-30° in the shallower part to 40°-50° below 40 km depth. They interpret this feature as the Adria plate underthrusting the Apennines.

At the end in the upper crust there are evidences of a narrow belt of predominantly normal faulting earthquakes below the central portion of the Apenninic belt. The seismicity reveals a background activity that delineates a continuous release in a depth interval of 8-15 km. Some of this seismicity appears to be related to the ATF fault trend. The general trend is a plane dipping from west to east, extending from 100 km across the Apennines from a depth of 2-3 km to about 20 km, with a 15°-20° dip angle.

In the upper ~8 km of the crust the seismicity is clustered in narrow regions or nearly absent. The analysis confirm that the central belt is affected by normal faulting earthquakes, in the northern region no earthquakes deeper than 40 km are found and in the south (KL in Fig. 36) no earthquakes deeper than 20 km are found.

Ciaccio et al. (2005) study the Gualdo Tadino earthquake that struck the central Italy on April 3, 1998 with Mw=5.1. This earthquake was the last event of the Umbria-Marche seismic crisis, wich started in September 1997 in the Colfiorito area, about 15 km SE of Gualdo Tadino. As well as the Colfiorito mainshocks, the Gualdo Tadino earthquake was characterised by a normal fault mechanism, with a NE trending extension, in agreement with all kinematics that occurred in Umbria region (Norcia 1979, Perugia 1984). The 1998 aftershock sequences were recorded by both permanent and temporary stations, managed by Istituto Nazionale di Geofisica e Vulcanologia of Roma (INGV). The seismicity of this event was analysis in order to discuss the relationship between the activated fault and the deep geological structure. The Gualdo Tadino area is located at the western part of the Umbria-Marche Apennines ridge, arc-shaped fold and thrust belt, affected by

Quaternary extension. The axial ridge of Umbria-Marche Apennines is characterised by a widespread SW-NE extension, with moderate seismicity (5<M<7). Major earthquakes occurred along a system of SW dipping sub-parallel normal faults, for a length of about 150 km from Città di Castello to Norcia, the Umbria Fault System UFS (Fig. 37). In the northern sector the UFS faults are antithetic to a regional, east-dipping low-angle normal fault, the Alto Tiberina Fault.

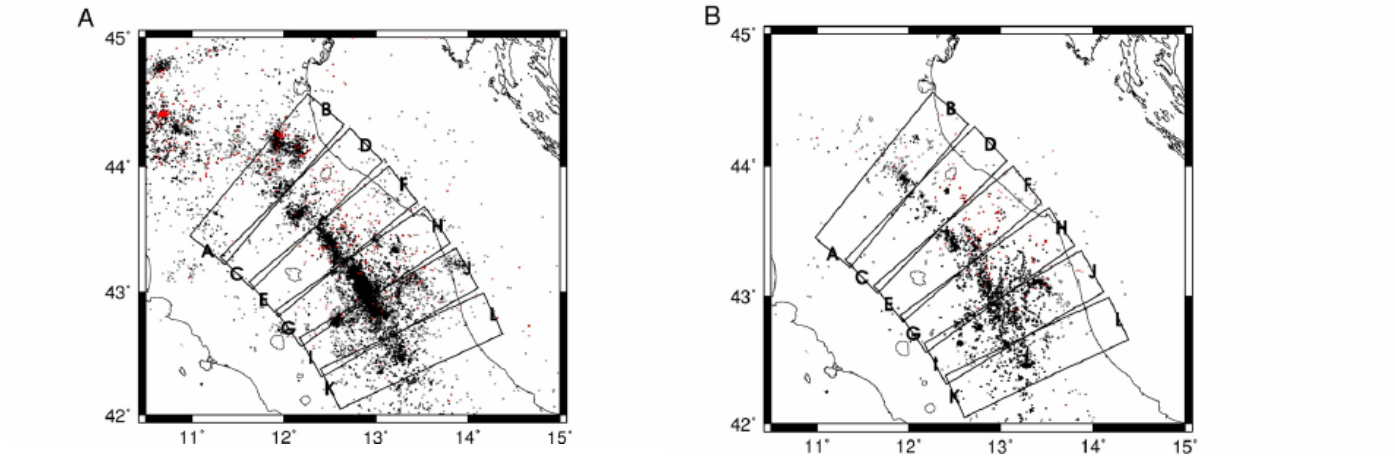

Figure 36. Location maps. Red circles are earthquakes below 25 km depth. (A) epicentral map and cross sections with CSI data set 1981-2001. (B) epicentral map and cross sections with integrated data set 2002-2006 (De Luca et al., 2009).

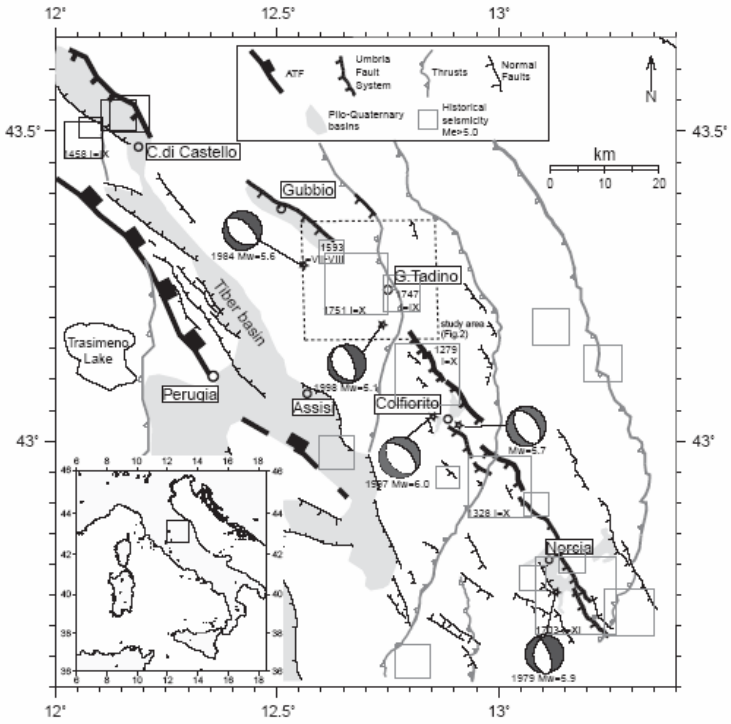

Figure 37. Structural map of the Umbria-Marche region and historical seismicity (Ciaccio et al., 2005)

This study confirmed that the Gualdo Tadino fault is consistent with the geometry and kinematics of the adjacent faults of the UFS. Seismological data indicate that the ruptured segment is a SW dipping normal fault, with a gentle dip of 30°-40°. A similar dip range characterises the fault activated in the Colfiorito area. Also the interdisciplinary analysis indicates that this earthquake originated above the top of the basement. A similar distribution of the seismicity has been observed for other normal faults pertaining to the UFS, such as Gubbio and Colfiorito.

As regard the geological setting, the Umbria-Marche Apennines are an arc-shaped, NE verging, thrust-and-fold belt corresponding to the easternmost part of the northern Apennines (Mirabella et al., 2008).

In the northern Apennines the upper crust is thinned by a set of east-dipping low-angle normal faults (LANF). These zone is characterize by a constant seismicity. The easternmost of these LANF coincides with the geometry and location of the ATF. The long-angle normal fault is generally believed as important structure for seismic hazard and resolution for regional crustal extension. In many case the low dip angle are justified as being related to passive rotations induced by successive normal fault sets.

The ATF, whose average dip is ~20°, borders the Upper Pliocene Quaternary Tiber basin and has a displacement of about 8 km. The axial zone of the Apenninic (Umbria-Marche Apennines) , located east of the Tiber basin, is also affected by a set of SW dipping active normal faults that border the continental, Quaternary basins of Gubbio, Gualdo Tadino, Colfiorito and Norcia (Collettini et al., 2002).

The northern Apennines consist of a NE verging thrust-fold belt formed as the result of the collision between the European continental margin and the Adriatic lithosphere. From the Oligocene to the present day there were two phase of migrating deformation: a compression with eastward directed thrusting and a later phase of extension. Older part of the extensional system are significantly exhumed to the west in the Tyrrhenian islands (Elba) and Tuscany, while the ATF is located in the inner sector of the Umbria-Marche Apennines (Fig. 38) where an extensional stress field is active today. Tyrrhenian sea and Tuscany sector are characterized by tectonic extension and also by wide spread and vigorous CO2 degassing occurrences.

Several author suggest that fluid play a key role in triggering earthquakes and control the evolution of seismicity (Chiodini et al., 2004). These active region is also the zone where the strongest historical and instrumental earthquakes are located.

The region includes a sequence of continental margin sedimentary rocks deposited upon a Paleozoic metamorphic basement. The base of the cover succession in represented by late Triassic Evaporites, overlain by Liassic platform carbonates, Jurassic-Oligocene pelagic sediments and Miocene-

Pliocene turbidites. In the Perugia area, the ATF is intersected by two boreholes where it is observed to juxtapose Miocene turbidites over the Triassic Evaporites, completely omitting the intervening Umbria-Marche carbonates. Near the surface, the ATF is represented by a splay of domino-like normal faults that detach downward onto the ATF at depth (Fig. 38) (Boncio et al., 2000).

The easternmost splay of this system bounds the Tiber basin. The asymmetrical shape of the area is consistent with movements along an east dipping extensional fault. In the hanging wall block, the seismic reflectors abruptly terminate against the fault trace. The seismic reflector corresponding to the Marne a Fucoidi formation located at 2 km depth in the ATF hanging wall.

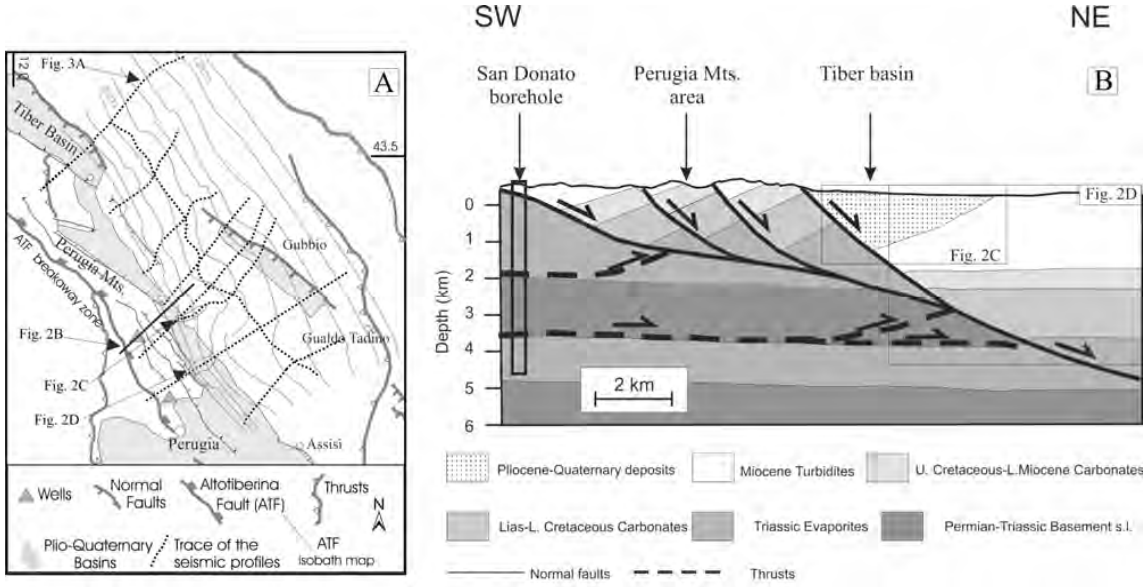

Figure 38. Geometry of the ATF constrained by surface geology, interpretation of seismic reflection profiles and borehole data. (A) Structural map of the study area. (B) Vertical geological cross section (see its location in Figure 2) integrating surface geology, borehole data, and seismic reflection profiles (Chiaraluce et al., 2007).

Chiaraluce et al. (2007) reconstructed the geometry of the ATF reflector by depth converting the seismic reflection profiles using seismic velocities obtained from borehole data in the area (Fig. 35) (Barchi et al., 1998), with these technique they are able to image the ATF continuously for about 60 Km longitudinally. At depth the attitude of the fault surface is constant with NNW-SSE strike direction and dip of 15°-20°, while near the surface the fault becomes steeper (30°-35°).

3.3.5 Results and discussion

The aim of this study is to analyse the velocity variations in the area of ATF in the northern of Umbria region. The dataset of continuous seismic noise waveforms was processed and analysed with the MWCS technique, described in the previous paragraph.

This area is considered a seismic area because in the past was struck by many earthquakes and it is characterized by a frequently microseismicity (Chiaraluce et al., 2003; De Luca et al., 2009). During the period analysed in this study (from November 2009 to December 2010), the monitoring networks have recorded a seismic sequence (Amato et al., 2010). The mainshock of this sequence is the earthquake on 15 April, 2010 at 01:45:36 UTC (Ml 3.8). The most of earthquakes of the sequence are occurred in about two weeks.

The INGV - Ancona provided the manual picking relative to P and S phase and the earthquake localizations.

Fig. 39 shows all the seismic events occurred from October 2009 to December 2010, in particular events of the sequence of April 2010 (red circles) with the most earthquake (yellow star) and the increase of seismicity of July 2010 (green circles). Blue triangles represented seismic stations used to estimate velocity variations from cross-correlations of seismic noise.

The analysis of the seismicity of the area shows that the seismic activity is always present (Fig. 40). Fig. 40A shows the distribution of magnitude values and they range especially between 0 and 1. Few earthquakes have magnitude great than 2. Fig. 40B represents the number of earthquakes per day. The number of earthquakes per day is elevated in April 2010 (from day 464 to 480, in Fig. 40B) respect to the normal seismic activity. The 15 April 2010 the seismic network detected about 250 events. An other increase of seismicity appears in July and August 2010 (from day 568 to 600, in Fig. 40B), with events per days in a number of about 40.

The energy released coincides with the two period of most seismic activity. The cumulative curve of energy per day release shows that during the first period, April 2010, the energy released is more than in the second period (July 2010) (Fig. 41). This effect is due to the elevated magnitude of some earthquakes and to the correspondence with the great number of events.

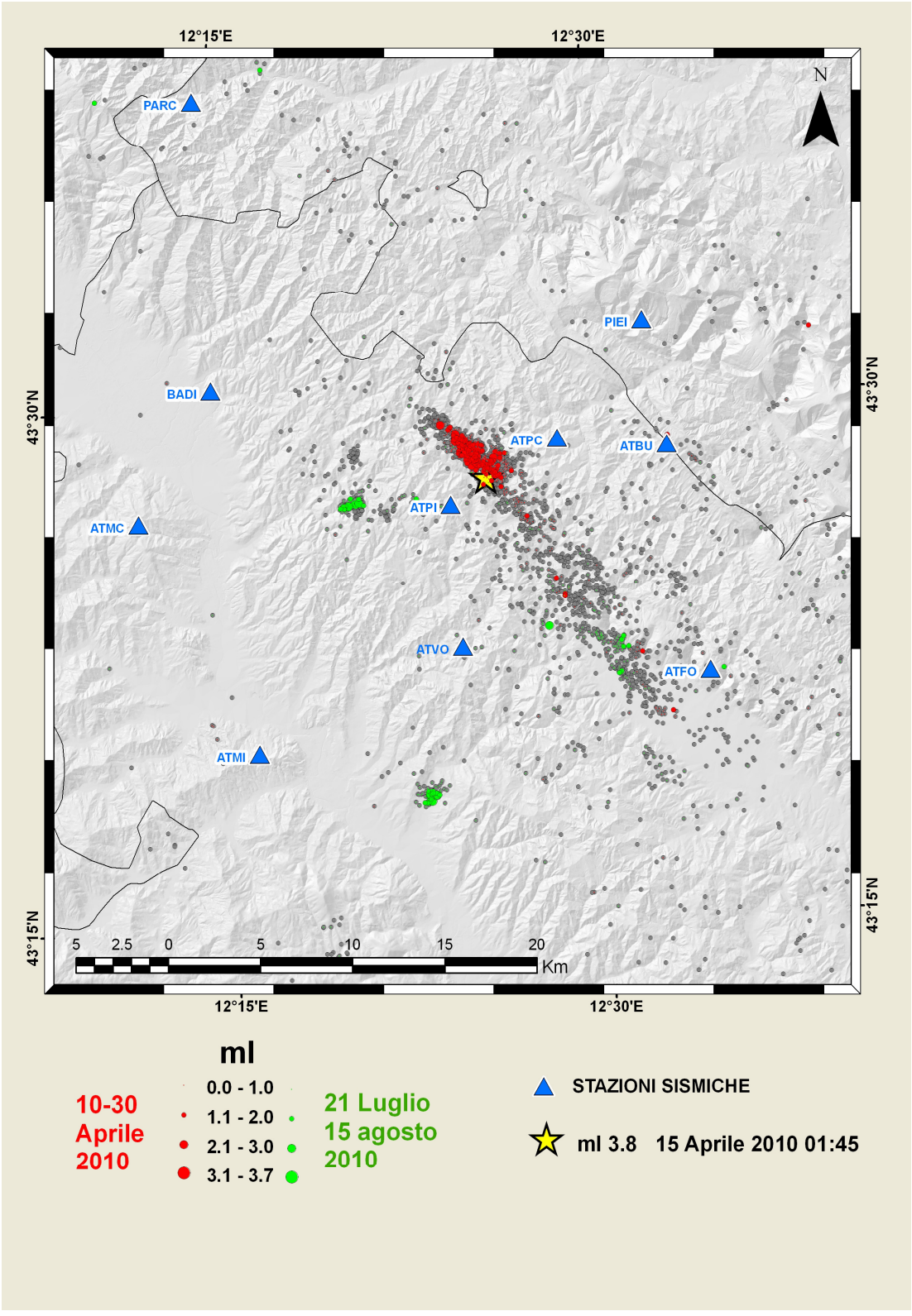

Figure 39. Seismicity of the area from October 2009 to December 2010. Red circles: seismic activity during the sequence in April 2010. Green circles: seismicity during July and August 2010. Blue triangles :seismic station. Yellow star: the event on 15 April, 2010.

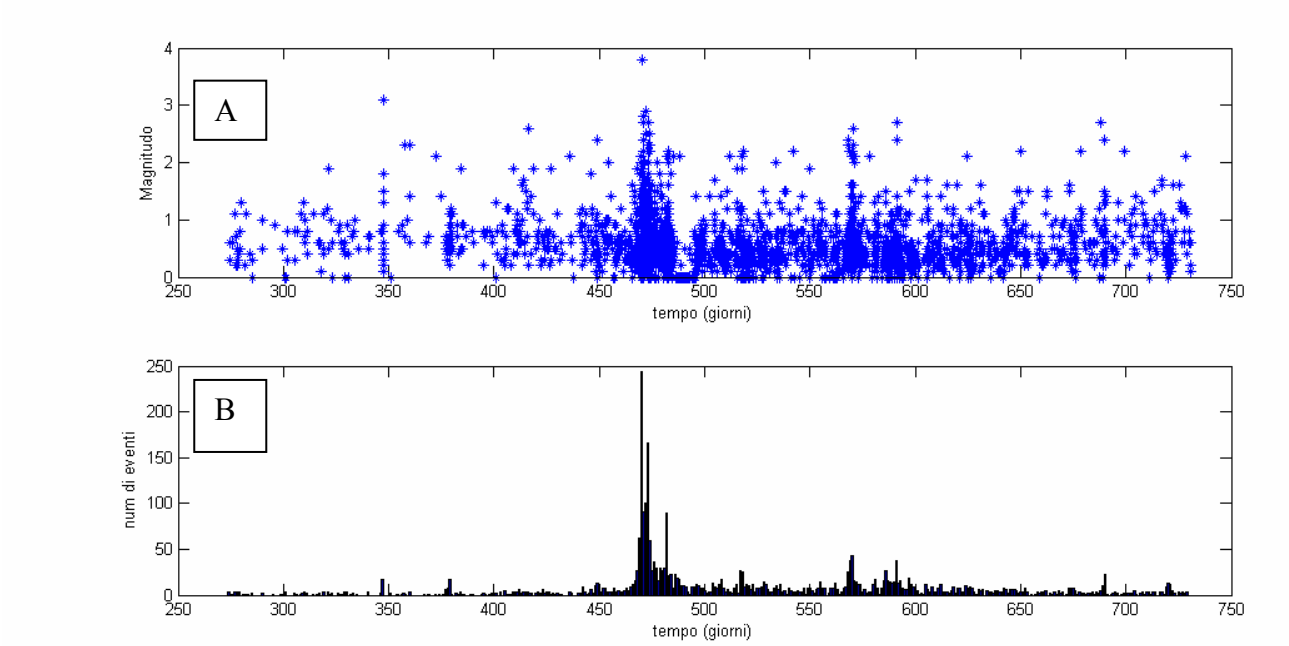

Figure 40. Seismic activity of the study area from October 2009 to December 2010. (A) Magnitude of seismic events (blue points). (B) Number of events during the time.

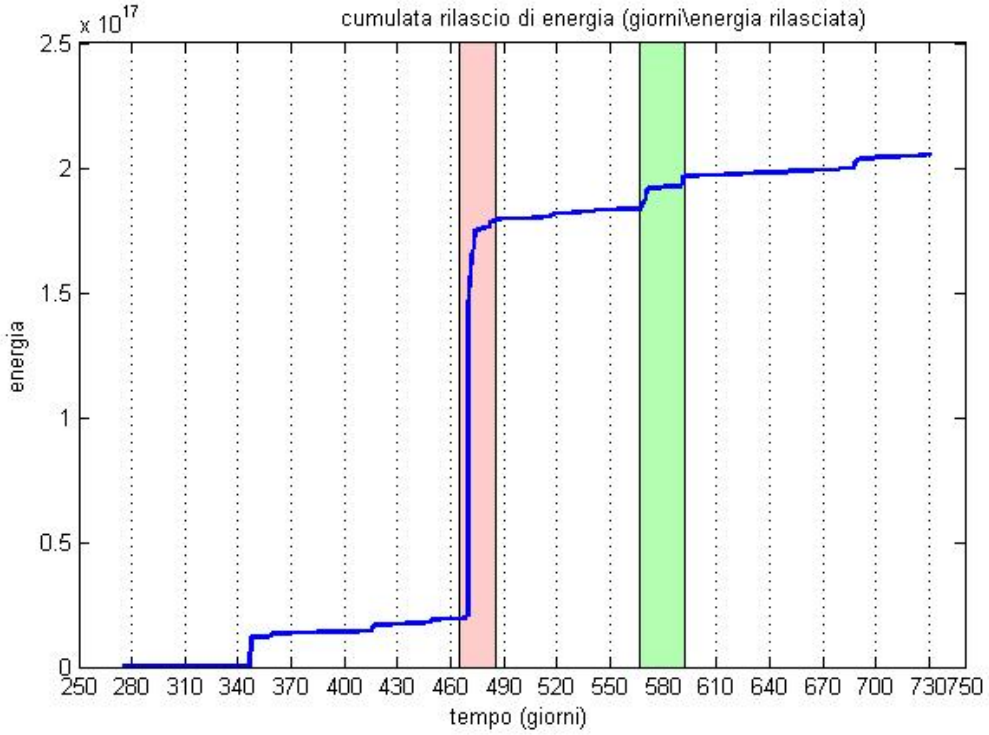

Figure 41. Cumulative curve of energy. Blue line: energy release. Red bar: seismic sequence in April 2010. Green bar: seismic activity in July-August 2010.

The analysis of the ratio between velocity of P wave and S wave (Vp/Vs) is conducted with the aim to find variations in the propagating medium.

The Vp/Vs average ratio for the seismic area is calculated with the Wadati modified method (Chatelain, 1878; Pontoise and Monfret, 2004). This method allow to calculate the ratio considering the all earthquakes recorded at seismic stations without the origin time calculation. In Fig. 42 the stars represents the 35431 observations obtained from all possibile combinations of the arrival time difference. In this study an earthquake is selected for the analysis when six stations have P and S picking with zero weight. The Vp/Vs average ratio for the area results 1.8662±0.0004.

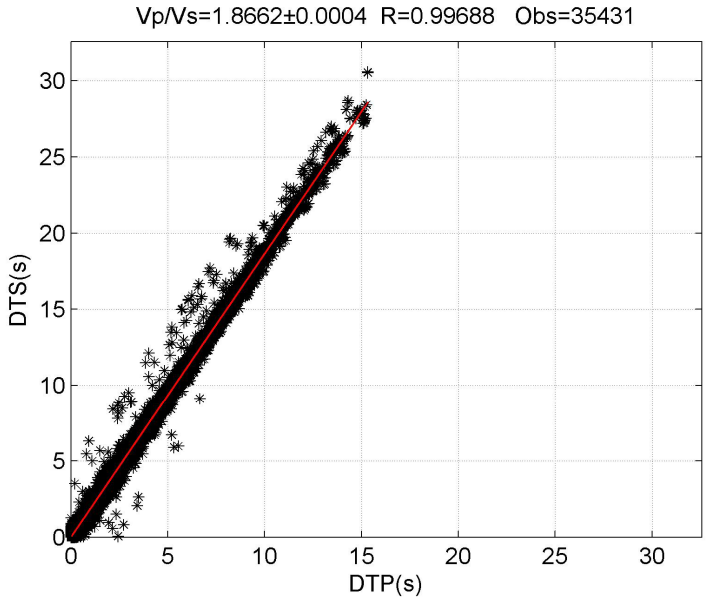

Figure 42. Wadati modified diagram of earthquakes in the study area. DTP: difference time of P phase. DTS: difference time of S phase. R: coefficient of determination. Obs: number of observations.

On the contrary, Wadati classic method (Wadati, 1933) is used to estimate Vp/Vs ratio relative to each earthquake selected in the area (Fig. 43). In this case the difference between the P phase and the origin time (OT) is related to the difference between S and P arrival time. Before the sequence in April 2010 there are only five earthquakes selected from the input parameters. In general these earthquakes show a Vp/Vs ratio less than Vp/Vs average ratio of the area (red line in Fig.43). These information not allows to describe the Vp/Vs trend before the sequence.

The earthquakes selected through the multiplets are used to describe the Vp/Vs ratio during the sequence in April 2010. A multiplet is an earthquakes group with similar waveform. In the area of the sequence in April 2010 there are eleven multiplets (Fig. 44, courtesy of INGV-Ancona) with cross-correlation coefficient ≥ 0.90.

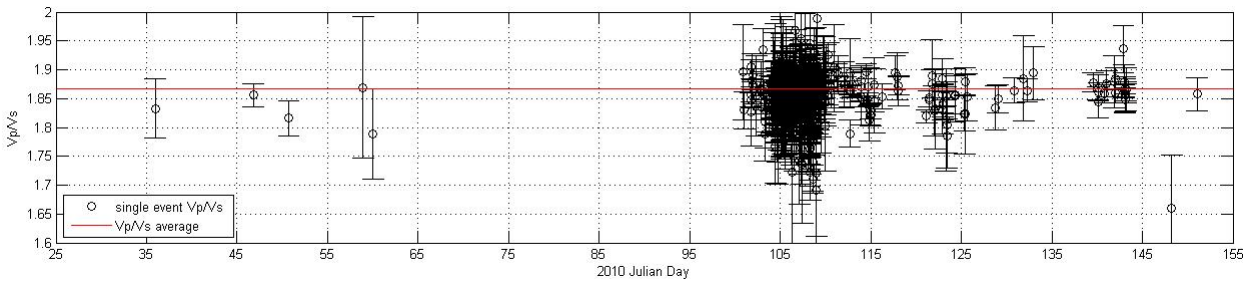

Figure 43. Black circles and error bar: Vp/Vs of single event. Red line: Vp/Vs average ratio. X axis: days of year 2010.

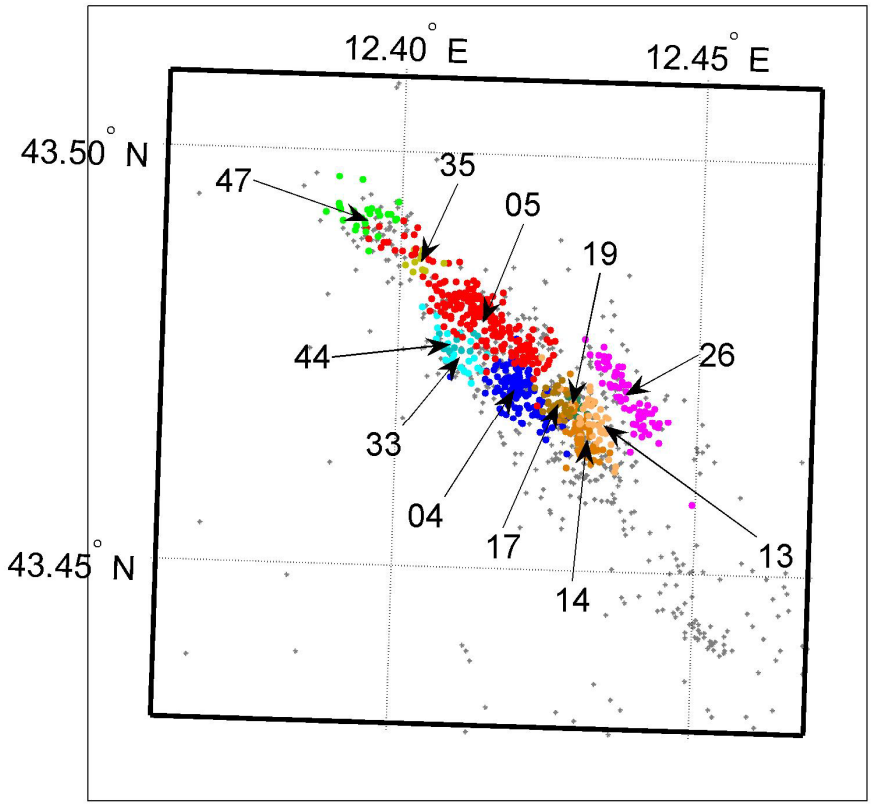

Figure 44. Multiplets of sequence in April 2010. Coloured points: multiples. Grey points: earthquakes of the area. Black number: multiplets identifier. The black arrow indicate the centroide of multiplets (courtesy of INGV- Ancona).

For each multiplet is calculated a Vp/Vs ratio with Wadati modified method. In Fig. 45 an example of Vp/Vs ratio for the multiplet 04. It is calculated with 6293 observations, R is 0.99821 and the Vp/Vs is 1.8637.

The Wadati diagrams of the eleven multiplets are presented in Appendix D.

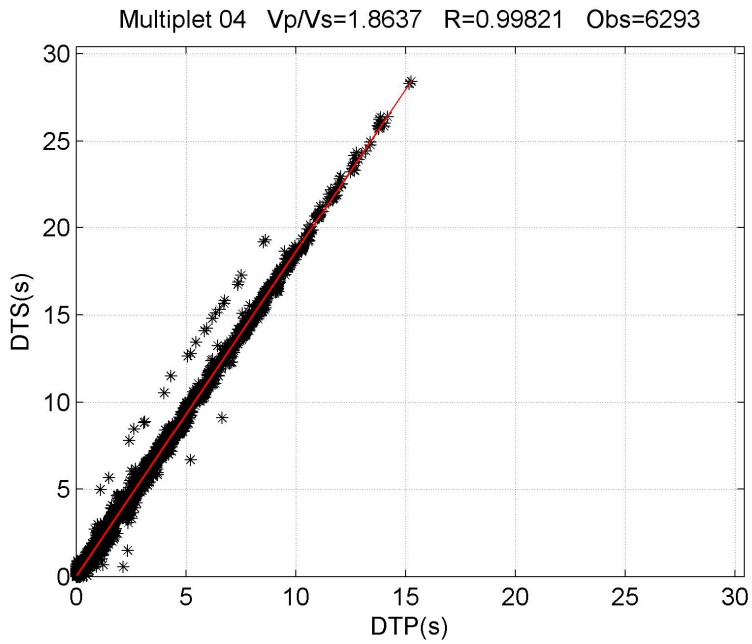

Figure 45. Wadati modified diagram for multiplet 04. DTP: difference time of P phase. DTS: difference time of S phase. R: coefficient of determination . Obs: number of observations.

Also for the mainshock on April 15, 2010, is calculated the Vp/Vs ratio with a Wadati classic method (Wadati, 1933). The result for the mainshock is Vp/Vs = 1.878±0.008 obtained from 42 pairs of P and S arrival time (Fig.46).

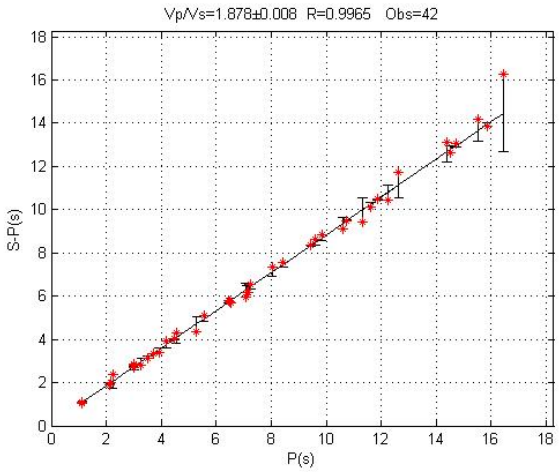

Figure 46. Wadati diagram for the mainshock on 15 April 2010 01:45:36 UTC (Ml 3.8). Red stars: observations. Black vertical bar: residuals. Black line: linear regression. X axis: arrival time of P phase from origin time. Y axis: difference between S and P arrival time.

Fig. 47 and Tab. 2 resume the results of Vp/Vs ratio of multiplets. In Fig. 47 the multiplets are sorted in ascending order according to the chronology of every multiplets. The start time of each multiplets is showed in the Tab.2, 'Start' field. It is not possible to design a clear temporal trend of

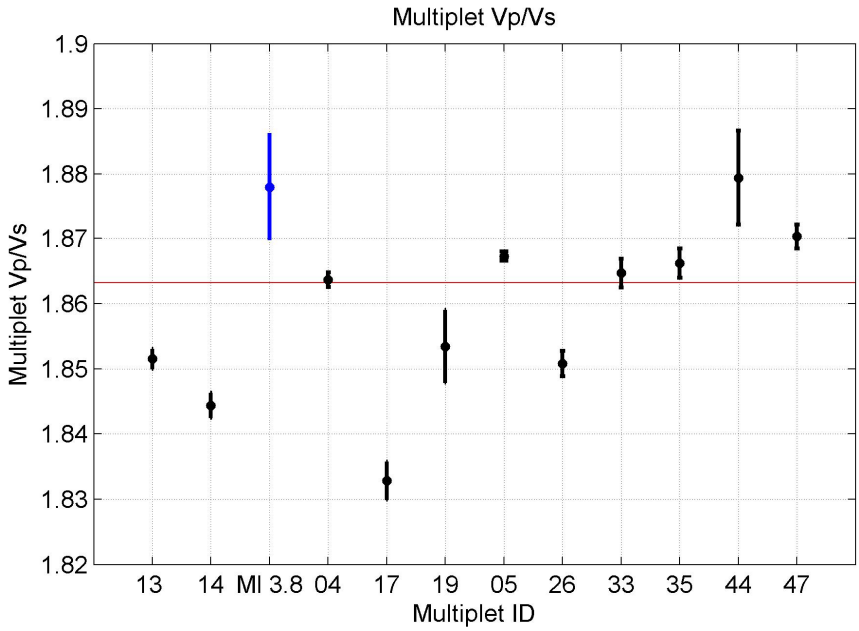

Figure 47. Results of Vp/Vs ratio. Black points and error bar: Vp/Vs of multiplets. Blue point and error bar: mainshock. Red line: Vp/Vs average of the area.

ID	Nev.	START	Vp/Vs	S	R	obs	min Ml	max Ml	depth
13	47	100410212028	1,8515	0,0015	0,9986	1932	0,1	2,1	4,7
14	49	100412081619	1,8444	0,0019	0,9974	2071	0,3	1,9	4,5
04	125	100415015343	1,8637	0,0011	0,9976	6293	0	2,7	4,1
17	36	100415015344	1,8328	0,0029	0,9976	878	0,1	1,8	4,6
19	10	100415024306	1,8534	0,0055	0,9965	297	0,4	1,6	4,6
05	205	100415054540	1,8673	0,0007	0,9984	11069	0	2,9	5,2
26	64	100416045023	1,8508	0,0019	0,9992	727	0	2,1	3,8
33	23	100417134932	1,8647	0,0022	0,9978	1419	0,2	1,7	4,3
35	11	100418191651	1,8662	0,0023	0,9986	856	0,1	0,3	5,5
44	13	100424231352	1,8794	0,0073	0,9967	156	0	1,7	4,2
47	26	100427062716	1,8703	0,0018	0,9996	419	0	2,2	5,1

Table 2. ID: multiplet identifier. Nev: number of events. START: origin time of the first event of the multiplets. Vp/Vs: value of Vp/Vs ratio. S: standard deviation of Vp/Vs. R: correlation coefficient. Obs: number of observed. Min Ml, max Ml: minimal and maximum magnitude of the multiplet. Depth avg: average depth of the multiplets.

Vp/Vs. The multiplets 13 and 14 start and end before the mainshock and they have a Vp/Vs ratio less than Vp/Vs average of the area. The mainshock and the most multiplets that start after it have a Vp/Vs higher than Vp/Vs of the area. The multiplets 17, 19 and 26 don't follow this trend. The multiplets 17 and 19 are located near multiplets 13 and 14, whereas the multiplets 26 is located in the eastern part of the sequence. Then, the results show that the multiplets with the higher Vp/Vs,

are located to the north of the mainshock. The high values of Vp/Vs are often attributed to fluid migration in the crust (Lucente et al., 2011, Chiarabba et al., 2011, Di Luccio et al., 2010).

The seismic stations located in the area of the AVT belong to the RSN of INGV and AVT network. The digital data of these stations are transmitted in real time to acquisition centre of Rome and Ancona, respectively. The seismic data that arrive to Rome are transmitted also to Ancona. The seismic data collected at Ancona are archived in MSEED format (http://www.iris.edu/manuals/SEED_appG.htm). The seismic data of stations in Fig. 39 are analysed with the MWCS technique to obtain velocity variations by cross-correlations of seismic noise. During this analysis the MWCS technique is applied to seismic data of 12 seismic stations. The cross-correlations are calculated for 26 stations pairs. The chose of the parameters for the last part of the analysis reduced the number of stations pairs at 11. The requirements for the cross-correlation calculation are the present of seismic data simultaneously in the stations pair; the cross-correlation coefficient chose at 0.85, under which the data are not considered. These are the two most important parameters that have influenced the choice of stations pairs. The presence of continuous seismic data allows to obtain reliable estimates of velocity variations and their discrete representation in the time without gaps.

The selected 11 stations pairs have different distance, from minimum distance of 6 km up to 35 km (Table 3). The greater distant is ATMI-PARC with 35 km, the nearest stations pair are ATBU-ATPC with 5.9 km (Fig. 48). The stations pairs cover the area with most seismic activity and the layout of their directions include many azimuths. This geometry allows to average the characteristics of seismic noise because the signal that crosses through stations pairs comes from sources distributed in the space. Different azimuths of the stations pairs attenuate the effects of strong directivity in the frequency band of the microseisms (0.1-1 Hz).

The parameters used in this analysis are chosen with tests. ‘Tout’ is the portion of the signal eliminated in the central part of the cross-correlation. It is calculated considering the distance between the stations and divided for a default value of 2.5(km/s, the velocity of the S waves). ‘Tout’ has a value of 10s. To eliminate the possible spikes in the lags of the cross-correlation obtains with the comparison between the current and reference cross-correlation in their coda a parameter ‘Interval’ is used. It has a value of 70s. This involve that in a max lag of 100s of the cross-correlation the last 30 s of the coda are eliminated, in the casual and anticasual part. Then, the value of ‘Wind’ is the length of the any window in which the current and the reference cc are compared. It is value is 8 s, it is shifted of 50%.

The final parameter chosen is the coefficient of cross-correlation, it is set to 0.85; under this parameter the cross-correlations between the current and the reference cross-correlation are not considered and it indicates the similarity of the current and reference cross-correlation.

The results of the velocity variations obtained from the cross-correlation of the seismic noise are showed in Fig.49 and Fig50.

In Fig. 49 the time series of velocities variations started on March 9, 2010. Every point of observation represent the middle point of the stack of the 35 daily cross-correlations.

The velocity variation is described day by day up to 11 July 2010. After the 11 July the most part of the data are excluded by the analysis. Although the temporal gap, the seismic data allow to describe the variation about a month before and three months after the sequence on April 15, 2010 (red area in Fig. 49 and Fig. 50).

The results show a detectable change in the seismic velocity variation trend at the same time of the seismic sequence in April. The change of trend starts on April 10 and the maximum drop from an observation to the next corresponds on April 15, when there is the mainshock (Ml 3.8) and the seismic activity. After this sequence the velocity variations increase again from May 1 until the beginning of July.

As described in Fig. 39 an increase of the seismic activity in the area is found in July month.

With the aim to estimate the velocity variations also in this time interval is performed a reanalysis of velocity variation. A more sever selection of the seismic stations pairs has deleted 5 stations pairs. The principal cause is the absence of the seismic data in the analysed period.

The stations pairs used in this second pair are 2, 3, 4, 5,6 and 8 (Table 3, ‘Pair ID’). The results of the reanalysis are show in Fig. 50.

In correspondence to the seismic sequence in April the velocity variations calculated with 6 pair confirmed the variation seen in the previous case. In Fig. 50 the time series is reconstructed also for the period from July to September. In this time interval it is possible to point out two remarkable oscillations of the velocity variations. The period of increasing seismic activity in July 2010 (green circles, Fig. 40 and Fig.41) falls between the two oscillations (green area in Fig. 50). Therefore, the increase of the seismic activity is not related to any velocity variations. On the contrary, it is not possible to understand and explain the velocity variations peaks corresponding to the low seismic activity (Fig.40).

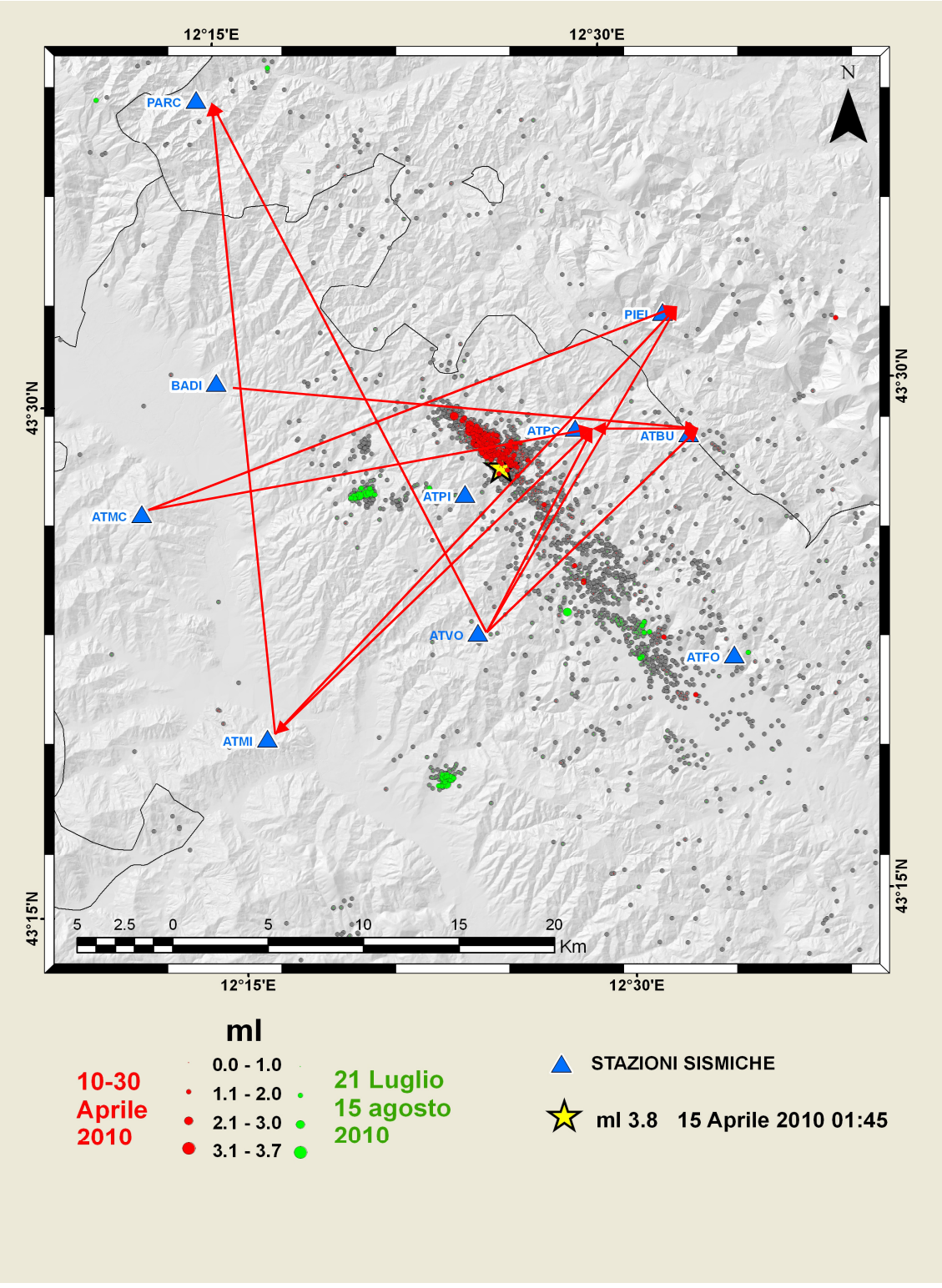

Figure 48. Localization of 11 stations pairs selected in the study. Blue triangles: seismic stations. Red circles: sequence in April 2010, green circles: seismic activity in July 2010. Yellow star: event on April 15, 2010 (Ml 3.8).

Pair ID	SP	Distance (Km)
1	ATMI-PARC	35
2	ATMI-PIEI	31
3	ATPC-ATMI	23.3
4	ATVO-ATPC	12.2
5	ATVO-PIEI	19.9
6	ATVO-ATBU	15.48
7	ATVO-PARC	32.5
8	BADI-ATBU	24.8
9	ATMC-ATPC	23.15
10	ATMC-PIEI	29.3
11	ATBU-ATPC	5.9

Table 3. Distance between pairs of stations. Pair ID: identifier of stations pairs. SP: stations pairs. Distance: distance between stations in km.

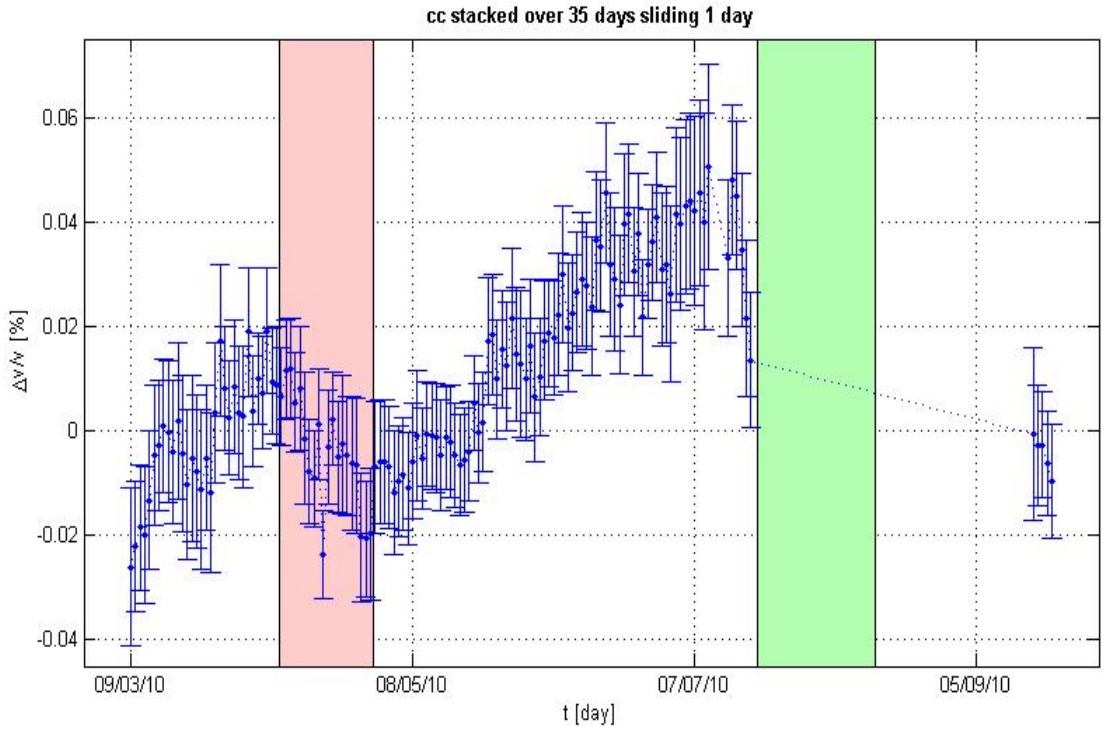

Figure 49. Velocities variation calculated with 11 stations. Red bar: sequence in April 2010, green bar: seismic activity in July 2010. Blue line: velocities variation. In correspondence to the seismic sequence on April the velocity variation shows a stronger variation, a detectable reduction of seismic velocities. During the second sequence it is not possible to understand the velocities trend for the absence of seismic data.

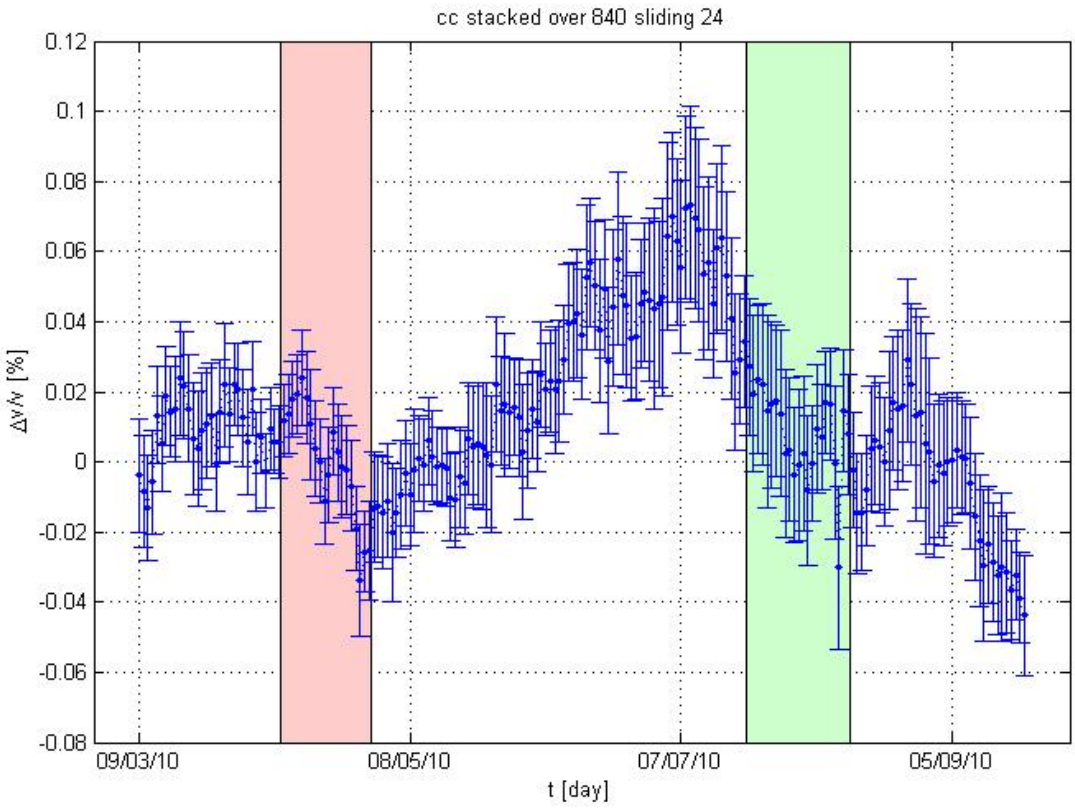

Figure 50. Velocities variation. Red bar indicates the sequence on April 2010, the green bar indicates the sequence on July 2010. Blue line show velocities variation during the period. In correspondence to the seismic sequence on April the velocity variation confirmed that is seen also in the previous case, then a detectable reduction of seismic velocities is present in correspondence of the second sequence.

The MWCS was used in literature applied to seismic data to monitoring velocity variations around great earthquakes (Poupinet et al., 1984; Brenguier et al., 2008, Chen et al., 2010; Zaccarelli et al., 2011). The authors of these study cases indicate that different physical mechanism may be responsible for the variations in the properties of crust. Brenguier et al. (2008) argue that the possible mechanisms are: the strong ground shaking damage the shallow layers and variations of co-seismic stress is followed by the post seismic relaxation.

Poupinet et al. (1984) connect the change of velocity to decrease in stress of the crust or seasonal variation in the ground water conditions.

Zaccarelli et al.(2011) declare that the co-seismic velocity reduction can be attributed to increasing crack and void densities and/or to reduced compaction of the granular material in the shallow crust; moreover, the presence of fluid in the crust can contributed to change the seismic properties.

The co-seismic velocity drop for the 2009 L'Aquila earthquake (Mw 6.1) is about 0.3% (Zaccarelli et al., 2011). This value is significantly larger than the value (about 0.08%) measured in Brenguier et al. (2008) and Chen et al. (2010) during M_w 6.0 Parkfield and the M_w 7.9 Wenchuan earthquake,

respectively. These different values suggest that factors such as local geological condition, focal mechanism and source depth may control the co-seismic velocity variation that is not a simple function of the total moment release (Zaccarelli et al., 2011).
A dense seismic network may be sensitive to the process occurring in the near field of the fault where the velocity perturbations are expected to be important. Change velocity of the order of 0.01% should be monitored with an accurate digital recording system (Poupinet et al., 1984).
In the case of the sequence of the AVT, the MWCS technique was applied to seismic data during an intense seismic activity which the magnitude range that don't exceed Ml 3.8.
The most relevant result is to characterize the velocity variation with the small drop of 0.02% during the sequence in April 2010. The short distances of several seismic stations have allowed to obtain this result. Unfortunately, it is not possible to infer a mechanism to explain the velocity variation in April 2010 and the long two oscillations in the year. The most oscillation has an amplitude of 0.08%; it is more higher of those reported in Brenguier et al. (2008, Fig.3).

In the end, an analysis of the microseismic sources with the aim to exclude the influence of these sources on the estimate of the velocity variations is performed.
The continuous data of seismic station PIEI (Fig.1) are used to assess the spectral characteristics in the frequency band between 0.1 and 0.9 Hz. The Power Spectral Densities (PSD) are calculated with 5 moving windows with length of 300 s and overlap of 50%. The seismic data are processed to obtain PSD as in Marzorati and Bindi (2006), but with a KO smoothing (Konno-Omachi, 1998). The maximum value of each PSD is calculated in two frequency bands: 0.1-0.25 Hz and 0.25-0.9 Hz. Also the frequency corresponding to the two maxima are collected. In general, Marzorati and Bindi (2006) indicate these two frequency bands with the Atlantic and Mediterranean microseisms, respectively.
In Fig. 51 are represented the maxima of the PSD (top panel) and their frequency (bottom panel). The blue series corresponds to the frequency band 0.1-0.25 Hz and the red series corresponds to the frequency band 0.25-0.9Hz. The two data series have a typical annual trend with maxima values in winter and minima in summer (Fig. 51 top panel). The peaks of the series are very frequently and a peak represent a single microseismic event. The differences between the two series is more appreciate in the bottom panel of Fig. 51, where frequencies of PSD maxima have different trend. The red area in Fig. 51 indicates the seismic sequence in April 2010; in this time interval there are not anomalous events.
Fig. 52 is a portion of microseismic time-series from day 90 to day 120 of year 2010. The days between 90 and 100 are the time interval before the sequence. The sequence starts the day 100. in

Fig. 52 are evident five microseismics events. The amplitude and the frequency of these events are similar to the others events in the year and their arrival-time are not correlated with the seismic sequence. In the frequency band 0.25-0.9 Hz the frequency variation is sudden. Likely, this feature is due to Mediterranean microseismics that are nearest to seismic stations and shortest respect to Atlantic microseismics (Marzorati and Bindi, 2006; Marzorati and Bindi, 2008). This hypothesis is confirmed by comparison between seismic spectral data in Fig. 53 and atmospheric-pressure maps and the sea level map in Appendix D and E. The sea level maps in Appendix E don't show strong phenomena on 4 April 2010. The 5 April 2010, 03:00 UTC the forecast sea level map shows the high level of sea wave near and in direction of Sardegna and Corsica coasts. This sea event can be retained the source of microseism in day 95 of Fig. 53. The seismic data, in Fig. 53, represent high amplitude in the frequency band 0.25-0.45 Hz and a migration of frequency from high to low values of about 12 hours. The high frequency microseim ends in the day 95 (Fig. 53). The next day the seismic data show high amplitude in the frequency band 0.1-0.2 Hz and the slow frequency migration from low to high values. The microseismi of day 96 corresponds to the atmospheric pressure map on 6 April 2010 in Appendix D. This pressure map shows the strong and focus pressure area in front of Scotland coast; the low pressure area is generated in the middle of Atlantic Ocean on 5 April 2010. The sea waves dash against the Scotland coast and their reflection caused probably the microseism at lower frequency on 96 day (Fig.53).

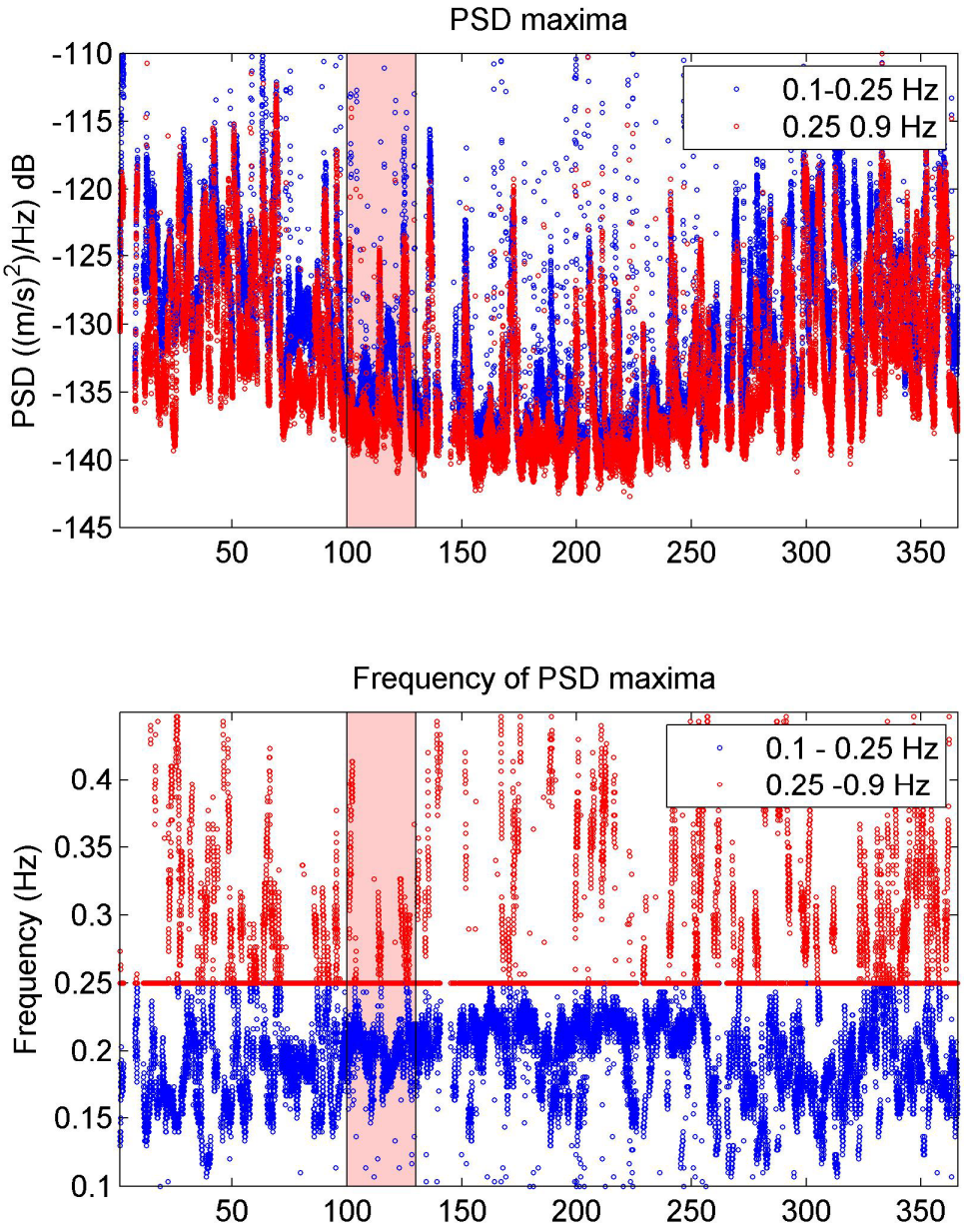

Figure 51. Microseismis recorded at PIEI stations in 2010. Top panel: PSD maxima at PIEI. Bottom panel: frequency of PSD maxima. Blue circles: values of frequency band 0.1-0.25 Hz. Red circles: values of frequency band 0.25-0.9 Hz. Red area: time interval on April 2010.

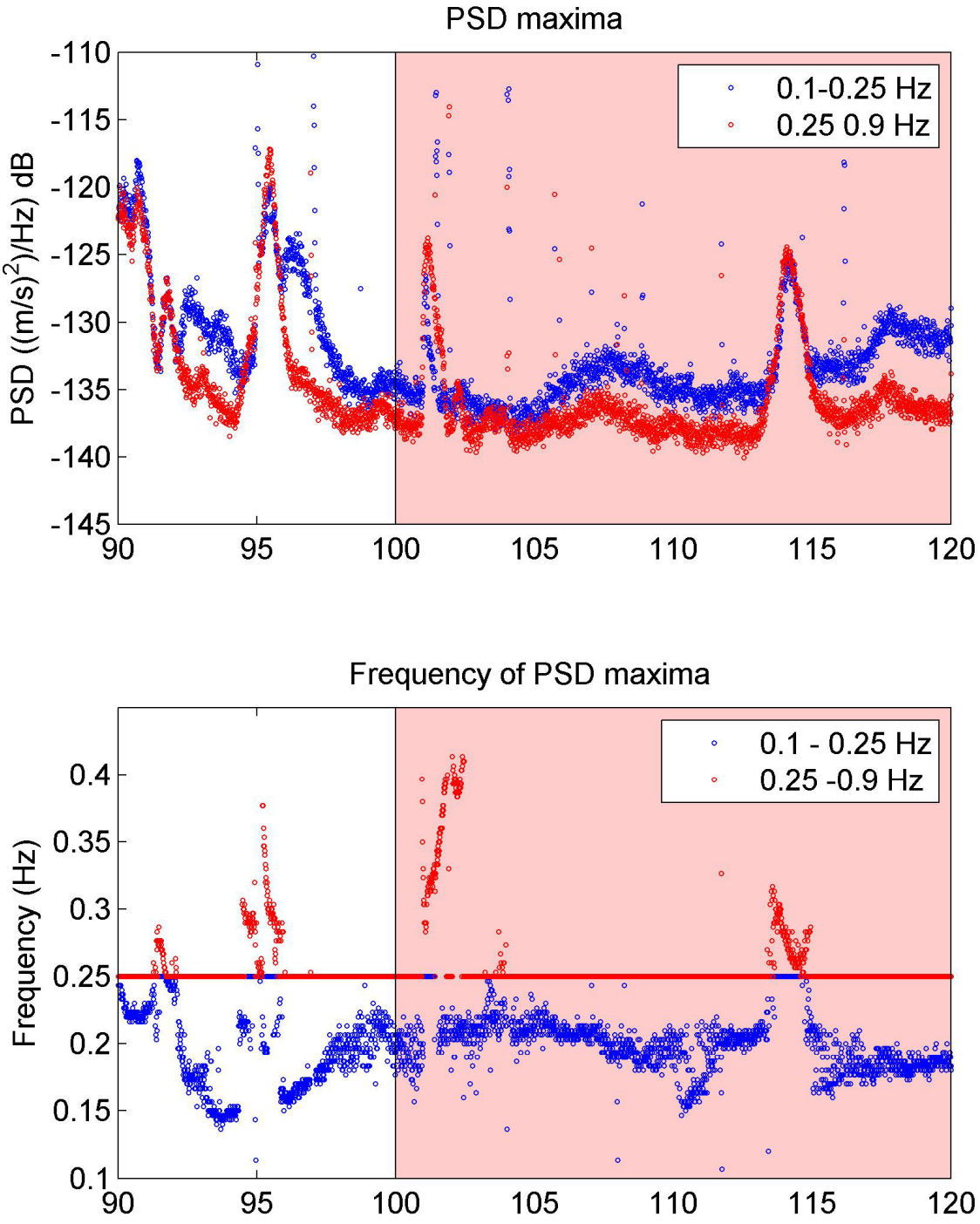

Figure 52. Microseismis recorded at PIEI stations from day 90 to 120 of year 2010. Top panel: PSD maxima at PIEI. Bottom panel: frequency of PSD maxima. Blue circles: values of frequency band 0.1-0.25 Hz. Red circles: values of frequency band 0.25-0.9 Hz. Red area: time interval on April 2010.

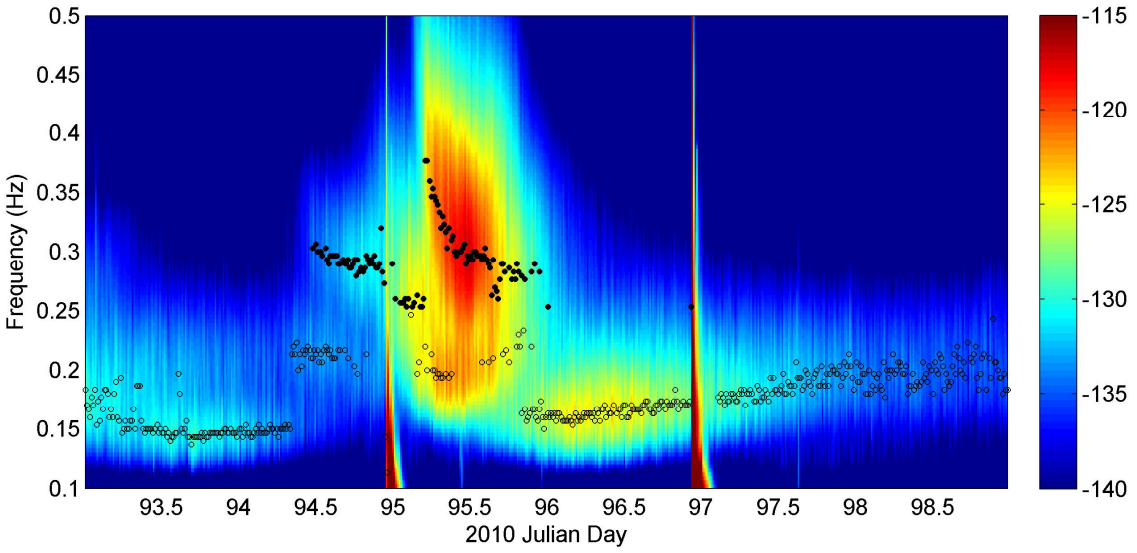

Figure 53. PSD of PIEI station, vertical component. Color bar is in db unit ((m/s)^2/Hz). Filled black circles: PSD maxima in the frequency band 0-25-0.9 Hz. Empty black circles: PSD maxima in the frequency band 0.1-0.25 Hz.

References

. Aki, K., B. Chouet, Origin of coda waves: source, attenuation and scattering effects, J. Geophys. Res. 80, 3322 (1975).

. Amato, A., and F. Mele (2008), Performance of the INGV National Seismic Network from 1997 to 2007, Ann. Geophys., 51, 417–431.

. Bagnaia R., D'Epifanio A. & Sylos Labini S. (1992) – Aquila and subequan Basins: an example of Quaternari evolution in Central Apennines, Italy. Quarter. Nova, 1: 1-23.

. Barchi, M., R. Minelli, and G. Pialli ,1998, The crop 03 profile: A synthesis of results on deep structures of the northern Apennines, Mem. Soc. Geol. Ital., 52, 383– 400.

. Bard, P-Y., 1999, Microtremor measurements: a tool for site effect estimation?, in The Effects of Surface Geology on seismic Motion, K. Irikura, K. kudo, H. Okada and T. Sasatani (Editors), Balkema, Rotterdam, 1251-1279.

. Beaudoin, B. C, G. S. Fuis, W. D. Mooney, W. Nokleberg, and N. I. Christensen, 1992, Thin, low-velocity crust beneath the southern Yukon Tanana terrane, east central Alaska: Results from Trans-Alaska Crustal Transect refraction/wide-angle reflection data, J. Geophys. Res., 97, 1921– 1942.

. Beneo E. (1942) – Foglio geologico 146 "Sulmona", Carta Geologica d'Italia (scala 1:100.000). R. Uff.Geol.it.Roma.

. Bensen, G. D., M. H. Ritzwoller, M. P. Barmin, A. L. Levshin, F. Lin, M. P. Moschetti, N. M. Shapiro, Y. Yang, Processing seismic ambient noise data to obtain reliable broad-band surface wave dispersion measurements, *Geophys. J. Int.* (2007) 169, 1239–1260 doi: 10.1111/j.1365-246X.2007.03374.x

. Bindi D., S. Parolai, F. Cara, G. Di Giulio, G. Ferretti, L. Luzi, G. Monachesi, F. Pacor, and A. Rovelli (2009). Site Amplifications Observed in the Gubbio Basin, Central Italy: Hints for Lateral Propagation Effects, Bull. Seism. Soc. Am., 99, 741 - 760.

. Boncio, P., F. Brozzetti, and G. Lavecchia, 2000, Architecture and seismotectonics of a regional low-angle normal fault zone in central Italy, Tectonics, 19, 1038– 1055.

. Boore D.M. and Bommer J.J. (2005). Processing of strong-motion accelerograms: needs, options and consequences. Soil Dyn. Earthq. Eng. 25, 93–115.

. Borcherdt RD (1970) Effects of local geology on ground motion near San Francisco Bay. Bull Seismol Soc Am 60:29–61

. Boschi, E., G. Ferrari, P. gasperini, E. Guidoboni, G. Smriglio and G. Valensise, 1995. Catalogo dei forti terremoti in Italia dal 461 a. C. al 1980, ING-SGA, Bologna.

. Bosi, C., Bertini T., 1970, Geologia della media valle dell'Aterno, Mem. Soc. Geol. It. 9, 719-777

. Brenguier, F., N. M. Shapiro, M. Campillo, A. Nercessian, and V. Ferrazzini (2007), 3-D surface wave tomography of the Piton de la Fournaise volcano using seismic noise correlations, Geophys. Res. Lett., 34, L02305, doi:10.1029/2006GL028586.

. Brenguier, F., Campillo M., Hadziioannou C., Shapiro N. M., Nadeau R. M., Larose E., 2008a, Postseismic relaxation along the San Andreas fault at Parkfield from continuous seismological observations, Science 321, 1478, doi:10.1126/science.1160943

. Brenguier, F., N. M. Shapiro, M. Campillo, V. Ferrazzini, Z. Duputel, O. Coutant, and A. Nercessian (2008b), Towards forecasting volcanic eruptions using seismic noise, Nat. Geosci., 1, 126–130.

. Buech F., Davies T. R. and Pettina J. R. (2010). The Little Red Hill Seismic Experimental Study: Topographic Effects on Ground Motion at a Bedrock-Dominated Mountain Edifice, Bull. Seism. Soc. Am., 100, no. 5Am., p. 2219-2229.

. Campillo, M., 2006, Phase and correlation in 'random' seismic fields and the reconstruction of the Green Function, Pure Appl. Geophys. 163, 475-502

. Campillo, M., Paul A., 2003, Long-Range correlations in the diffuse seismic coda, Science 299, 547, doi:10.1126/science.1078551

. Cattaneo, M., P. Augliera, G. De Luca, A. Gorini, A. Covoni, S. Marcaci, A. Nichelini, G. Monachesi, D. Spallarossa, L. Troiani and Xgumus, 2000. The Umbria-Marche (Italy)earthquake sequence: analysis of the data recorded by the local and temporary networks, J. Seism. 4, 401-414.

. Cattaneo, M., D'Alema, E., Frapiccini, M., Marzorati, S. e Monachesi, G., (2011). Sistemi di alimentazione della rete Alto Alta Val Tiberina. In: "Monitoraggio sismico del territorio nazionale: stato dell'arte e sviluppo delle reti di monitoraggio sismico", a cura di M. Cattaneo e M. Moretti, Miscellanea INGV, N° 10, 91-93.

. Celebi M. (1987), Topographical and geological amplifications determined from strong motion and aftershock records of the 3 March 1985 Chile earthquake, Bull. Seism. Soc. Am., 77, 4, 1147-1167.

. Chatalain. J. L.,(1978), Etude fine the la sismicite en zone de collision continental à l'aide d'un réseau de stations portables: La region Hindu-Kush-Pamir, Thèse de 3 éme cicle, Univ. De Grenoble, Grenoble, France

. Chàvez-Garcia, F. J. and Rodriguez M., 2007, The correlation of microtremors: empirical limits and relations between results in frequency and time domains, *Geophys. J. Int.* (2007) 171, 657–664 doi: 10.1111/j.1365-246X.2007.03529.x

. Chiarabba, C., De Gori P., Boschi E., 2011, Pore-pressure migration along a normal-fault system resolved by time-repeted seismic tomography, Geology , 37, no. 1, p. 67-70

. Chiaraluce, L., W. L. Ellsworth, C. Chiarabba and M. Cocco, 2003. imaging the complexity of an active normal fault system: the 1997 Colfiorito (central Italy) case study, J. Geophys. Res., 108 (B6), 2294

. Chiaraluce, L., Amato A., Cocco M., Chiarabba C., Selvaggi G., Di Bona M., Piccinini D., Deschamps A., Margheriti L., Courboulex F. and Ripete M.. ,2004, Complex normal faulting in the Apennines Thrust and fold belt: The 1997–1998 seismic sequence in central Italy, Bull. Seismol. Soc. Am., 94(1), 99– 116.

. Chiaraluce, L., Chiarabba C., Collettini C., Piccinini D. and Cocco M ,2007, Architecture and mechanics of an active low-angle normal fault: Alto Tiberina Fault, northern Apennines, Italy, J. Geophys. Res., 112, B10310, doi:10.1029/2007JB005015

. Chiodini, G., C. Cardellini, A. Amato, E. Boschi, S. Caliro, F. Frondini, and G. Ventura, 2004, Carbon dioxide Earth degassing and seismogenesis in central and southern Italy, Geophys. Res. Lett., 31, L07615, doi:10.1029/2004GL019480.

. Cho, K. H., Herrmann R. B., Ammon C. J., Lee K., 2007, Imaging the upper crust of the Korean Peninsula by Surface-Wave Tomography, BSSA, 97, pp. 198-207, doi: 10.1785/0120060096

. Ciaccio, M., M. Barchi, C. Chiarabba, F. Mirabella, and E. Stucchi, 2005, Seismological, geological and geophysical constraints for the Gualdo Tadino fault, Umbria-Marche Apennines (central Italy), Tectonophysics, 406, 233 – 247.

. Clarke, D., L. Zaccarelli, N. M. Shapiro, and F. Brenguier, 2011, Assessment of resolution and accuracy of the Moving Window Cross Spectral technique for monitoring crustal temporal variations using ambient seismic noise, Geophys. J. Int., 186, 867–882, doi:10.1111/j.1365-246X. 2011.05074.x.

. Collettini, C., Barchi, M., 2002. A low-angle normal fault in the Umbria region (Central Italy): a mechanical model for the related microseismicity. Tectonophysics 359 (1–2), 97–115.

. Converse A.M. and Brady A.G. (1992). BAP—basic strong-motion accelerogram processing software; Version 1.0. United States Geological Survey Open-File Report, p. 174, 92–296A.

. Cooley, J. W. and Tukey J.W., 1965, An algorithm for machine calculation of complex Fourier series, Math. Comp., 19, 297-301

. Cultrera G. and Luzi L. (Co-Authors: Ameri G., Augliera P., Azzara R.M., Bergamaschi F., Bertrand E., Bordoni P., Cara F., Cogliano R., D'Alema E., Di Giacomo D., Di Giulio G., Duval A.-M., Fodarella A., Franceschina G., Gallipoli M.R., Harabaglia P., Ladina C., Lovati S., Marzorati S., Massa M., Milana G., Mucciarelli M., Pacor F., Parolai S., Picozzi M., Pilz M., Puglia R., Pucillo S., Régnier J., Riccio G., Salichon J., Sobiesiak M.,2009, Valutazione della risposta sismica locale di alcuni siti dell'alta e media valle dell'Aterno, *Progettazione sismica*, ISSN1973-7432, Capitolo1, Azione sismica ed effetti di sito. http://www.progettazionesismica.it/

. D'Alema, E., Cattaneo, M., Frapiccini, M., Marzorati, S., Monachesi, G. e Ferretti, M., (2011). Rete Sismometrica Marchigiana e sua integrazione con la RSN e Rete AVT. In: "Monitoraggio sismico del territorio nazionale: stato dell'arte e sviluppo delle reti di monitoraggio sismico", a cura di M. Cattaneo e M. Moretti, Miscellanea INGV, N° 10, 19-21.

. D'Amico, V., M. Picozzi, D. Albarello, G. Naso and T. Tropenscovino, 2004, Quick estimates of soft sediment thickness from ambient noise horizontal to vertical spectrla ratios: a case study in southern Italy, J. Earthq. Eng., 8, 895-908

. D'Amico, V., M. Picozzi, F. Baliva and D. Albarello, 2008, Ambient Noise Measurements for preliminary Site-effects characterization in the Urban Area of Florence, Italy, BSSA, vol. 98, n.3, 1373-1388

. Davis L. L. and West L. R. (1973). Observed effects of topography on ground motion. Bulletin of the Seismological Society of America, 63, 283-298.

. De Luca, G., M. Cattaneo, G. Monachesi, A. Amato, Seismicity in Central and Northern Apennines integratine the Italian national and regional networks, Tectonophysics, 2009, doi: 10.1016/j.tecto.2008.11.032

. Delladio A., 2011, Riassunti estesi del 1° workshop tecnico , Miscellanea INGV, numero 10 ISSN 2039-6651

. Deschamps, A., D. Iannaccone, and R. Scarpa, The Umbrian earthquake (Italy) of 19 September 1979, Ann. Geophys., 2, 29– 36, 1984.

. Di Luccio, F., G. Ventura, R. Di Giovambattista, A. Piscini, and F. R. Cinti (2010), Normal faults and thrusts reactivated by deep fluids: The 6 April 2009 M_w 6.3 L'Aquila earthquake, central Italy, *J. Geophys. Res.*, 115, B06315, doi:10.1029/2009JB007190.

. Donati S., Marra F. and Rovelli A. (2001), Damage and ground shaking in the town of Nocera Umbra during Umbria-Marche, central Italy, earthquakes: the special effect of a fault zone. Bull. Seism. Soc. Am.,91, 511-519.

. Duvall, T. L., S. M. Jefferies, J. W. Harvey and M. A. Pomerantz, 1993, Time distance helioseismology, Nature, 362, 430-432

. Faccioli E. (1986), Elementi per una guida alle indagini di Microzonazione Sismica-Progetto Finalizzato "Geodinamica" monografie finali Vol.7, Consiglio Nazionale delle ricerche Quaderni de "La ricerca scientifica", Roma. 72-82 (in Italian)

. Fäh, D., F. Kind,. and D. Giardini (2001). A theoretical investigation of average H/V ratios, Geophys. J. Int. 145, 535-549.

. Falcucci, E., Gori, S., Moro, M., Galadini, F., Marzorati, S., Ladina, C., Piccarreda, D., Fredi, P., (2009). Evidenze di fagliazione normale tardo-olocenica nel settore compreso fra la conca Subequana e la Media Valle dell'Aterno, a sud dell'area epicentrale del terremoto di L'Aquila del 6 Aprile 2009. Implicazioni sismotettoniche. Presentazione: XXVIII Convegno Nazionale GNGTS, 16-19 Novembre 2009, Trieste.

. Falcucci, E., 2011, Evoluzione geomorfologica e geologica del Quaternario della conca Subequana e della media valle dell'Aterno, Appennino Abruzzese, Tesi di Dottorato, ciclo XXIII.

. Ferretti G., Massa M., Isella L. e Eva C. (2007). Site amplification effects based on teleseismic wave analysis: the case of Pellice Valley (Piedmont, Italy), Bull. Seism. Soc. Am., 97, 605-613.

. Field EH, Jacob KH (1995) A comparison and test of various site-response estimation techniques, including three that are not reference-site dependen. Bull Seism Soc Am 85:1127–1143

. Fiorini,E., F. Pacor, D. Bindi, A. Rovelli, F. Cara, G. Di Giulio, G. Milana, G. Monachesi, D. Nieto, G. Bohm, D. Albarello, V. D'Amico, M. Picozzi, M. Mucciarelli, G. Scarascia Mugnozzq, S. Rivellino, Università di Urbino – M. Menichetti, GFZ- Potsdam- S. Parolai, S. Richwalski, I. Orpsal, 2007 Progetto S3 – Scenari di scuotimento in aree di interesse prioritario e/o Strategico TASK 6 – GUBBIO - DELIVERABLE D21

. Fletcher J. B., J. Boatwright, A.G. Lindh (2003). Wave Propagation and Site Response in the Santa Clara Valley, Bull. Seism. Soc. Am., 93, 1, 480–500.

. Frémont, M.-J and S. Malone, High precision relative locations of earthquakes at Mount St Helens, J. Geophys. Res., 92, 10223-10236, 1987

. Froment, B., M. Campillo, P. Roux, P. Gouedard, A. Verdel, and R.L. Weaver (2010), Estimation of the effect of nonisotropically distributed energy on the apparent arrival time in correlations, Geophysics, 75, SA85–SA93.

. Gouédard, P., L. Stehly, F. Brenguier, M. Campillo, Y. Colin de Verdière, E. Larose, L. Margerin, P. Roux, F. J. Sánchez-Sesma, N. M. Shapiro, and R. L. Weaver, 2008, Crosscorrelation of random fields: mathematical approach and applications: Geophysical Prospecting, 56, 375-393.

. Gruppo di Lavoro MS–AQ (2010) Microzonazione sismica per la ricostruzione dell'area aquilana. Regione Abruzzo – Dipartimento della Protezione Civile, L'Aquila, 3 vol. e Cd-rom.

. Guo, Z., X. Gao, H. Yao, J. Li, andW. Wang (2009), Midcrustal low-velocity layer beneath the central Himalaya and southern Tibet revealed by ambient noise array tomography, Geochem. Geophys. Geosyst., 10, Q05007, doi:10.1029/2009GC002458.

. Haessler, H., Gaulon, R., Rivera, L., Console, R., Frogneux, M., Gasparini, G., Martel, L., Patau, G., Siciliano, M., Cisternas, A., 1988. The Perugia (Italy) earthquake of 29 april 1984: a microearthquake survey. Boll. Soc. Geol. Am. 78 (6), 1948–1964.

. Holcomb, L.G., 1998. Spectral structure in the Earth's microseismic background between 20 and 40 s, *Bull. seism. Soc. Am.,* 88, 744–757.

. Koller MG, Chatelin JL, Guillier B, Duval AM, Atakan K, Lacave C, Bard PY (2004) the SESAME participants. Practical user guideline and software for the implementation of the H/V ratio technique on ambient vibrations: measuring conditions, processing method and results interpretation. In: Proceedings of the 13th orldn conference on earthquake engineering, 13WCEE, Vancouver, BC, Canada, August 1–6, 2004, Paper no. 3132

. Ibs-von Seht, M., and J. Wohlenberg (1999). Microtremor measurements used to map thickness of soft sediments, *Bull. Seism. Soc. Am*. 89, 250-259.

. Idriss I. M. and Seed H. B. (1967). Response of earth banks during earthquakes. Journal of the Soil Mechanics and Foundations Division, ASCE, 93 (SM 3), 61-82.

. Lachet, C., and P.-Y. Bard (1994). Numerical and theoretical investigations on the possibilities and limitations of Nakamura's technique, J. Phys. Earth 42, 377-397.

. Larose, E., A. Derode, M. Campillo, and M. Fink (2004), Imaging from one-bit correlations of wideband diffuse wavefields, J. Appl. Phys., 95, 8393–8399.

. Levret A, Loup C, Goula X. (1986). The Provence earthquake of June 11th, 1909 (France). New assessment of near-field effects. Proceedings of the VIII European Conference on Earthquake Engineering, Vol. 2, Lisbon, 4.2.79.

. Lin,F. C., M. P. Moschetti, M. H. Ritzwoller, 2008, Surface wave tomography of the western United States from ambient seismic noise: Rayleigh and Love wave phase velocity maps, Geophys. J. Int. (2008) 173, 281–298 doi: 10.1111/j.1365-246X.2008.03720.x.

. Li, H., Bernardi F., Michelini A., 2010, Surface wave dispersion measurements from ambient seismic noise analysis in Italy, Geophysical Journal International, doi:10.1111/j.1365-246X.2009.04476.x.

. Lermo J, Chavez-Garcia FJ (1993) Are microtremors useful in site response evaluation?. Bull Seismol Soc Am 84:1350–1364

. Levshin, A. L., T. B. Yanocskaya, A. V. Lander, B. G. Bukchin, M. P. Barmin, L. I. Ratnikova, and E. N. Its, 1989, Seismic Surface Waves in a Laterally Inhomogeneous Earth, edited by V. I. Keilis-Borok, Kluwer Acad., Norwell, Mass.

. Lobkis, O. I., Weaver R. L., 2001, On the emergence of the Green's function in the correlations of a diffuse field, J. Acoust. Soc. Am., 110, doi: 10.1121/1.1417528.

. Lovati. S., 2011, Groung motion amplification induced by topographic irregularities: results, open issues and future developments, Tesi di Dottorato, ciclo XXIII.

. Lucente, F. P., P. De Gori, L. Margheriti, D. Piccinini, M. Di Bona , C. Chiarabba, N. Piana Agostinetti (2010) Temporal variation of seismic velocity and anisotropy before the 2009 MW 6.3 L'Aquila earthquake, Italy , Geology, 38, 1015-1018.

. Malcolm, A. E., J. A. Scales, and B. A. van der Tiggelen (2004), Retrieving the Green function from diffuse equipartitioned waves, Phys. Rev. E, 70, doi:10.1103/PhysRevE.70.015601.

. Margerin, M., M. Campillo, N. M. Shapiro, B. van Tiggelen, The time of residence of diffuse waves in the crust and the physical interpretation of coda Q. Application to seismograms recorded in Mexico, Geophys. J. Int. 138, 343 (1999).

. Marra F., R. Azzara, F. Bellucci, A. Caserta, G. Cultrera, B. Mele, B. Palombo, A. Rovelli and E. Boschi (2000), Large amplification of ground motion at rock sites within a fault zone in Nocera Umbra (central Italy), Journal of Seism., 4, 543-554.

. Marsan P., Milana G., Pugliese A. and Sano' T. (2000), Local amplification effects recorded by a local strong motion network during the 1997 Umbria-Marche Earthquake, Proc. 12th World Conference on Earthquake Engineering, Aukland New Zealand, Paper No. 1046.

. Marzorati, S. and Bindi, D., (2006). Ambient noise levels in north central Italy. Geochem. Geophys. Geosyst., 7, Q09010, doi:10.1029/2006GC001256.

. Marzorati, S. and Bindi D., (2008), Characteristics of Ambient Noise Cross Correlations in Northern Italy within the Frequency Range of 0.1–0.6 Hz Bulletin of the Seismological Society of America June 2008 v. 98 no. 3 p. 1389-1398

. Marzorati, S., Ladina C., Falcucci E., Gori S., Saroli M., Ameri G., Galadini F., 2011, Site Effects "On the Rock": the case study of Castelvecchio Subequo (L'Aquila, Central Italy), Bulletin of Earthquake Engineering, Vol.9, N.3, 841-868, DOI:10.1007/s10518-011- 9263-5

. Marzorati. S., C. Ladina, D. Piccarreda, G. Ameri, 2010, Campagna di misure sismiche nella conca subequana, Rapporti Tecnici INGV, Num. 156

. Massa M., Ferretti G., Cevasco A., Isella L. e Eva C. (2004). Analysis of site amplification phenomena: an application in Ripabottoni for the 2002 Molise, Italy, earthquake, Earthquake Spectra, 20, issue S1, 107-118.

. Mazza, S., M. Olivieri, A Mandiello, and P. Casale (2008), The Mediterranean Broad Band Seismographic Network Anno 2005/06, in Earthquake Monitoring and Seismic Hazard Mitigation in Balkan Countries, NATO Sci. Ser., vol. 81, pp. 133–149, Springer, Dordrecht, Netherlands, doi:10.1007/978-1-4020-6815.

. McNamara, D. E. and Buland, R. P., (2004). Ambient noise levels in the continental United States. Bull. Seismol. Soc. Am., 94(4), 1517–1527.

. Meier, U., N. M. Shapiro, and F. Brenguier (2010), Detecting seasonal variations in seismic velocities within Los Angeles basin from correlations of ambient seismic noise, Geophys. J. Int., 181, 985–996, doi:10.1111/j.1365-246X.2010.04550.x.

. Mirabella, F., M. Barchi, A. Lupattelli, E. Stucchi, and M. G. Ciaccio, 2008, Insights on the seismogenic layer thickness from the upper crust structure of the Umbria-Marche Apennines (central Italy), Tectonics, 27, TC1010, doi:10.1029/2007TC002134.

. Monachesi G., Cattaneo M., 2010. La dorsale radio Wi-Fi per il monitoraggio multiparametrico in Alta Val Tiberina. Rapporti Tecnici INGV N°129.

. Monachesi, G., Cattaneo, M., D'Alema, E., , Frapiccini, M., Marzorati, S., Ferretti, M., (2011). Sistemi di controllo in uso al centro di acquisizione della sede di Ancona. In: "Monitoraggio sismico del territorio nazionale: stato dell'arte e sviluppo delle reti di monitoraggio sismico", a cura di M. Cattaneo e M. Moretti, Miscellanea INGV, N° 10, 19-21.

. Moretti et al., 2011, 2011, Riassunti estesi del 1° workshop tecnico , Miscellanea INGV, numero 10 ISSN 2039-6651

. Moschetti, M. P., Ritzwoller M. H., Shapiro N. M., 2007, Surface wave tomography of the western United States from ambient seismic noise: Rayleigh wave group velocity maps, Geochemistry Geophysics Geosystems, 8, Q08010, doi: 10.1029/2007GC001655

. Nakamura, Y., (1989). A method for dynamic characteristics estimations of subsurface using microtremors on the ground surface. Quarterly Rept. RTRI Japan, 30, pp. 25-33.

. Nakamura, Y. (2000). Clear identification of fundamental idea of Nakamura's technique and its applications, Proc. XII World Conf. Earthquake Engineering, New Zealand, Paper n. 2656.

. Okada, H., H. Watanabe, H. Yamashita, and I. Yokoyama, Seismological significance of the 1977-1978 eruptions and the magma intrusion process of Usu volcano, Hokkaido, J. Volcanol. Geotherm. Res., 9, 311-334, 1981.

. Paul, A., M. Campillo, L. Margerin, E. Larose, and A. Derode ,2005, Empirical synthesis of time-asymmetrical Green functions from the correlation of coda waves, J. Geophys. Res., 110, B08302, doi:10.1029/2004JB003521.

. Peterson, J., (1993). Observations and modeling of background seismic noise. U.S. Geol. Surv. Open File Rep., 93-322.

.Pitilakis, K, 2004, Site effects, in Recent Adavnces in Earthquake Geotechnical Engineering and Microzonation, A. Ansal (Edito), Kluwer, Hingham, Massachusetts, 139-198.

. Pontoise. B., Monfret, T., 2004, Shallow seismogenic zone detected from an offshore-onshore temporary seismic network in the Esmeraldas area (northern Ecuador), Geochemistry Geophysics Geosystems, 5, Q02009, doi: 10.1029/2003GC000561

. Poupinet, G., Ellsworth, W. and Frechet, J., 1984. Monitoring velocity variations in the crust using earthquake doublets:an application to the Calaveras faults, California, J. Geophys. Res., 89, 5719-5731.

. Rao. S., Salvaterra L., Acerra C., 2010, Software per l'installazione e la configurazione della stazione sismica GAIA2. Rapporto Tecnici INGV n. 130

. Ratdomopurbo and Poupinet 1995. Monitoring a temporal change of seismic velocity in a volcano: application to the 1992 eruption of Mt. Merapi (Indonesia), Geophys. Res. Lett., 22(7), 775-778

. Rickett, J., and J. Claerbout (1999), Acoustic daylight imaging via spectral factorization: Helioseismology and reservoir monitoring, Leading Edge, 18, 957–960.

. Roux, P., W. A. Kuperman, and the NPAL Group (2004), Extracting coherent wavefronts from acoustic ambient noise in the ocean, J. Acoust. Soc. Am., 116, 1995– 2003.

. Paolucci R. (1999). Numerical evaluation of the effect of cross-coupling of different components of ground motion in site response analyses, Bull Seism Soc Am, 89, 877-887.

. Philippe Roux and Mathias Fink, Green's function estimation using secondary sources in a shallow water environment J. Acoust. Soc. Am., 113 (3), pp. 1406-1416, March 2003.

. Pischiutta M., Cultrera G., Caserta A., Luzi L. and Rovelli A. (2010). Topographic effects on the hill of Nocera Umbra, central Italy, Geophysical Journal International, Vol. 182, 2, 977–987.

. Rao, S., Salvaterra L., Acerra C. Software per l'installazione e la configurazione della stazione sismica GAIA2, Rapporti tecnici INGV N°130.

. Roux, P., K. G. Sabra, P. Gerstoft, W. A. Kuperman, and M. C. Fehler ,2005, P-waves from crosscorrelation of seismic noise, Geophys. Res. Lett., 32, L19303, doi:10.1029/2005GL023803.

. Roux, P., 2009, Passive seismic imaging with directive ambient noise: application to surface waves and the San Andreas Fault in Parkfield, CA, *Geophys. J. Int.* (2009) 179, 367–373 doi: 10.1111/j.1365-246X.2009.04282.x.

. Sabra, K. G., P. Roux, and W. A. Kuperman (2005a), Arrival-time structure of the time-averaged ambient noise cross-correlation function in an oceanic waveguide, J. Acoust. Soc. Am., 117, 164–174.

. Sabra, K.G., Gerstoft, P., Roux, P., Kuperman,W.A. & Fehler, M.C., 2005. Extracting time-domain Green's function estimates from ambient seismic noise, *Geophys. Res. Lett.,* 32, L03310, doi:10.1029/2004GL021862.

. Sabra, K. G., P. Roux, P. Gerstoft, W. A. Kuperman, and M. C. Fehler, 2006, Extracting coherent coda arrivals from cross-correlations of long period seismic waves during the Mount St. Helens 2004 eruption, Geophys. Res. Lett., 33, L06313, doi:10.1029/2005GL025563.

. Sanchez-Sesma, F., and M. Campillo (2006), Retrieval of the green function from cross correlation: The canonical elastic problem, Bull. Seismol. Soc. Am., 96(3), 1182– 1191, doi:10.1785/0120050181.

. Sadik Bakir B., H. Sucuoglu and T. Yilmaz (2002). An Overview of Local Site Effects and the Associated Building Damage in Adapazari during the 17 August 1999 Izmit Earthquake, 92, 1 509-526.

. H. Sato, M. Fehler, Seismic Wave Propagation and Scattering in the Heterogeneous Earth (Springer-Verlag and American Institute of Physics Press, 1998).

. Sens-Schönfelder, C.&Wegler, U., 2006. Passive image interferometry and seasonal variations of seismic velocities at Merapi volcano, (Indonesia), Geophys. Res. Lett., 33, L21302, doi:10.1029/2006GL027797.

. SESAME European project, 2005. Guidelines for the implementation of the H/V spectral ratio technique on ambient vibrations - Measurements, processing and interpretation. Deliverable D23.12. http://sesamefp5. obs.ujf-grenoble.fr/SES_TechnicalDoc.htm

. Shapiro, N. M., Singh S. K., 1999, A systematic error in estimating surface-wave group-velocity dispersion curves and a procedure for its correction, BSSA, 89, pp.1138-1142

. Shapiro, N. M., Campillo M., 2004, Emergence of broadband Rayleigh waves from correlations of the ambient seismic noise, Geophysical Research Letters, vol. 31, L07614, doi:10.1029/2004GL019491

. Shapiro, N. M., Campillo M., Stehly L., Ritzwoller M. H., 2005, High-Resolution surface-wave tomography from ambient seismic noise, Science, 307, doi: 10.1126/science.1108339

. Shapiro, N. M., M. H. Ritzwoller, and G. D. Bensen, 2006, Source location of the 26 sec microseism from crosscorrelations of ambient seismic noise, Geophys. Res. Lett., 33, L18310, doi:10.1029/2006GL027010.

. Snieder, R., Grêt A., Douma H. and Scales J., 2002a, Coda wave interferometry for estimating nonlinear behaviour in seismic velocity, Science, vol 295

. Snieder, R. 2002, Coda wave interferometry and the equilibration of energy in elastic media, Phys. Rev. E 66, 046615.

. Snieder, R., 2006. The theory of coda interferometry, Pure appl. Geophys., 163 (2), 455-473

. Spudich P., Hellweg M., and Lee W.H.K. (1996). Directional topographic site response at Tarzana observed in aftershocks of the 1994 Northridge, California, earthquake: implications for mainshock motions, Bull. Seism. Soc. Am., 86, 193-208.

. Stehly, L., M. Campillo, and N. M. Shapiro 2006, A study of the seismic noise from its long-range correlation properties, J. Geophys. Res., 111, B10306, doi:10.1029/2005JB004237

. Stehly, L., M. Campillo, B. Froment, and R. L. Weaver (2008), Reconstructing Green's function by correlation of the coda of the correlation (C3) of ambient seismic noise, J. Geophys. Res., 113, B11306, doi:10.1029/2008JB005693.

. Theodulidis NP, Bard PY (1995) Horizontal to vertical spectral ratio and geological conditions: an analysis of strong motion data from Greece and Taiwan (SMART-1). Soil Dyn Earthq Eng 14:177–197

. Thomas, A. M., Nadeau R., M., Bürgmann R., 2009, Tremor-tide correlations and near-lithostatic pore pressure on the deep San Andreas fault, Nature, vol. 462, 24/31, doi:10.1038/nature08654

. Tokimatsu, K. (1997). Geotechnical site characterization using surface waves, Earthquake Geotech. Eng. 1333-1368.

. Wadati K., 1933, On the travel time of earthquakes waves. Part II, Geophys. Mag., 7, 101-111.

. Weaver, R. L., and O. I. Lobkis (2001), Ultrasonics without a source: Thermal fluctuation correlations at MHz frequencies, Phys. Rev. Lett., 87, 134301, doi:10.1103/PhysRevLett.87.134301.

. Weaver, R. L., and O. I. Lobkis (2003), Elastic wave thermal fluctuations, ultrasonic waveforms by correlation of thermal photons, J. Acoust. Soc. Am., 113, 2611 – 2621.

. Weaver, R. L., and O. I. Lobkis (2004), Diffuse fields in open systems and the emergence of the Green's function, J. Acoust. Soc. Am., 116, 2731–2734.

. Weaver, R., Froment B., Campillo M., 2009, On the correlation of non-isotropically distributed ballistic scalar diffuse waves, J. Acoust. Soc. Am., 126, doi: 10.1121/1.3203359

. Wegler, U., and C. Sens - Schönfelder (2007), Fault zone monitoring with passive image interferometry, Geophys. J. Int., 168, 1029–1033.

. Wegler, U., Nakahara, H., Sens-Sch¨onfelder, C., Korn, M. & Shiomi, K., 2009. Sudden drop of seismic velocity after the 2004*Mw* 6.6 mid-Niigata earthquake, Japan, observed with Passive Image Interferometry, J. geophys. Res., 114(B06305), 1–11.

. R. S. Wu, K. Aki, Multiple scattering and energy transfer of seismic waves - separation of scattering effect from intrinsic attenuation, II. Application of the theory to Hindu Kush Region, Pure Appl. Geophys. 128, 49 (1988).

. Yamanaka, H., M. Takemura, H. Ishida, and M. Niwa (1994). Characteristics of long period microtremors and their applicability in the exploration of deep sedimentary layers, Bull. Seism. Soc. Am. 84, 1831-1841.

. Yang, Y., M. H. Ritzwoller, A. L. Levshin, N. M. Shapiro, 2007, Ambient noise Rayleigh wave tomography across Europe, *Geophys. J. Int.* (2007) 168, 259–274 doi: 10.1111/j.1365-246X.2006.03203.x

. Yang, Y., and M. H. Ritzwoller (2008a), Characteristics of ambient seismic noise as a source for surface wave tomography, Geochem. Geophys. Geosyst., 9, Q02008, doi:10.1029/2007GC001814.

. Yang, Y., M. H. Ritzwoller, F.-C. Lin, M. P. Moschetti, and N. M. Shapiro (2008b), Structure of the crust and uppermost mantle beneath the western United States revealed by ambient noise and earthquake tomography, J. Geophys. Res., 113, B12310, doi:10.1029/2008JB005833.

. Zaccarelli, L., N. M. Shapiro, L. Faenza, G. Soldati, and A. Michelini (2011), Variations of crustal elastic properties during the 2009 L'Aquila earthquake inferred from cross - correlations of ambient seismic noise, Geophys. Res. Lett., 38, L24304, doi:10.1029/2011GL049750.

. Zawslavsky Y. and Shapira A. (2000). Experimental study of topographic amplification using the Israel Seismic Network. Journal of Earthquake Engineering, 4, 43-65.

APPENDIX

Appendix A

Horizontal to Vertical Spectra Ratio (HVSR) of Castelvecchio Subequo

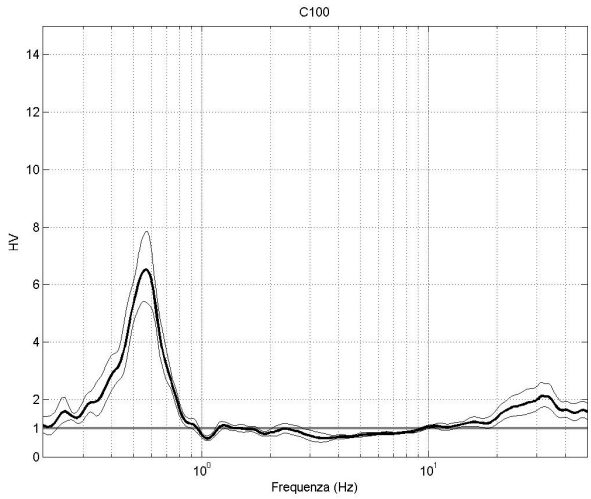

HVSR at the station C100. The spectral peak is between 0.5 and 0.6 Hz.

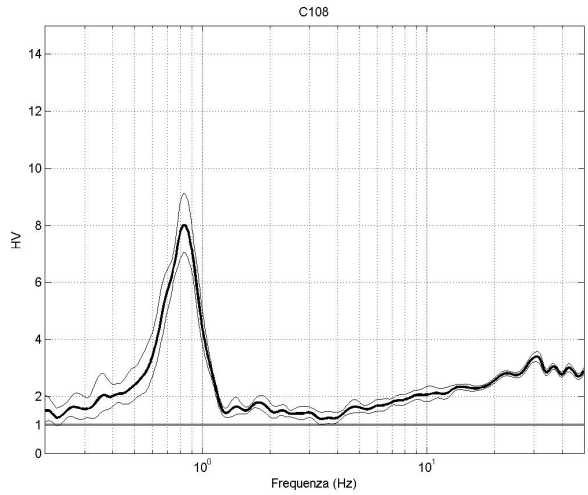

HVSR at the station C108. The spectral peak is between 0.8 and 0.9 Hz.

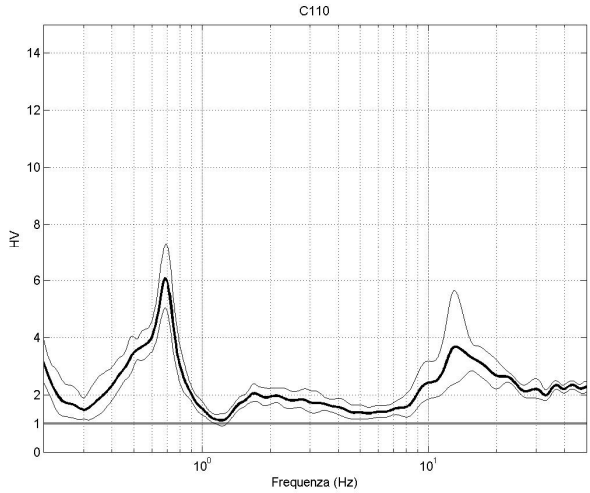

HVSR at the station C110. The first spectral peak is between 0.6 and 0.7 Hz, the second between 10 and 11 Hz.

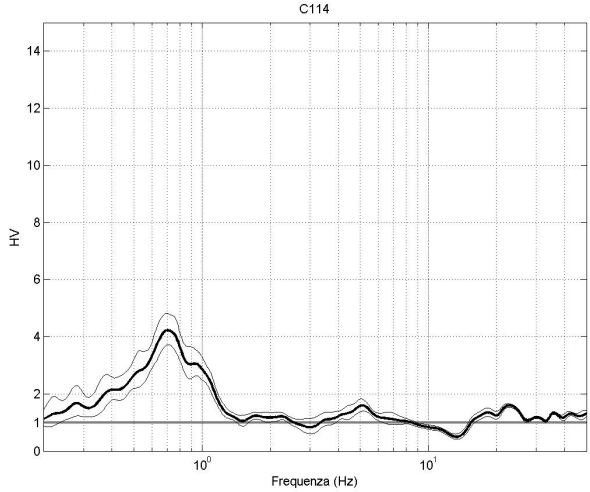

HVSR at the station C114. The spectral peak is 0.7 Hz.

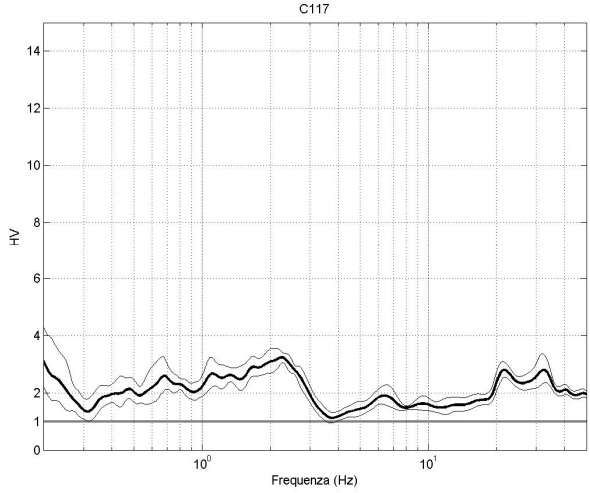

HVSR at the station C117. The spectral peak is about at 2-3 Hz.

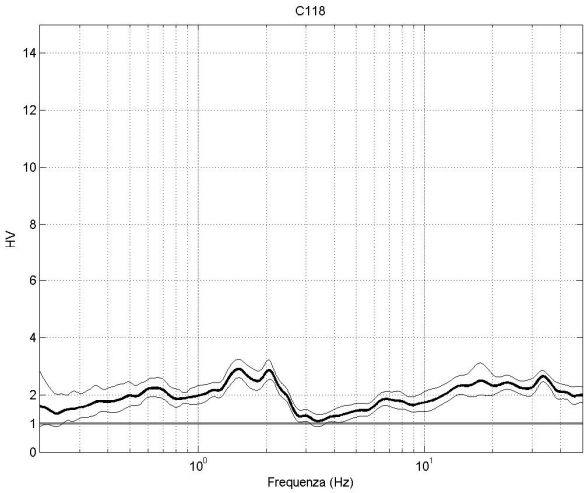

HVSR at the station C118. The spectral peak is at 1-2 Hz.

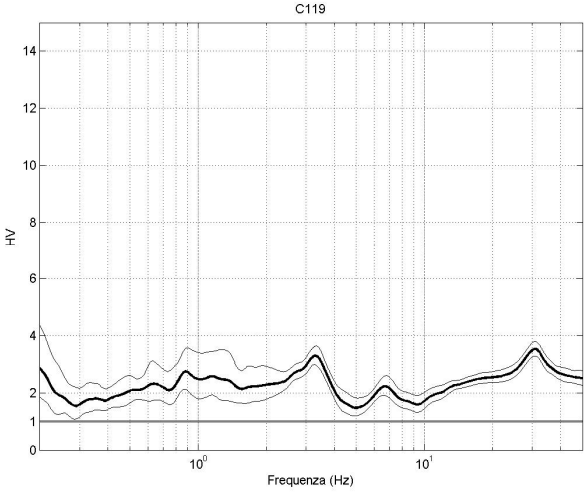

HVSR at the station C119.

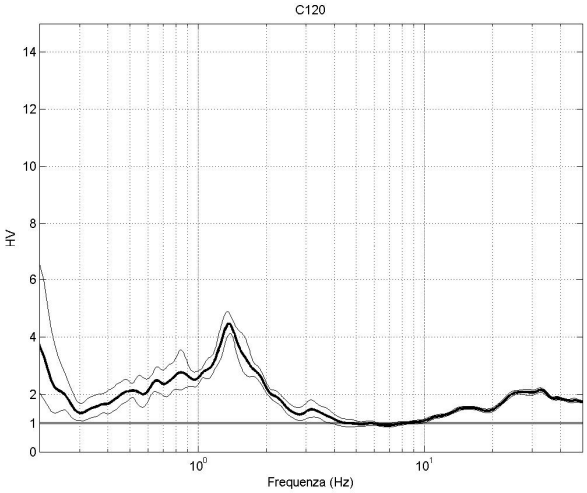

HVSR at the station C120. The spectral peak is between 1 and 2 Hz.

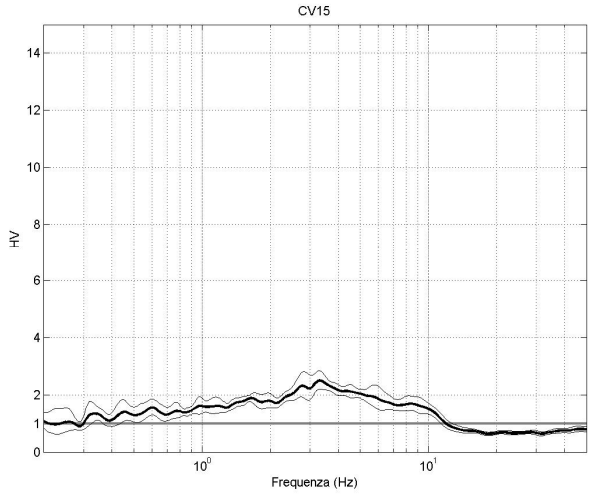

HVSR at the station CV15.

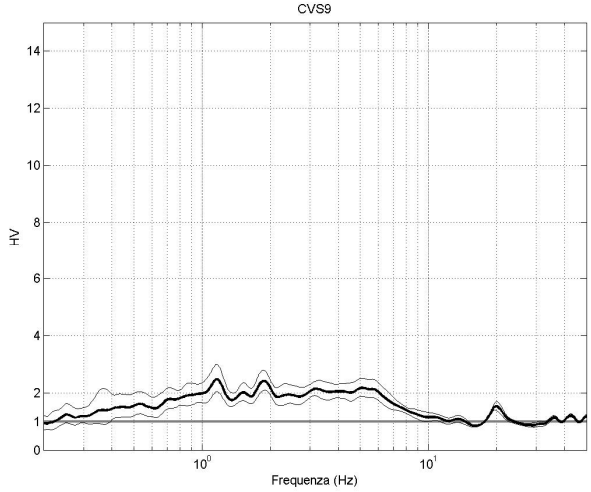

HVSR at the station CVS9.

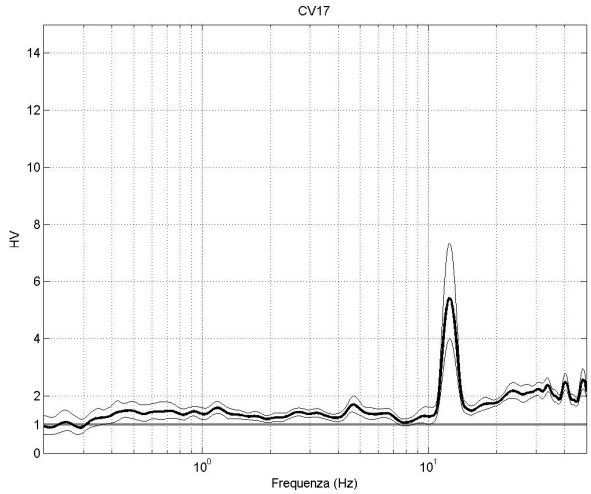

HVSR at the station CV17. The spectral peak is at 10-11 Hz.

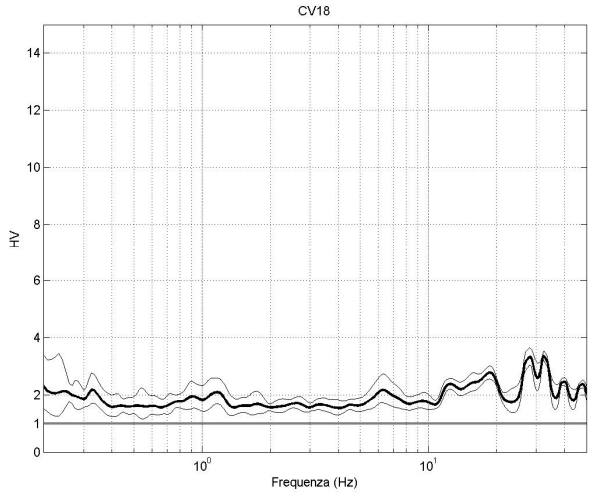

HVSR at the station CV18.

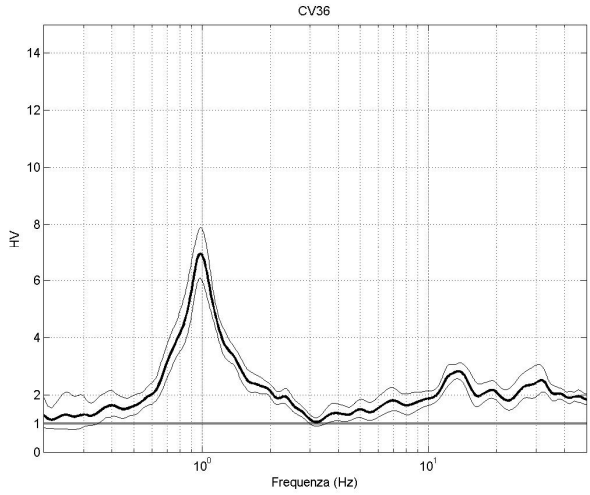

HVSR at the station CV36. The spectral peak is at 1 Hz.

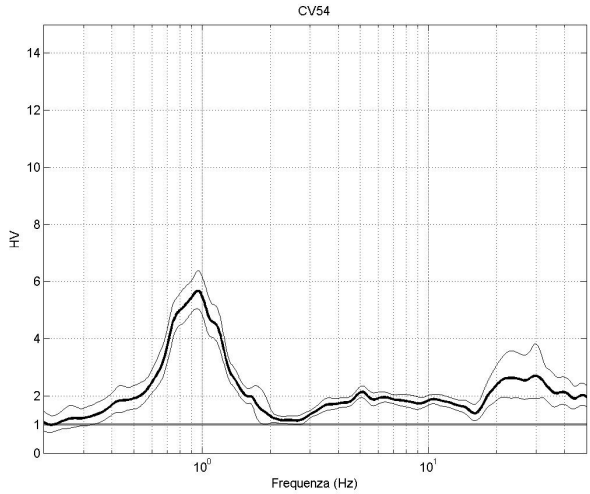

HVSR at the station CV54. The spectral peak is between 0.7 and 1 Hz.

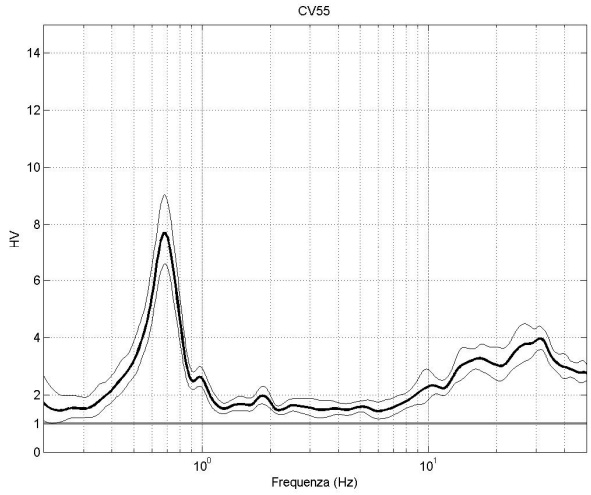

HVSR at the station CV55. The spectral peak is between 0.6 and 0.7 Hz.

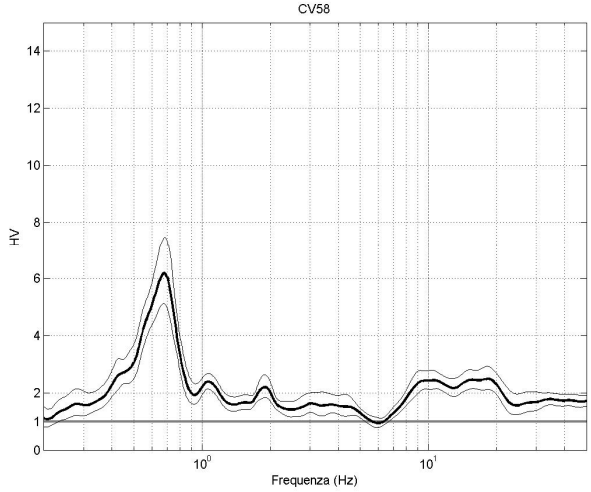

HVSR at the station CV58. The spectral peak is between 0.6 and 0.7 Hz.

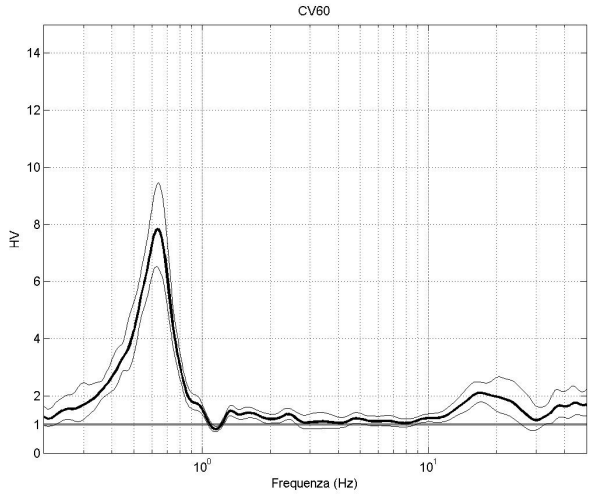

HVSR at the station CV60. The spectral peak is at 0.6 Hz.

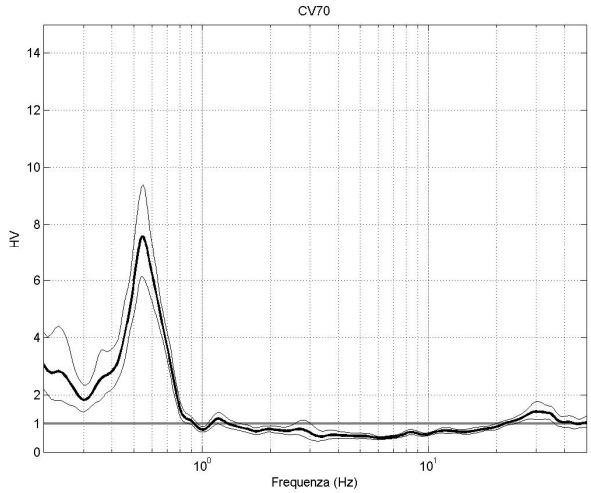

HVSR at the station CV70. The spectral peak at 0.6 Hz.

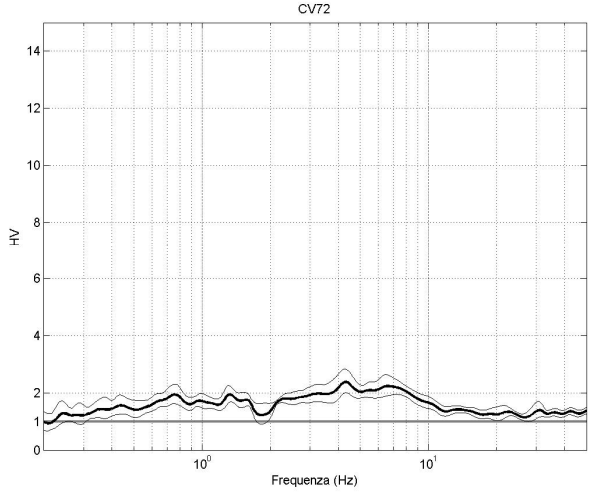

HVSR at the station CV72.

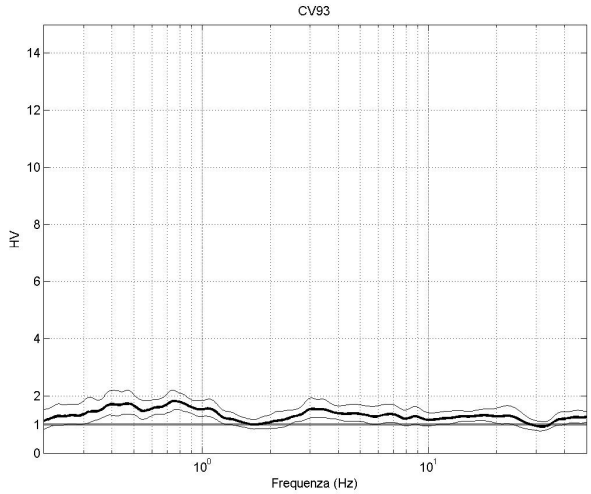

HVSR at the station CV93.

Appendix B
“leggibinarysac.m” script

```
%legge i file sac binari %%%%%%%%%%%%%%%%%%

%input:
%   filesac = file SAC name
%   nf = number of files
%   pt = 'l' little indian and  'b' big indian
%output
%headersac
%%%%%%%%%%%%%%%%%%%%%%%%%%%%%%%%%%%%%%%%%%%%%%%%
%%%%%%%%%%%%%%%%%%%%%%%
fidsac=fopen (filesac,'r',pt);

h1=fread (fidsac,70,'float32');%=>single'); %prima parte dell'header, tutti i 70 campi float 32
headersac(nf).delta = h1(1);
headersac(nf).depmin = h1(2);
headersac(nf).depmax = h1(3);
headersac(nf).scale = h1(4);
headersac(nf).odelta = h1(5);
headersac(nf).b = h1(6);
headersac(nf).e = h1(7);
headersac(nf).o = h1(8);
headersac(nf).a = h1(9);
headersac(nf).internal = h1(10);
headersac(nf).t0 = h1(11);
headersac(nf).t1 = h1(12);
headersac(nf).t2 = h1(13);
headersac(nf).t3 = h1(14);
headersac(nf).t4 = h1(15);
headersac(nf).t5 = h1(16);
headersac(nf).t6 = h1(17);
headersac(nf).t7 = h1(18);
headersac(nf).t8 = h1(19);
headersac(nf).t9 = h1(20);
headersac(nf).f = h1(21);
headersac(nf).resp0 = h1(22);
headersac(nf).resp1 = h1(23);
headersac(nf).resp2 = h1(24);
headersac(nf).resp3 = h1(25);
headersac(nf).resp4 = h1(26);
headersac(nf).resp5 = h1(27);
headersac(nf).resp6 = h1(28);
headersac(nf).resp7 = h1(29);
headersac(nf).resp8 = h1(30);
headersac(nf).resp9 = h1(31);
headersac(nf).stla = h1(32);
headersac(nf).stlo = h1(33);
headersac(nf).stel = h1(34);
```

```
headersac(nf).stdp = h1(35);
headersac(nf).evla = h1(36);
headersac(nf).evlo = h1(37);
headersac(nf).evel = h1(38);
headersac(nf).evdp = h1(39);
headersac(nf).unused1= h1(40);
headersac(nf).user0= h1(41);
headersac(nf).user1= h1(42);
headersac(nf).user2= h1(43);
headersac(nf).user3= h1(44);
headersac(nf).user4= h1(45);
headersac(nf).user5= h1(46);
headersac(nf).user6= h1(47);
headersac(nf).user7= h1(48);
headersac(nf).user8= h1(49);
headersac(nf).user9= h1(50);
headersac(nf).dist= h1(51);
headersac(nf).az= h1(52);
headersac(nf).baz= h1(53);
headersac(nf).gcarc= h1(54);
headersac(nf).internal1= h1(55);
headersac(nf).internal2= h1(56);
headersac(nf).depmen= h1(57);
headersac(nf).cmpaz= h1(58);
headersac(nf).cmpinc= h1(59);
headersac(nf).unused2= h1(60);
headersac(nf).unused3= h1(61);
headersac(nf).unused4= h1(62);
headersac(nf).unused5= h1(63);
headersac(nf).unused6= h1(64);
headersac(nf).unused7= h1(65);
headersac(nf).unused8= h1(66);
headersac(nf).unused9= h1(67);
headersac(nf).unused10= h1(68);
headersac(nf).unused11= h1(69);
headersac(nf).unused12= h1(70);

h2=fread(fidsac,40,'int32');%seconda parte dell'header valori integer
headersac(nf).nzyear= h2(1);
headersac(nf).nzjday= h2(2);
headersac(nf).nzhour= h2(3);
headersac(nf).nzmin= h2(4);
headersac(nf).nzsec= h2(5);
headersac(nf).nzmsec= h2(6);
headersac(nf).nvhdr= h2(7);
headersac(nf).internal3= h2(8);
headersac(nf).internal4= h2(9);
headersac(nf).npts= h2(10);
headersac(nf).internal5= h2(11);
headersac(nf).internal6= h2(12);
headersac(nf).unused13= h2(13);
```

```
headersac(nf).unused14= h2(14);
headersac(nf).unused15= h2(15);
headersac(nf).iftype= h2(16);
headersac(nf).idep= h2(17);
headersac(nf).iztype= h2(18);
headersac(nf).unused16= h2(19);
headersac(nf).iinst= h2(20);
headersac(nf).istreg= h2(21);
headersac(nf).ievreg= h2(22);
headersac(nf).ievtyp= h2(23);
headersac(nf).iqual= h2(24);
headersac(nf).isynth= h2(25);
headersac(nf).unused17= h2(26);
headersac(nf).unused18= h2(27);
headersac(nf).unused19= h2(28);
headersac(nf).unused20= h2(29);
headersac(nf).unused21= h2(30);
headersac(nf).unused22= h2(31);
headersac(nf).unused23= h2(32);
headersac(nf).unused24= h2(33);
headersac(nf).unused25= h2(34);
headersac(nf).unused26= h2(35);
headersac(nf).leven= h2(36);
headersac(nf).lpspol= h2(37);
headersac(nf).lovrok= h2(38);
headersac(nf).lcalda= h2(39);
headersac(nf).unused27= h2(40);
%terza parte dell'header campi carattere
t1=fread(fidsac,8,'*char');
headersac(nf).kstnm= t1';
t2=fread(fidsac,16,'*char');
headersac(nf).kevnm= t2';
t3=fread(fidsac,8,'*char');
headersac(nf).khole= t3';
t4=fread(fidsac,8,'*char');
headersac(nf).ko= t4';
t5=fread(fidsac,8,'*char');
headersac(nf).ka= t5';
t6=fread(fidsac,8,'*char');
headersac(nf).kt0= t6';
t7=fread(fidsac,8,'*char');
headersac(nf).kt1= t7';
t8=fread(fidsac,8,'*char');
headersac(nf).kt2= t8';
t9=fread(fidsac,8,'*char');
headersac(nf).kt3= t9';
t10=fread(fidsac,8,'*char');
headersac(nf).kt4= t10';
t11=fread(fidsac,8,'*char');
headersac(nf).kt5= t11';
t12=fread(fidsac,8,'*char');
```

```
headersac(nf).kt6= t12';
t13=fread(fidsac,8,'*char');
headersac(nf).kt7= t13';
t14=fread(fidsac,8,'*char');
headersac(nf).kt8= t14';
t15=fread(fidsac,8,'*char');
headersac(nf).kt9= t15';
t16=fread(fidsac,8,'*char');
headersac(nf).kf= t16';
t17=fread(fidsac,8,'*char');
headersac(nf).kuser0= t17';
t18=fread(fidsac,8,'*char');
headersac(nf).kuser1= t18';
t19=fread(fidsac,8,'*char');
headersac(nf).kuser2= t19';
t20=fread(fidsac,8,'*char');
headersac(nf).kcmpnm= t20';
t21=fread(fidsac,8,'*char');
headersac(nf).knetwk= t21';
t22=fread(fidsac,8,'*char');
headersac(nf).kdatrd= t22';
t23=fread(fidsac,8,'*char');
headersac(nf).kinst= t23';
%traccia
headersac(nf).datasac= fread(fidsac,inf,'float32');

fclose (fidsac);
```

Appendix C
SAC Data Format

NPTS = point numbers
B = Reference time (Initial value of independent variable, in seconds)
E = Final value (seconds)
O = Start Time (value in seconds starting from the beginning of trace)
KO = Variable label of Start Time (T0) IFTYPE = type of file
LEVEN = TRUE (data spaced in time)
DELTA = sampling step (ms)
DEPMIN = minimum value
DEPMAX = maximum value
DEPMEN = medium value
AMARKER = begin of trace
KZDATE = reference date (month, day, julian day, year)
KZTIME = tempo di riferimento
IZTYPE = type of reference time
KINST = type of digitizer
KSTNM = station code
CMPAZ = azimut component (0,90)
CMPINC = inclination component (0,90)
STLA = geographic coordinates of seismic station (Latitude)
STLO = geographic coordinates of seismic station (Longitude)
STEL = geographic coordinates of seismic station (Quota)
KEVNM = regional reference for temporary network
EVLA = event latitude
EVLO = event longitude
EVDP = event depth
DIST = epicentral distance (km)
AZ = azimuth earthquake-station (degree)
BAZ = azimuth station-earthquake (degree)
LOVROK = if TRUE allows to overwrite the file
USER0 = sensitivity value (1500 for Trillium, 400 Lennartz, 10 Episensor 2g)
USER1 = digitizer constant for the conversion from count to Volt
USER2 = baseline removal (1=rtrend on; 0=rtrend off)
USER3 = tapering (1=tapering on; 0=tapering off)
USER4 = mean removal (1=rmean on; 0=rmean off)
USER5 = filterec trace (1=filter Butterworth on; 0=filter Butterworth off)
KUSER0 = sensitivity unit (V/m/s if velocimeter, V/g for accelerometer) # Gain (1, 32)
KUSER1 = data measure unity (microV, Counts)
KUSER2 = sensor name
NVHDR = header number version (corrent 6)
LPSPOL = TRUE if components have positive polarity
LCALDA = TRUE if DIST, AZ, BAZ e GCARC are calculated starting from station and event coordinates
KCMPNM = recorded ground motion component, SEED codification (Last Field: z,n,e for vertical, Nord/Sud, Est/Ovest)
KNETWK = network name (RAIS, INGV)

Appendix D

Wadati diagrams of eleven multiplets of the seismic sequence in April 2010

DTP: difference time of P phase. DTS: difference time of S phase. R: regression coefficient. Obs: number of observations.

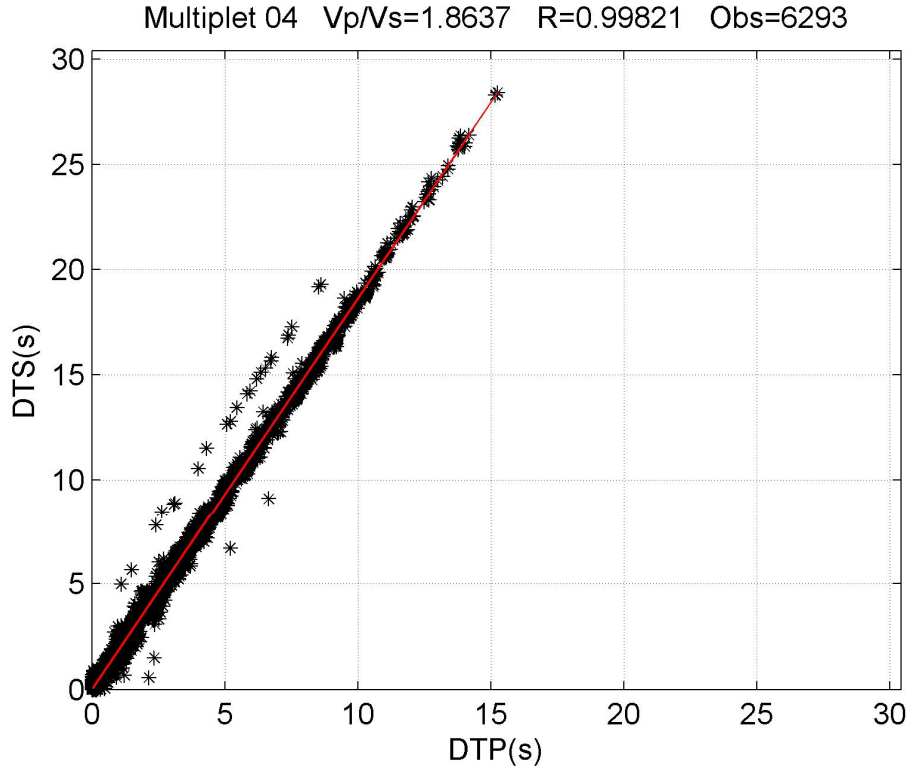

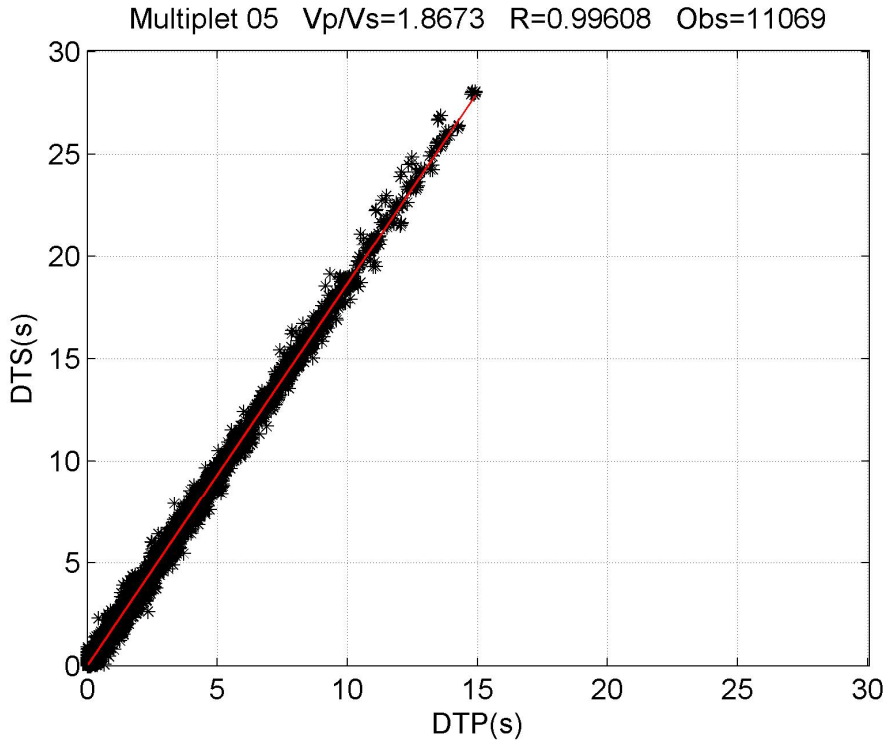

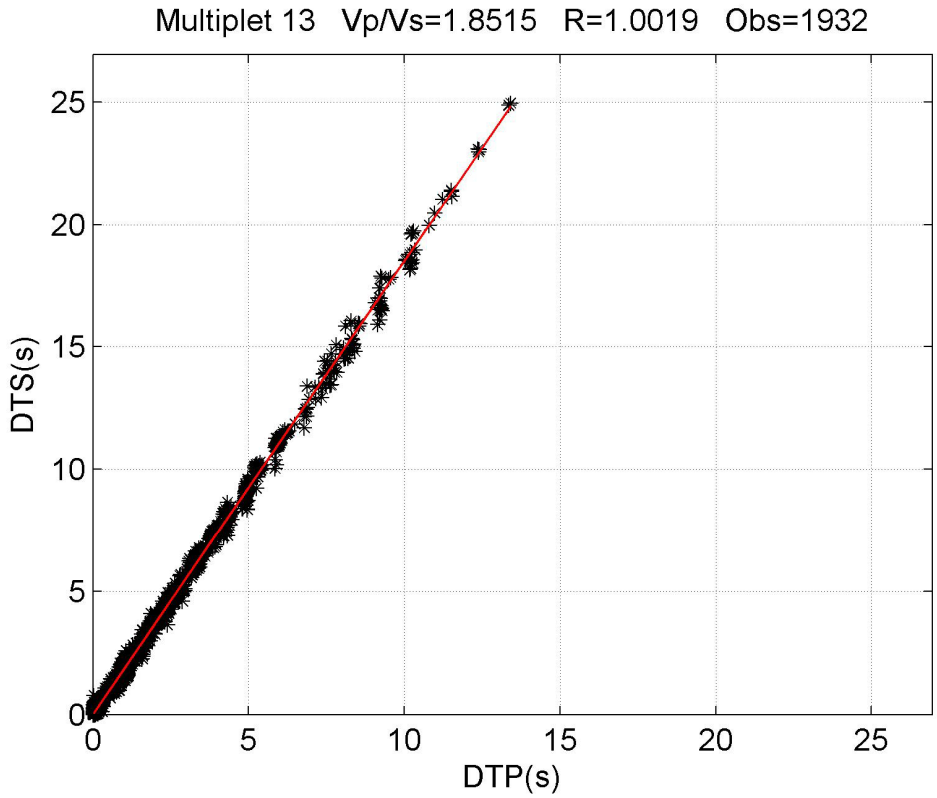
Multiplet 13 Vp/Vs=1.8515 R=1.0019 Obs=1932
DTS(s)
DTP(s)
0
5
10
15
20
25

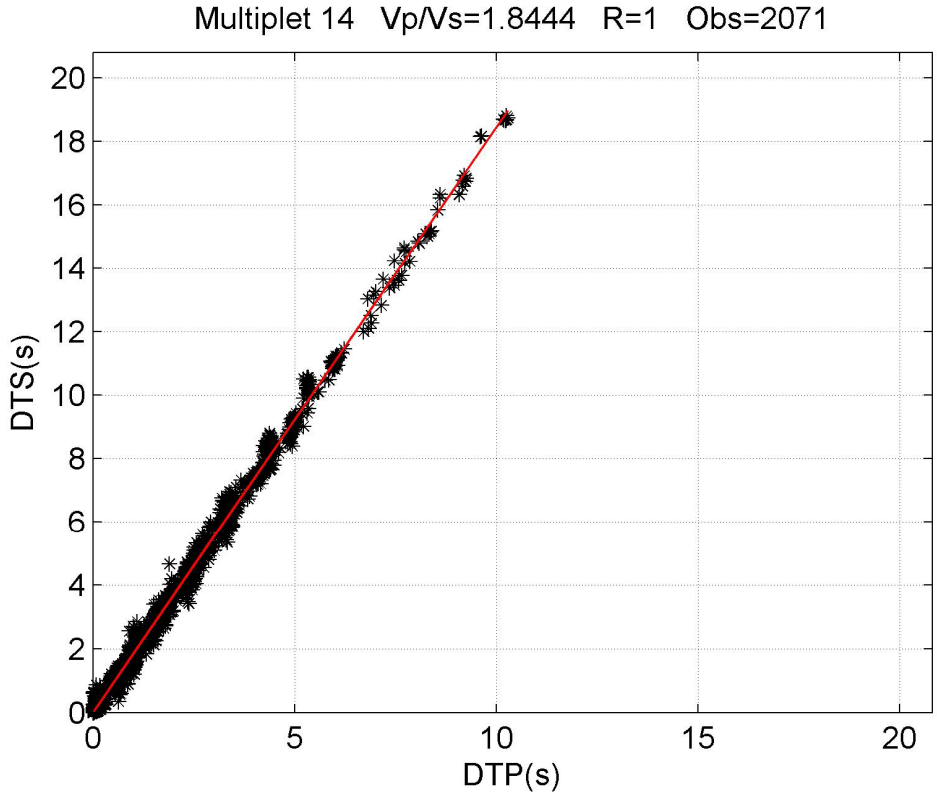
Multiplet 14 Vp/Vs=1.8444 R=1 Obs=2071
DTS(s)
DTP(s)
0
2
4
6
8
10
12
14
16
18
20

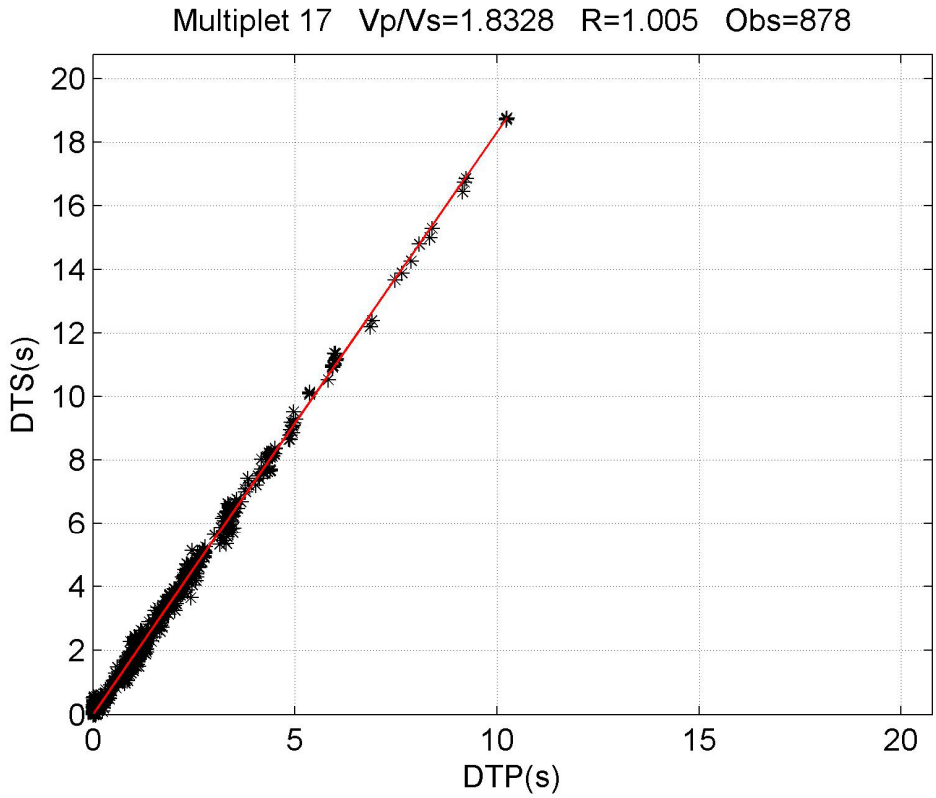
Multiplet 17 Vp/Vs=1.8328 R=1.005 Obs=878
DTS(s)
DTP(s)
0
2
4
6
8
10
12
14
16
18
20
0
5
10
15
20

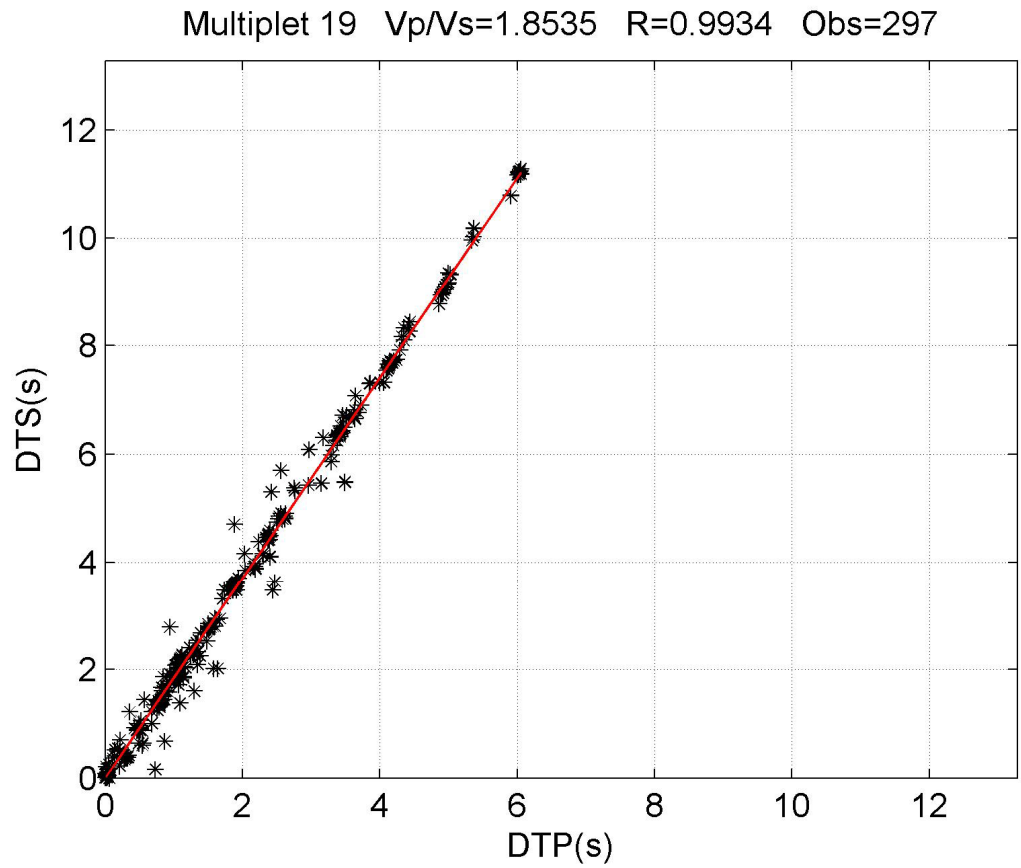
Multiplet 19 Vp/Vs=1.8535 R=0.9934 Obs=297
DTS(s)
DTP(s)
0
2
4
6
8
10
12
0
2
4
6
8
10
12

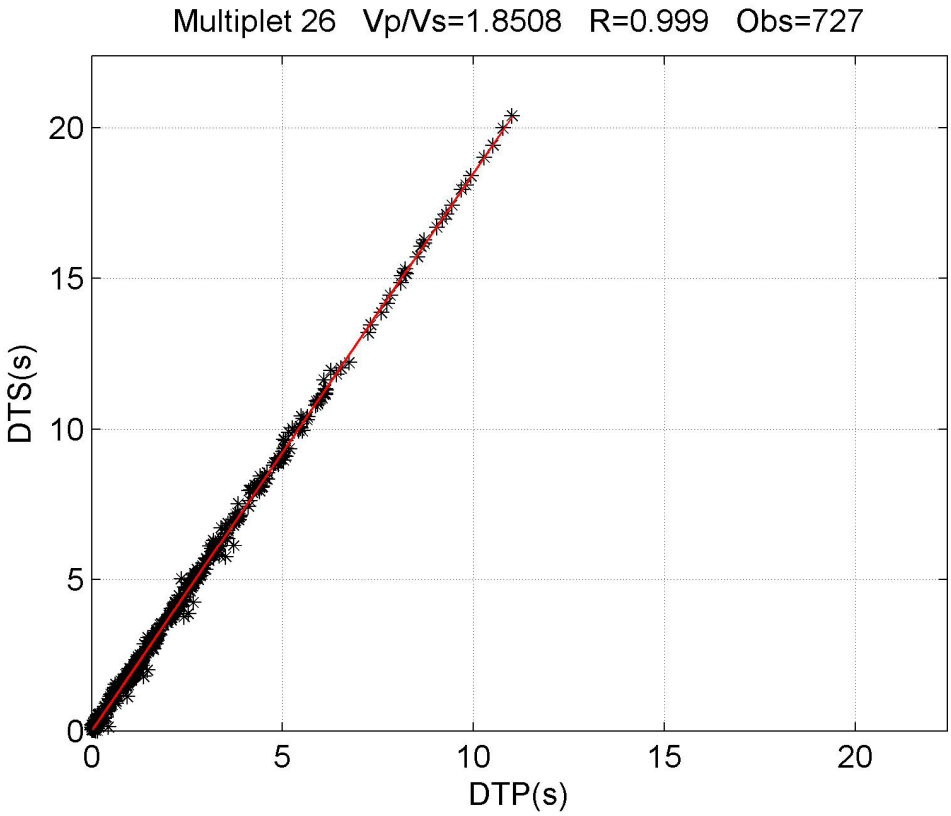
Multiplet 26 Vp/Vs=1.8508 R=0.999 Obs=727
DTS(s)
DTP(s)
0
5
10
15
20

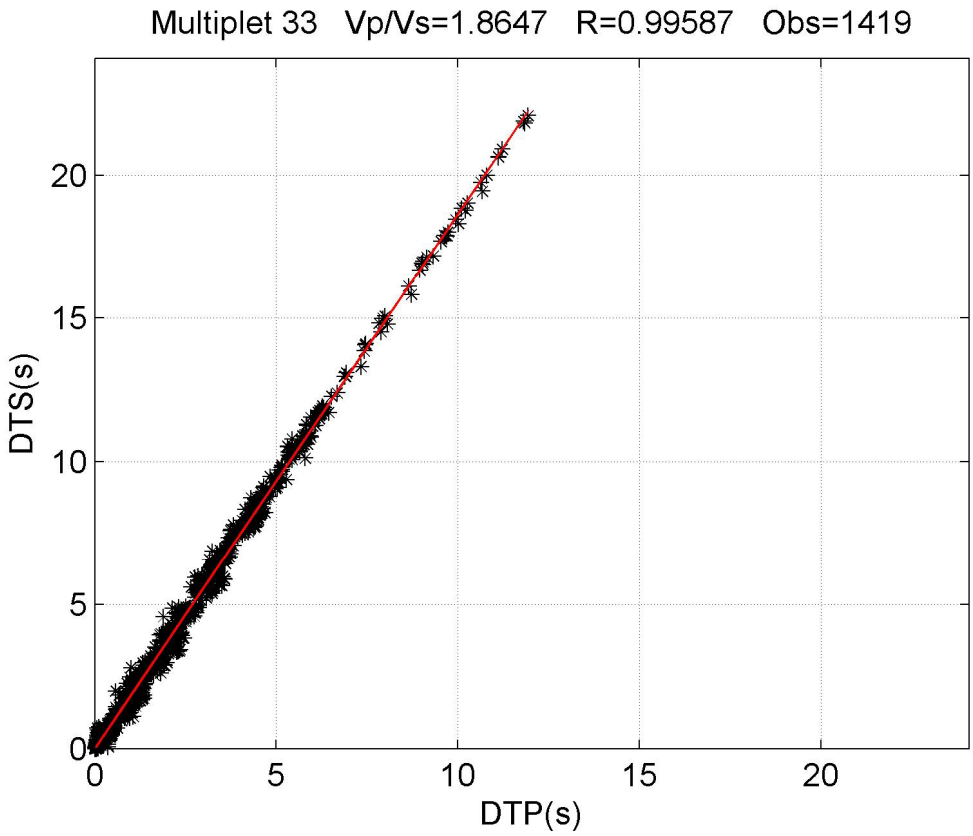
Multiplet 33 Vp/Vs=1.8647 R=0.99587 Obs=1419
DTS(s)
DTP(s)
0
5
10
15
20

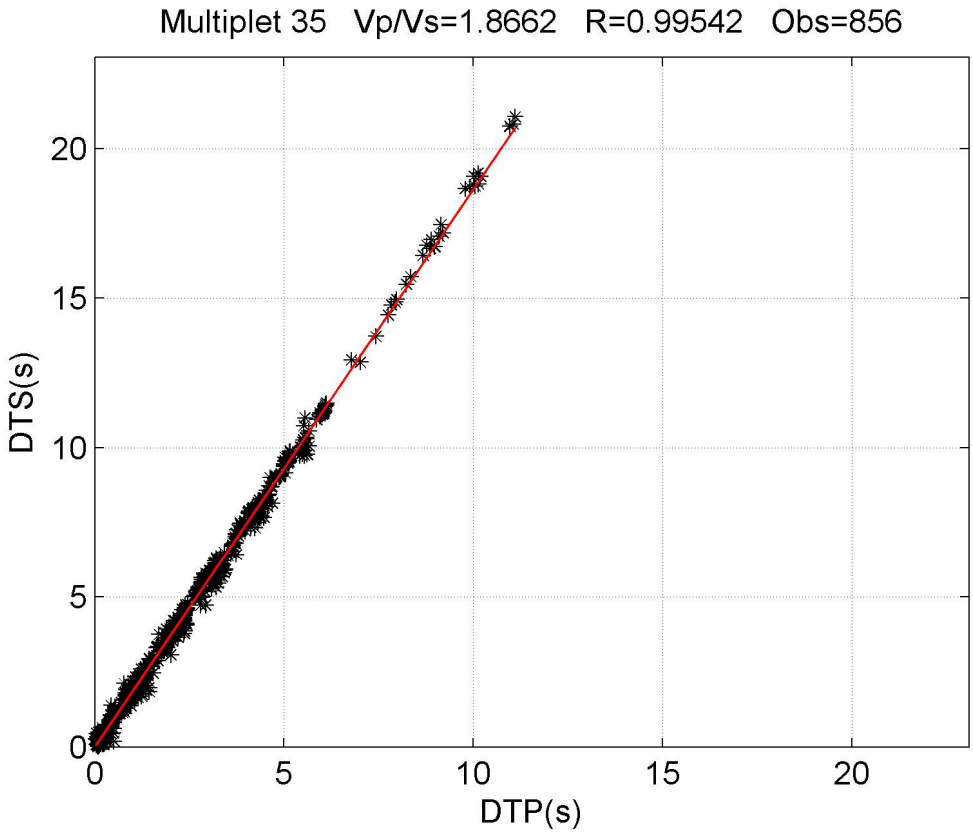
Multiplet 35 Vp/Vs=1.8662 R=0.99542 Obs=856
DTS(s)
DTP(s)
0
5
10
15
20

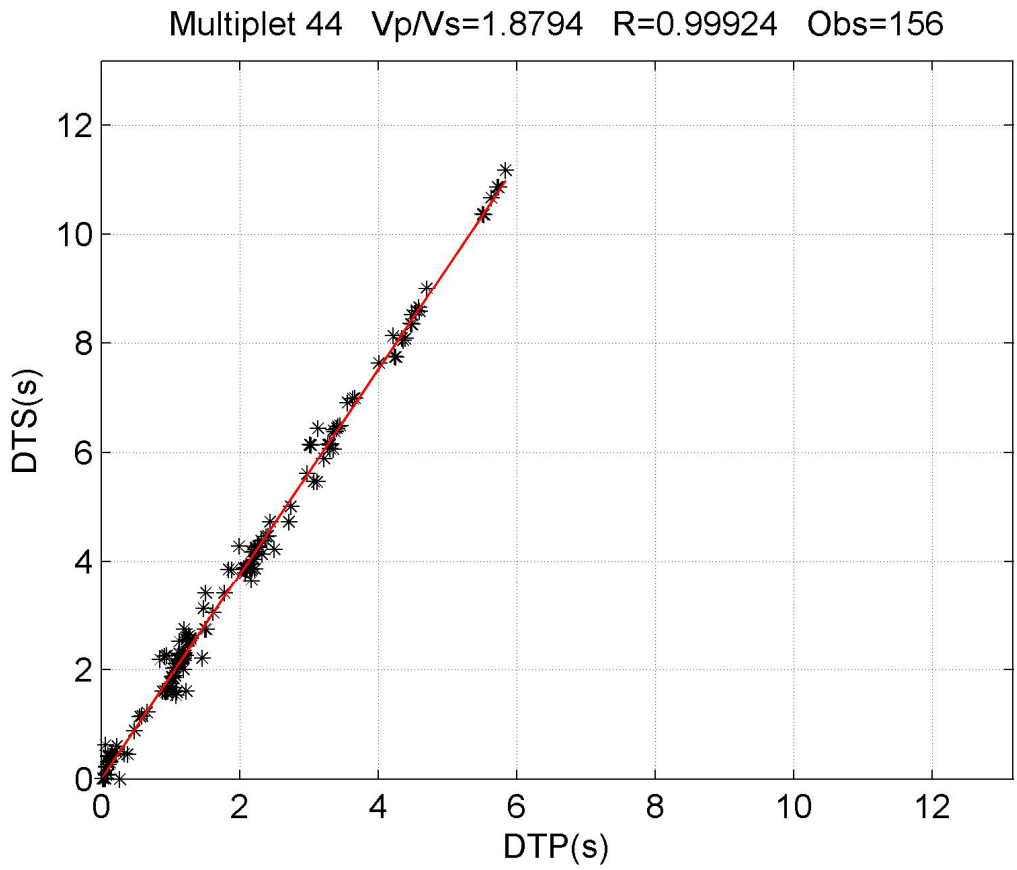
Multiplet 44 Vp/Vs=1.8794 R=0.99924 Obs=156
DTS(s)
DTP(s)
0
2
4
6
8
10
12

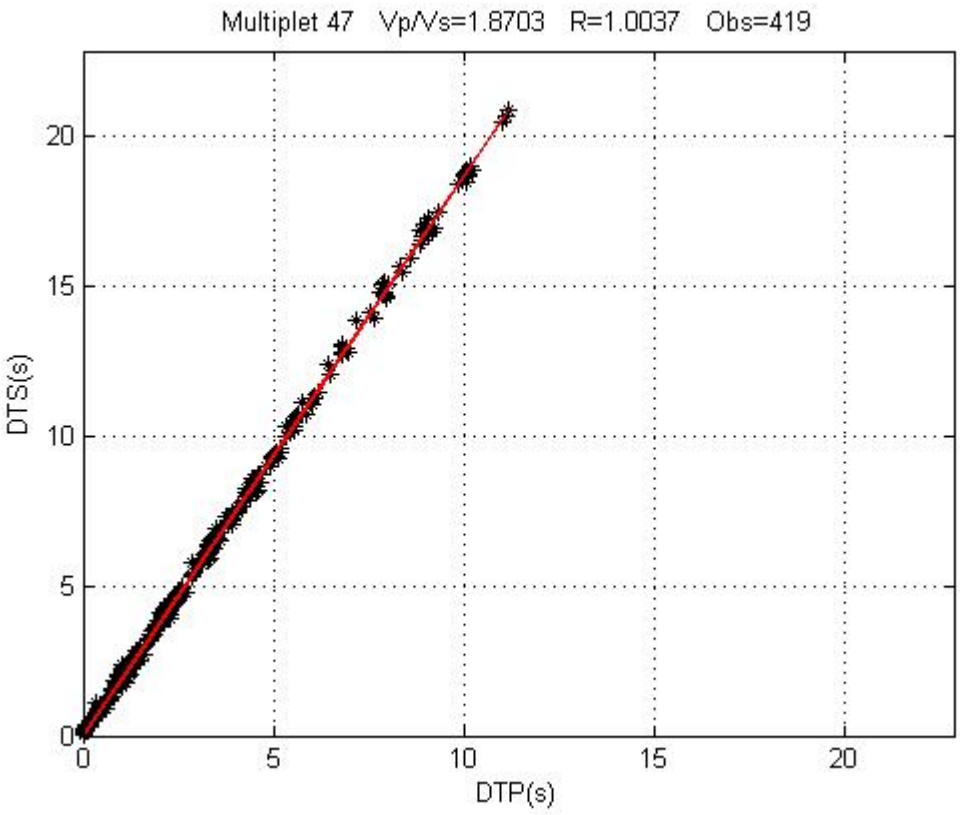
Multiplet 47 Vp/Vs=1.8703 R=1.0037 Obs=419
DTS(s)
DTP(s)
0
5
10
15
20

Appendix E

Atmospheric pressure maps (http://www.wetterzentrale.de/)

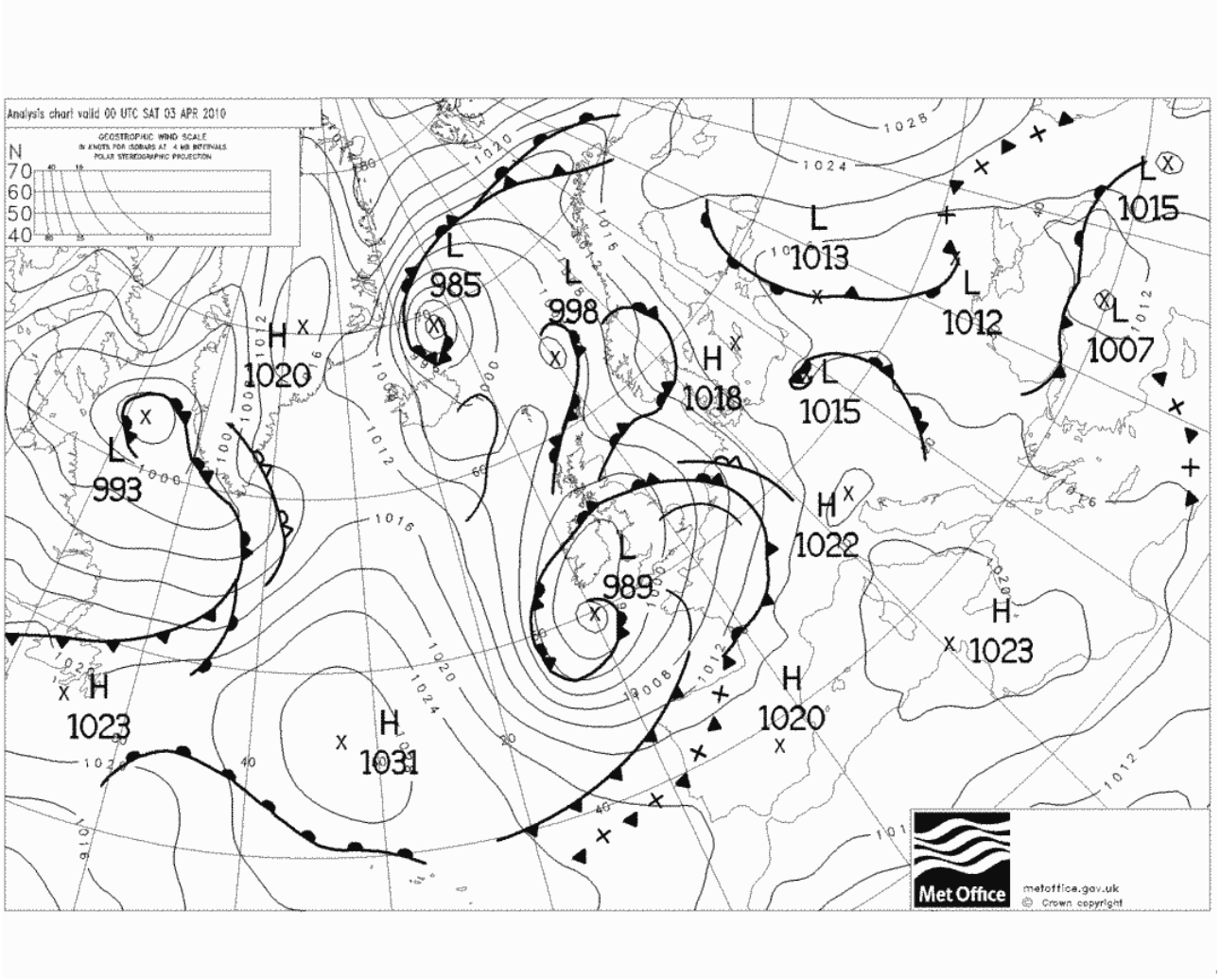

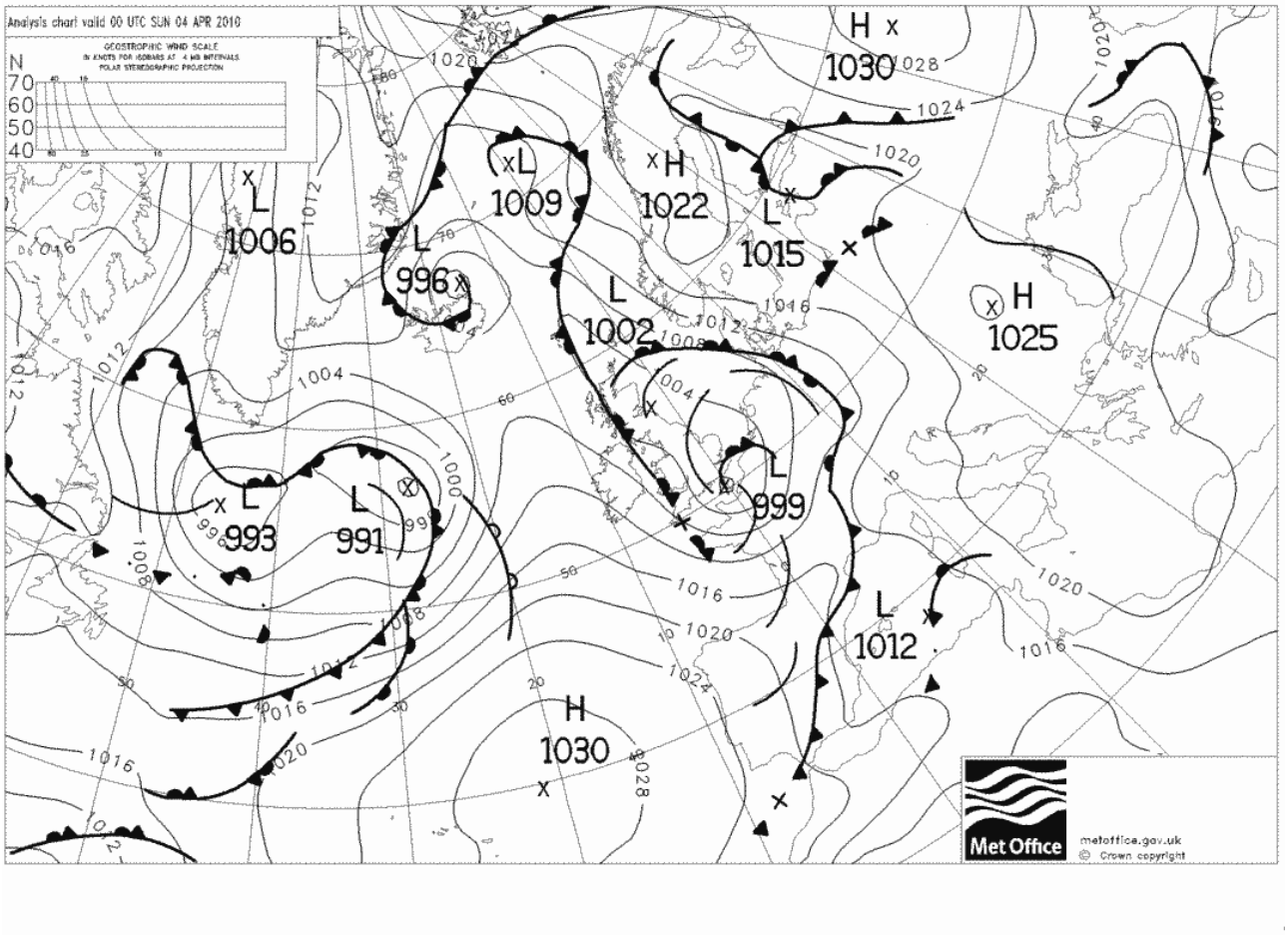
Analysis chart valid 00 UTC SUN 04 APR 2010
GEOSTROPHIC WIND SCALE
IN KNOTS FOR ISOBARS AT 4 MB INTERVALS
POLAR STEREOGRAPHIC PROJECTION
N
70
60
50
40
H
1030
L
1009
H
1022
L
1006
L
996
L
1015
L
1002
H
1025
L
999
L
993
L
991
L
1012
H
1030
Met Office
metoffice.gov.uk
© Crown copyright

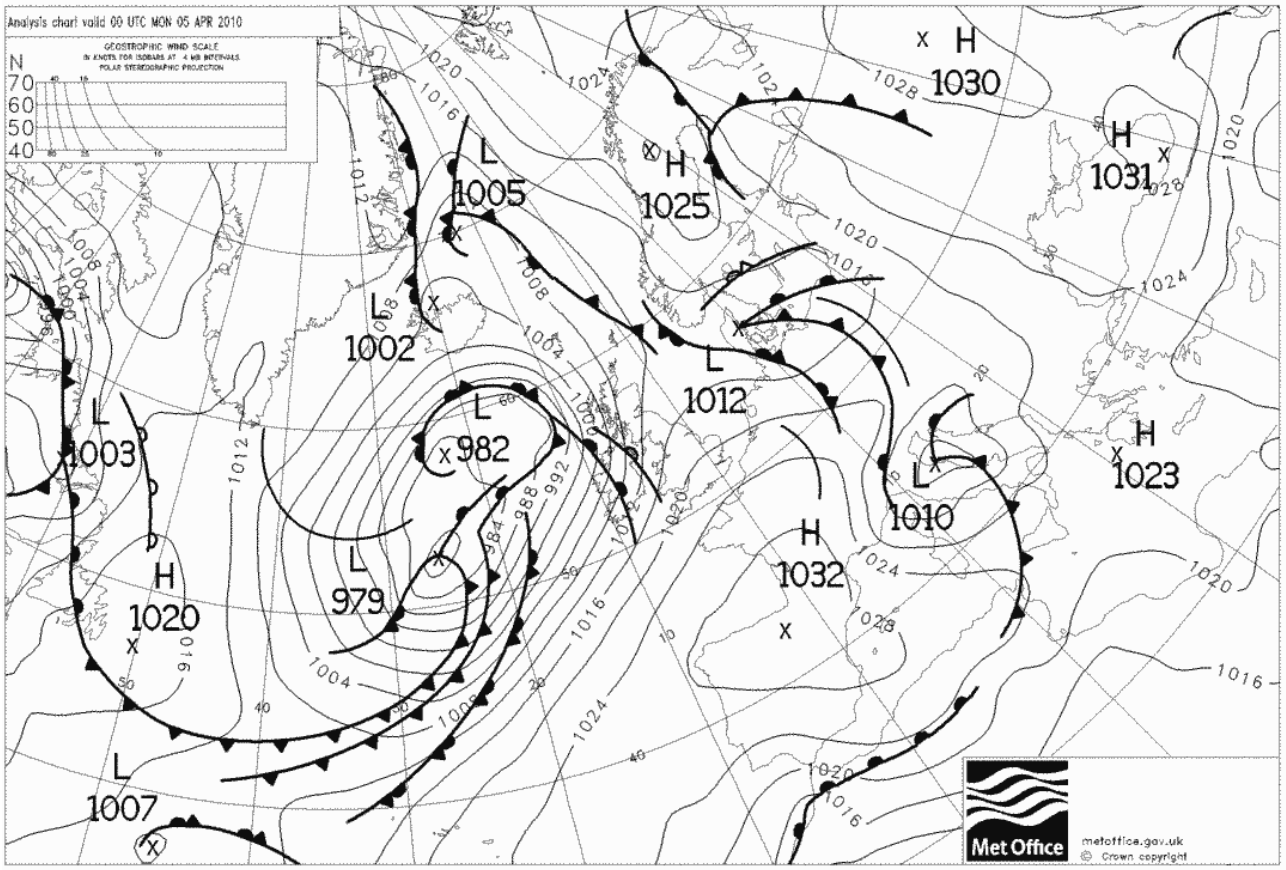
Analysis chart valid 00 UTC MON 05 APR 2010
GEOSTROPHIC WIND SCALE
IN KNOTS FOR ISOBARS AT 4 MB INTERVALS
POLAR STEREOGRAPHIC PROJECTION
N
70
60
50
40
L 1005
H 1025
H 1030
H 1031
L 1002
L 1012
L 1003
L 982
H 1023
L 1010
H 1032
H 1020
L 979
L 1007
Met Office
metoffice.gov.uk
© Crown copyright

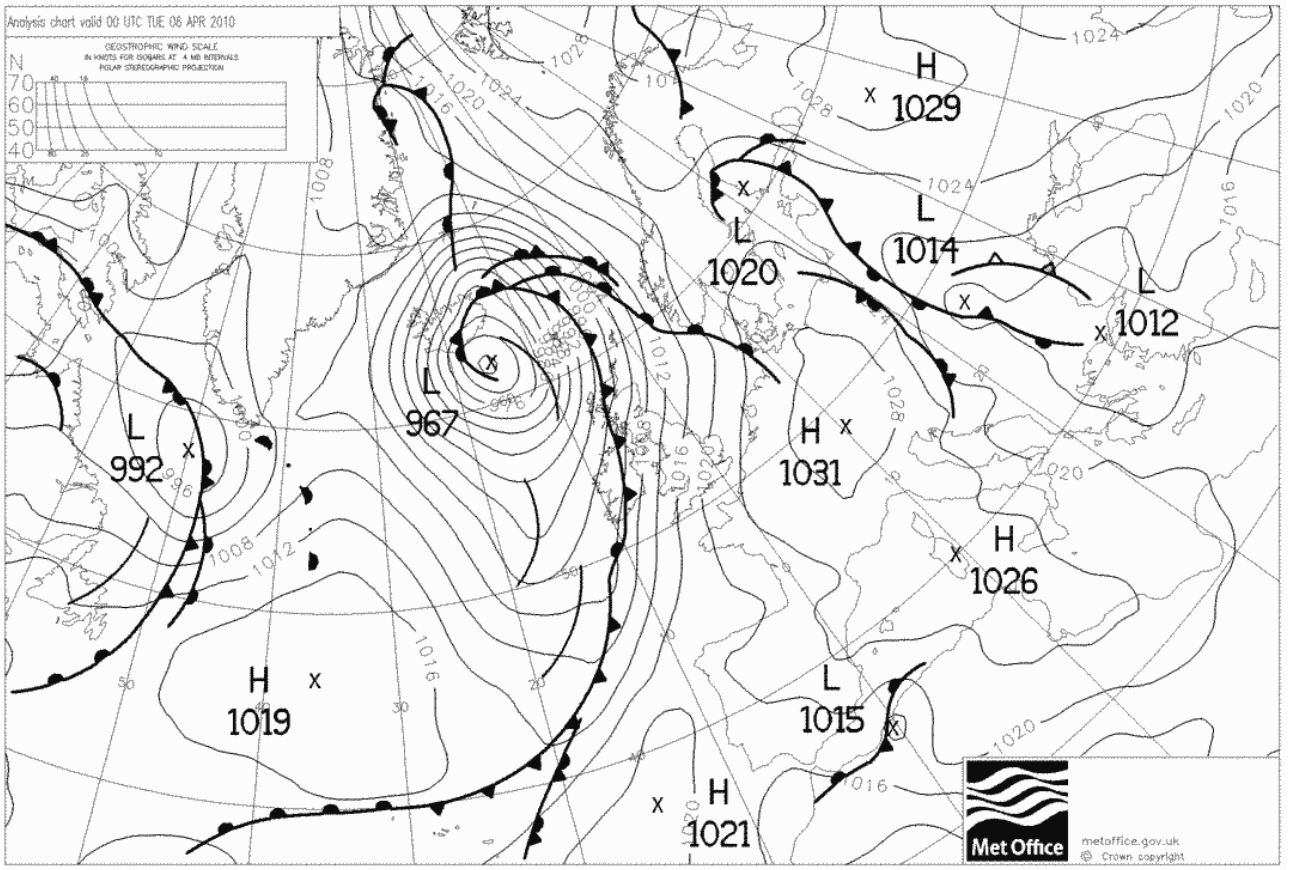
Analysis chart valid 00 UTC TUE 06 APR 2010
GEOSTROPHIC WIND SCALE
IN KNOTS FOR ISOBARS AT 4 MB INTERVALS
POLAR STEREOGRAPHIC PROJECTION
N
70
60
50
40
H
1029
L
1020
L
1014
L
1012
L
967
L
992
H
1031
H
1026
H
1019
L
1015
H
1021
Met Office
metoffice.gov.uk
© Crown copyright

Appendix F

Sea level maps (from http://www.oc.phys.uoa.gr/)

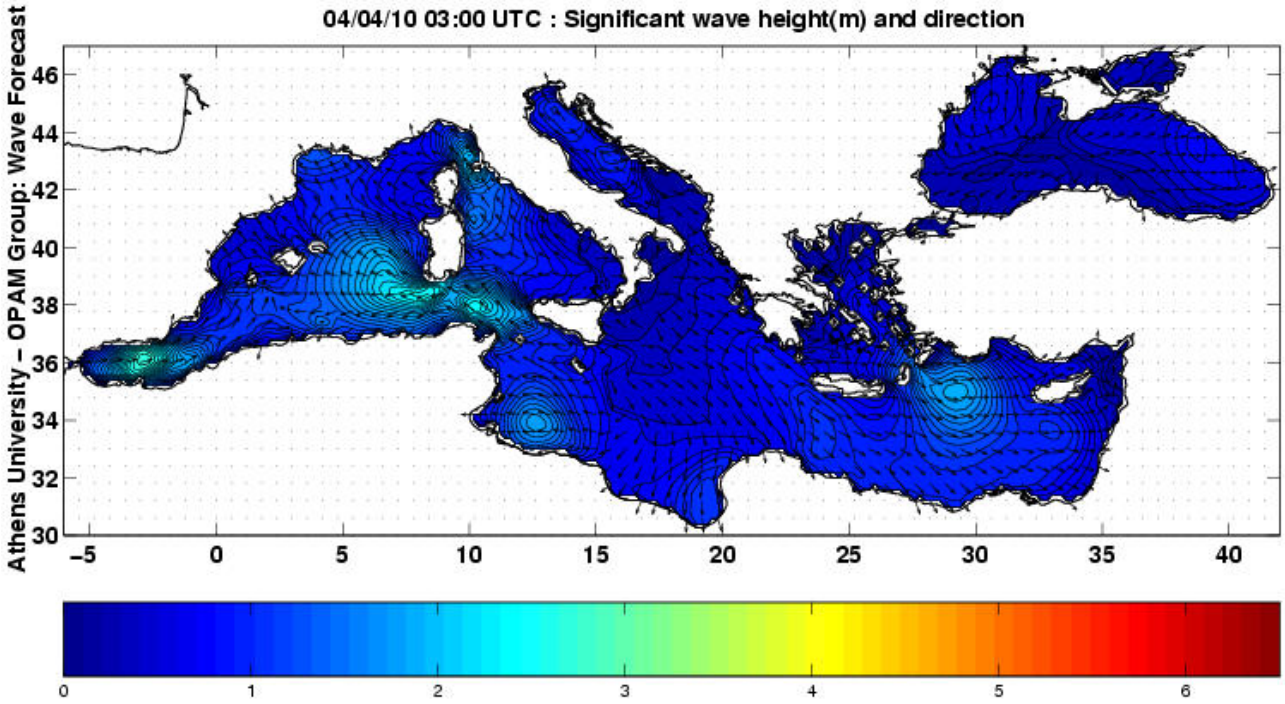

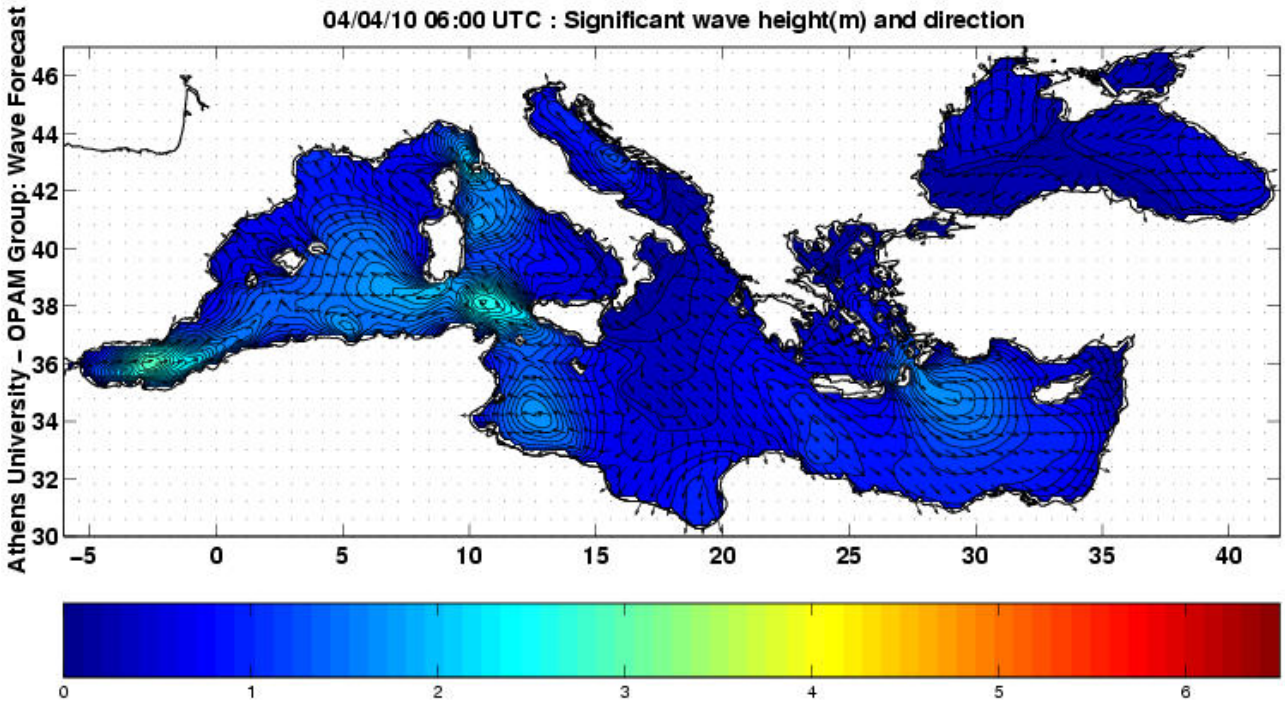

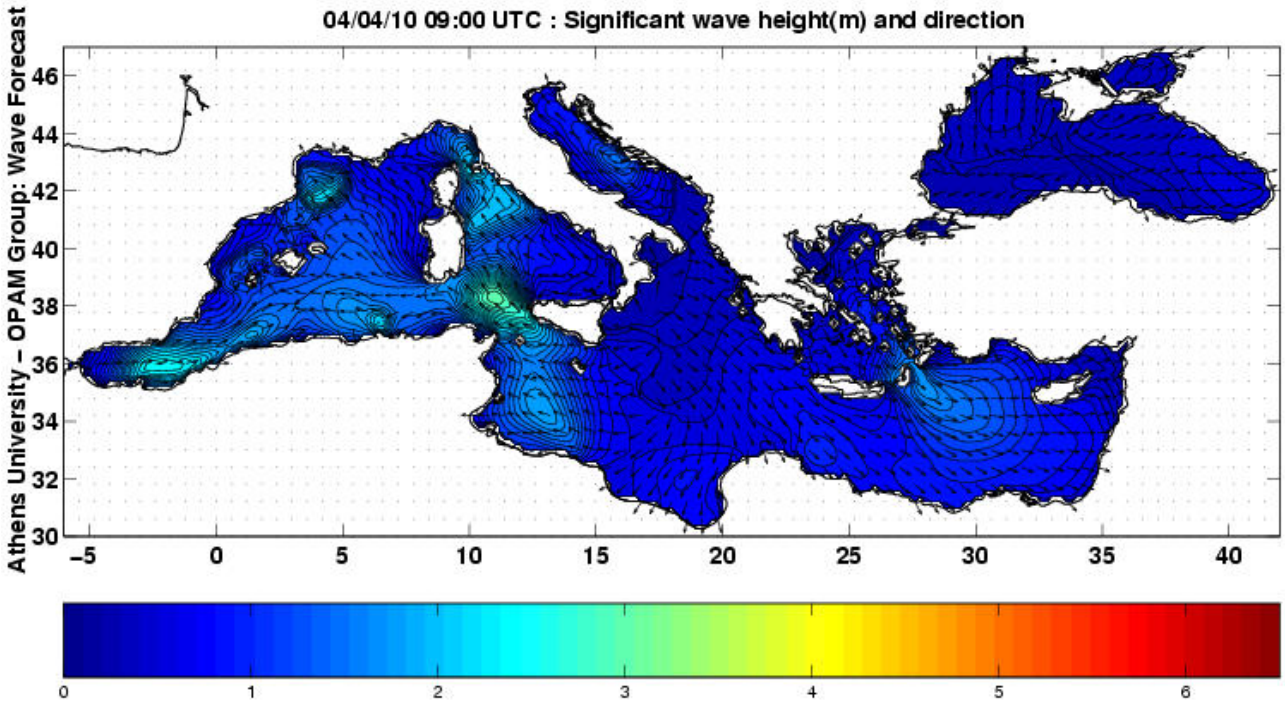
04/04/10 09:00 UTC : Significant wave height(m) and direction
Athens University – OPAM Group: Wave Forecast
46
44
42
40
38
36
34
32
30
−5
0
5
10
15
20
25
30
35
40
0
1
2
3
4
5
6

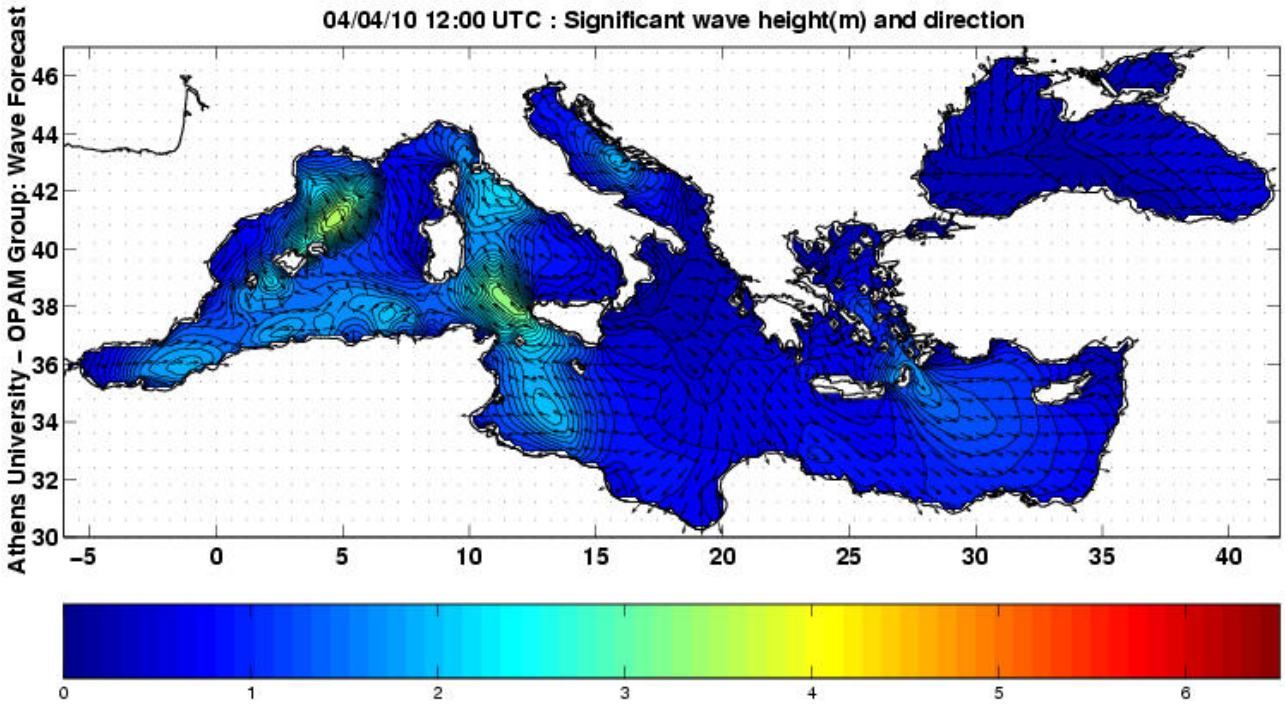
04/04/10 12:00 UTC : Significant wave height(m) and direction
Athens University – OPAM Group: Wave Forecast
46
44
42
40
38
36
34
32
30
−5
0
5
10
15
20
25
30
35
40
0
1
2
3
4
5
6

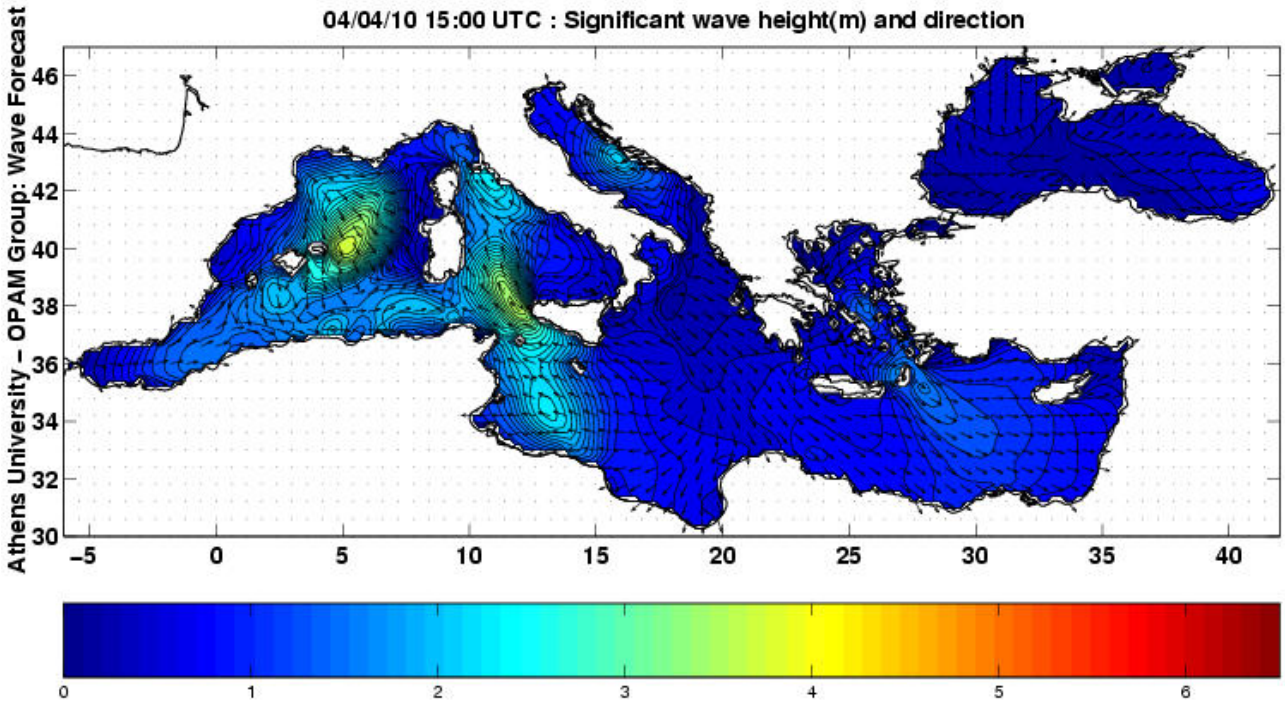
04/04/10 15:00 UTC : Significant wave height(m) and direction
Athens University – OPAM Group: Wave Forecast
46
44
42
40
38
36
34
32
30
−5
0
5
10
15
20
25
30
35
40
0
1
2
3
4
5
6

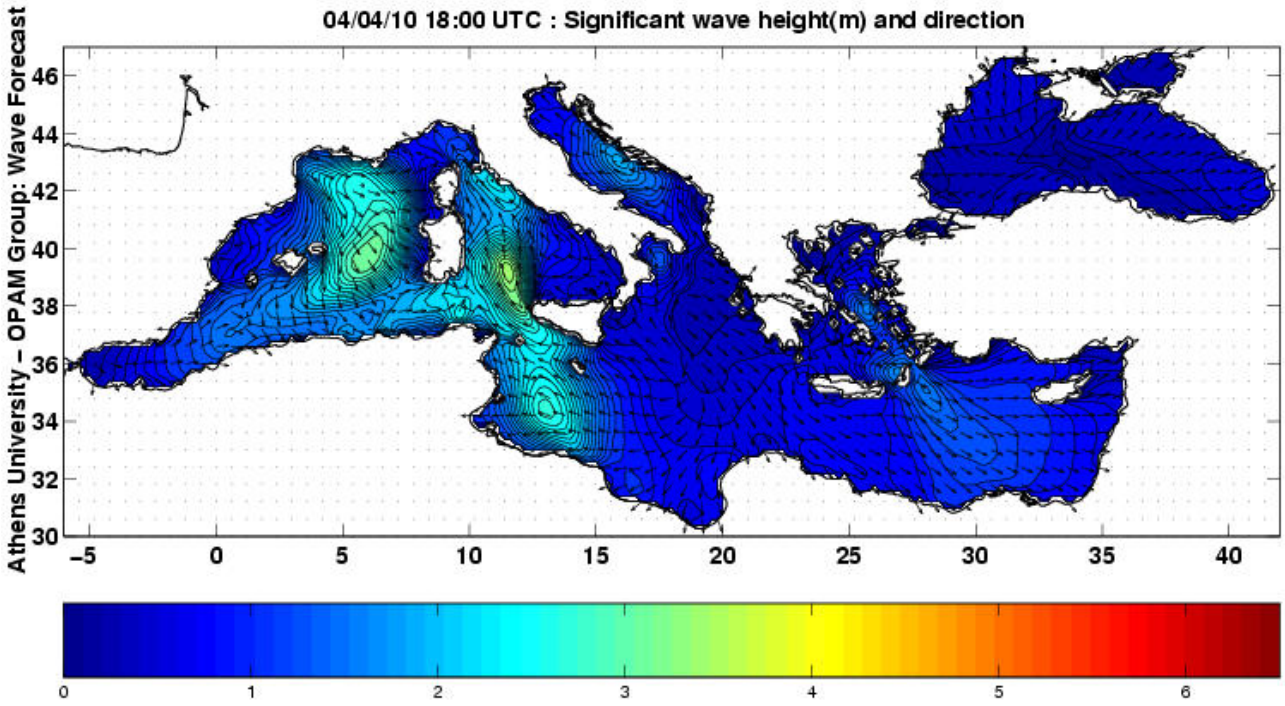
04/04/10 18:00 UTC : Significant wave height(m) and direction
Athens University – OPAM Group: Wave Forecast
46
44
42
40
38
36
34
32
30
−5
0
5
10
15
20
25
30
35
40
0
1
2
3
4
5
6

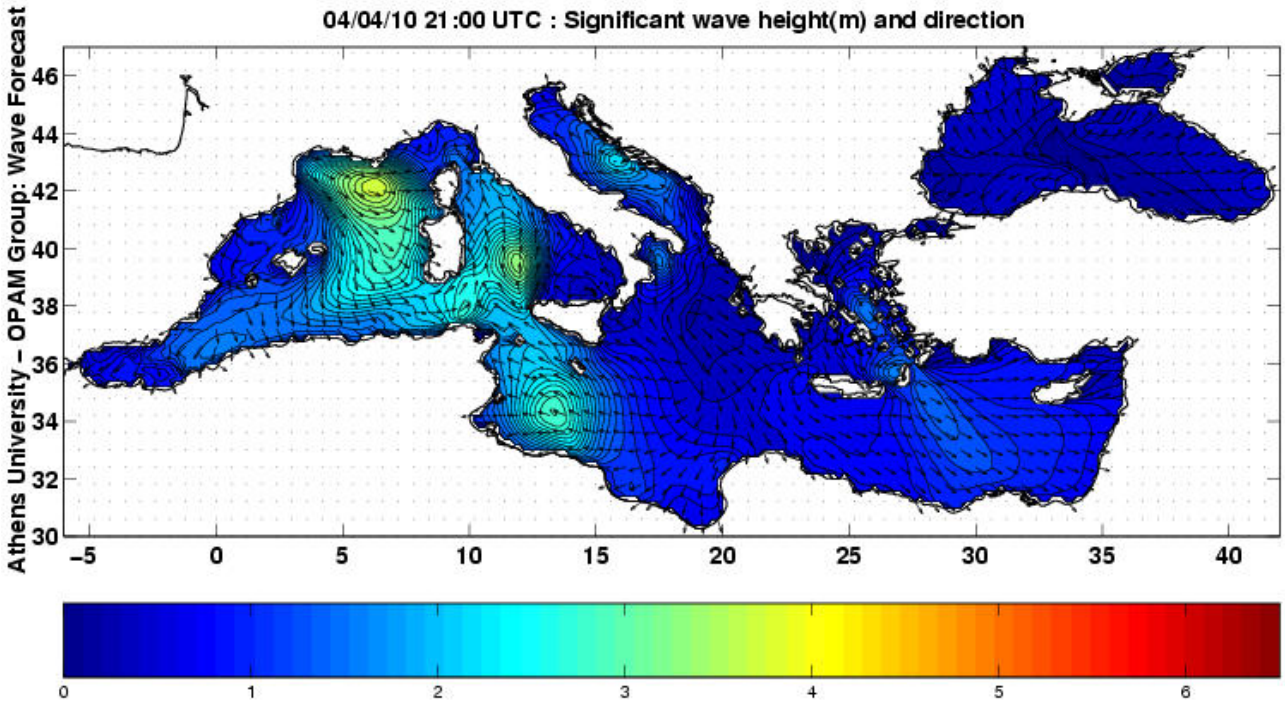
04/04/10 21:00 UTC : Significant wave height(m) and direction
Athens University – OPAM Group: Wave Forecast
46
44
42
40
38
36
34
32
30
-5
0
5
10
15
20
25
30
35
40
0
1
2
3
4
5
6

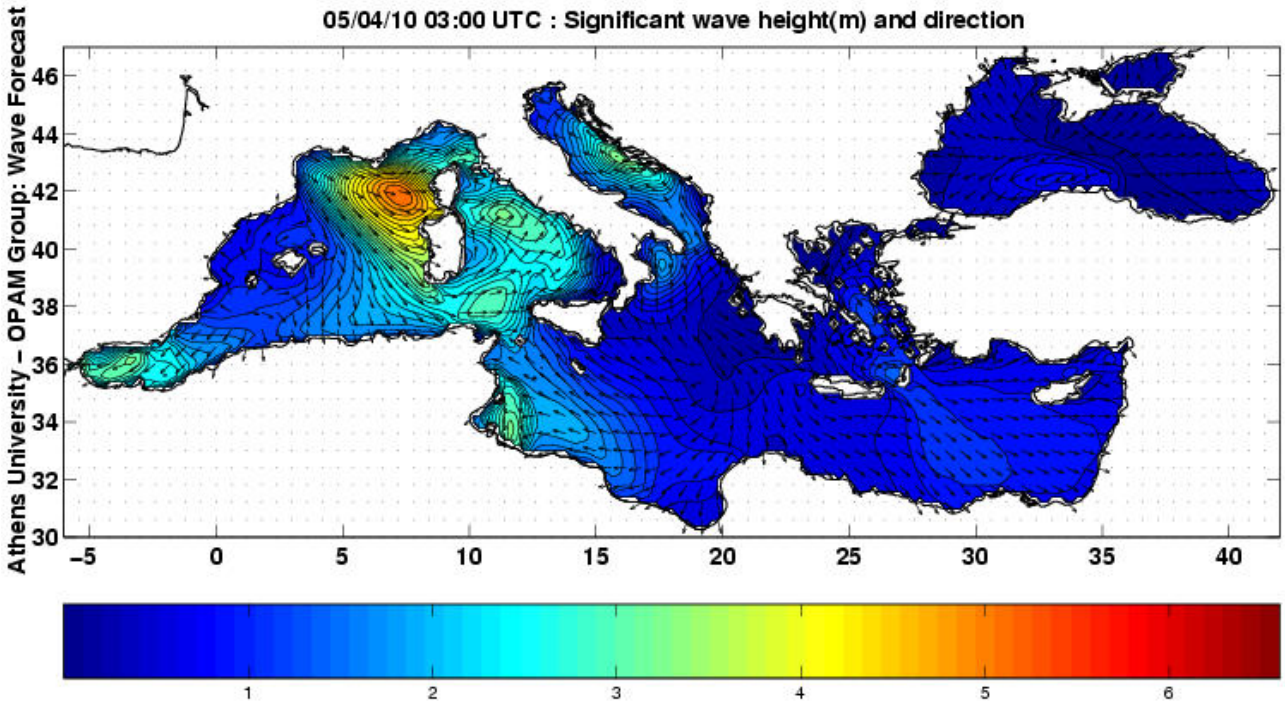
05/04/10 03:00 UTC : Significant wave height(m) and direction
Athens University – OPAM Group: Wave Forecast
46
44
42
40
38
36
34
32
30
-5
0
5
10
15
20
25
30
35
40
1
2
3
4
5
6

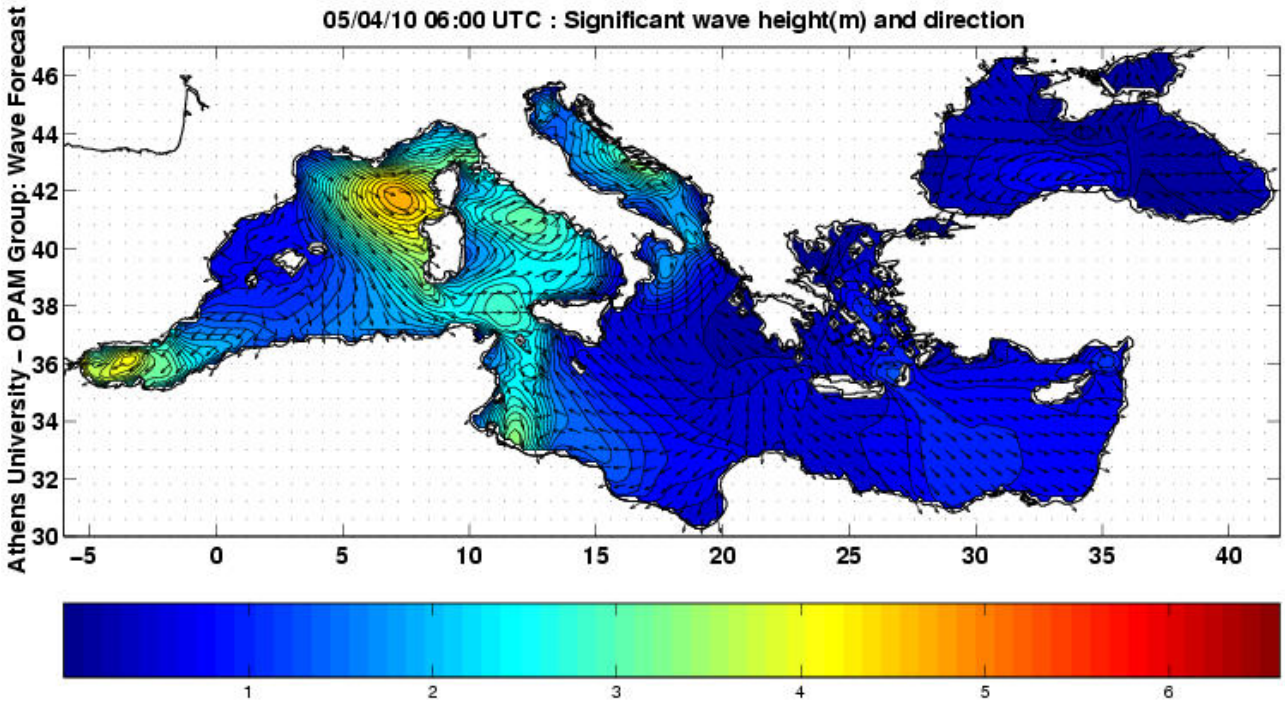
05/04/10 06:00 UTC : Significant wave height(m) and direction
Athens University – OPAM Group: Wave Forecast
46
44
42
40
38
36
34
32
30
−5
0
5
10
15
20
25
30
35
40
1
2
3
4
5
6

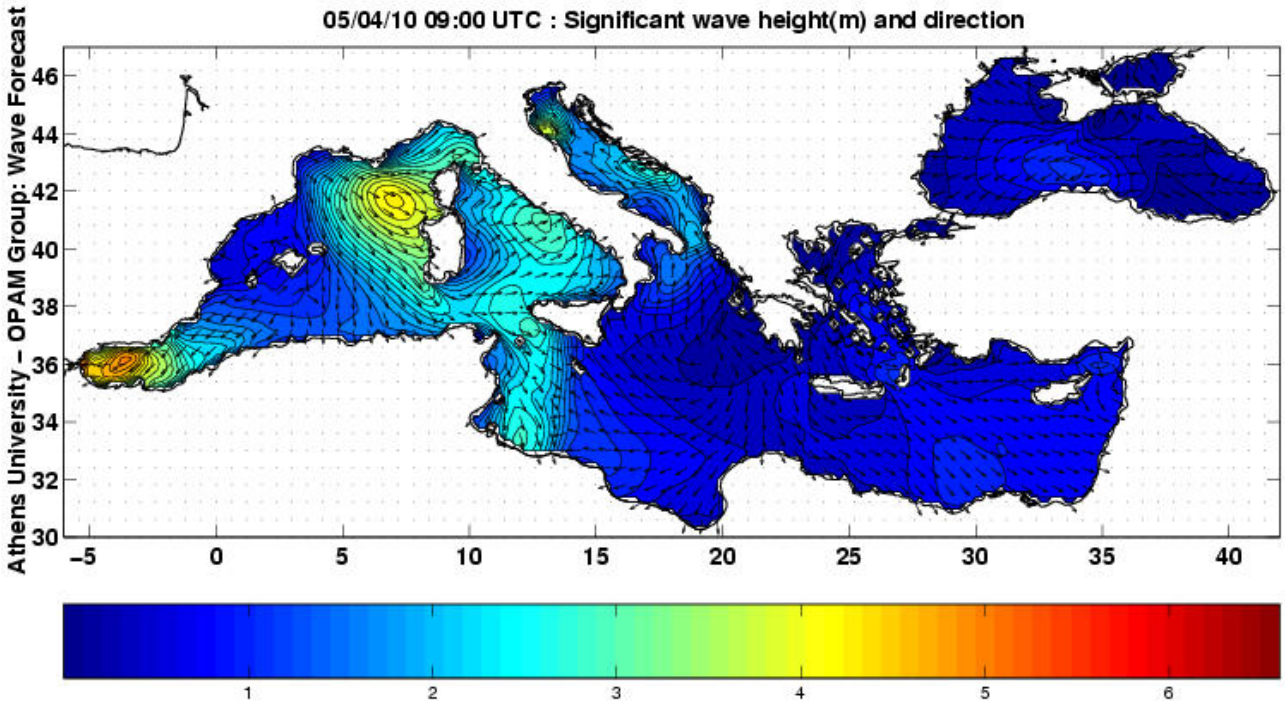
05/04/10 09:00 UTC : Significant wave height(m) and direction
Athens University – OPAM Group: Wave Forecast
46
44
42
40
38
36
34
32
30
−5
0
5
10
15
20
25
30
35
40
1
2
3
4
5
6

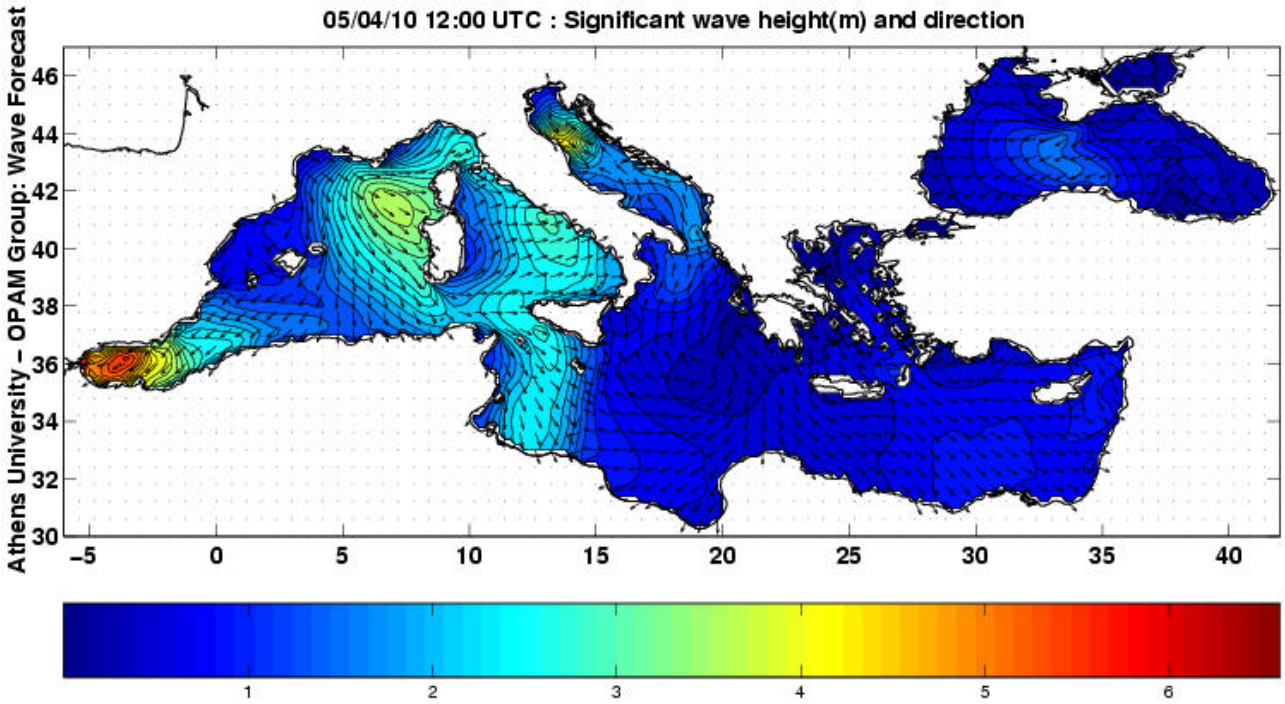
05/04/10 12:00 UTC : Significant wave height(m) and direction
Athens University – OPAM Group: Wave Forecast
46
44
42
40
38
36
34
32
30
-5
0
5
10
15
20
25
30
35
40
1
2
3
4
5
6

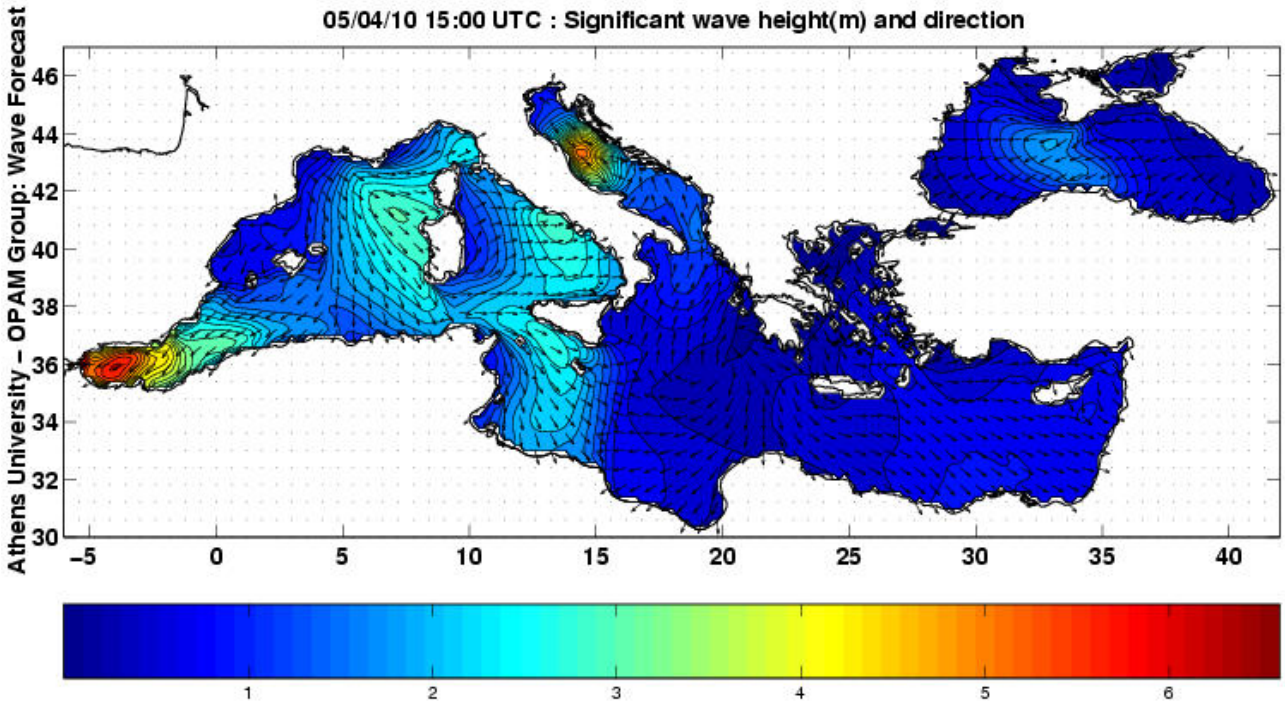
05/04/10 15:00 UTC : Significant wave height(m) and direction
Athens University – OPAM Group: Wave Forecast
46
44
42
40
38
36
34
32
30
-5
0
5
10
15
20
25
30
35
40
1
2
3
4
5
6

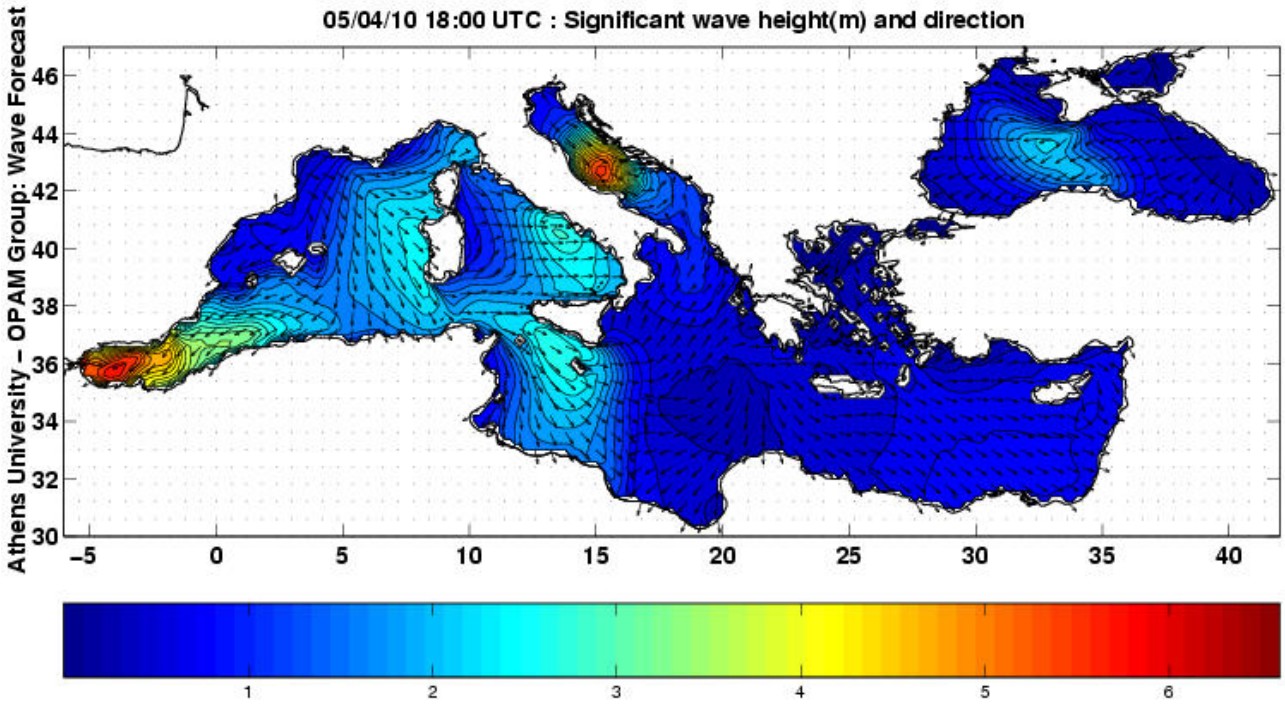
05/04/10 18:00 UTC : Significant wave height(m) and direction
Athens University – OPAM Group: Wave Forecast
46
44
42
40
38
36
34
32
30
−5
0
5
10
15
20
25
30
35
40
1
2
3
4
5
6